Dipl.- Ing. Wenzel Prochazka

A mechanistically deduced ageing model for lithium-ion cells

Thesis

in Partial Fulfillment of the Requirements for the Degree

Dr. techn.

Graz University of Technology

Faculty of Mechanical Engineering

Advisors:

Univ.-Prof. Dipl.-Ing. Dr. techn. Christof Sommitsch

Univ.-Prof. Dr. Martin Winter

In Cooperation with:

Virtual Vehicle Research Center, Inffeldgasse 21/A, 8010 Graz, Austria

Graz, 2013

Abstract

Modelling of the electrical behaviour of aged lithium-ion cells is a topic in which not only the ways of comprehensive modelling, but also the ageing behaviour itself is under research. Ageing changes the behaviour of lithium-ion cells in ways, not accurately predictable today. Therefore making products, using such cells, is a risk for many enterprises, especially to car makers using large quantities of cells in packages. A model providing rather reliable information about the electrical behaviour, the thermal sources and changes in electrical behaviour of a lithium-ion cell over the course of ageing is a well needed instrument. This also includes describing the causes of the ageing induced changes and how interactions between the cells' electrical and thermal load are given.

This work presents the reader an electrochemical base knowledge of lithium-ion cells and their intrinsic processes during short-term operation as well as during long term cell ageing. Thereof a mechanistically based electrical and thermal model, reproducing the short-term electrical behaviour of the cells under the influence of changing temperature, is deduced. The main features of the model shall be ease of parameterization, fast calculation times and a large range of applicability. The applicability is considered in two areas, first the different cell chemistries shall be modelled with the same model equation, and second a wide range of operation limits in electrical and thermal load shall be covered with the same equation and parameter set for single cell chemistries.

A large-scale ageing experiment is conducted with two different cell chemistries to research the cause dependence of single ageing effects on externally applicable influence factors. The four factors under research are the current rate, the temperature, the state-of-charge amplitude and the average state-of-charge. During the experiment over 180 cells are aged under singular pulse load only, in order to trace the causes of externally visible ageing effects. These, in electrical or thermal behaviour, noticeable ageing effects are equal to the change, increase or decrease, in parameter values received when fitting the short-term model to a new or an aged cell.

The identified aged parameters for the model are linked to ageing effects via a damage accumulation type model. Using the cell load data – the load history of the cells in form of two connected rain flow matrices – a second set of parameters for the damage accumulation model will be identified in order to describe the changes of the short-term model parameters over cell ageing.

Finally two application examples will show the ease of use of the fully integrated ageing and short-term model in stand-alone or coupled analysis settings using automotive use cases.

Acknowledgment:

The author would like to acknowledge the financial support of the "COMET K2 - Competence Centers for Excellent Technologies Program" of the Austrian Federal Ministry for Transport, Innovation and Technology (BMVIT), the Austrian Federal Ministry of Economy, Family and Youth (BMWFJ), the Austrian Research Promotion Agency (FFG), the Province of Styria and the Styrian Business Promotion Agency (SFG).

I would furthermore like to express my thanks to the supporting industrial and scientific project partners, namely AVL List GmbH, GAIA Akkumulatorenwerke GmbH, Volkswagen AG, University of Münster and to Graz University of Technology.

Furthermore a thank you appertains to Dr. Cifrain and my colleagues at the Virtual Vehicle Competence Center, as well as to my advisors Prof. Sommitsch and Prof. Winter.

A special thank you to Dr. Igelchen, my family & friends.

Content

1 Introduction

Research focussing on lithium-ion cells as energy storage has focussed on material development [Yabuuchi03, Muraliganth10, Fisher10], production technologies [Kim09, Kurfer12] and material ageing [Abraham02, Vetter05, Wiedemann07], as well as the modelling [Doyle95, Newman04, Christensen05, Dreyer11] and simulation [Herb10, Safari10, Safari10A] of these issues, for more than a decade [Aurbach99]. The applications for lithium-ion cells are numerous, ranging (in the order of amount of energy stored) from portable devices [Tröltsch05], to automotive [Fischnaller11, Dubarry11B], to airborne [Marks13] and grid tied stationary [Kawakami10, Pourmousavi10] applications. Except for portable devices, all of the named applications feature requirements in cell lifetime of more than five years on average [Markel08, Notter10, Dubarry11]. Hence the question arouses, whether a certain cell type can withstand the load of the application for the time required while designing a product. Answering this question is the focus of the latest research in simulating the short-term behaviour of lithium-ion cells [Vergossen11, Andre11, Schmidt10] and calculating the changes thereof while the cell ages [Ramasamy07, Hartmann08, Herb10]. For long, models which only featured the short-term behaviour (e.g. voltage as a function of current, state-of-charge and temperature) were used to simulate voltage response to the load [Buller03, Waag13] and separate models, only featuring derived quantities as capacity or resistance, were used to estimate ageing of the cells [Kim08D, Smith09, Duderzert09, Thomas08]. These models do have the advantage of easy parameterization [Sauer08, Ecker12], but do not give the engineer all the information about the cell, necessary for the system integration into complex mechatronic application, such as automobiles or planes [Kim07, Guo11B, Prochazka11]. Bridging this gap, by developing a consistent, electrochemically based process from cell measurement all the way to the short-term simulation of an aged cell is the central motivation of this work.

The derived quantities, such as capacity decrease of aged cells are documented in literature for different loads, like high temperature [Smith12], low temperature [Jansen07, Abraham08B], high current [Kassem12] or no current at all (calendar ageing) [Zhang07F, Belt11]. Most of the time the experiments were done with proprietary cells, featuring only partly specified chemistries [Broussely01, Liaw05], so the results are not comparable except for the basic notion. Some researchers tried to extend their test towards more influences and/or test full-factorial [Fischnaller11, Hartmann08], but still only derived data is published [Safari11B]. In order to characterize the cells' dependence on multiple influence factors and measure the base data for the short-term simulation of cells in their aged states, a large scale experiment was performed [Prochazka13]. This experiment introduced design-of-experiment methods for larger scale lithium-ion cell ageing experiments known from fuel cells [Wahdame09] or combustion engines [Haselgruber08].

The short-term modelling available in literature can be categorized in three model types: electrochemical models solving partial differential equations for simulation [Newman03, Newman04, Dees08, Safari11, Bernardi11, Latz11, Scharrer11]; equivalent circuit models using simple algorithms but large parameter arrays [Sauer08, Andre10, Herb10] and empirical models trying to use first principles to reduce the amount of parameters while keeping the algorithms comparably simple [Ning04, Prosini05, Hartmann08]. The ageing models are dependent on the type of short-term model: for the electrochemical short-term

models special model extensions exist, which greatly increase the complexity of the models [Christensen03, Christensen04, Christensen05, Safari09], while the empirical and RC models mostly use simple models connecting the parameters to some average application load values [Hartmann08, Herb10] or models dealing with derived quantities are used without coupling to an aged short-term model [Pesaran09, Thomas08, Fischnaller11]. The herein presented short-term model is a mechanistically deduced model of the empiric type, where the ageing model has also been deduced using the mechanistic cause-effect relations. The ageing model is an integral part of the short-term model for aged cells. This model topology was selected to overcome the limitations of either extensive calculation time or electrochemical parameter measurements as in mechanistic models [Zhang11B] and the complete disconnection of parameters to mechanisms during ageing as in equivalent circuit models.

1.1.1 Guide to the work

The work follows a general modelling and simulation process, wherein the problem is identified first and measurements or equivalent information is generated. Next are a description and parameterization of the model, followed by a simulation of an application problem.

Figure 1.1.1-a - Process of modeling and simulation as presented in this work

This process is depicted in Figure 1.1.1-a for the lithium-ion cell ageing model presented in this work. Each step is marked by an arrow with the task performed and the subchapters in which the description thereof can be found. The last segment states the motivation behind the work done as being the ability to simulate cell durability.

Figure 1.1.1-b is showing the steps to be taken to reach this target in more detail. The theoretical chapters of the work, positioned in the top left corner in the figure, are base information needed for the reader to understand the chains of thought in the following chapters. Arrows indicated the logical path through the chapters, standing either for an input to another chapter or a detail of the previous chapter being treated in the next chapter.

The two input chapters are recapitulation of the knowledge found in literature, adapted only to have consistent naming. All the other chapters are filled with the description of the work performed by the author. The chapters 2.1.3, 2.2.1, 2.1.4, and 3.1.2 contain the theoretical description of the main scientific achievements of the works. The two output chapters describe the results received from the experiment as well as from simulation.

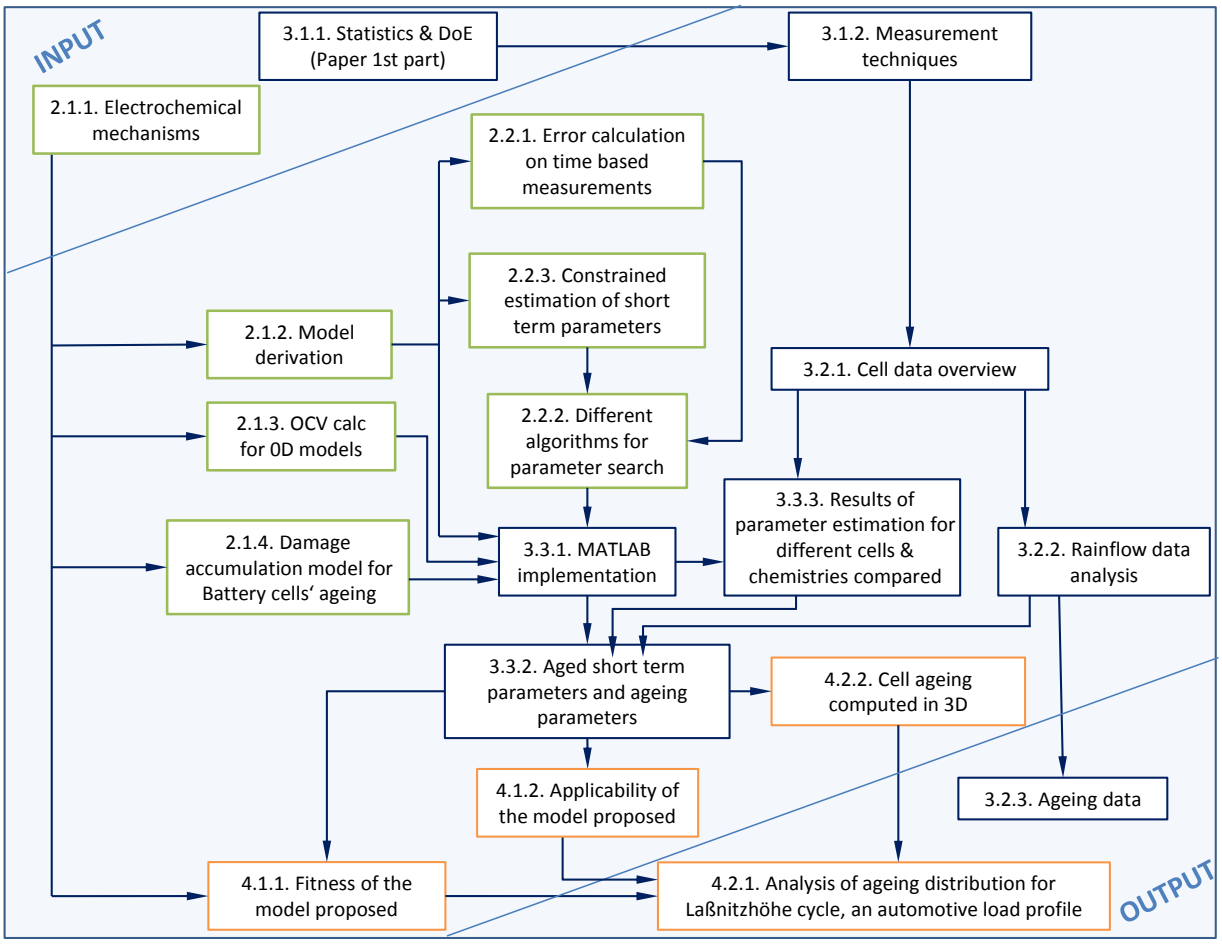

Figure 1.1.1-b - Flow diagram of the subchapters as presented

2 Theory & Methods

The following chapters are based on an in-depth knowledge and systematic understanding of the physical and chemical processes in the confined space inside the can or pouch of a lithium-ion cell. Although some of the mechanisms lie in the dark of future grasp, this work will try to connect those mechanisms known in literature and the theories of mechanical engineering with the respective, but not always conforming, views of chemistry, physics, engineering and mathematics.

In the first subchapter, the basic theory and the herein applied methods will be presented, starting from an electrochemical view into the depths of cell chemistry, followed by an interpretation of the mechanisms and driving forces by the likes of an engineer. The model building and statistic parameterization processes lead into the mathematical statistics.

2.1 The model of the electrochemical cell processes

2.1.1 Electrochemical mechanisms

Any statement in this chapter, which is not explicitly cited from another source, is based on the three primary books on electrochemistry used by the author. These books are [Bard01, Linden02, Vielstich98].

2.1.1.1 The basics

An electrochemical energy storage and conversion device converts chemical into electrical energy on demand. It is usually made of two electron conducting electrodes spaced apart by the ion-conducting electrolyte and usually a separator to prevent electrical short circuit between electrodes. Redox reactions, which take place at both electrode surfaces, produce electrons (e^-) in the oxidation reaction (anodic reaction under discharge conditions) and consume them in the reduction reaction (cathodic reaction under discharge conditions).

Oxidation reaction: $A \rightarrow A^+ + e^-$ (2.1.1-1)

Reduction reaction: $C^+ + e^- \rightarrow C$ (2.1.1-2)

In some electrochemical systems, these equations are not reversible (discharge only), called primary cells. In other systems, as lithium-ion cells, the reactions are close to fully reversible. The parts which are not reversible – plus some additional, irreversible reactions – are known as ageing of the cells. For lithium-ion systems the basic redox reaction of lithium metal is as follows:

$$Li \rightleftharpoons Li^+ + e^- \quad (2.1.1\text{-}3)$$

This reaction takes place at the surface (interface) between electrode and separator/electrolyte. To provide a high current capability cells are built from active particles, forming a porous structure with a large inner surface.

For better electronic conduction the cathode and the anode in lithium-ion cells are made of compounds of an electrically conductive foil and a thereon homogeneously distributed mixture of particulate lithium-ion active material and some inactive material for electron conduction and adhesion. The two active material compounds enclosing the separator are shown in Figure 2.1.1-a. The active material particles are pictured as circles (or ellipses), while the binder and conductive additive are distributed ideally at the contact points of those circles. This originates from the production process, wherein a fourth, wax-like component is mixed into the raw material, which, after shaping and pressing the electrode, is drained out by heating, leaving behind the empty pores of the porous structure. The active material particles show a statistical distribution in size, influenced by the concentrations and temperature of the raw reagents during the production [Drezen07, Shina10].

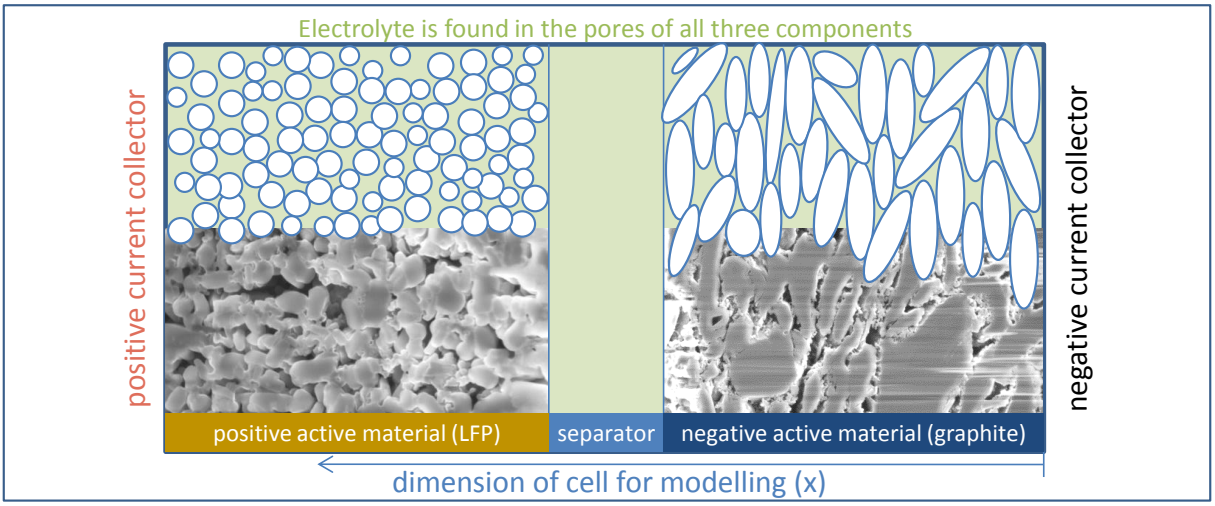

Figure 2.1.1-a - Porous electrodes for the example electrode pairing lithium iron phosphate (LFP) and graphite. Top half is the modelling assumption of diffusion plane spherical/elliptical particles, bottom half ion beam-cut scanning electron microscope (SEM) picture for comparison.

These electrodes are produced as large sheets, which are then stacked to form the layered structure. The stacked cell layers can be seen in Figure 2.1.1-b. This elementary stack is only several ten (to a few hundred) micrometres in height, but can be meters in length and depths, to reach cell sizes in the order of ampere hours. It is therefore more practical to stack more than one elementary layer or roll the stack so as to fit a large electrode area into a cell, which has all three dimensions of small size. The stacking or rolling of the electrode sheets enhances volumetric energy density of the cells to be used in energy demanding applications.

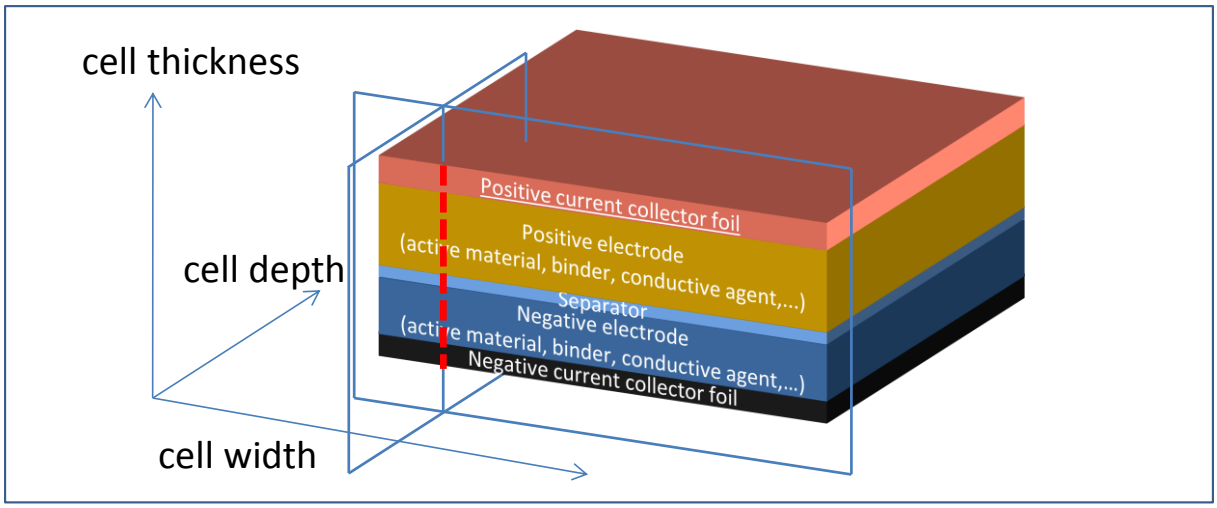

Figure 2.1.1-b – Schematic view of the elementary sheet structure of a lithium-ion cell geometry

2.1.1.2 Energy

Energy in terms applicable to a battery cell is defined as:

$$\text{Energy} = \text{Voltage} * \text{Current} * \text{Time} \quad (2.1.1\text{-}4)$$

$$[\text{Ws}] = [\text{V}] * [\text{A}] * [\text{s}] \quad (2.1.1\text{-}5)$$

To receive a high energy storage capability, a cell should have a high potential difference between the electrodes, good current flow capability and a large ion storage capacity.

The electrochemical cell is a non-ideal voltage source, meaning it supplies a specific electrical voltage while not supplying current. When current is flowing, the voltage, at which the current is supplied, becomes instable and decreases.

The meant ideal voltage is the external electrical voltage, which can be measured at the poles on the outside of the cell. Within the cell this voltage is found as the difference of the electrode potentials. The electrochemical definition of the electrode potential is more complicated, consisting of a highly interactive mixture of chemical and electrical potential fields [Bernardi85]. The chemical potential describes a species' ability to react with another species to form a third species. The electrical potential describes the electrostatic force field emitted by the lack or surplus of charges in an area, which is physically measured via the energy an unitary point charge would accumulate when put from infinity to this location [Stephan09].

So when regarding a piece of pure lithium metal, which is put into a solvent, each solvated lithium-ion leaves behind an electron on the surface of the metal,

$$Li + X\,solvent \rightleftharpoons [Li^{+}solvent_{x}] + e^{-} \quad (2.1.1\text{-}6)$$

thereby a surplus of electrons is formed in the metal surface and a negative electrostatic potential field builds within and around the metal in the solvent. This same potential field inhibits the now solvated positive ions leaving the surface of the metal, forming the well-known double layer, a layer of positive ions on the liquid side of the imaginary phase boundary, and a second layer, in which the electrons have their highest probability of dwelling on the inside of the solid [Guo11]. The layers of charges are displayed in Figure 2.1.1-c.

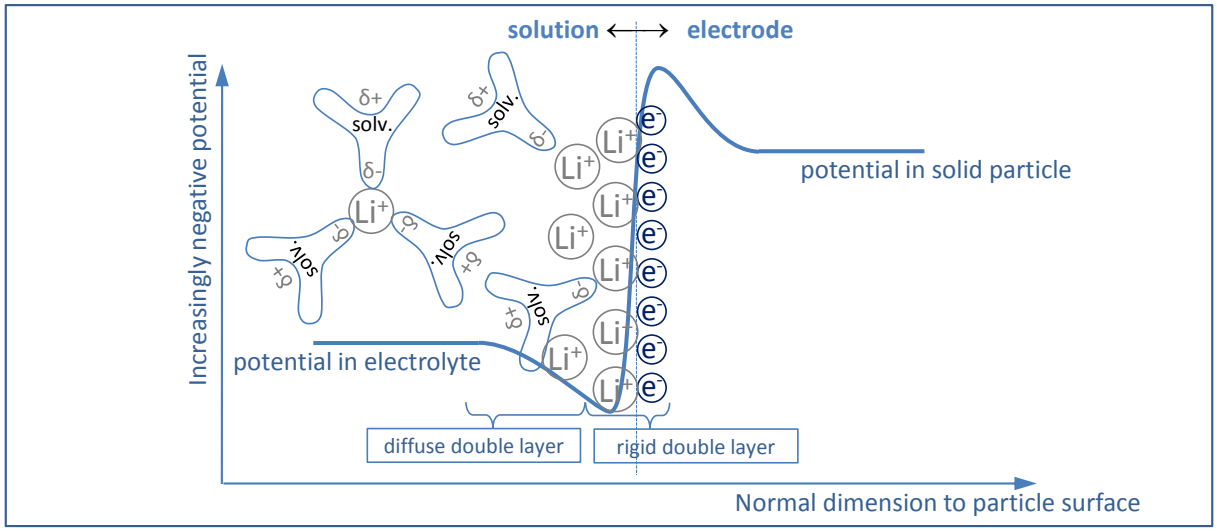

Figure 2.1.1-c - Detail of the potential at the phase boundary

This effect becomes measureable only, when two pieces of different metals are put in the same solvent (or electrolyte, when a salt was added) container, as difference in electrical potential (= electrochemical cell voltage) of the two metal pieces. The difference in electrical potential is also dependent on the chemical potential of the metal in focus in relation to the solvent used. Metals release positively charged ions, whereby the amount of release is dependent on the chemical potential of the material, thus causing different field strengths, when measured against a reference electrode. More noble metals release less ions, becoming more positive when compared to less noble metal, this order is known as the standard electrode potential series.

Not only metals, but any electron conducting material can form an electrical phase boundary potential, a basic requirement for energy storage (2.1.1-4), also intercalation materials. These materials have the capability to host for example lithium ions in their interstitial lattice spaces [Allan08], They can form a double layer by dissolving lithium, but the lithium is not being oxidized for solvation, rather is the host material oxidized to free the lithium ion [Karthikeyan08, Kang11].

$$[Li^{+}Hostmaterial^{-}] \rightleftharpoons Li^{+} + e^{-} + Hostmaterial \qquad (2.1.1\text{-}7)$$

Whereby the main difference of intercalation materials is the distance between the ionic lithium and the place in the host material where the electron (negative charge) is located. [Benedek08]. Cathode materials should have large potential differences to lithium metal, so the electron is far from lithium-ion. Whereas a good anode material should be more metal-like, with a close coordination of electron and intercalated lithium ion. But the potential difference should not be less than 2mV according to [Harris10], so as to avoid forming of metal deposition on the surface of the anode [Tang09A].

Both electrodes in a lithium-ion cell have negatively charged solids and the external electrical voltage must therefore also be related to the differences in amount of currently solvated ions per electrode. In this case the remaining concentration of the ions within the host material plays an important role in defining the strength of the electrical potential [Muraliganth10]. This relation is most often characterized in relation to a pure metal electrode of the same ionic species, known as half-cell open circuit voltage (hcOCV), or, if measured for both working electrodes at once, as full cell open circuit voltage (OCV).

Another factor in building the electrode potential is the electrolyte used. An electrolyte is a solvent mixture wherein a salt is solvated. The salt consists of positive cations, those which are supposed to be transported and intercalated (e.g. Li^+), and the negative anions, which are physically necessary to balance the charge neutrality within the solution. The salt concentration within the cell has two effects, which are notable for the cell voltage. First, it enhances the transport of charge from one electrode to the other, by supplying ions to one electrode and retrieving them from the other one without the necessity to transport one and the same ion the whole distance [Zugmann11]. Second, as described by Nernst's equation (2.1.1-8), it lowers the amount of ions in the double layer since solvation becomes less and less attractive the more ions are already dissolved, resulting in a lower electrical potential when increasing concentration; see [Stephan09] for a complete derivation from Gibbs Free Energy formulation.

$$E = E^0 + \frac{RT}{zF} \ln\left(\frac{c\left(A^+\right)}{c\left(A\right)} \right) \tag{2.1.1-8}$$

A lithium cell system of two electrodes, e.g. a metal electrode in conjunction with an intercalation material counter electrode, is regarded. The more negative material released more ions into the liquid phase to become so, compared to the more positive material. If one would close the electrical circuit and let electrons flow between the two electrodes, the electrons would flow from the negative to the positive electrode. The ions in the cell would also transfer in the same direction, but through the electrolyte.

Since all species in the cell move on their own only if the inner energy in the new state is lower than before, two statements can be made for lithium-ion cells specifically. On the one hand the discharge process, when releasing energy, means that electrons and ions flow from the negative electrode to the positive electrode creating a current. When charging a cell, moving the electrons and the ions to the negative electrode, energy has to be supplied to the cell (secondary cells only). On the other hand this means that the lithium-ions have a lower

state of inner energy when intercalated in the cathode than in the anode, while the electrodes are more positively charged the less lithium ions are within them.

2.1.1.3 Intercalation materials for lithium ions

Cathode materials used for commercial lithium-ion batteries today are mostly made from transition metal oxides or from iron phosphate. They all feature mean potential levels of around 3 to 4 volts against lithium metal. Except for lithium iron phosphate, which has a mostly flat characteristic around 3.35 volts [Zaghib08], the potential versus lithium concentration curves of the metal oxides materials are slopes with a drop at around 3.2 to 3.3 volts and a steep rise at around 4.4 to 4.5 volts [Liu10].

The main differences of the materials are given by four material properties, the open circuit potential, the gravimetric capacity, the lithium diffusion rate and finally the material stability at elevated temperatures. Whereas the metal oxides can deliver Coulombic capacities in excess of 200 mAh/g [Tran11] and good 2-dimensional diffusion of lithium within the particles, but compromised stability due to oxygen release at higher temperatures, the iron phosphate cathodes feature Coulombic capacities of up to 172 mAh/g [Sinha10], diffusion along a single crystallographic axis, and a good material stability.

Cells with both types of cathodes are used in this work. Iron phosphate cathodes will be marked by their three letter abbreviation (LFP) of the chemical short name $LiFePO_4$. From the group of transition metal oxides the “NCA 80/15/5” has been used. This abbreviation stands for $LiNi_{0.8}Co_{0.15}Al_{0.05}O_2$.

For these cathode materials the reaction equations, assumed for this work, feature the transfer of the electron via the host material as postulated by [Karthikeyan08].

LFP:

$$Fe^{(+III)}PO_4 + e^- + Li^+ \rightleftharpoons Li^{(+I)}Fe^{(+II)}PO_4 \qquad (2.1.1\text{-}9)$$

NCA:

$$Ni_a^{(+III)}Co_b^{(+III)}Al_c^{(+II)}O_2 + e^- + xLi^+ \rightleftharpoons Li_x^{(+I)}Ni_{a-x}^{(+III)}Ni_{a-x}^{(+II)}Co_b^{(+III)}Al_c^{(+II)}O_2 \qquad (2.1.1\text{-}10)$$

The anode material used in most lithium-ion cells nowadays is a kind of carbon. Carbon exists in many natures, from amorphous structures in hard carbons to highly ordered graphene layers in natural graphite. All different types are used in lithium-ion cells for their differences in properties, like diffusion rate, capacity and ageing rate [Flandrois99].

There are several alternative materials available or in research, but none has yet reached the ubiquity of carbon. Those alternatives have the advantage of providing one of the three material properties at a very high level, but the disadvantage of having the other two at very low levels or being overly expensive [Christensen06, Stewart08C]. This leaves us to explain some properties of the graphite, as it is the single anode used in this work.

The base structure is made up of hexagonally connected graphene layers stacked in an AB order when empty, meaning that one layer is set off the other such that the carbon atom of the second layer is just above the middle of the hexagonal structure of the first layer. The following third layer is exactly congruent to the initial layer. The spaces in between those layers are available to the lithium ions, see Figure 2.1.1-d, while their electrons remain in the graphene layers for good conductivity [Wang11]. When filled with lithium ions, the layers are all congruent, hence the stacking is AA.

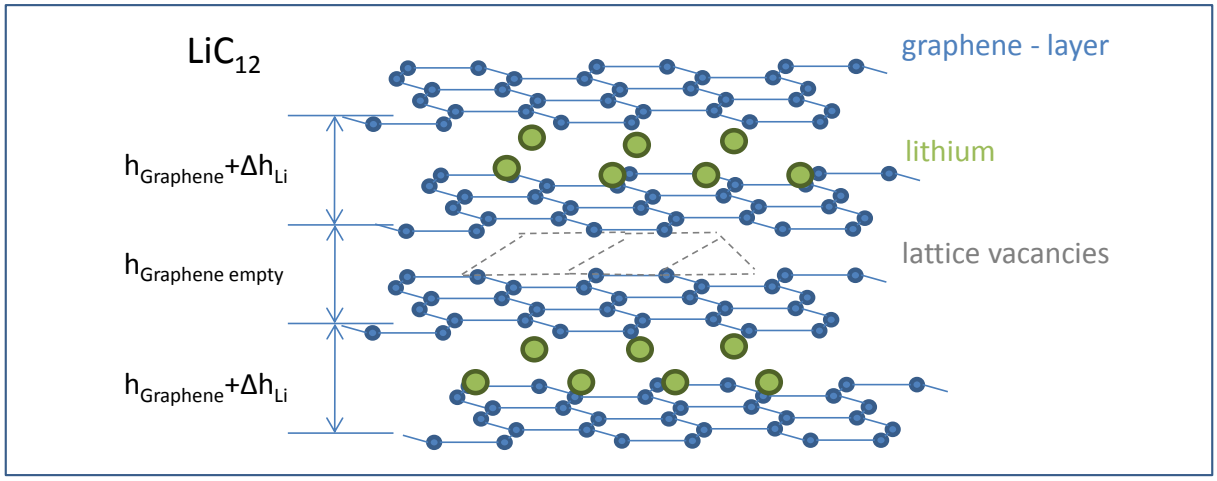

Figure 2.1.1-d - Lithium intercalation in graphite

Every time a new layer is opened by the first lithium ions, the graphite structure is widened and the chemical potential is increased. Nearly amorphous structures of hard carbons, made of many very small grains of layered material, allow diffusion along the grain boundaries in all three dimensions of space, but this diffusion is rather slow, while graphene layers have very high diffusion rate in plane direction, but none perpendicular to the plane [Persson10]. Also according to this literature source, the reaction equation for lithium intercalation in graphite can be written as:

$$xLi^{+} + e^{-} + C_6 \rightleftharpoons Li_x^{(+\delta I)} C_6^{(-\delta I)} \qquad \text{wherein}: \quad \delta \le 1 \quad x \le 1 \tag{2.1.1-11}$$

The energy stored within the graphitic material has two main energy storage mechanisms, the dissociation of the lithium-ion and the electron, and a small part is the material elasticity of pushed apart layers.

2.1.1.4 Electrolytes featuring lithium ions

An electrolyte consists of a mixture of solvents and salt containing lithium as cation (positively charged ion). The base ingredients for today's electrolyte mixtures are organic solvents like ethylene carbonate (EC), diethyl carbonate (DEC), dimethyl carbonate (DMC) or

propylene carbonate (PC) [Geoffroy02]. Since those species have different solution strengths and melting points, they are not used in pure form, but in mixtures like EC:DMC 3:7. This mixture has the advantage of being a good solvent for a lithium salt and being liquid with sufficiently low viscosity at normal operating temperatures.

The salt, which is added to the solvent, is also not restrained in selection. There exist several commercially available lithium salts with anions such as hexafluorophosphate (PF_6^-), perchlorate (ClO_4^-) or bis(oxalato)borate ($[B(C_2O_4)_2]^-$) [Taeubert10]. They feature different properties in diffusion rate, polarization strength (or ionic conductivity) [Zugmann11], cost and most important in formation of a stable insulation layer on the graphitic anode (or generally any electrode which polarizes stronger, than the molecules can resist), the solid electrolyte interphase layer (SEI-layer) [Abraham08]. This layer is an electronically insulating layer, protecting the electrolyte's anions and solvent from entering too far into the electrostatic field emitted by the electrode solid material. This is necessary since the anion and solvent molecules can not resist these potentials and would be continuously decomposed by reacting with the electrode materials offered electrons, forming gas and a corrosion product layer [Christensen04]. Luckily for lithium-ion cells, this layer formed is transmissive to desolvated lithium-ions. Effective lithium-ion diffusion rate in the SEI-layer depends on the layer composition [Edstroem04]. On the other hand, this reaction mechanism is one of the main reasons for ageing of the cells regarded in this work. There are lithium-ion cells close to not affected by this phenomenon, see LTO/LFP cells [Ahn11]. In chemical literature there exists the notion of potential stability window for electrolyte components, to explain when this phenomenon applies to electrodes of very low (anodes made from graphite or silica) and very high potentials ("5V-cathode-materials") for a specified solvent and salt mixture.

Since organic solvents are rather large molecules, the usual concentrations of around 1 mol of salt per litre solvent lead to concentrated solutions, meaning that not many un- or low-coordinated solvent molecules are left in the electrolyte. With the above mentioned base ingredients one obtains electrolytes in which about every second, or two out of three, solvent molecules are coordinated to an ion. So above concentrations of around three moles, depending on composition [Moosbauer10], the electrolyte is saturated. This plays an important role for the transport properties of the electrolyte needed for the ion transfer between the electrodes – the diffusion rate and the polarization strength. At circa 1 mol per litre the ionic conductivity shows a maximum [Valoen05, Zugmann11]. In concentrated solutions one has always to consider the concentration dependence of these properties, because concentrated solutions are the transition state between a very loosely coordinated solution and a highly coordinated gel [Nyman08]. During this transition many thinkable, differently fast working transport mechanisms have been reported, depending on concentration and temperature [Park10, Nyman11A].

2.1.1.5 Short-term physical processes

A chemical system is said to be in equilibrium, when every participant achieved equilibrium of efforts onto the species. Those efforts can be of very different physical properties (electric, magnetic, mixture entropic…). When one of the efforts is displaced in its strength (e.g. electrons are exchanged through the outside of the system, the system temperature is

increased…), the system reorders itself into a new equilibrium state, which might favour products of electrochemical reactions more than before, or attracts charges to the phase boundaries. These changes happening during the reordering, sorted by the influencing effort, are called the physical processes, [Stephan09].

This definition seems a little vague, but has its reason in helping to ease of grasping the complex whole. In reality, the molecules do not submit themselves to diffusion or to migration only. They always follow the combined effort the entropy field around them is exerting onto them. But for ease of understanding, the processes are regarded as single entities in which every class of effort has its proper flux response (see chapter 2.1.4.1). While this is a good description when single effects are much stronger than all others, interactions between the effects are defined when necessary (for example in electrochemistry) to reproach reality.

The main processes, which are needed to elucidate the function of lithium-ion cells, are explained in the following paragraphs (for more physicochemical in-depth information see the standard literature [Bard01, Linden02, Stephan09]):

- Diffusion: The process of diffusion is caused by chemical concentration gradients. It results in a particle mass flow, which has the property not to change the systems overall centre of gravity, as opposed to convection. The phenomenon ceases as all particles are evenly distributed among the others. In the state of equilibrium of concentration the entropy of mixing is at its maximum, therefore on a stochastic level no further mass flow is induced. On atomistic level diffusion is a constant exchange in positions of atoms either on grids or interstitial spaces, as in solids, or of arbitrary positions in fluids or passing directions in gases, all of which never cease even when maximum entropy is reached [Gardiner10].
- Migration: The process of migration is caused by an electrical potential field acting on a charged particle. It results in an attraction or repulsion of the charge, causing a mass flow of charged particles or an ordering of dipoles. Maximum entropy is reached when the whole system is in the state of electroneutrality, meaning that there are no macroscopic gradients (caused by an even distribution of sources and sinks – read positive and negative charges) in the potential field. On atomistic level electroneutrality means constant attraction or repulsion of all charges against all others. In [Dreyer12] this process is described as the main driver for the phase boundary double layer capacity, contrary to the depiction in most popular battery models. It is not macroscopically acting in the free electrolyte, which orders itself in electro-neutral compositions.
- Convection: The process of convection is caused by a gradient in mass density of the liquid or gas in focus. Since higher density or higher ordering means less entropy, it causes a mass flow distributing the particles evenly over the system. In lithium-ion cells this effect is associated with two sources, first a thermally induced density change of the electrolyte and second the coordination of solvent molecules to the moving ions. It is not quite clear how influencing this effect is, but there are indications that it is negligible in cells with single layers of thin separator material [Latz11].
- Reaction: The electrochemical process of reaction of species is caused by a gradient in entropy (not in a physical dimension but on the reaction (or the time)

coordinate) not specified in its physical order. A reaction can reduce the thermal, mixture or any other energy of the reactants releasing the freed energy in form of thermal or ordering or any other form of energy and not necessarily in the energy form that was reduced by the reaction. Furthermore reactions take place until the system enters a minimum in total inner energy (thermodynamic equilibrium) or no more reactants are available. In macroscopic levels the reaction is characterized by a reaction speed and an energy barrier for its activation. On atomistic levels the reaction speed is a statistic over how many atoms meet and choose to react, as opposed to fall back in their original state. The energy barrier is the energy needed for atoms to get close enough together to enable reaction processes at all. A reaction causes a mass flow along the reaction coordinate which corresponds to a conversion of species in the physical coordinates.

- Phase boundary movement: The process of moving phase boundaries originates from one of three causes. One is an imbalanced reaction, which mainly transports mass from one side of the phase boundary to the other (e.g. deposition or solvation reactions) [Christensen04], the other is geometric stress exerted from one side of the boundary onto the other (e.g. pressure due to volume expansion) [Zhang08]. The third is a two stable two phase material diffusion, as in LFP [Dreyer07].

All of these processes are inherent to lithium-ion cells as studied in this work. For more information on atomistic models and their relevance in lithium-ion cells see [Park10, Dreyer11, Gardiner10, Linden02].

2.1.1.6 The lithium-ion cell as a system

In the previous chapters the base materials of the lithium-ion cell and their proper functional processes were laid out. Now a system made of these components can be defined and a description of how it should work as a system. The ageing changes, why it does not always stay like described here, can be found in the next chapter.

Although an intercalation type lithium-ion cell is assembled in the fully discharged state (all cyclable lithium is in the cathode) and has to be charged first (the first charge is called formation), the description of the system given here will be a discharge. The sequence of activity is displayed as a comic strip in Figure 2.1.1-e, beginning with the cell in rest state (1). In reality this is not a sequence of but coinstantaneous processes, but for ease of explanation a sequence is postulated [Latz10]. The described process is the switch from a rest (1) into a constant current discharge (2-8). In the pictograms two to seven the dynamic build-up of the overpotential is described.

(2) When closing the external electrical circuit, the electrons are conducted from the anode current collector foil to the more positive cathode current collector via the outside of the system boundary. In a charged cell there are certain amounts of electrons available on both electrodes, on the inside of the solid material, close to the phase boundary. The amount is proportional to the number of positive ions, minus the influence of negative ions close to the surface in the liquid phase [Dreyer12].

(3) When an electron is changed over to the cathode, it simultaneously frees a positive charge into the electrolyte from the surface of the negative electrode. The charge transfer of the positive charge can be accomplished in two different ways. On the one hand by a positive lithium-ion being displaced from the anode‘s surface, creating an imbalance (gradient) in charge in the electrolyte, causing another lithium-ion, already closer to the cathode to enter into the double layer there. This positive ion binds the negative charge at that surface. On the other hand, the charge balance can be obtained by the transfer of a negatively charged ion (anion) in the opposite direction – from the cathode double layer to the anode double layer. Since the anions are very agile in lithium-ion systems, this will happen very fast, before the slow solvated lithium ion complexes can move. During short pulses or alternating current the ratio of the anion movement compared to the solvated cation movement is described as transference number in literature [Valoen05, Zugmann11].

(4) The charge is upon arriving at the positive electrode recoupled with the electron, leaving a negative charge in form of an anion in the electrolyte or double layer. This uncoordinated anion will move closer to the now slightly more positive (overpotential!) anode. And will take over the next positive charge available, accelerating the chain reaction of positive charge movement from the anode to the cathode [Kang11].

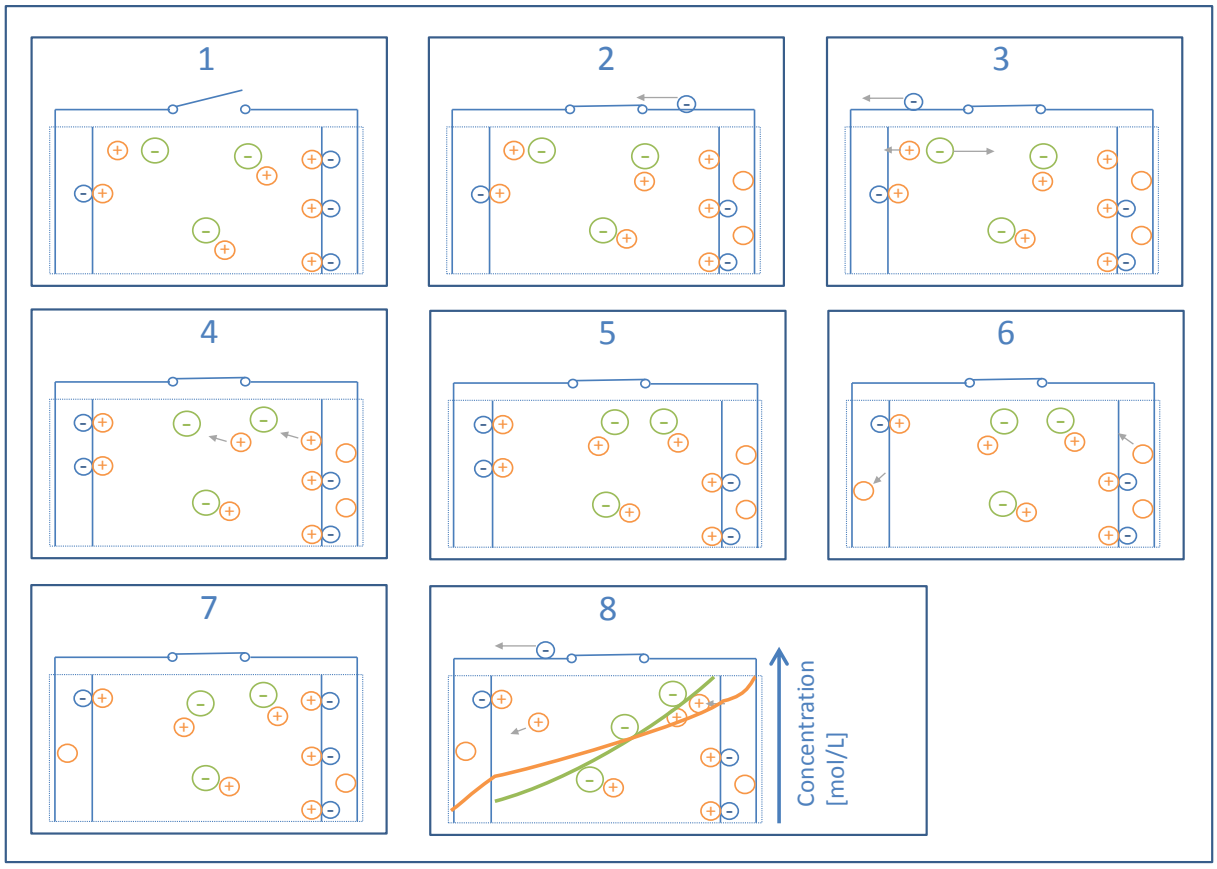

Figure 2.1.1-e – Comic strip of discharge of lithium-ion cell. Anode right, cathode left, picture 1 displays the fully charged relaxed state. Picture 8 represents the steady state discharge ion movements and concentration gradients. Electrons are blue; lithium-ions orange, anions green, cell geometry and surfaces also blue. Arrows mark concurrent movements.

(5) During a constant current discharge of a cell, it would be impossible to continue to transfer charges between the electrodes by anions. So the anion concentration gradient between the electrodes starts to stabilize (= electrolyte overpotential) and pure cation conduction keeps the current flowing.

(6) This is the point where the intercalation of lithium-ions into the host materials comes into play. On the cathode surface there is an excess of electron-cation pairs, increasing the chemical potential. So the active material and the ion-electron pairs react and the ion intercalates into the active material. On the anode the inverse process runs, because of a lack of ion-electron pairs in the double layer, ions from the material leave their electrons behind and are solvated [Bisquert02, Burch09, Gu11].

(7) By this intercalation and reaction process the electrode surface potentials are regulated.

(8) The last picture exhibits the concentration gradients within the cell at discharge as good as is possible with three ion pairs. Both processes are certainly not only dependent of the amount of ions in the liquid, but also strongly depend on the transport within the solid [Zhou08].

From the outside of the cell, nothing but the difference in electrical potential of the two current collectors and the associated electrical current is measurable. Both values can be measured as instantaneous values and accumulated over time, giving four measurement values in total. These values can be recorded over variable state-of-charge (see 2.1.2.1), temperature or pressure of the system (see later chapters for temperature influences; pressure was not considered in this work, see [Zhang08]).

Out of these four values, four remarkable output variables of the system can be deduced:

1. *Open circuit voltage (U_{OCV} or OCV)*: This is the potential difference of the electrodes of the system when at rest for long times, mapped over the different concentrations of the intercalation materials. It exists in the form of half cell (one intercalation electrode against a lithium metal reference electrode) [Karthikeyan08] and full cell mappings. The full cell mappings are a dilated combination of two half cells' measurements, as the cell balancing is set by the electrode active material loading during production (and shifts during ageing) [Safari11B].
2. *Overpotential*: From the outside of the cell it describes the effect an electrical engineer would describe as internal resistance of the cell. It is the change in voltage a non-ideal voltage source carries out when a certain current is required [Bernardi11].
3. *Capacity* of the cell (C): When charging or discharging a cell the current can be integrated over time to receive a Coulombic capacity. If this is done after charging the cell to some defined upper voltage and then discharging to another – defined – lower potential, then the Coulombic charge transferred in between those two points is the capacity of the cell. It has to be remarked that special measurement procedures have to be applied to overcome the influence of overpotential onto this measurement. But so far no standard measurement procedure, which can fully integrate all effects during the systems change over ageing, has been conceived.

4. *Current capability*: This describes the voltage change over time when a fixed current step is conducted. Since the cell is limited by prescribed boundary potentials (which are not physical boundaries, but rather borders of regions at which it was proven that the system starts ageing faster than usual), the overpotential may limit the current magnitude a cell is able to deliver while staying within the given boundaries. Since the overpotential increases with current step length, as concentration gradients build up, the current ability of a cell is dependent of the current step length and the overpotential limit voltage. This capacitive reactance of the system is often described by resistance-capacitor-equivalent circuits.

If reconsidering the discharge of a cell at mechanistic level as described previously, how are the output variables related to the mechanisms?

The interactions of the different processes are strong and there are many associated geometric properties and material properties adding to the complexity. In Figure 2.1.1-f an illustration has been tempted to show the complexity of the dependencies in this network. The figure starts from production properties of the system on the left and connects these to the output variables on the right via the described mechanisms and their interactions. The material properties are coloured in light blue, the geometric variables in dark blue, state variables of fields or flows in green. This illustration is by no means considered complete, but it can demonstrate the complexity of the system at hand.

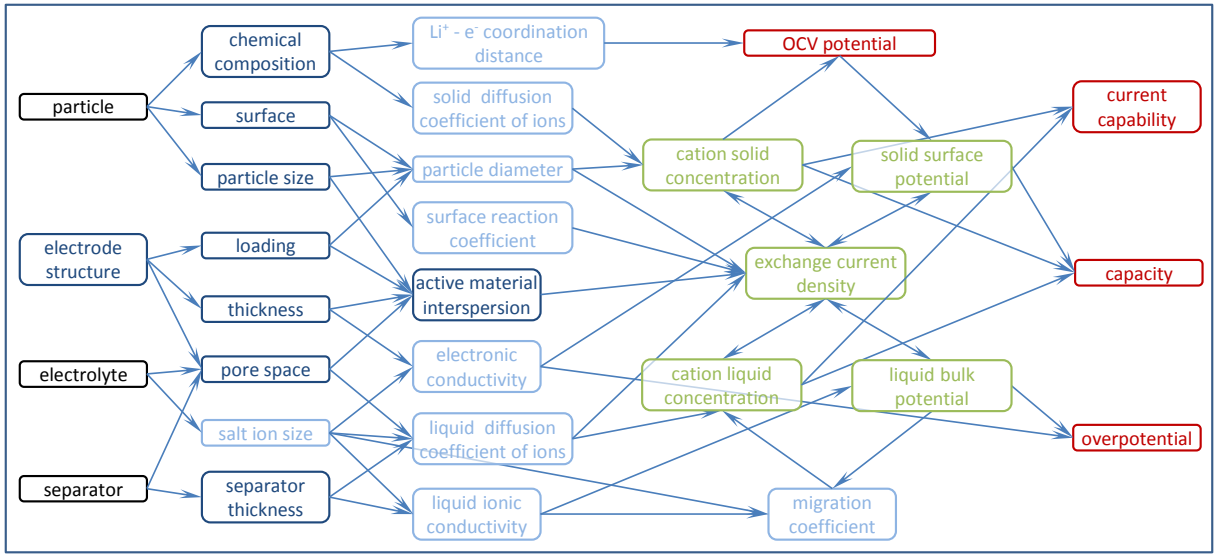

Figure 2.1.1-f – Interaction network of physical parameters onto the function parameters of the cell

2.1.1.7 Long term evolution (ageing) of the system

Ageing of energy storage devices depends on the grade of reversibility of the electrochemical reactions inside the cell.

Lithium-ion cells are commonly known to “age” over time. The processes of ageing and measurements thereof can be quite differently described, looking at different sources in

literature [Vetter05, WohlfahrtMehrens04]. Their strength can be generally defined by the loss of efficiency of energy storage and increasing losses during the recuperation of energy. Since efficiencies require very accurate measurement equipment for quantification, a simple loss in capacity to store energy is often used as the defining value for the ageing progress.

Ageing is a constant evolution of the lithium-ion cell system from its ideal, functional state, described in the last chapter, towards a simple double layer capacitor [Reichert13]. Diverse literature sources (e.g. [Arora98, Bloom01, Kumaresaran06, Zhang07F]) describe that the lithium-ion system can almost completely loose its function to store energy by intercalation.

The evolution of the processes is described to start during the first charging of the cell, which is called the “formation” of the cell [Abraham08]. From then on, the processes, which cause this evolution, take place at any time, only influenced in their speed by the surrounding environment. Some of them reduce their speed after formation, others start very slowly and gain over time and increased use of the cell. The change in ageing speed can be influenced by the environment and the usage conditions of the cell.

To handle the amount of information about cell ageing available in literature, a method from quality management was applied, a Failure Mode & Effects Analysis (FMEA) [Stamatis03]. It was not solely part of this works, but was done in conjunction with other projects requiring very detailed information of electrochemical ageing reactions and whereabouts in the cell to look for them. The inter-project cooperation helped getting together more than 10 experts in different fields of cell ageing.

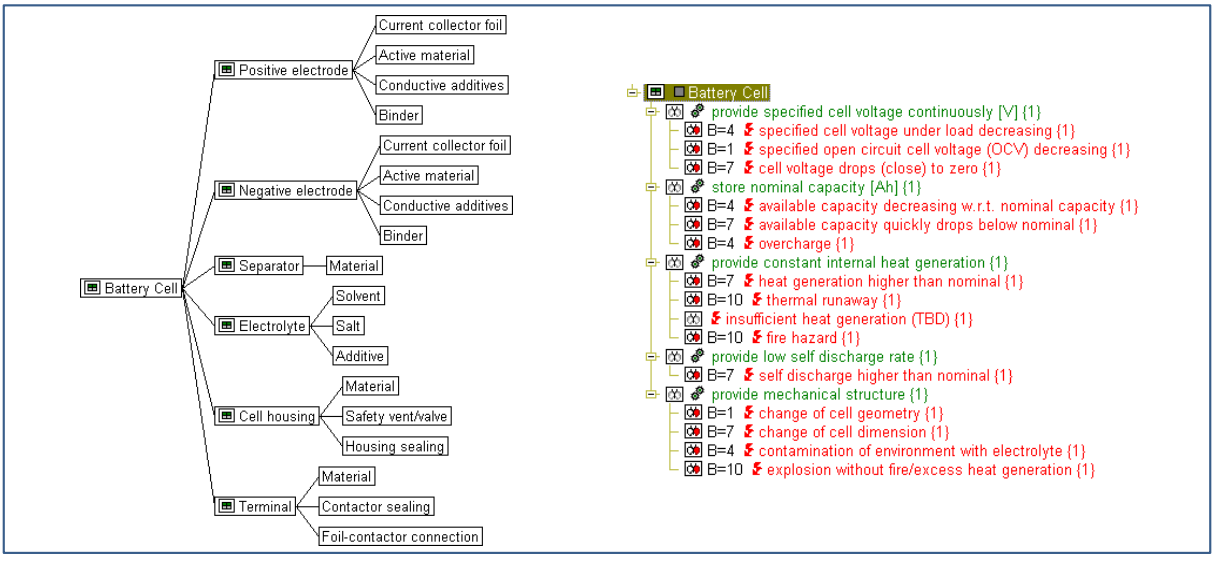

Figure 2.1.1-g – Overview FMEA, left: structure of components under consideration, right: functions (green) and failure effects (red) of the top level battery cell with the respective severity (B) rating.

In Figure 2.1.1-g the basic structure of the FMEA system tree is shown to the left. In the right part of the figure, the provided functions of the top level “battery cell” are written in green and the according failure modes are shown in red writing. Such lists of provided functions and their possible failure modes were generated for every component (middle column in tree graph) and sub-component (right column in tree graph). Then, all the failure modes were

connected to failures of their parent component, to generate a failure mode network. And in a last step all failures were rated in three criteria classes:

1. Severity: How severe is the failure with regard to the function loss of the component?
2. Occurrence: How often is this failure known to occur in cells which are used within specification? Abuse or deliberate damaging of the cells was not regarded, since an assessment of cell ageing under normal use was the target of the FMEA.
3. Detection: Is the failure easy to detect when the cell is in use?

The rating criteria for all three classes are displayed in Table 2.1.1-ii.

Finally one can generate a list of identified ageing effects and calculate a general “risk priority number” for the single effects. The list of the 14 ageing effects identified as top priority is given in Table 2.1.1-i. The ageing effects identified in the FMEA are the effects targeted for modelling also.

From the data of the influence network of the failure modes, a graph of the effective interactions of the ageing effects was derived (Figure 2.1.1-h). This graph shows the interactions between the external influence factors of ageing (top, white box) and the values defined as measures for ageing (bottom, white box).

RPN	Element	Function	Failure	Effects
1000	Current Collector Foil Cathode	Maintain low surface contact resistance	Electrical contact loss due to mechanical stress	high ohmic heating in positive electrode (RPN 1000); capacity decrease per area in positive electrode (RPN 400)
700	Active cathode material	Enable desolvatisation of lithium ions	Surface clogging	loss of homogeneity in cathode (RPN 700); electrical impedance increasing (RPN 700); specified electrode overpotential increasing (RPN 490); capacity decrease per area (RPN 280)
700	Active anode material	Enable desolvatisation of lithium ions	Surface clogging	loss of homogeneity in anode (RPN 700); electrical impedance increasing (RPN 490); specified electrode overpotential increasing (RPN 280); capacity decrease per area (RPN 280)
700	Binder in Cathode	Maintain porous structure	Loss of binding capabilities due to loss in elasticity	electrical impedance increasing in positive electrode (RPN 700); contact loss due to mechanical separation (RPN 490)
700	Binder in Cathode	Maintain porous structure	Loss of binding capabilities due to corrosion	electrical impedance increasing (RPN 700); contact loss due to mechanical separation (RPN 490)
700	Salt (LiPF6)	Provide formation of time-stable SEI	Formation of corrosive products from anion decomposition	electrical impedance increasing in cathode (RPN 700); electrical impedance increasing in anode (RPN 490)
700	Active cathode material	Maintain particle structure/integrity	particle cracking enlarging the interface surface area	contact loss due to mechanical separation (RPN 700); capacity decrease per area (RPN 400); structure becomes ordered and less porous (RPN 400)
700	Current Collector Foil Cathode	Maintain low surface contact resistance	Electrical contact loss due to thermal stress	high ohmic heating in positive electrode (RPN 700); capacity decrease per area in positive electrode (RPN 280)
700	Current Collector Foil Cathode	Maintain low surface contact resistance	Electrical contact loss due to primer decomposition	high ohmic heating in positive electrode (RPN 700); capacity decrease per area in positive electrode (RPN 280)
700	Current Collector Foil Cathode	Maintain low surface contact resistance	Contact loss due to mechanical separation	high ohmic heating in positive electrode (RPN 700)
700	Salt (LiPF6)	Maintain chemical stability of anion	Salt decomposition due to too low/high potentials	decreasing ion conductivity (RPN 700)
560	Active cathode material	Maintain same crystal structure	Change of inner crystal structure	specified electrode overpotential increasing (RPN 560); formation of (micro) cracks (RPN 560); specified open circuit electrode potential decreasing (RPN 320); capacity decrease per area (RPN 320)
500	Binder in anode	Maintain porous structure	Binder swelling out of normal range	loss of homogenity (RPN 500); structure becomes ordered and less porous (RPN 200)
490	Salt (LiPF6)	Maintain constant average concentration	Decrease of average concentration	specified cathode overpotential increasing (RPN 490); decreasing ion conductivity (RPN 490); increasing freezing point (RPN 490); specified open circuit cathode potential decreasing (RPN 280); specified anode overpotential increasing (RPN 280); specified open circuit anode potential increasing (RPN 70)

Table 2.1.1-i – The ageing effects identified as most important to research for the chemistries LFP and NCA versus graphite sorted by risk priority number.

The colours of the boxes indicate the component affiliation of the ageing effect written in the box (yellow – anode; cyan – cathode; green – electrolyte; violet – separator). The colours of the arrows are black for interactions of ageing factors, dashed for external influences on single ageing effects and coloured for the measurement value influences.

The ageing effects are described in vast detail in literature and are not repeated here [e.g. Arora98, Aoshima01, Abraham02, Vetter05, WohlfahrtMehrens04, Liu05, Markervich05, Bhattacharya12].

When stepping back from the detailed level to the process level, one can find four groups of causes for describing most of the above mentioned ageing mechanisms.

1. *Production failures causing misconnections or bottlenecks.* These will not be further regarded in this work, since they are concerns of quality management (which to find is the intent of the applied tool)
2. *Electrochemical reactions caused by electrical and/or chemical potential exceeding material stability*. When a species is confronted with a high electrical potential and has the ability to electrochemically react with the material available, it will do so. Especially the organic solvent molecules are drawn to react

irreversibly with lithium or any of the other materials present in the cell when electrical potential fields are strong [Cherkashinin12]. When approaching an electrode surface and being confronted with high electron availability, they decompose and form products which deposit directly on the electrode, react with otherwise inactive materials like binder and form gases. The best known such decomposition and deposition reaction chain in lithium-ion cells is the formation of what is called the solid electrolyte interphase (SEI) layer [Herstedt04, Abraham08]. Thereby the electrolyte decomposes, due to the steep potential gradients near the anode, and forms a partly organic, partly inorganic composite layer on the surface of the electrode. Some other products of this reaction are known to be gaseous ([WohlfahrtMehrens04]) and some others form corrosive layers on the current collectors [Gaberscek08] or on the opposite electrode [Edström04]. The layer itself has two very interesting features, first it lets lithium-ions move through and second most of its constituting species are electrical insulators. The first function differentiates lithium-ion systems from many other potential battery systems in which these layers block ion transfer and make energy storage uses impossible. The second function is very helpful in reducing the speed of the decomposition reaction. As the layer grows, less of the solvent molecules can come into the zone of influence of the potential gradient and therefore decomposition is reduced. (This indicates that the desolvation and the intercalation reaction can be spatially separated, which should be modelled in future works...).

3. *Electrochemical reactions enhanced by excessive or too low temperature.* Most of the above mentioned electrochemical reactions are sensitive to the temperature [Brandhauer11]. The operating temperature of a cell can influence otherwise unobtrusive reaction chains to shift to unwanted reaction paths, as in the case of lithium plating [Harris10].

4. *Geometric movement within the electrode assembly*. The reason for geometric movement in the electrode assembly is the volume expansion of the active material when intercalating lithium-ions. Some materials do expand very little (< 5%) [Sayle09B, Park11] some others double their volume [Song10, Chen11B]. Regarding the electrode structure being made of little particles of active material, one can imagine the jostling of the particle while changing their concentration slightly differently depending on size and ions flow pathways. This causes particles to loosen their electrical contact, build and constantly grow insulating layers all around the particle or even break apart. Experiments with nano-templated anode materials indicate that particle composed cells have some settlement period during the first part of their life [Arrebola06, Cheng08]

Rating	Severity	Severity criteria	Occurrence	Occurrence criteria	Detection	Detection criteria
10	hazardous effect	- fire hazard or explosion - non-compliance with government regulations - toxic substances emitted in excess - uncontrollable short circuit - effect of the failure mode is unknown	almost certain	- failure mode occurred always - no preventive countermeasures are defined / known / or planned	almost impossible	- detection only in field possible - methodology not available
9	serious effect	- destruction of the cell - venting - rupture (disintegration without flying parts) - short circuit induced thermal load high - thermal runaway of cells	very high	- newly developed component - failure mode occurred often - mode of operation of cell for this failure mode equivocal	remote	- detection only in large fleet test possible - methodology available but operating conditions (duty cycle,…) unclear / not def.
8	extreme effect	- complete loss of cell voltage or capacity - cell cannot be switched on - leakage of non-perilous or little toxic substances - scheduled maintenance costs too high for repair	high	- newly developed component - failure mode occurred often - mode of operation of the cell for this failure mode clear	very slight	- detection in fleet test with serial production cells - methodology costly
7	major effect	- strongly reduced performance but battery is in operation - limp home - repair/exchange is needed	moderately high	- component tested - moderate number of failure modes registered - mode of operation of cell for this failure mode equivocal	slight	- durability test on test bed with serial production parts - functional test after formation
6	significant effect	- durability and reliability targets not achievable - reduced performance but battery is in operation	medium	- component tested - moderate number of failure modes registered - mode of operation of the cell for this failure mode clear	low	- serial production parts - formation or initial cycles
5	moderate effect	- moderate effect on the battery performance - partial power loss	low	- component tested long time - occasional number of failures likely - mode of operation of cell for this failure mode equivocal	medium	- production line - cell test during production
4	minor effect	- minor effect on the battery performance - user will notice effect over time	slight	- component tested long time - occasional number of failures likely - mode of operation of the cell for this failure mode clear	moderately high	- production line - component test during production
3	slight effect	- slight effect on the battery performance - most of the effect is reversible by offboard service measures/provisions	very slight	- component produced and tested long time - seldom failure modes registered - mode of operation of cell for this failure mode equivocal	high	- research cells - cell test during development
2	very slight effect	- very slight effect on the battery performance - most of the effect is reversible by onboard measures (i.e. reset of safety device,…)	remote	- component produced and tested long time - seldom failure modes registered - mode of operation of the cell for this failure mode clear	very high	- research cells - component test during development
1	insignificant effect	- effect is only noticeable by experts	almost never	- failure modes have not occurred	almost certain	- carry over with feedback from field - design & simulation

Table 2.1.1-ii – Rating and criteria for the three FMEA categories severity, occurrence and detection of failures.

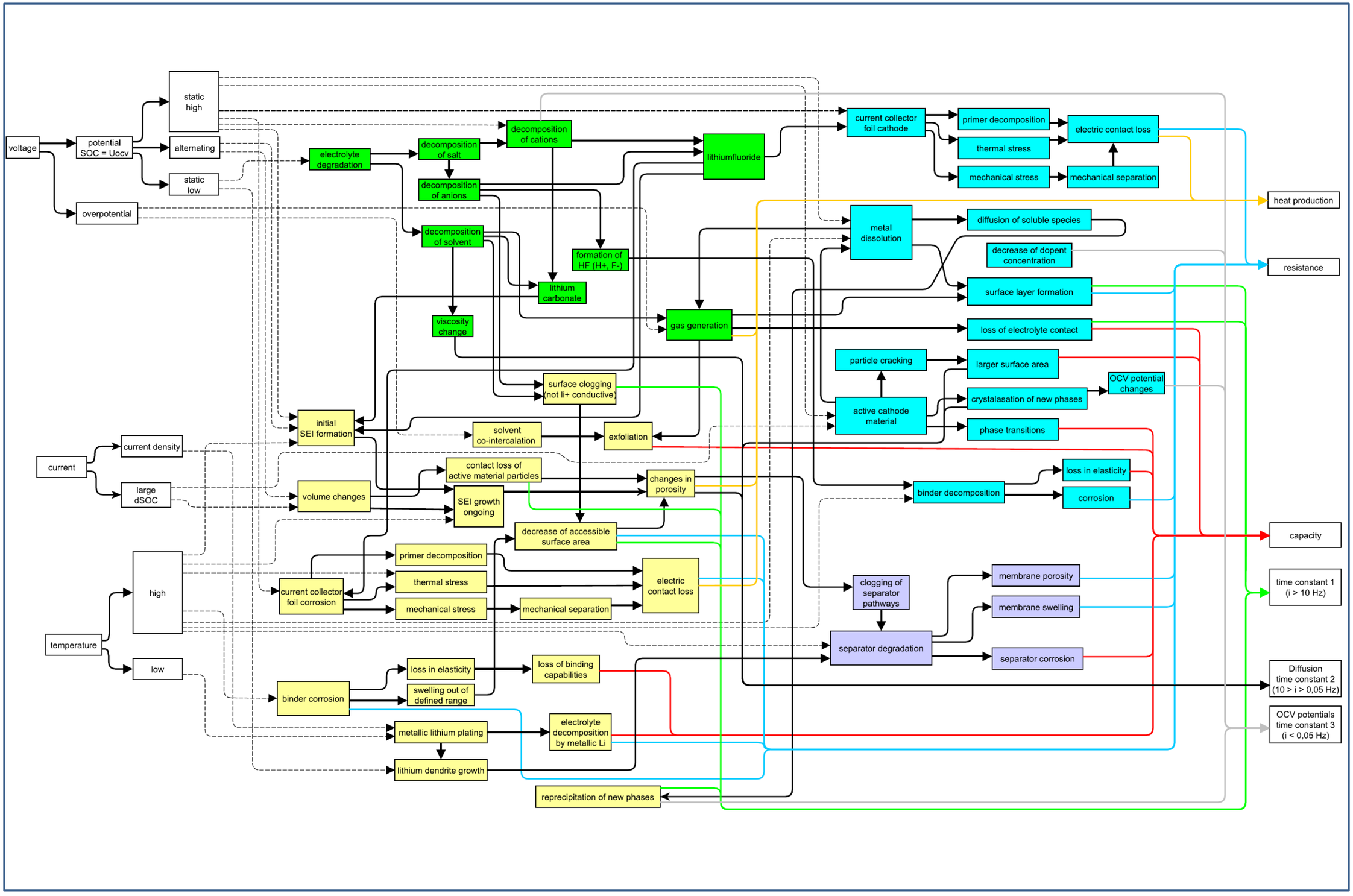

Figure 2.1.1-h – Overview of influence factors, ageing effect, the connections between the effects and their externally measureable ageing effects

2.1.2 Model derivation

In this chapter the theoretical mechanisms, described in the previous chapter, will be transformed into formal descriptions and a numerical model. Therefore some definitions will be made first and then a complex mechanistic model will be introduced. This model is then simplified for easy and fast calculation. Especially the introduced method for dynamic OCV calculation will advance the mechanistically deduced model for lithium-ion cells over previous model attempts. An empirical, energy flow based, statistical modelling technique will be applied, to introduce the ageing mechanisms to the simplified model.

2.1.2.1 Definition State-of-Charge

The cells output variables are strongly dependent on the average lithium concentrations in the intercalation materials, as can be seen in Figure 2.1.1-f. But while measuring from the outside of the cell, it is not possible to gain insight into the concentration profiles over the electrodes. It is therefore necessary to define a measurement technique and a calculation scheme for an approximation of those concentrations. Since the concentrations are related to the remaining Coulombic discharge capacity of the cell, the name State-of-Charge (SoC) has been established in literature.

The value range of the SoC is 0 – 100%, denoting the remaining Coulombic capacity in the cell. Zero and 100% are defined by potentials to which the cell has to be charged to or discharged to and sustain them with a small current. The evolution of the SoC from one point in time (t) to the next (t+dt) is calculated in the following fashion:

$$SoC_{t+dt} = SoC_t + \frac{Idt}{C} \qquad (2.1.2\text{-}1)$$

This definition has proven to be too simple, giving irreproducible results, due to the following reasons:

- The cut off voltages are given, but normally the current, at which the voltage has to be reached, is just defined as “small”. Due to the existence of dynamic overpotentials the actual potentials strongly depend on the current. Hence gathering pinpoint SoC information is impossible, only considering the voltage limit without a specified current limit. Results of different current amount limits, even at the same cut off potential, are hardly comparable.
- To increase reproducibility, constant voltage (CV) charging / discharging steps, reducing the current to very small quantities, are included into measurement protocols to ameliorate accuracy and reproducibility, but these are rather time consuming and not very practicable for an automotive application.

- The cell balancing changes over time and the voltage limits for measurement are usually kept at the same level causing the operating voltage window to drift. That means that 50% SoC does not imply the same concentrations in the active material at beginning of cell life (BoL) and at the end of its life (EoL).

Therefore it will be amended for this work to include the specification of a CV step during charge to 100% and a current limit of a current corresponding to <0.05 C-rate (see below) and a lower cut off current of <0.2 C-rate. While no assumption about the SoC is made when not at 100% or 0%. The 0% point will be kept as a voltage limit with a current equal or smaller than 0.2 C-rate.

The ageing drift of the open circuit potentials cannot be modelled, since the amount of base data or theories are not sufficient, yet.

2.1.2.2 Definition of C-Rate (Cr)

To relate differently sized cells to each other, a specific current has to be defined. In literature a normalization specific to the amount of active material within the cell is widely accepted. Therefore the C-Rate (Cr) is defined as a measure of the current per capacity [A/Ah or 1/h] [Linden02].

When discharging a full cell with 1 C, it will deliver 100% of its available Coulombic charge within one hour. If discharged at 2C, by definition, it should theoretically endure around ½ hours, but due to a rising overpotential and a reduced lithium exploitation it will be less in reality.

2.1.2.3 Definition State-of-Health

Analogous to the SoC, a measure of how much further a cell stays functional for its application is needed. So comparably the State-of-Health (SoH) was defined by Bloom [Bloom01]. Due to the different requirements for application, the definitions of the cell variable and its value when being “broken” varies in its numerical range (from 100% to 0%, from 1 to 0, some even do not define loss of function at 0% but at 80%) in literature. Also the cell output variable indicating a loss of function is defined depending on the authors’ needs (either capacity for energy applications or impedance for power applications).

A definition by a single criterion for the loss of function is not always practical, therefore a new definition, suitable for most automotive applications, was conceived by the author [Prochazka12], which will be used in this work.

Since there are four output variables of the cell, all four should be treated as possible functional criteria. So for each output the reduction / increase from the initial to the current value is defined and written in the quality-of-battery vector (QoB); additionally an end-of-life-criteria vector (EoLc) was defined. To receive the SoH the two vectors are compared element wise and the minimum value will be considered as SoH, since this is the quantity, which is closest to reaching its functional limit. This will yield an SoH in the range from 1 (new cell) to 0 (cell has reached one EoLc). For a graphical representation of this workflow see Figure 2.1.2-a.

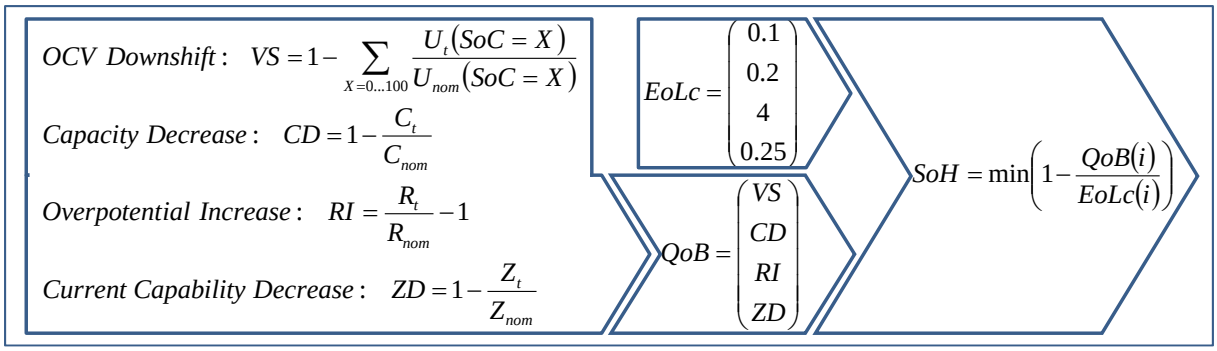

Figure 2.1.2-a – Workflow of SoH calculation

This definition has the advantage of having a single, continuous SoH output, readily available for display and easy understanding, while at the same time the information needed for calculation and control of the cell are saved in the QoB.

2.1.2.4 Mechanistic system model

All processes described in chapter 2.1.1 can be modelled on the atomistic level [Sayle09B, Kramer09, Hoang11, Kang11], but this nano-sized calculation scale causes large models with long calculation times for even as simple loads as pulses of one second duration. That is why more macroscopic models were developed over the last decades [Newman93, Newman03, Newman04, Christensen04, Dreyer07, Latz11].

These models simplify the processes by leaving the discrete nature of matter and stepping one scale level up to describe the mechanisms as a stochastic averaged motion of the original processes. Since in confined spaces molecules' random interactions always combine well to a repeatable and deterministic pattern, these models are effective in describing what can be observed. This knowledge is used in as "simple macroscopic laws" as Fick's law of diffusion and can be extended as far as to describe systems like the lithium-ion cell.

Because this way of modelling is common place, the formulas which will be presented in this chapter are well known in literature. Even though the formulas may not look alike, since the parameter names had to be adapted to form a consistent system, the corresponding reference to the source of the model will always be given at the first mention of the formula. The reference also applies to any boundary conditions or transformations coming along with the formula and will not be explicitly marked in this context. Most of what is written here originates in textbooks of physical chemistry, of which just two shall be cited here and which apply to this whole subchapter [Bard01].

Also it should be noted that the system of equations given here will be the basis for the simplified model derivation and an argumentative step between theory and the way of modelling the cell ageing. Solution and validation of the mechanistic model will not be presented her, as it was already by other members of our research group at the Virtual Vehicle [Pichler11, Scharrer11, Scharrer12, Scharrer12C] and the Graz University of Technology [Sommer12]. It is also given here since the author put a lot of work into forming and understanding the effects this equation system shows. Some of the deductions and

conclusions during empiric modelling would not have been possible, without the preceding extensive study of the differential equation system.

Within a simplified, single-particle geometry of the cell [Santhanagopalan06], one can differentiate between five domains of calculation, marked by a roman number from I through V in Figure 2.1.2-b. Each domain has a specified subset of equations and accordingly of boundary conditions. Some of the domains are further split up in subdomains, indexed by a subscript Latin letter, wherein the equations are basically the same, but the main parameters' values are different for each subdomain. The domains are:

I…Solid material on cathode

I_a… Active material particles

I_b… Inactive materials on cathode (binder, conductive additive,…)

II…Liquid space within pores on cathode

III…Liquid space within separator pores

IV…Liquid space within pores on anode

V…Solid material on anode

V_a… Active material particles

V_b… Inactive materials on anode (binder, conductive additive,…)

V_c... Solid-Electrolyte Interphase on anode

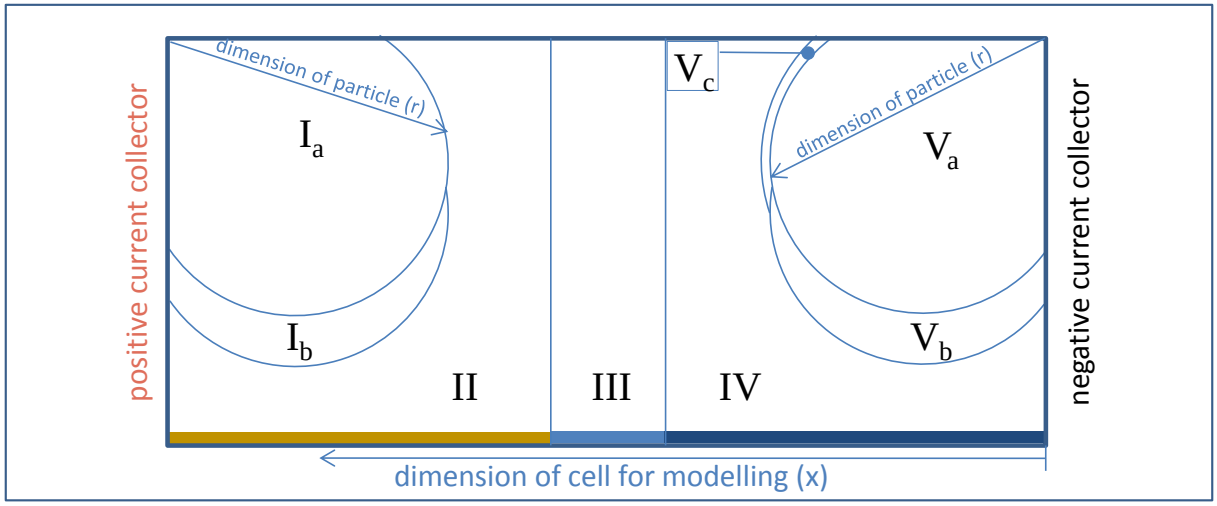

Figure 2.1.2-b – Modelling domains of a cell geometry simplified to 1.5 dimensions

The most basic formula is the definition of the energetic potential of a species in an electrochemical system. All subsequent flow field equations will be derived from this equation.

$$E = E^0 + \frac{RT}{zF}\ln(\gamma(c)\cdot c) + \varphi \quad (2.1.2\text{-}2)$$

For the potential field and the diffusion equations in the electrochemical cell, the argumentation of Newman [Newman04] is followed. Although these equations are not suitable for highly concentrated solutions, as the electrolytes in lithium-ion cells are, these equations do model the basic process. For more equations following concentrated solution theory please see [Dreyer12].

The static flow field for the potential field is proportional to the energetic potential definition as shown:

$$0 = -\nabla\cdot i \quad (2.1.2\text{-}3)$$

$$i \propto -\nabla E_i \quad (2.1.2\text{-}4)$$

When introducing a proportionality constant κ [S/m] (called the conductivity) the following equation results:

$$0 = -\nabla\cdot\left(\kappa\nabla\varphi + \frac{RT}{zFc}\kappa\left(1+\frac{\partial\ln(\gamma)}{\partial\ln(c)}\right)\nabla c\right) \quad (2.1.2\text{-}5)$$

Which is valid for the liquid-filled domains (domains II, III and IV in Figure 2.1.2-b). Within the solid active material, the lithium-ions are modelled as uncharged atoms and only the electrons are shifting the potential field. Since electrons are considered pure charge and not particle, the second gradient term in (2.1.2-5) falls for the potential field in the solid, electron conducting active material (domains I and V in Figure 2.1.2-b), reducing the equation to Ohm's law:

$$0 = -\nabla\cdot(\kappa\nabla\varphi) \quad (2.1.2\text{-}6)$$

The ionic concentration flow field in the can be derived in analogy to the potential field with the following base definition and proportionality constant from (2.1.2-4):

$$\frac{\partial c}{\partial t} = -\nabla\cdot i \quad (2.1.2\text{-}7)$$

$$k_{prop} = \frac{D}{RT}c \quad (2.1.2\text{-}8)$$

Hence, one receives the Nernst-Plank equation for diffusion and migration. This equation is used in the electrolyte domain near the solid interphase (domains II and IV in Figure 2.1.2-b). It is valid for cations and anions:

$$\frac{\partial c}{\partial t} = \nabla \cdot \left(D \left(\left(1 + \frac{\partial \ln(\gamma)}{\partial \ln(c)} \right) \nabla c + \frac{zF}{RT} c \gamma \nabla \varphi \right) \right) \tag{2.1.2-9}$$

Within the free electrolyte (domains III in Figure 2.1.2-b), where ions can arrange themselves to form zones of local electro-neutrality, a polarisation-free form of the equation is valid:

$$\frac{\partial c}{\partial t} = \nabla \cdot \left(D \left(1 + \frac{\partial \ln(\gamma)}{\partial \ln(c)} \right) \nabla c \right) \tag{2.1.2-10}$$

Equation (2.1.2-10) is also applied to model diffusion within the active material particles. Since it is assumed that the electron is sufficiently close to the lithium ion, so polarisation effects can be neglected for the modelling of the mass transport.

Out of these four transport and potential field equations, always two have to be solved per domain and boundary conditions have to be formulated to couple the domains together. Most of them are conventional Dirichlet or Neumann boundary conditions [Pichler11], except for the interface between the solid and the electrolyte domains (I & II, IV & V). At this interface the redox reaction take place. The classical reaction boundary condition of Butler-Volmer [Newman93, Bard01 etc.] is used here as a sharp interface model of the reaction. Sharp interface means that the reaction zone, extending a couple nanometres into both adjacent domains, is modelled a sharp, 0-dimensional boundary between the two domains:

$$j_{BV} = zFk'(T) \left(\cdot \exp\left(\frac{\alpha_A zF\left(\varphi_S - \varphi_L - \Delta E^0\right)}{RT} \right) - \cdot \exp\left(\frac{-\left(1-\alpha_K\right) zF\left(\varphi_S - \varphi_L - \Delta E^0\right)}{RT} \right) \right) \tag{2.1.2-11}$$

Often the reaction current occurring at no electronic overpotential is reduced to the variable i_0 for ease of notation:

$$i_0 = zFk'(T) \left(\cdot \exp\left(\frac{\alpha_A zF\left(\Delta E^0\right)}{RT} \right) - \cdot \exp\left(\frac{-\left(1-\alpha_K\right) zF\left(\Delta E^0\right)}{RT} \right) \right) \tag{2.1.2-12}$$

2.1.2.5 Simplified modelling of short-term effects

After having experienced the complexity of a PDE model and at the same time regarding very simple but validity restricted models as in [Hartmann08], it seems to be clear that an appropriate model should combine the best features of both model approaches together. This is especially true, since the aim of the work is to provide a short-term (UI) model which can treat the UI-simulation of an aged cell as well as for a new cell. To identify 40+ parameters of an electrochemical model for aged cells under different influence factors would result in a huge analytical expenditure, not considering the fact that not all parameters of an electrochemical model are accessible to measurement today [Safari11].

The basic modelling approach is to generate a short-term model of the cell voltage, as it is a voltage source, in dependence of the current, the state-of-charge and the temperature. The model should consider the sum of the dynamic voltage changes of the physical processes added to the open-circuit voltage of the cell. The experience from the electrochemical model show, that the important parts of the voltage changes are attributed to three effects [Bernardi11]:

1. the reaction overpotential
2. the electrolyte potential gradients
3. the potential gradients caused by solid diffusion of lithium within the particles, distorting the OCV (explained in chapter 2.1.3)

The basic equation (2.1.2-13) contains the OCV term, two terms for the reaction and the liquid overpotentials. The last term is added at a later stage to compensate for diffusion gradients over the cell's electrode surface and is mostly influenced by the cell's macro geometry [Smith09].

$$U_{cell}(I, SoC, T) = U_{OCV} + U_{reaction} + U_{liquid} + U_{solid} \quad (2.1.2\text{-}13)$$

This formula is applicable for the whole cell at once. Hence, when simplifying the equations of the electrochemical model the equation, the boundary conditions and the discretization grid for the whole cell has to be taken into consideration together.

U_{ocv}

The U_{OCV} term will be explained in chapter 2.1.3.

$U_{reaction}$

The first of the added terms is the reaction overpotential $U_{reaction}$. In the electrochemical model, the Butler-Volmer equation (2.1.2-11) is used for calculating the reaction flow in dependence of the two phase potentials [Bard01]. In the simplified modelling this equation is requested inversed in its dependence. So when assuming an α = 0.5 (symmetry factor set to

equality of intercalation and deintercalation) the equation can be inversed. To apply the logarithm on the exchange current, it is necessary to take the absolute value and multiply with the signum function of the current (2.1.2-14). In the formulas the abbreviation log is used for the natural logarithm, another base would be marked by subscript ("$\log_{10}$").

$$U_{reaction} = \frac{RT}{zF}\log\left(\frac{|j_{BV}|}{i_0}\right) sign(I) \quad (2.1.2\text{-}14)$$

Since the formula shall apply for the whole cell at once, it has to incorporate both electrodes and all sites on those electrodes ($I_{cell} = |\int j_{BV}\, dA|$). So the assumption is that there is only a single current flowing through a single particle surface per electrode.

For ease of notation and distinction of the electrochemical model the exchange current density (i_0) is replaced by a general model parameter. The temperature dependent parts can all be drawn together to form an Arrhenius-like temperature term and the remaining constants (Gas constant, Faraday constant, charge number & conversion from j_{BV} [A per square meter particle surface] to I [A]) are put into a general resistance variable. The temperature will be input in [°C] and internally recalculated in [K] and the term, as all in the model, is normed with T_{ref} = 293K so as to avoid numeric problems. Thus the equation can be written as:

$$U_{reaction} = R_{BV}\exp\left(\frac{k_6}{T - Tref}\right)\log\left(\frac{|I|}{k_7}\right) sign(I) \quad (2.1.2\text{-}15)$$

Throughout the document k_i will be the denomination of the i^{th} parameter and R_j will be the j^{th} general resistance term of the short-term model.

Additionally, two empirical modifications have been made to incorporate effects seen in current lithium-ion cell chemistries. One is a treatment of hysteresis [Dreyer07, Dedryvere08] and the other is an asymmetry factor for charge and discharge entropy differences [Thomas03, Latz11].

The numerical treatment of hysteresis is subject of some publications [Dodd07, Dreyer09], but most of these approaches are complicated, highly non-linear calculations. So a very simple way of introducing the hysteresis directly into the reaction term has been conceived. It consists of an additional parameter within the logarithm, which is always larger than 1, and a special signum function to replace the standard function. This special function avoids the zero state, having only the states 1 or -1 and a memory thereof. It switches based on the actual value of the current and its own last value:

$$I > 0 \rightarrow +1$$
$$I < 0 \rightarrow -1 \qquad (2.1.2\text{-}16)$$
$$I = 0 \rightarrow \text{Last value of signF}$$

This causes some error for current profiles switching closely around zero current, but proved to be generally acceptable. So the reaction term is written as follows:

$$U_{reaction} = R_{BV} \exp\left(\frac{k_6}{T - Tref}\right) \log\left(\frac{|I|}{k_7} + k_{16}\right) signF(I) \qquad (2.1.2\text{-}17)$$

Since the reaction term is a single term for the reactions on both electrodes in parallel, the asymmetry factor for the difference in charge and discharge entropy (mostly only on one of the two electrodes) is a sum of both asymmetries. It is basically the, mathematically not entirely correct, reintroduction of α. The alphas of both electrodes together take the form of the model parameter k_8.

$$U_{reaction} = R_{BV} \exp\left(\frac{k_6}{T - Tref}\right) \log\left(\frac{|I|}{k_7} + k_{16}\right) k_8^{sign(I)} signF(I) \qquad (2.1.2\text{-}18)$$

The exponent is a standard signum function, setting the influence to 1 in case of no current. This is believed to depict the reality very well, since during relaxation no additional energy is available for charge levelling over the electrode surface by charging and discharging single particles in which process this entropy imbalance would be applicable.

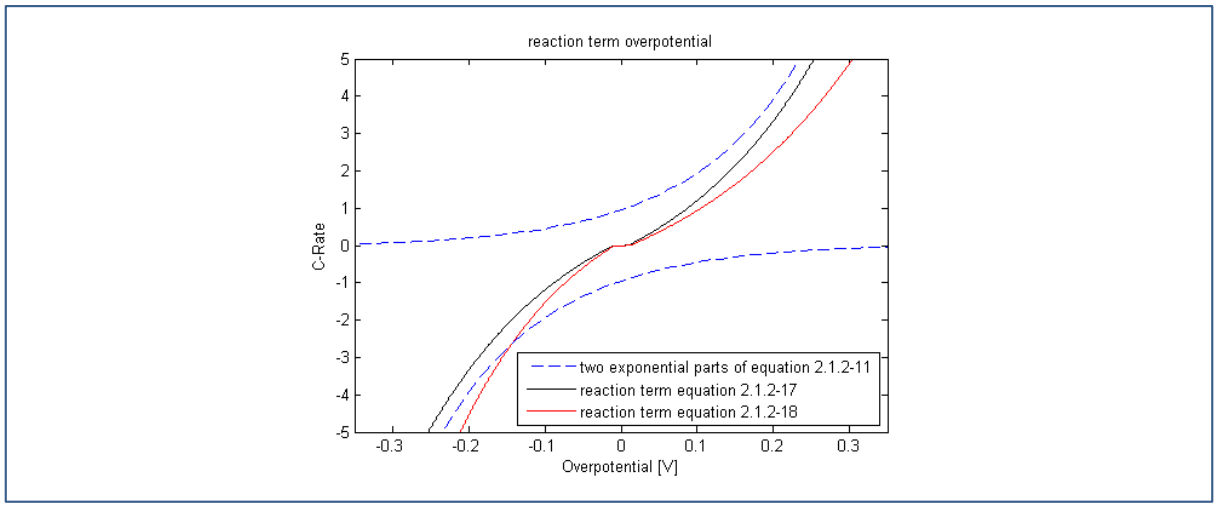

Figure 2.1.2-c – Reaction term overpotential comparison of Butler-Volmer behaviour with simplified equations, all plotted with generic parameters

The original Butler-Volmer equation with two separated branches and the above approximations are plotted in Figure 2.1.2-c. The plot uses the parameter conversion as described in the text to match the approximation of (2.1.2-17) to the original function (2.1.2-11). The asymmetric plot (2.1.2-18) is offset by using a k_8 of 0.95.

U_{liquid}

The second additional voltage term is the electrolyte's contribution to the overpotential. On the one hand it results from the concentration gradients of cations and anions in the free electrolyte within the separator. The ionic gradients within the porous electrodes are mostly consumed or counteracted by the reaction overpotential linked to the solid ionic concentrations and are therefore a smaller part of the electrolytes contribution to the overpotential visible at the outside of the cell. So, for the simplified modelling, only the free electrolyte concentration gradients are taken into account.

On the other hand the potential gradients, causing ionic migration within the cell, would lead to an implicit formulation of the simplified equation, but they are one of the influences defining relaxation and very fast pulse behaviour. So when leaving this process out of modelling, in favour of faster model calculation, it is expected that those areas will be prone to higher errors in reproduction of behaviour.

For the diffusion equation (simplification of (2.1.2-9)), when discretized on a linear grid and with boundary conditions of constant concentration at on one side and free movement on the other, there exists a fundamental solution for the 1-dimensional flow field as displayed in the following formula:

$$\frac{\partial c_L}{\partial t} = \nabla \cdot \left(D_L \left(\nabla c_L \right) \right) \Rightarrow H\left(c_L \right) = \frac{1}{\sqrt{4\pi D_L t}} \exp\left(-\frac{c_L^2}{4 D_L t} \right) \quad \text{(2.1.2-19)}$$

c_L…concentration of lithium in electrolyte [mol/L], D_L…diffusion coefficient of lithium cations in electrolyte [m²/s], H…homogeneous solution.

This would give us the whole solution in every discretized point, but for the simplified model only the difference between the charges of the ionic species at the boundaries are of interest. So the term is constructed by a R_L, containing the charge to overpotential conversion and the terms in the square root of (2.1.2-19), again an Arrhenius temperature term and finally some exponential function which depends on time, diffusional speed and current flowing. The electronic current gives the equivalent to the ionic flow over the boundary of porous electrode to free electrolyte. Therefore the current (I) can replace the ion concentration (c_L) in the formula.

$$U_{liquid} = R_L \exp\left(\frac{k_9}{T - Tref} \right) \exp\left(f\left(t, D_L, I \right) \right) \quad \text{(2.1.2-20)}$$

This last term is equivalent to a low-pass filter of 1st order, filtering the current applied to the cell with the diffusion rate as time delay constant τ.

Since the model should have very high calculation speed, the requirement for implementation of the filter was a calculation method, which could deal with variable time-step sizes and require a single backward input only. The following simple formula was implemented as a function called LPF (low pass filter). It consists of two exponential functions using four parameters (time-step size Δt, time constant τ, the last filtered value Y_t, and the new input $X_{t+\Delta t}$) to calculate the new filtered value ($Y_{t+\Delta t}$) and is called in the form LPF($X_{t+\Delta t}$, Y_t, Δt, τ).

$$Y_{t+\Delta t} = \exp\left(-\frac{\Delta t}{\tau}\right)Y_t + \left(1-\exp\left(-\frac{\Delta t}{\tau}\right)\right)X_{t+\Delta t} \qquad (2.1.2\text{-}21)$$

The function notation will be used in the following formula notations, with an index for the different time constants of the filtered current. (LPF_1 is the filter of the OCV term, LPF_2 is the filter of the liquid term and LPF_3 is the filter of the solid term).

Since it is known that the diffusion rate in the electrolyte strongly depends on the temperature of the liquid [Zugmann11], the time constant will be given with two parameters in the model, one for the speed at 25°C and the second to give the temperature dependence. So using the introduced function, the term for the electrolyte's contribution can be written as follows:

$$U_{liquid} = R_L \exp\left(\frac{k_9}{T-Tref}\right) LPF_2\left(I, LPF_2(t-\Delta t), dt, k_{10}\left(\frac{Tref}{T}\right)^{k_{11}}\right) \qquad (2.1.2\text{-}22)$$

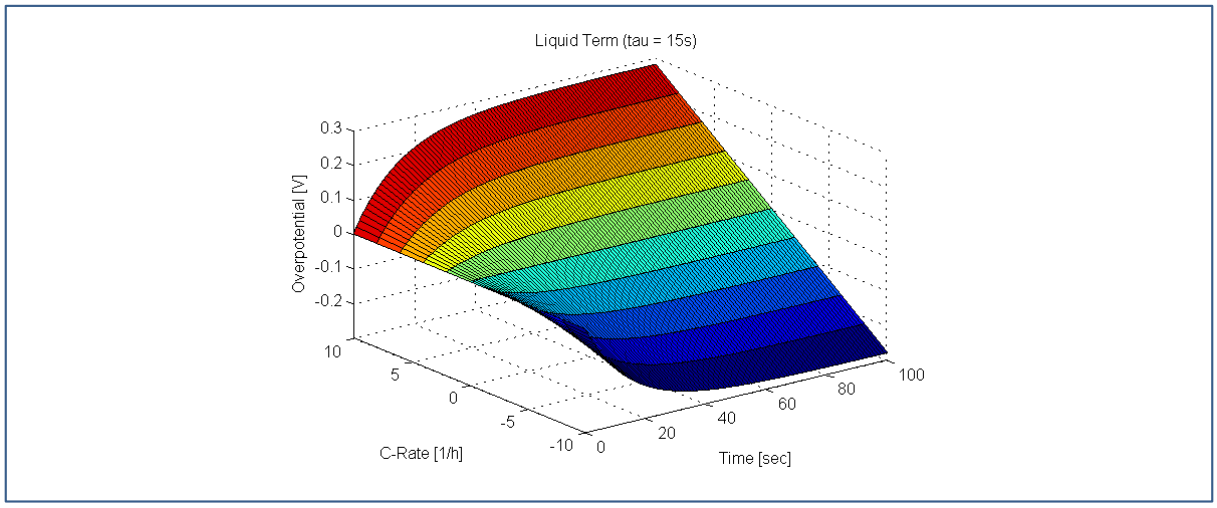

Figure 2.1.2-d – Liquid term overpotential plotted with generic parameters

In Figure 2.1.2-d one can see the overpotential caused by the liquid term plotted versus the time for different current rates. In Figure 2.1.2-e one of the plausibility checks, performed during model development, is displayed. The dashed line displays only the exponential transformation of the reaction term. It shows, after an initial rise, a perfect Tafel straight as would be expected by the theory textbooks [Bard01]. The continuous line represents the combined reaction and the liquid terms of the model. One can see that a behaviour as expected from real world measurements appears – the Tafel straight is imperfect and curves outward to the right and left. This behaviour is known in electrochemistry as diffusion limited kinetics.

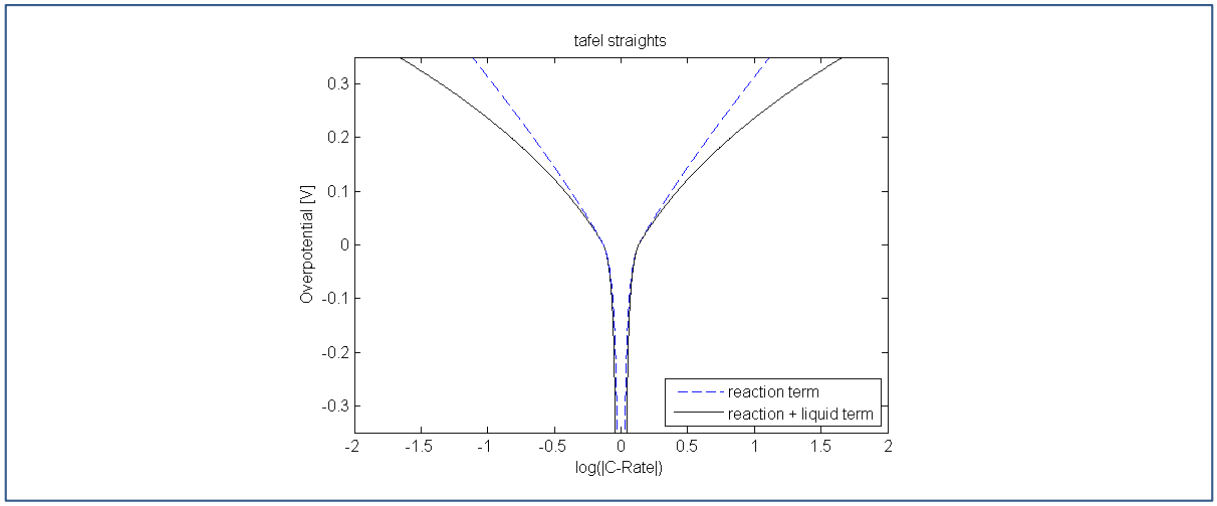

Figure 2.1.2-e – Reaction term Tafel plot with and without diffusion limitation

U_{solid}

The third overpotential term is not directly derived from the classical 1D electrochemical model, but from the need to simulate whole cells. If one simulates many of the 1D models in parallel in order to represent the surface of the unravelled cell, one will notice that the potential gradients within the current collectors (from the pole connection current tabs to the farthest end of the current collector foil) cause differences in exchange current and hence differences in concentrations. Especially, in high-current pulse situations those cell gradients strongly apply. [Reimer06, Liu10B]

This term has a structure very much alike the liquid term, but with the addition of an exponential dependence of the general resistance on the current.

$$U_{solid} = R_S \exp\left(\frac{k_9}{T - Tref}\right)\exp\left(\frac{|I|}{k_{13}}\right)LPF_3\left(I, LPF_3(t), dt, k_{14}\left(\frac{Tref}{T}\right)^{k_{15}}\right) \quad (2.1.2\text{-}23)$$

The resulting overpotential will only come into play at high currents and it should have a far slower time constant than the liquid term, since ions with the same diffusional speed have to

cover physical distances in the order of centimetres (10^{-2}m) instead of micrometres (10^{-6}m). Single ions will not move the whole way, but an increase of path by a factor of 2 to 3 seems plausible (important for the constraint estimation of short-term parameters, chapter 2.2.3).

P_{Heat}

Since the overpotentials are those effects causing the joule heating in a cell [Latz11], also a very simple heat source term was implemented in the model.

$$P_{heat} = \left(U_{reaction} + U_{liquid} + U_{solid}\right)|I| \quad (2.1.2\text{-}24)$$

This heat source contains the overpotentials caused by the ionic transport and reaction only, it does not contain any pretended overpotential due to gradients in state-of-charge, respectively OCV, of the cell.

Supporting equations

Since all equations presented in this chapter are C-rate based, the transformation of the given current into c-rate is the first supporting equation. The c-rate is used in the model to substitute the specific current density per electrode surface [A/cm²] used in electrochemical models. As written in the following formula, the current input is divided by the actual capacity (C) of the cell. This capacity is not the usual 1C-rate capacity measured and given for the cells, but rather the hypothetical capacity of an infinitesimally small discharge current. This is especially important when looking at aged cells, since their apparent 1 C-rate capacity is mostly a lot lower than the capacity used here due to impedance increase.

$$C-rate = \frac{I}{C} \quad (2.1.2\text{-}25)$$

After the time-step voltage is calculated, the SoC has to be updated for the next time-step. This is done by the Coulomb counting method already described with the addition of a Coulombic efficiency factor η_c. This factor scales the added term in (2.1.2-26) if the current is positive only, this is achieved by the term with the signum function of the current. The calculation form owes to the fact of faster calculation for many cells in parallel compared to an “if” command.

$$SoC_{t+dt} = SoC_t + \frac{I \cdot dt}{C}\left(1 - \left[\left(1-\eta_C\right)\left(0.5 + 0.5\,sign\left(I\right)\right)\right]\right) \quad (2.1.2\text{-}26)$$

Finally there is an equation to correct the initial SoC of a current profile to simulate. This is necessary to compensate for the differences in temperature and cell impedance when trying

to charge a cell to the 100% SoC point and a relaxed state. This point is defined by the cell being at the upper cut-off voltage after a constant voltage charge at this cut-off voltage and a relaxation rest was applied to the cell. Since temperature and ageing impedance can shift this point in electrochemical equivalent, a correction was implemented. This formula contains another two short-term model parameters and is given in (2.1.2-27).

$$SoC'_{t=0} = k_{f2}\, SoC_{t=0}\, \exp\left(\frac{k_{f3}}{T - Tref}\right) \qquad (2.1.2\text{-}27)$$

2.1.3 OCV calculation for 0D models

In most 0D models, the OCV calculation is a simple interpolation of a single voltage-SoC relation [Sauer08, Hartmann07, Herb10]. It depends on the Coulomb-counted SoC of the model at the time instant of interpolation. But when looking at the electrochemical model, one realises that each particle can have its proper OCV depending on its atomic/ionic concentration and diffusional transport speed [Dreyer07, Kasavajjula08].

So a new method of calculation of a dynamic OCV (dOCV) for the simplified model was deduced from the electrochemical model (ECM) behaviour. In literature this behaviour as “Diffusion polarization of the solid phase” [Nyman10]. In the left hand graph of Figure 2.1.3-a one can see a particle surface concentration profile (solid green line) over the depth of an electrode, while doing a discharge of that electrode. The mean concentration, equal to the concentration reached after a long relaxation period (thin red line), corresponds to the average concentration (≈ SoC) an external Coulomb counter would attribute to the cell. On the right hand graph, the same situation is viewed on the OCV curve. It becomes visible that during this discharge, not only a single OCV value is present, but a distribution thereof with a mean value (depending on electrode conductivity and liquid potential & concentration) “visible” to the outside at the current collector.

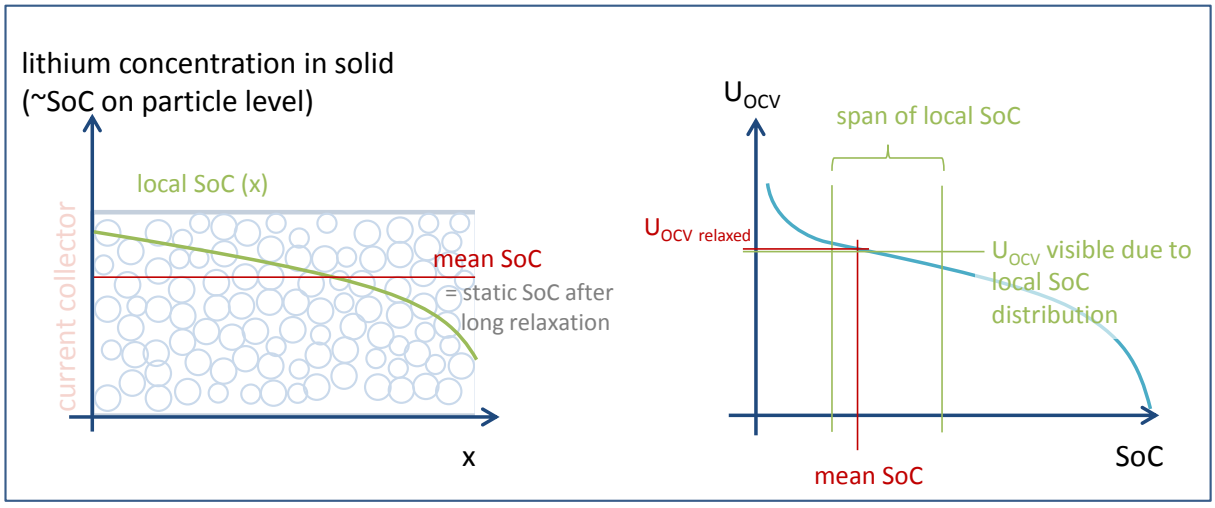

Figure 2.1.3-a – OCV as function of state and position in the porous electrode

This is why the new method contains a four-step, two-parameter interpolation instead of the common, one-parameter, single-step interpolation.

1. The cell’s average SoC is counted by a Coulomb counter and marked as the “real” SoC. This is also the value the cell returns to after ample relaxation time.
2. During a current-load profile, a low-pass filter of the current calculates the width of the SoC distribution over the cell (dSoC_D).
3. For 30 SoC’s, linearly spaced in between the SoC and the SoC + dSoC_D, the OCV I is interpolated
4. The dynamic OCV is the mean value of those 30 potentials.

In Figure 2.1.3-b these steps are pictured for a single time-step OCV request for better understanding. These steps are written as function OCV(SoC, dSoC_D, OCVdata), wherein OCVdata represents the measured OCV curve as a polynomial.

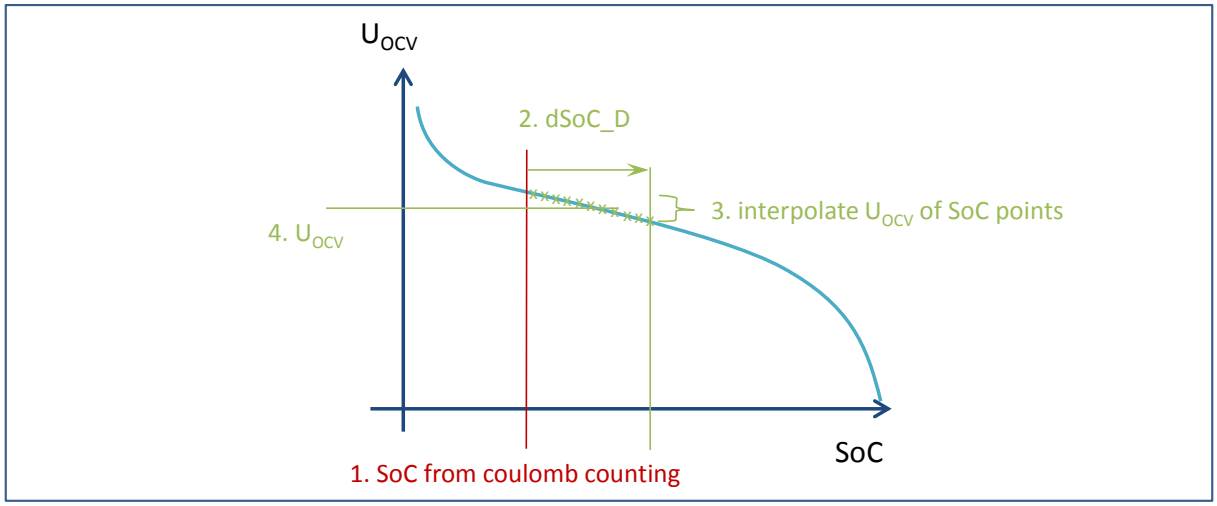

Figure 2.1.3-b – Dynamic U_{OCV} as function of state and dSoC_D

So finally the first term of the model can be given. It consists of a scaling parameter for measurement error, a temperature offset for the OCV and the OCV function itself. The dSoC_D is given by a fitting constant multiplied with the low-pass filter value of the current, which is in turn also temperature dependent.

$$U_{OCV} = k_1 \exp\left(\frac{k_5}{T - Tref}\right) OCV\left(SoC, k_2 LPF_1\left(I, LPF_1(t), dt, k_3\left(\frac{Tref}{T}\right)^{k_4}\right), OCVdata\right) \quad (2.1.3\text{-}1)$$

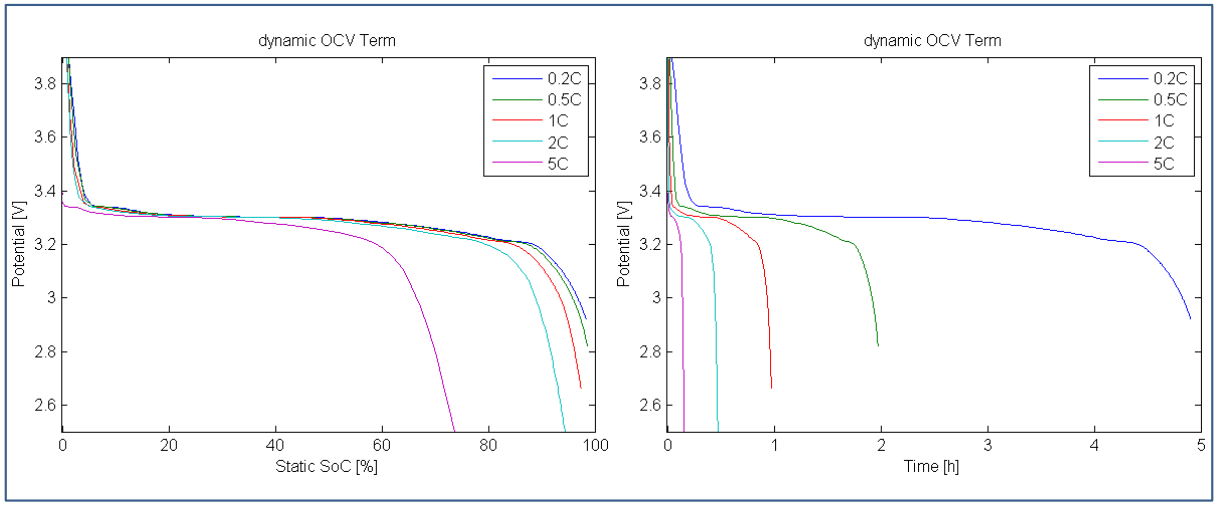

Figure 2.1.3-c – Dynamic U_{OCV} term output plotted as function of the c-rate of discharge, left over static SoC, right over time; both at 30°C fitted for a new LFP 18650 cell from A123 Systems

In Figure 2.1.3-c the results of the simulation of this term, standalone, are displayed. One can easily see that the shortening of the discharge curve is current dependent and no additional measures have to be taken to simulate low and high current rates with this model.

Without the understanding and the solution of the differential equation system of the electrochemical model, the understanding of this interplay of potentials and concentrations would not have been possible and therefore this method would not have been affected.

2.1.4 Damage accumulation model for battery cells‘ ageing

2.1.4.1 Energy-based modelling of ageing effects

During battery usage, charge and discharge pulses are applied. Figure 2.1.4-a shows a plot of two such pulses, being of equal length and current in an axis set of voltage versus SoC. The pulse cycle starts at an OCV and rises as charge current is applied. After the pulse end and a relaxation time, the voltage is back to the OCV. Now the discharge pulse is started.

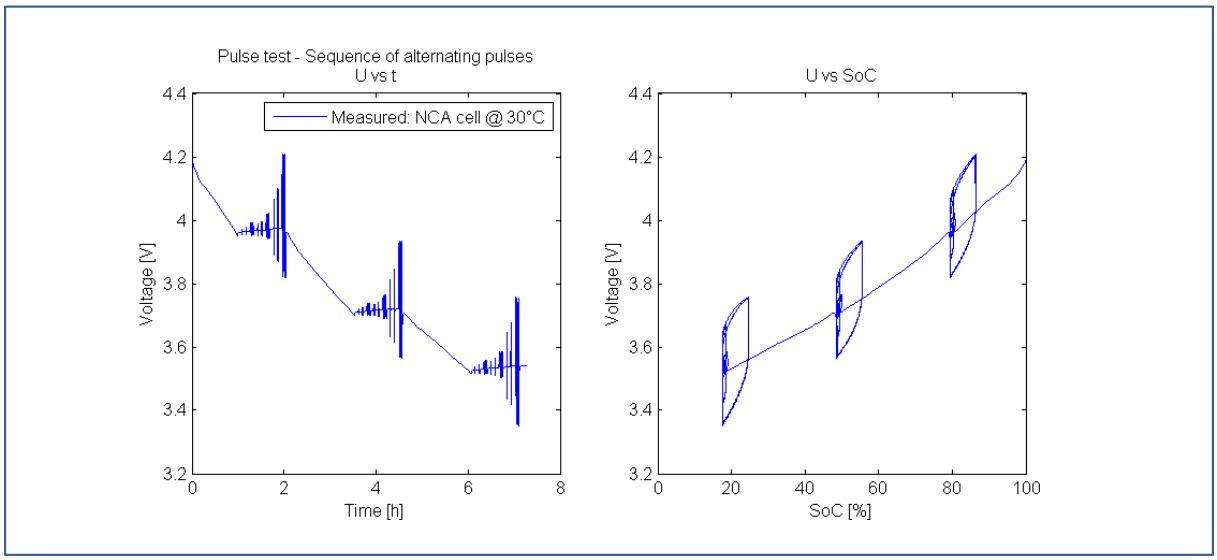

Figure 2.1.4-a – Hysteresis loop for charge and equal discharge pulses in the pulse test sequence. Different c-rates and pulse durations form hysteresis loops of different size.

Regarding this cycle, it is obvious that it encloses an area of the plot. This area represents the energy, which was lost, while forcing the cell to cycle. The larger the area is, the lower the cell cyclic efficiency is. The energy is mostly dissipated as thermal energy into the surrounding by heating up the cell. But a smaller part is used for other processes like ageing processes, as described in chapter 2.1.1.7: geometric movement of cell components and dissolution of material. For an efficient ageing model, one has to identify the measurement quantities which can characterize this energy loss.

$$\text{Energy} = \text{effort} * \text{flow} * \text{time} \qquad (2.1.4\text{-}1)$$

During the FMEA, two effort and two flow variables (although from three different physical energy domains) have been identified for the two main ageing effect groups. The flow variables are the cell current, as it is directly proportional to the ionic reaction/diffusion current within the cell, and the delta-SoC (dSoC). The latter is, via the intercalation volume expansion of the active material, directly proportional to the amount of geometric movement in the electrodes and therefore within the whole cell. The effort variables identified are the temperature and the SoC. The temperature directly influences all reactions within the cell,

accelerating them by a factor of 1.5 - 2 every 10 °C of increase [Smith12]. The SoC is related to the potentials of the electrodes, which are a main factor for decomposition of salt (more often cited at cathode [Vetter 04, Broussley05]) and solvent (cited to happen at anode [WohlfahrtMehrens04]) of the electrolyte.

The next couple of subchapters describe how the ageing of the parameters of the short-term model is modelled in dependence of these four cause variables.

2.1.4.2 List of parameters of the model

Since not all of the model parameters are thought to change over ageing, a list of the parameters, their meaning and their assumed ageing causality is given:

k_1 A vertical scale factor for the OCV potential, for eventual interpolation and measurement errors. Ageing lowers the OCV [Safari11B], as can also be seen in Figure 3.2.3-e.

k_2 The length factor for the dynamic OCV gradient. This factor is affected by ageing, especially if particles are lost or solid diffusion paths get blocked. [Lei05]

k_3 The time constant for the dynamic OCV. The parameter is affected by ageing due to the same reasons as k_2. Since the gradients over the porous space will enlarge and be built up faster, this time constant will shorten during ageing.

k_4 The exponent of temperature dependence of the OCV time constant. No ageing effect was linked to this parameter. The parameter was held constant during aged parameter fitting.

k_5 The exponent of temperature dependence of the OCV. No ageing effect was linked to this parameter. The parameter was held constant during aged parameter fitting.

k_6 The exponent of temperature dependence of the reaction resistance. No ageing effect was linked to this parameter. The parameter was held constant during aged parameter fitting.

k_7 The standard rate constant. Only weak dependencies were found to be linked to this parameter (FMEA: “A change of reaction path for intercalation, to one which was not initially there, is rare”). The parameter was held constant during aged parameter fitting.

k_8 The asymmetry coefficient of the reaction. Since no change in reaction path was assumed, also their entropy asymmetry is going to stay constant. The parameter was held constant during aged parameter fitting.

k_9 The exponent of temperature dependence of the liquid resistance term. No ageing effect was linked to the temperature dependence of the transfer processes. The parameter was held constant during aged parameter fitting.

k_{10} The time constant for the liquid resistance term. The parameter is affected by ageing due to the blockage of diffusion paths in the liquid phase [Vetter05]. If larger gradients have to be built up to maintain transfer and information speed (ionic conductivity) drops, this time constant will be prone to lengthen.

k_{11} The exponent of temperature dependence of the liquid resistance time constant. No ageing effect was linked to the diffusion rate of ions. The parameter was held constant during aged parameter fitting.

k_{12} The exponent of temperature dependence of the solid resistance term. No ageing effect was linked to the temperature dependence of the potential distribution. The parameter was held constant during aged parameter fitting.

k_{13} This entirely empiric parameter, steering the exponential feature of the solid resistance term, is not taken into aged parameter fitting, since the first tests showed insignificance of changes of this parameter for aged fit quality.

k_{14} The time constant for the solid resistance term. The parameter is affected by ageing due to unevenly distributed ageing over the cell. [Smith09]

k_{15} The exponent of temperature dependence of the solid resistance time constant. No ageing effect was linked to the diffusion rate of ions. The parameter was held constant during aged parameter fitting.

k_{16} The hysteresis parameter of the reaction term. The parameter is taken into the aged parameter fit, since it is not quite clear how hysteresis resulting from multi particle effects [Dreyer09] is affected by ageing.

R_{BV} The general resistance parameter for the reaction term. The parameter is affected by many different ageing effects on both electrodes. [Vetter05]

R_L The general resistance parameter for the liquid term. The parameter is affected by the increase in gradients in the liquid phase. Furthermore effects of gas evolution and drying out have influences on this parameter [WohlfahrtMehrens04].

R_S The general resistance parameter for the solid resistance term. The parameter is affected by increasing differences in ageing over the cell.

C The actual cell capacity needed to scale the current down to a c-rate. The parameter is affected by multiple effects, as can be viewed in the FMEA or in literature [Vetter05, Tran11]. In this model it represents the change in cell capacity, which is not included in any of the other parameters.

η_c The Coulombic efficiency of the cell, needed to realistically calculate the SoC over longer periods of test time (> 2-3 weeks). The parameter is taken into aged parameter fitting due to reasons of cell ageing and also measurement accuracy checks.

k_{f2} This is the SoC-correction factor for not fully relaxed states after the constant voltage charge or any other preconditioning steps before the simulated profile starts. This factor can change over the age of the cell.

k_{f3} This is the temperature dependent SoC-correction factor for the difference in constant voltage charge states or any other preconditioning steps before the simulated profile starts. This factor can change over the ageing of the cell.

2.1.4.3 Rainflow counting for batteries

There are multiple approaches for connecting the ageing relevant parameters to the influence variables defined by the FMEA. In material science an approach called “rain flow counting” has been established over the last decades [Matsuishi68]. This method has the advantage of not involving an average over the load profile, but to accurately reproduce the number of load peaks and most importantly the number of times a hysteresis loop has been run through. From the original uniaxial, single input counting, publications have evolved the spectrum of application of rainflow counting to incorporate many ideas helping to make it useable for battery ageing, like multi-input, multi-axial loads [Genet06] or Markov models of measured load profiles [Johannesson99].

Rainflow counting for batteries, as is presented here, is not an algorithm for determining the SoH of a cell directly. It is a method for analysing measured load profiles and compressing the data in order to be used to calculated aged model parameters. If applying these parameters to simulate the cell, the SoH relevant quantities will be calculated.

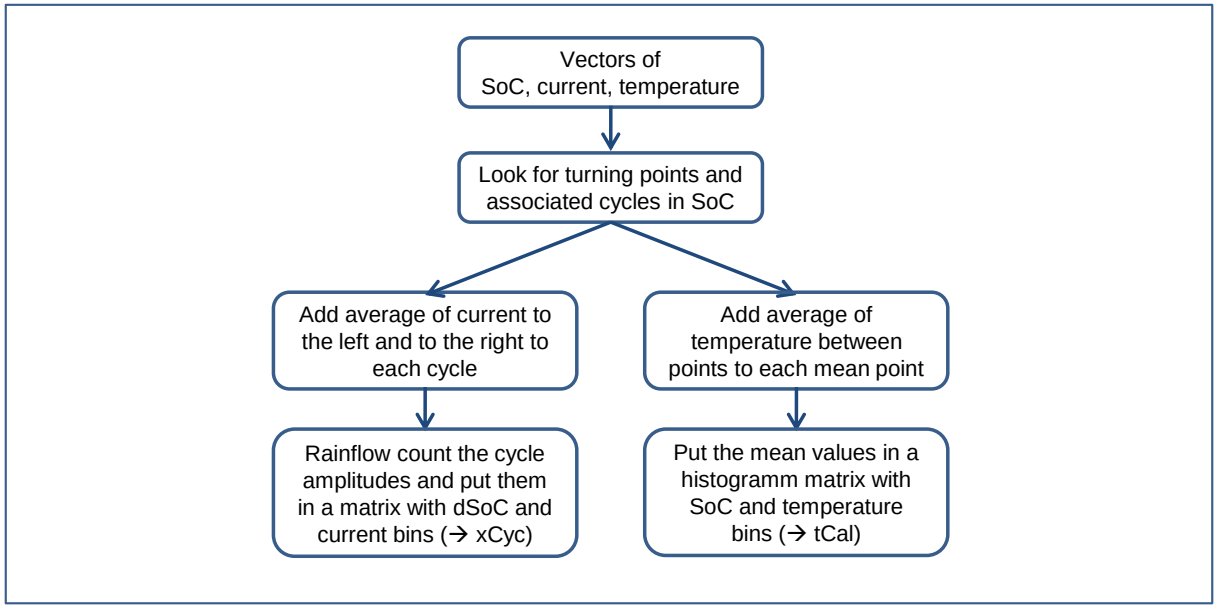

Figure 2.1.4-b – Flow chart for the rainflow counting process for battery ageing analysis. The cycle amplitudes (flow) / hours at state (effort) of the four influence variables are stored in two matrices xCyc (flow) and tCal (effort).

The proposed process of counting is partly developed standard and from composite materials rainflow analysis [Sweitzer05, Benasciutti05, Nijssen06], partly adopted by the author.

The rainflow counting process starts out with 3 vectors from measurement – the SoC, the current and the temperature. In a first step, analogous to classical rainflow, the turning points and cycles of the profile are identified (see Figure 2.1.4-c). The data of the cycles is stored in a matrix together with the turning point indices, the mean values and the amplitude values. In a second step, the time-based mean current and mean temperature for every cycle is added. The mean values are calculated time-based, since cycles can contain smaller cycles at different c-rates with higher measurement point densities (left plot in Figure 2.1.4-d). Finally

the histogram algorithm is called twice to create two data matrices, one (xCyc) with the cycle counts classified by delta-SoC and current strength and the other (tCal) with the hours of calendar ageing classified by temperature and SoC. The two matrices are displayed in Figure 3.2.2-a.

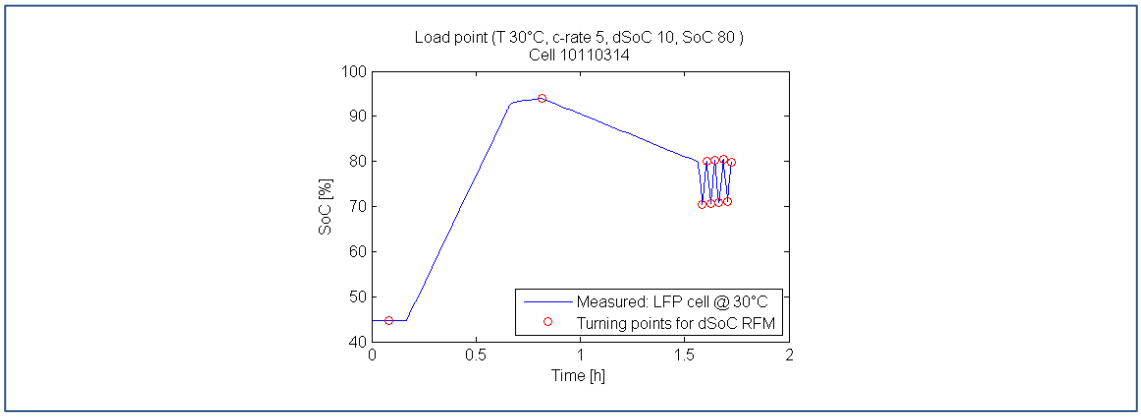

Figure 2.1.4-c – SoC of load cycle test with identified turning points. These are used to calculate the dSoC distribution in the "xCyc" rain flow matrix (RFM)

Often rainflow counting is modified to incorporate some kind of load sequence information for path dependent ageing analysis. In this case this information has been added by using the c-rate as current information. So if a pulse with fixed amperes and length is input, it is counted differently when the cell has aged already, since the cell capacity for the SoC and c-rate conversion is constantly adapted during load profile analysis.

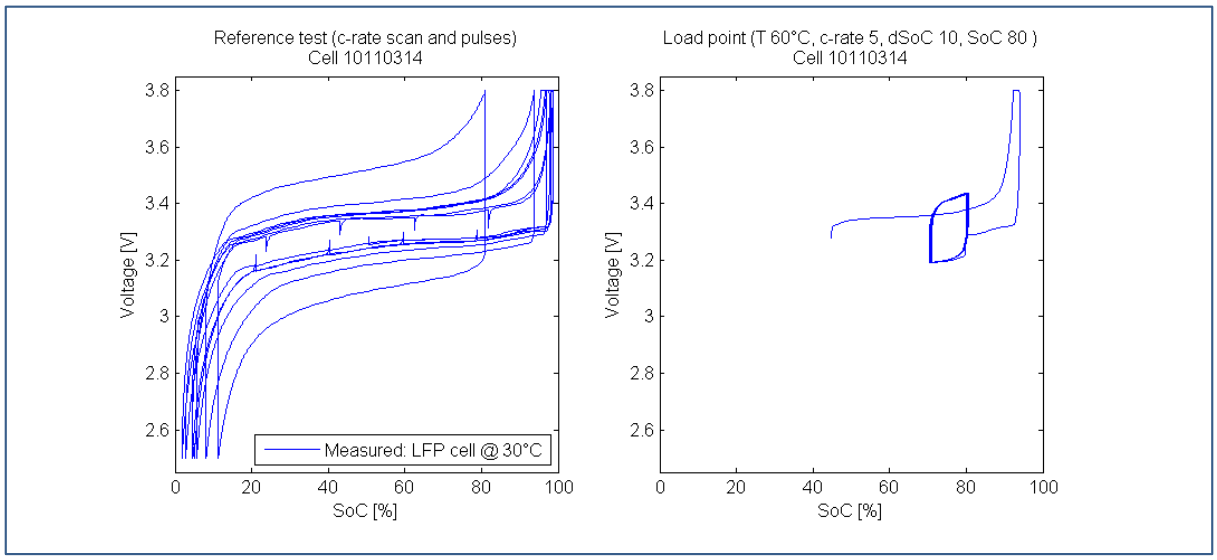

Figure 2.1.4-d – Voltage versus SoC load cycles. Left is a reference test procedure with full cycles, right is a constant amplitude load cycle test (with resets to planned mean SoC)

Although lithium-ion cells show staging behaviour in their overall capacity ageing (see chapter 3.2.3), this model does not contain any features trying to reproduce that special

behaviour, since the cells used in the experiment already show two very common but different staging behaviours (see Figure 3.2.3-j).

The whole algorithm has been implemented MATLAB m-script by modifying the basis of the rainflow counting algorithm by Adam Nieslony [Nieslony06].

2.1.4.4 Linear damage accumulation

The technique of damage accumulation for fatigue prediction was first published by Palmgren [Palmgren24]. Later work, based on this initial idea was published by Miner. [Miner45] Today it is mostly known as Palmgren-Miner damage accumulation rule. In the more recent time the theory was extended to composite material fatigue modelling [Boller69, Nyman99], which has primed the way for more complex fatigue load cycle analysis, as it further developed theories for multiple input treatment and multi-influence variables as reported in [Nijssen06] .

In case of linear damage accumulation, one calculates the damage induced in a piece of material under test by comparing the load cycles seen (n_x, from rainflow analysis) to the maximum number of load cycles (N_x) at this amplitude (x). Then those damage contributions are linearly summed up (2.1.4-2).

$$D = \sum_x \frac{n_x}{N_x} \tag{2.1.4-2}$$

The accumulated damage is then compared to the damage threshold. This threshold is for breakage standardized to be equal to 1, but depends largely on the application and data description while processing for N_x. For this work, the damage will be replaced by the quotient of the ageing of the parameters as suggested by Colombo et.al. [Colombo05]. This can be seen in the following formula (2.1.4-5):

$$\left(\frac{k_{i\_aged}}{k_{i\_new}} \right)^{c_i} - 1 = \sum_x \frac{n_x}{N_x} \tag{2.1.4-3}$$

The exponent c_i can only take two values, depending whether the parameter k_i is a growing or diminishing value, as displayed in (2.1.4-4).

$$\begin{cases} c_i = 1 & \frac{k_{i\_aged}}{k_{i\_new}} \geq 1 \\ c_i = -1 & \frac{k_{i\_aged}}{k_{i\_new}} \leq 1 \end{cases} \tag{2.1.4-4}$$

For reasons of the complex ageing behaviour of lithium-ion cells, some more complex, non-linear damage accumulations were researched as well. One is the accumulation according to Owen and Howe [Owen72], which was conceived for the ageing of composite material resin.

$$D = \sum_x \left[A\frac{n_x}{N_x} + B\left(\frac{n_x}{N_x}\right)^E \right] \quad (2.1.4\text{-}5)$$

This accumulation method was discarded, because data for intermediate ageing states was not sufficient to reliably fit the parameters B and E in (2.1.4-5). In future experiments additional data, for more support points of aged parameters should be measured, and then the author believes an ameliorated model can be deduced from data.

The data for the constant amplitude loading maximum cycle numbers (N_x) can be expressed as a function such as in (2.1.4-6). This function is then called the SN-curve (S for stress, N for cycle number). This formulation is the standard way of expressing an SN-curve, sometimes called Basquin's relation [Nijssen06, Genet 06].

$$N_x = CS_x^{\ b} \quad (2.1.4\text{-}6)$$

For the multi-dependent ageing of batteries, an extended form of this SN-curve (SNC) formulation is presented here. The extension develops SN planes rather than curves, which is in good agreement with the load data being in form of two dimensional matrices. For the cyclic load data a simple two part SN plane is suggested (2.1.4-7), while for the calendric data a constant term and an interaction between the two axis is proposed (2.1.4-8),

$$N_{Cyc} = a_{i1}S_x^{\ a_{i2}} + a_{i3}S_y^{\ a_{i4}} \quad (2.1.4\text{-}7)$$

$$N_{Cal} = a_{i5} + a_{i6}S_w + a_{i7}\left(S_wS_z\right) + a_{i8}S_z \quad (2.1.4\text{-}8)$$

which then allows to write the formula designated to describe the short-term model parameter change as a whole.

$$\left(\Delta\frac{k_{i\_new}}{k_{i\_aged}}\right)^{c_i} - 1 = \sum_{xy}\frac{n_{xy}}{a_{i1}S_x^{\ a_{i2}} + a_{i3}S_y^{\ a_{i4}}} + \sum_{wz}\frac{t_{wz}}{a_{i5}\sum_{wz}t_{wz}^{\ a_{i6}} + a_{i7}S_w + a_{i8}\left(S_wS_z\right) + a_{i9}S_z} \quad (2.1.4\text{-}9)$$

Throughout the document a_{ij} will be the denomination of the j^{th} parameter of the ageing model for the i^{th} parameter of the short-term model. Nine a_{ij} (j=1..9) are required to calculate one parameters k_i.of the short-term model.

This equation builds the basis of the long-term model, as it can also be transformed to model the capacity of the cell with an exchange of the right hand side. Formula (2.1.4-9) applies for all k's and R's. Formula (2.1.4-10) is used for C.

$$\frac{1}{1-normC(SoH=0)}\left(1-\frac{C_{aged}}{C_{new}}\right)=\sum_{xy}\frac{n_{xy}}{a_{91}S_x^{\,a_{92}}+a_{93}S_y^{\,a_{94}}}+\sum_{wz}\frac{t_{wz}}{a_{95}\sum_{wz}t_{wz}^{\,a_{96}}+a_{97}S_w+a_{98}(S_wS_z)+a_{99}S_z} \quad (2.1.4\text{-}10)$$

Similar damage accumulation models for lithium ion cells, but with a simpler rainflow data treatment and an uniaxial SN formulation of this split type (cyclic and calendar) was presented by [Safari10] during development of this work and earlier by [Thomas08, Duderzert09]. Hints on a path dependence of the ageing, and therefore a need to extend the damage information by a time information were not yet taken into account, as they seem largely inferior to the main ageing effects [Gering11].

2.2 Parameter Estimation

2.2.1 Error calculation on time based measurements

In order to find the parameters for the short-term model, an error has to be calculated as the difference between a measurement and the simulated equivalent, which is to be minimized during parameter fitting. This error can be calculated in many ways and the selection of these has an essential effect on the fitting speed and the parameter quality. In this chapter different error calculation definitions and their sensitivity to parameter variations will be compared under the special use case of the short-term battery model and a selection of algorithm is made.

The main problem with load profiles typical for battery is that the voltage response to a current excitation is biased with the OCV potential. This means that excitations, as they are produced by a normal usage profile, in the order of seconds to minutes long, produce very small amplitude responses in comparison with the response to a longer period excitation from SoC changes. In Figure 2.2.1-a in the upper left hand graph, one can see the voltage response of the battery cell to the current excitation in the graph just below. In the right hand column of Figure 2.2.1-a the last pulse sequence is zoomed onto. It is a full cycle (constant-current charge – constant-voltage charge – constant-current discharge) of low c-rate, with higher rate pulses overlaid. In the current excitation the pulses are clearly visible. Less so in the voltage response, to the extent that the error actually drops in these pulse sequences (third graph from top), even when the pulse shape of the simulation is in no good fit (top graph in right column). The error as displayed in the third graph is the residual sum of squares (RSS) when comparing simulation to measurement on a per-time-step basis.

Since the RSS drops in the pulse sequences, all parameters which have long time constants will be fitted correctly (OCV term, solid term), whereas the “faster” parts of the model, responsible for the pulse behaviour are going to lack a good fit (reaction and liquid term).

2.2.1.1 Time domain error calculation

Usually, when the problem of different frequency excitations and different amplitudes connected to the different frequencies is found, the calculation of the error is proposed to be done in frequency domain. [Buller05, Thele08]. In that domain, the frequency is the path variable, as for example in the Nyquist plot, whereas the amplitude difference (linear resistance) is the x-axis. Solving the initial problem, a new one arises – the transformation form time based measurement data to frequency domain data. This can be achieved via a Fourier-transformation of an especially measured sine wave or pulse answer measurement, but no measurements of simple full cycles or driving profiles could be converted. The pulse excitation is too biased by the OCV to be transformed correctly, so it is impractical [Jurczakowski04]. The sine wave measurements have to be performed on special equipment because of the high control and measurement frequency required for accurate reproduction of sine waves and scanning through frequencies takes some time. In literature a period duration of 0.1 mHz is usually the smallest frequency [Andre10], which would take about 3 hours for a single period and, to have a steady state, one needs at least three periods. So,

overall, the frequency domain is not an optimum solution for the task and the error calculation will be done in time domain.

In order to calculate time domain RSS errors, there are at least two areas in which a solution can be found. One is the weighing of single error points or segments during the test time and the second is numerical derivation of the data before RSS error calculation.

In Figure 2.2.1-a, in the lower three plots show the direct RSS, the RSS after the 1st derivation of the voltages and the RSS after the second derivation. Additionally the colour correspond to different norming and weighting of the steps. Norming the error was important for the summation of the different error profiles, since it is required to return scalar back to the optimization (except for the Pareto DE, which takes a vector of four values, see chapter 2.2.2).

The weighting of the time-steps was first tried to be done by manually selecting areas of great interest and giving them an increased weight, but as more data became available, this method proved to be too time intense to continue. So the weighting was changed to a two-step process. First, all data points which did not produce an additional information in the simulated response were deleted from the input profile. This was done by always comparing the normal distance of a data point to the shortest connection between its two neighbouring points. If it was below a threshold of 1mV, the point was taken out. This reduced calculation time of the fitting tests as well. The second step was to weight each time-step by the inverse of its step length. This is very helpful, since the short steps are the ones where the short-term dynamics are excited (reaction and liquid term). So basically one could describe the weighting strategy as: “the slower the change in measured response, the smaller the weight of the error”.

The next step was to use the RSS errors of both derived profiles (lower two graphs) and add them to the directly calculated RSS error (middle graph in both columns). One can see that the error of the 2nd derivation, the curvature of the data, is high during the short pulses and diminishes in between by around 10 orders of magnitude. The error of the 1st derivation does not quite show such a selective behaviour, so it was added with less priority. So the error calculation used for the parameter optimization was defined as written in (2.2.1-1), wherein d_1 and d_2 were equal to 1 and 10^3 respectively.

$$Err = \sum_t \left(\left\| U_{meas} - U_{sim} \right\|^2 + d_1 \left\| \frac{\frac{\partial U_{meas}}{\partial t} - \frac{\partial U_{sim}}{\partial t}}{\Delta t} \right\|^2 + d_2 \left\| \frac{\frac{\partial^2 U_{meas}}{\partial t^2} - \frac{\partial^2 U_{sim}}{\partial t^2}}{\Delta t} \right\|^2 \right) \quad (2.2.1\text{-}1)$$

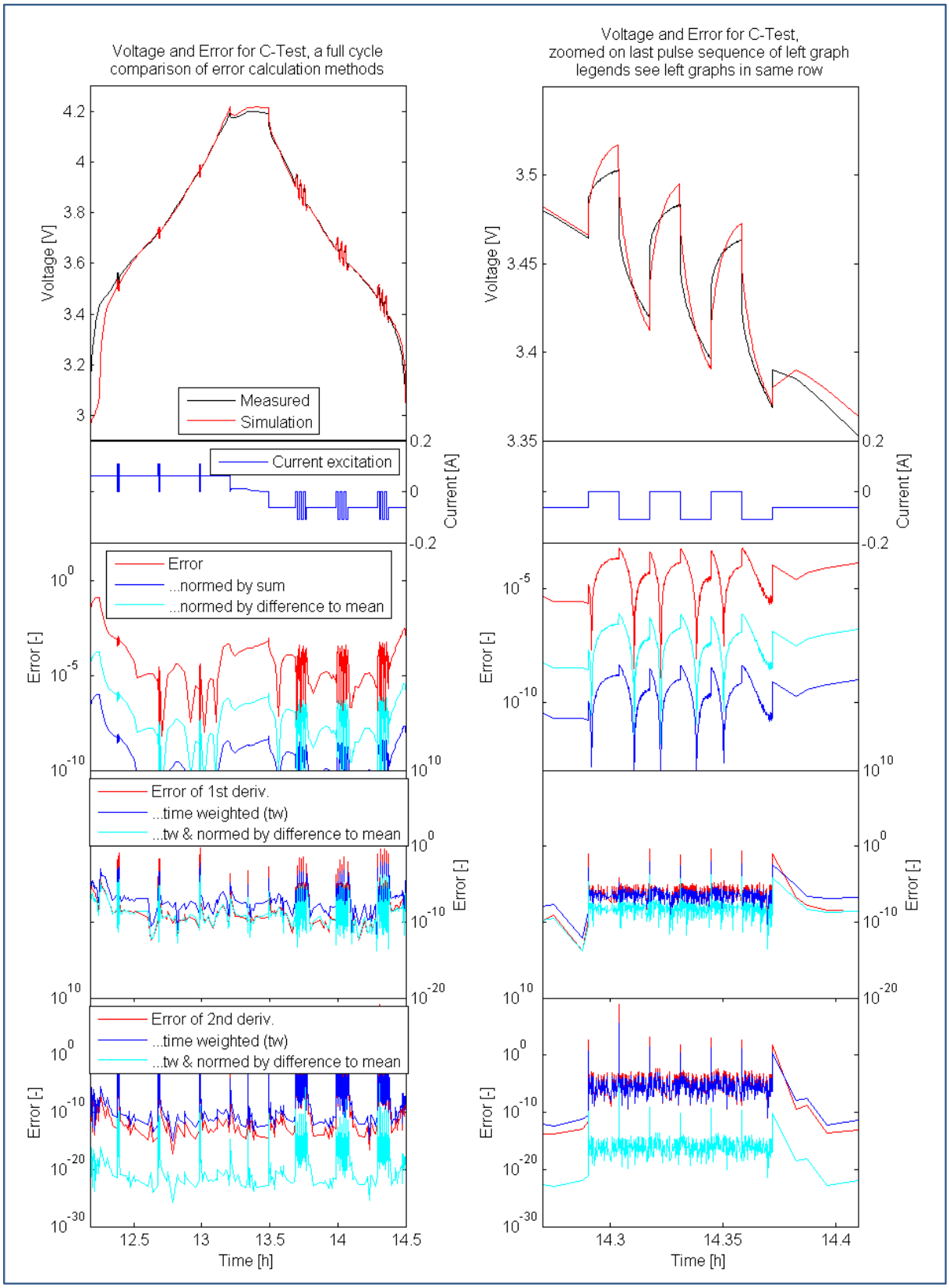

Figure 2.2.1-a – Comparison of methods for error calculation in time domain. Error is always calculated as the residual sum of squares (RSS) of the difference of the measured to the simulated voltage and the 1st & 2nd derivations of this difference in voltage. The colours indicate a variation in norming those errors for concurrent use. Red is the error in base RSS, dark blue is the error weighted by time-step size or total error and cyan indicates the error as weighted and normed by the mean of the error.

2.2.1.2 Sensitivity of error to parameter variations

The sensitivity of the error definition (2.2.1-1) to changes in the parameters is to be closely looked at. The sensitivity will, at fitting time, determine how fast and in which order the parameters are going to be optimized and if finding a global minimum is possible. A parameter with a high sensitivity in the error will likely be optimized primarily, since it represents the larger gain in fitting error. If the sensitivity of the parameters is too different, this behaviour can easily lead to error-induced local minima in the parameter space, especially if using zooming search algorithms (see 2.2.2.2). This means that the error for the very sensitive, but not independent parameter is reduced to a local minimum. Then the other parameters are optimized, not further changing the minimum value for the first parameter any more. This behaviour effectively inhibits finding a global minimum when error sensitive and non-sensitive parameters have strong interactions.

In Figure 2.2.1-b the sensitivity of the error is presented for two simple parameter variations. The red lines represent the base parameter set, from which the R_{BV} is doubled (dark blue lines) and the time constant of the liquid term, k_{10}, is put to one third of its base value (cyan lines). The topmost graph shows the voltage profiles for the simulations with the variants. The middle and the lower graphs show the three summands (one per graph) of the RSS error as specified in (2.2.1-1). These are, as indicated by the abbreviation “tw”, already the time-step size weighted values, but not yet accumulated over time and error species.

Both modifications show that the error stays within a similar order of magnitude. The modification of the resistance influences mainly the direct RSS, as visible in the third row graphs, while the time constant modification touches all error sorts and especially influences the 2nd derivation error, it rises by nearly two magnitudes. Overall, the error for the base is 0.83, for the variation in resistance its 1.3 and for the time-constant variation 6.57.

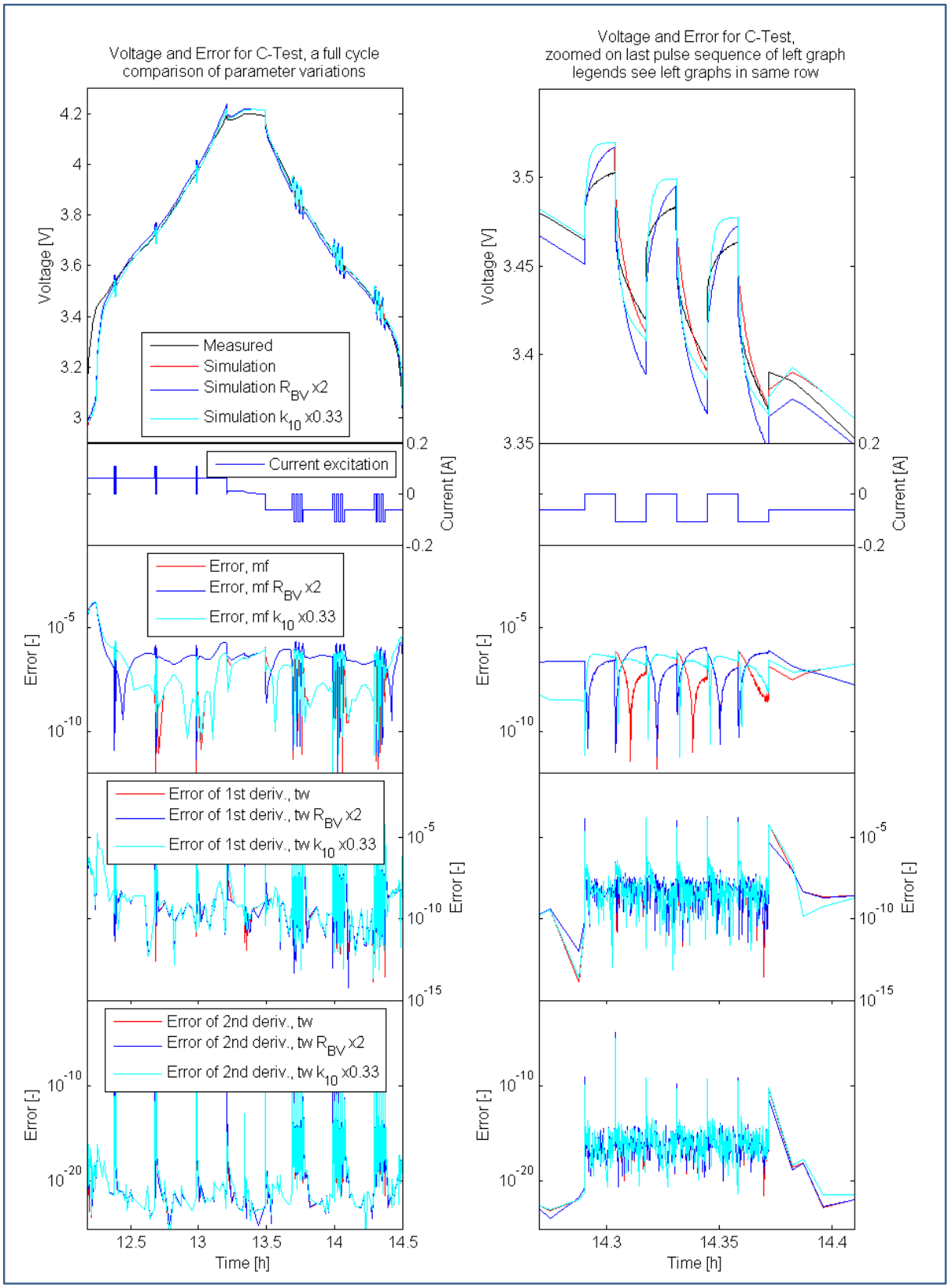

Figure 2.2.1-b – Comparison of parameter variations and its influence on the calculated error. The error calculation used is normed error of the direct RSS and the time-step size weighted RSS of the derivations. In blue is the parameter set used as standard, the red set indicates an increase in RBV, a linear resistance parameter – influences in error seen mainly in direct error. In cyan is a variation of a time constant – its influence is mainly visible in 1st & 2nd derivation errors.

2.2.2 Different algorithms

2.2.2.1 Short-term model parameter fit

The short-term model has to be fitted to cells in their new and aged state. Per cell and state, a total of 26 parameters for new cells and 10 parameters for an aged state are to be fitted (see 2.1.4.2 and also Table 2.2.3-i for information about which ones are selected for aged state). During this work a total of 8 different new cells' parameter sets (see chapter 3.3.2) and 76 aged parameter sets of two of the new cells' chemistries (see chapter 3.3.2) were identified.

For this purpose stochastic parameter fitting algorithms were used. The first two algorithms were implemented and tested, but found to be neither very accurate nor fast nor stable in convergence. So a third more complex algorithm was implemented and used for the final work. They will be compared in this chapter for their advantages and their problems, since there are many problems, which can be solved with the initial two algorithms as well. There was no deterministic algorithm used, since it is not possible to calculate the complete derivation matrix (Jacobian) for the presented model other than numerically, which would in turn give no advantage for these kind of algorithms.

2.2.2.2 Differential Evolution (DE)

The differential evolution algorithm is one of the base algorithms in stochastic optimization [Storn97], as it is a very simple method. This is also the reason for it being the first algorithm tried on the problem. The advantage of a simple method is the speed of implementation and, in this case, the large repertoire of techniques to improve this algorithm available in literature [Brest06, DosSantos09].
Two of those algorithms were integrated in the implementation. A Pareto sorting and archiving, as well as an adaptive zooming into the parameter space were applied. The Pareto sorting has the advantage of allowing multiple error calculation methods at the same time and not diluting the effects of the parameters on the single errors. The method searches for the Pareto optimal solution, which means that the result is a pool of solutions which are best in at least one of the error measures. This feature can effectively avoid the effect of the error induced local minima described in chapter 2.2.1.2, since the parameters have different sensitivities on the different error definitions.
The zooming algorithm is used to produce more accurate fitting results in a shorter time. Because the movement of the individual is proportional to the zoomed parameter space and not the initial search space, allowing smaller step sizes, finding of smaller footprint minima or just better localizing the minimum found is possible. This way the convergence speed is increased.
The algorithm flow chart is presented in Figure 2.2.2-a. It features a single loop over the generations of the parameters. First an initial random simulation run is performed to fill the archive. During the search loop the new positions are calculated as points on the difference vector of an archived position to the best position archived (differential evolution). Some random exchanges of coordinates (crossover) and random insertion of new positions (genetic extension) help in increasing coverage of the test. After the simulation is done, the

Pareto sorting of the combined new and archive data is performed and the parameter space is zoomed to reflect some of the changes in the archive.

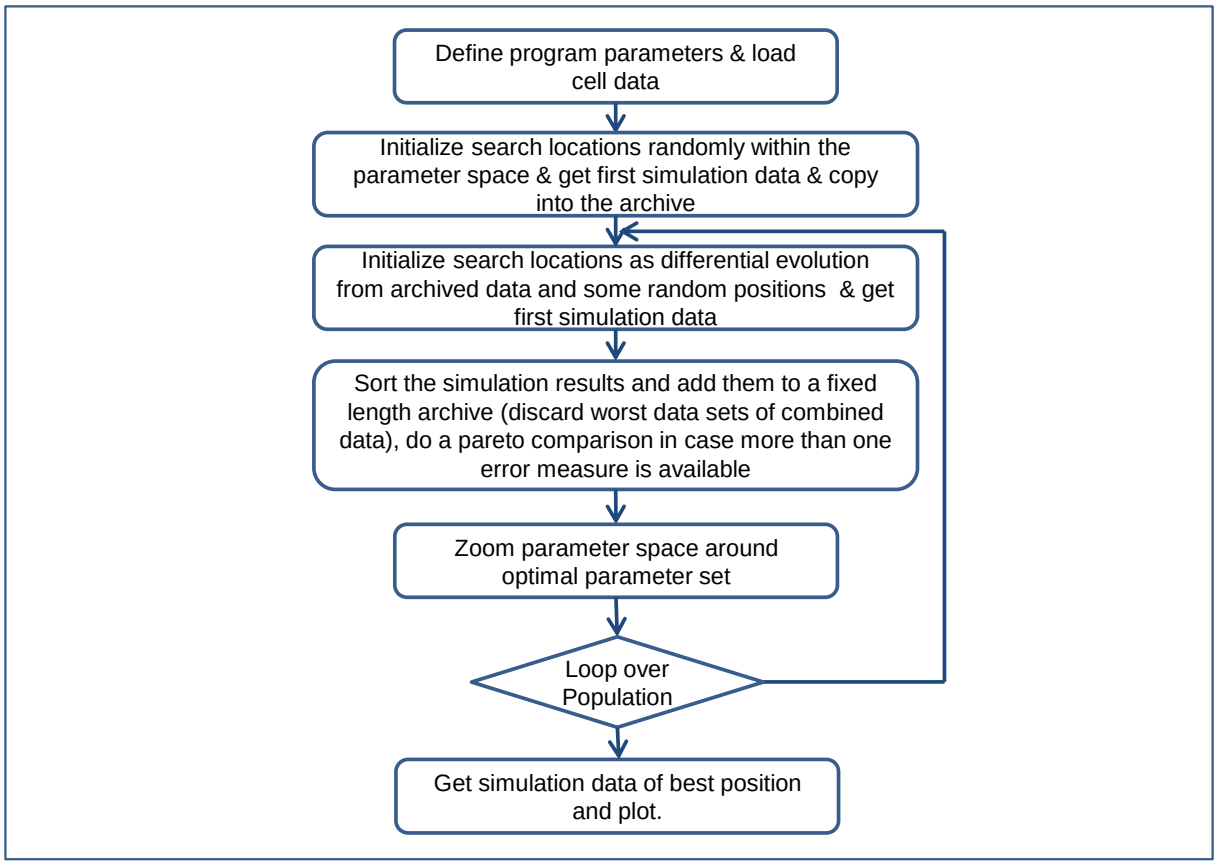

Figure 2.2.2-a – Calculation flow chart for a DE optimization algorithm, first used for parameter identification. Pareto comparison and archiving was CPU intense

This algorithm was the second best used in this work. It is slower than the GABC (see chapter 2.2.2.4), but it can handle the different error calculations at once and avoid the local minima problem to a good extent.

2.2.2.3 Surrogate Model

This algorithm was selected, since it uses some Design-of-Experiment and linear model ideas, which were also applied in the experiment [Sondergaard03]. It is the most calculation intense search algorithm of the ones presented here, since the surrogate model fitting is a time consuming feature (Figure 2.2.2-b).

During testing phase, this algorithm seemed faster than both of the others. This was due to the testing problem used, the Rosenbrock function [Rosenbrock60]. For this very smooth surface, the linear models of third and fourth order were perfectly fitted and the minima were exactly predicted. During the calculation on real data, it showed that the fourth order functions were not enough to reliably fit surrogate models to the highly interacting error measures of the 26 parameter-dimension problem. The fitting of the surrogate linear model took longer than the actual battery model simulation. Zooming was performed and helped the convergence, but only at high point densities per iteration (> 700 individuals per iteration).

Summing up, this algorithm is very fast for smooth problems when the surrogate model order is higher than the parameter dimensions.

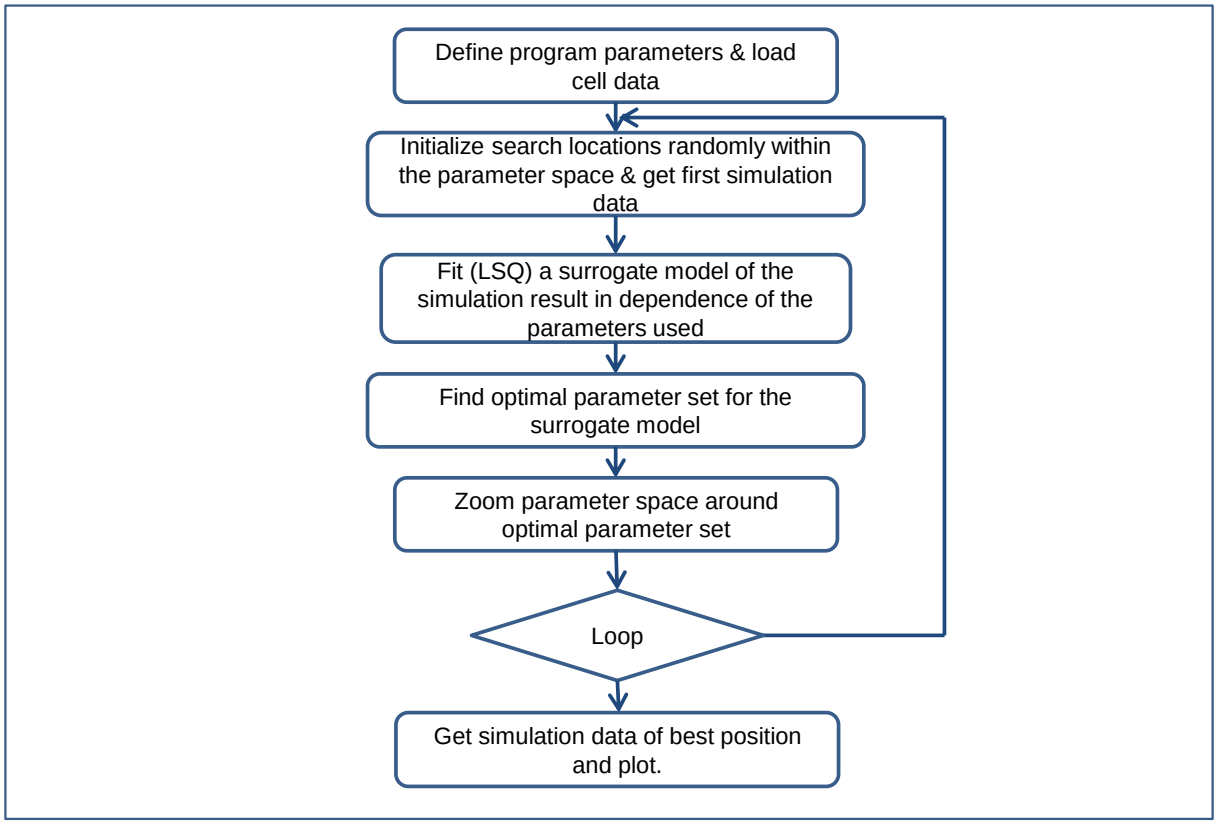

Figure 2.2.2-b – Calculation flow chart for a surrogate optimization algorithm. Building sufficiently representative models for a 20+ dimensional parameter space is not a lot of time saving compared to simulating the problem model.

2.2.2.4 Gaussian Artificial Bee Colony (GABC)

This algorithm was first presented by [Karaboga07] and later republished by dos Santos and Alotto [DosSantos11]. It has a rather complex structure due to the three blocked simulation evaluations and the divided paths during the optimization loop. It has an integrated archiving feature (employed positions), a continuous random insertion of points (scout positions) and a differential evolution part (onlooker positions), while exchanging information not once (like DE), but twice per iteration. Simple greedy selections are computationally very fast compared to surrogate models or Pareto archives.

Error-induced local minima problems are kept to a minimum since the selection of the employed positions only compares the new and the old value, not to all positions like in an archive. So the randomly initialized positions work their way to the best solution over the iterations, only changing their direction and speed when another position has the lead.

The implementation of the algorithm was done according to the flow chart displayed in Figure 2.2.2-c, which was derived from [DosSantos11]. Due to its split path architecture, it has some limitations in selecting the number of individuals (always a multiple of 4 times the number of CPUs used in parallel).

This algorithm was used to fit all of the short-term model parameter sets presented in this work.

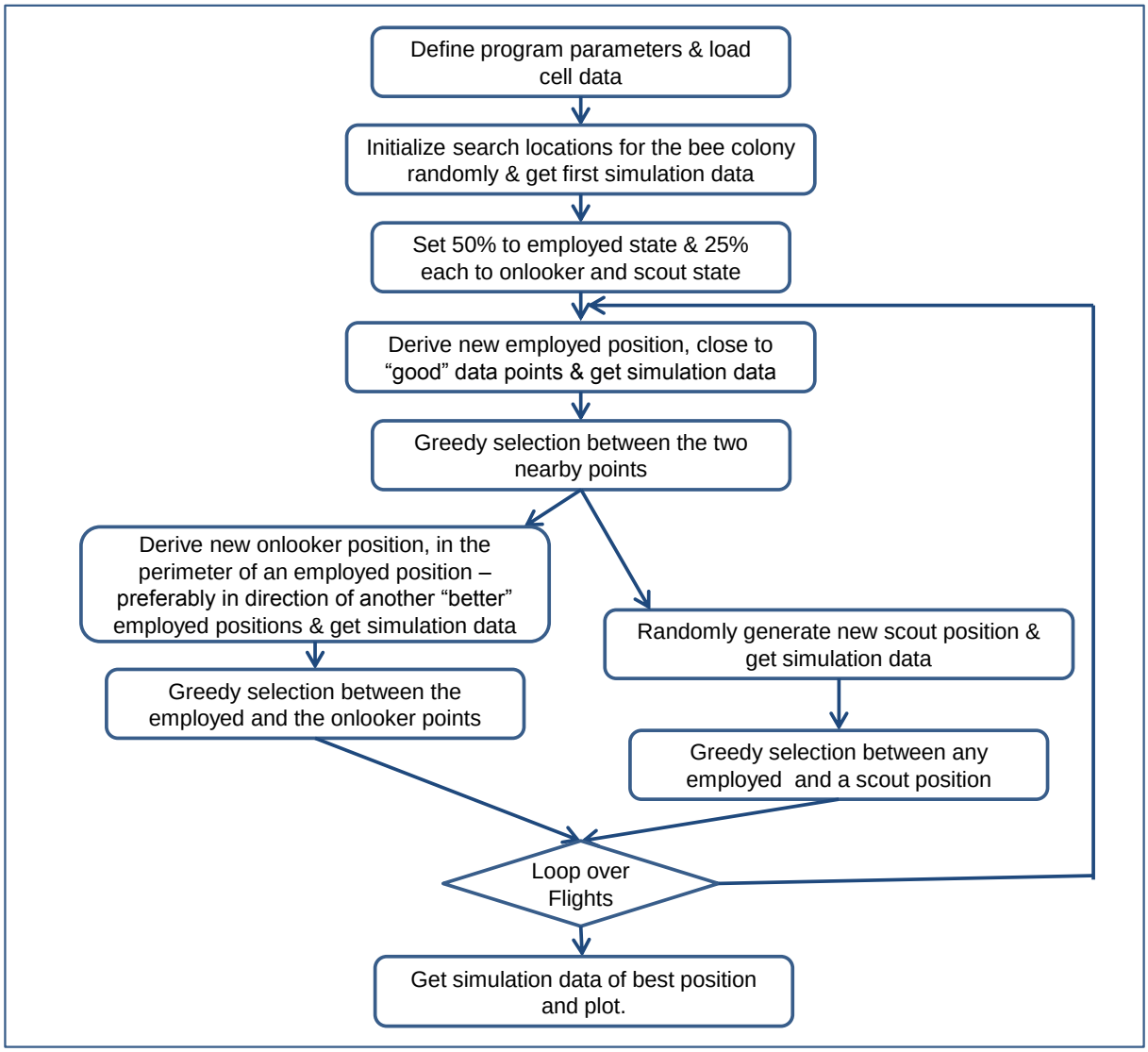

Figure 2.2.2-c – Calculation flow chart for the Gaussian Artificial Bee Colony (GABC) optimization algorithm, which was finally used for parameter identification. This biologically inspired algorithm showed the best performance, due to flexibility in parameter space and good CPU load distribution.

2.2.2.5 Comparison of stochastic fitting algorithms for high dimensional problems

All three algorithms were implemented in MATLAB using the parallel computing toolbox to parallelize to model evaluation. The fitting was run on a 12 core workstation with 36Gb of shared RAM. All given figures refer to this setup.

The three algorithms were tested against each other, to present the finding when applying these stochastic algorithms to high dimensional fitting problems. The ranking would not have been the same for up to 3 parameters.

In total, one can say, that for the short-term model parameters, the GABC, with about 2 times the number of employed positions as dimensions to fit, is slightly superior to a DE with

Pareto archiving and zooming and both are distinctly better than the surrogate model algorithm with DoE or random point distribution and linear models. This is also displayed in Table 2.2.2-i, where the first column is the run time of the fitting process for a single parameter set, 100 individual evaluations per iteration and 100 iterations. The second column is the average fitting quality of 10 runs of the algorithm. It is calculated as the average of the lowest errors found in relation to the average of the lowest errors of the GABC. The last column gives the standard deviation for the averaging step of the errors.

Optimization Algorithm	Time [min] for 100 iterations (1 cell, 100 individuals / bees)	Average fitting quality after 10 x 100 iterations (compared to GABC)	Standard deviation of fitting quality after 10 x 100 iterations (compared to GABC)
DE	288	1.13	0.09
Surrogate Model	361	1.4	0.54
GABC	247	1	0.05

Table 2.2.2-i – Comparison of run time and fitting quality of the different algorithms, run for the Standard LFP (SoH=1) parameter set.

2.2.2.6 Ageing parameters

The parameters of the ageing models' SNC curves were identified using a nonlinear least squares fitting. This is provided by the MATLAB Optimization Toolbox via the function "lsqnonlin". One fitting process finds the nine (j) parameters a_{ij}, which describe one parameter k_i per chemistry.

The reason for using a built-in, deterministic optimization function for this problem is, that the ageing model is very fast in evaluation (<0.005 seconds) compared to the short-term model (>5 seconds) and additionally the SNC curves' analytical derivations for each parameter are known. So a Jacobian matrix can be constructed and returned to the fitting function.

Since the routine is deterministic, it is sensitive to the initial values of a_{ij}. A simple workaround has been put in place. Since fitting works so fast, for each parameter set the function is called 10 times with randomly distributed initial values. The best of the 10 results is taken as final set. If none of the ten sets do have similar parameters as result, the fitting is called another 10 times.

2.2.3 Constrained estimation of short-term parameters

In an electrochemically deduced model, as the one presented here, parameters have a certain effect or a material property in behind. Most of the parameters contain some physics constants or other known parts. Those parameters are at least bound by being either positive or negative values from model building. Arrhenius exponents for example are awaited to fit in a certain range of size. For some processes, for example time constants, boundaries are known where other processes start to dominate and these can be translated in values for maximum and minimum parameter space constraints for fitting.

Due to the special model structure, in which every summand stands for a physical effect in the cell, it is important that the time constants are not interfering with each other during fitting. Additionally when doing the aged cell identification, one does not want all parameters to start freely in the whole parameter space, but rather to commence where the new cell has been identified and then optimized to the aged status. This idea has been followed to an extent, where only those parameters, which have an ageing effect in theory, are optimized. Their aged parameter spaces have boundaries close to the new values and the other boundaries are moved in the expected ageing directions.

Hence the parameter fitting algorithms all featured constrained optimization for the short-term model parameters. In Table 2.2.3-i the parameter spaces used for identification are listed. The first two columns give the minimum and maximum constraints for optimization. The third column features the ageing directions of those parameters identified to have an ageing influence (see chapter 2.1.4.2). All rows with a dash were held at their new cell parameter values. The last column gives the modified boundaries, for example if there is “down” written in column three, then it is the adapted minimum value for the aged parameter fit.

The constrained optimization is intended to lead to physically and electrochemically based parameter values and to stable and fast fitting results. On the contrary this technique can also lead to numeric problems if the boundaries are incorrectly placed. Parameter spaces of similar effects are overlapping too much or the spaces are simply too small. The last point is directly counteracting the speed of the parameter regression, so it is the most common error in constrained optimization. The parameter spaces given in Table 2.2.3-i are the result of a two stage research process. First the knowledge about the theoretical values of those parameters that were known were assessed. The Arrhenius-like exponents are one group of parameters where this was especially fruitful. Also the parameters for the reaction term could be constrained by theoretical consideration to a very suitable range. In a second step, test fitting was run on a trial-and-error basis with very different cell chemistries and cell geometries (see chapter 3.3.2). The parameter spaces as presented were able to easily find parameters within to incorporate all these cells and not unnecessarily prolong the fitting run time.

parameter	new value fit minimal	new value fit maximal	aging direction	aged value fit new directional boundary
k_1	1	1.01	down	0.98
k_2	0.001	0.15	up	0.2
k_3	150	600	down	100
k_4	-50	0	-	-
k_5	-250	100	-	-
k_6	2000	5000	-	-
k_7	0.1	5	-	-
k_8	0.7	1.1	-	-
k_9	3500	5000	-	-
k_{10}	10	50	up	120
k_{11}	-30	50	-	-
k_{12}	2000	5000	-	-
k_{13}	1	5	-	-
k_{14}	600	1000	up	1200
k_{15}	-50	25	-	-
k_{16}	1	2	-	-
R_{BV}	0.0001	0.1	up	0.3
R_L	0.00001	0.01	up	0.3
R_S	0.00001	0.005	up	0.01
C	0.97	1.03	down	0.25
η_C	0.9999	1.0001	both	0.995 / 1.005

Table 2.2.3-i – Parameter spaces for new cells and aged cells. Those constraints are used for every cell fitted during this work.

3 Results – Experiment to Model

3.1 Design-of-Experiment [Prochazka13]

The experiment was conceived as large-scale ageing experiment; therefore more than 150 cells were subjected to ageing conditioning. Apart from planning how to distribute the sample points into the possible operating space of the cells, also the restrictions of the cycling equipment had to be taken into consideration.

Pouch cells of two different chemistries were studied: 99 cells which featured lithium-iron-phosphate cathodes and high-power graphite anodes (further referred to as LFP cells) and 78 cells which featured nickel-aluminium-cobalt-oxide cathodes and high-energy graphite anodes (further referred to as NCA cells). For reasons of energy consumption and safety of the experiment, a small cell size was selected for the cells. The cells showed initial capacities of 50mAh (LFP) and 60 mAh (NCA) and consist of three square electrode sheets of sequence anode (single layered) – cathode (double layered) – anode (single layered). The cell production process is shown in Figure 2.2.3-a. During the whole experiment the cells were pressurized by using plastic clamps sitting on the outside of the pouch foil, in analogy to the straps commonly used in automotive applications, to hold the electrodes in place firmly. A common carbonate electrolyte (EC/EMC) and PP separator were used. The cells were especially designed and built for this experiment, using base electrode materials from Südchemie AG and cell building know-how from our project partner GAIA Akkumulatorenwerke GmbH.

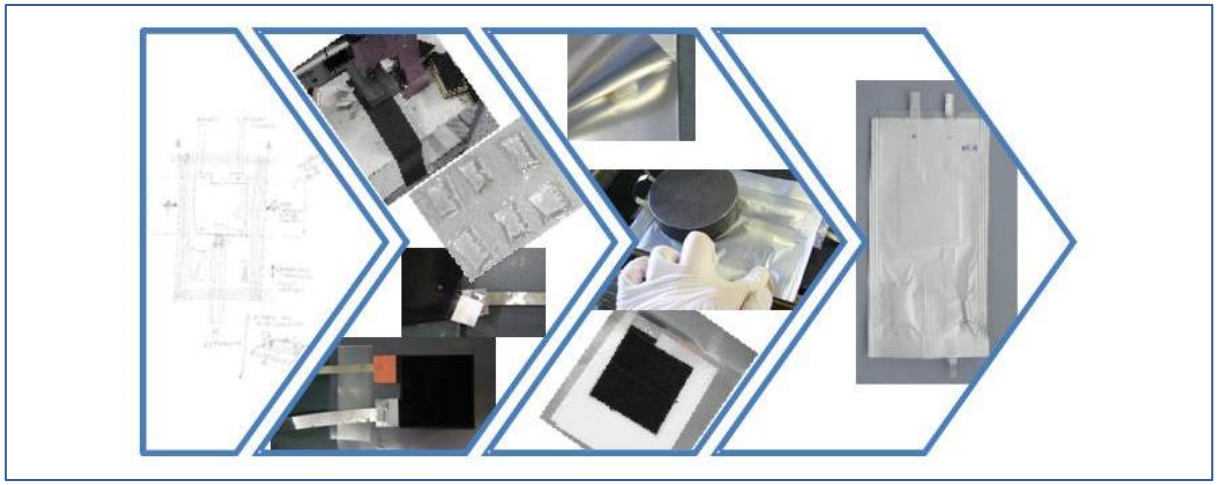

Figure 2.2.3-a – Cells were built from custom-punched square electrodes at our project partner GAIA

3.1.1 Statistics & DoE

Parallel to building cells, a Design-of-Experiment (DoE) was conducted. The DoE is a procedure which helps to plan and conduct an experiment such as to obtain statistically valid

and objective conclusions [Montgomery 05]. It consists of 5 steps, of which the first four will be explained in this subsection, for the last step see the explanations in chapter 3.2.3.

The first step is an accurate statement of the experimental target. In this study, the aim was to determine the optimal settings of the key exterior influence factors on the target values “cell capacity decrease” and “impedance increase” [WohlfahrtMehrens04]. The influence factors will be tested such as to find the optimum settings to prolong the time until the end-of-life criterion for one of the target values is reached. Taking into account the limited availability of cycling test equipment (max. 96 channels in parallel), only four exteriorly applicable parameters, were chosen for a given cell chemistry and geometry. The four factors are current, temperature, state-of-charge (SoC) and delta-SoC (dSoC). The end-of-life criterion (EoLc) was formulated according to [Prochazka12], as being a certain percentage of capacity, retention as compared to the initial measurement. The limit was set to 60% remaining capacity for reasons of testing more than just the commonly required range of 80%. For the impedance increase a limiting percentage of 300% was chosen. Both values had to be measured always at the same temperature, which was found especially important for the impedance.

The second step of the DoE procedure is the screening of the tested cells as well as the conception of the full factorial test plan. Screening means defining the range limits of the settings of the external influence factors (i.e. -15, 20, 50 °C are settings for the factor “temperature”) and testing of these limits regarding the cells’ sensitivity in voltage response to setting combinations (i.e. are high c-rates at low temperatures possible?). The screening was mainly done by literature research, where many single-factorial variation experiments are on display [Ramadass03, Dudezert09, Kumaresaran06, Dubarry07, Smith12]. The fishbone-diagram in Figure 3.1.1-a was created out of the testing constraints and the results found in literature, wherein the controllable design factors are the influence factors to be actively varied in the test plan. From the number and assumed influences of uncontrollable factors the number of repetitions of each test point was determined to be at least three times, in order to obtain statistically valid results. On the bottom side of the effect arrow in Figure 3.1.1-a the factors are listed, which require special attention during the planning phase. It must be ensured that the “held-constant factors” are truly constant for the whole duration of the experiment, whereas the nuisance factors are points, where very accurate calibration or additional measurement and measurement devices are supplied.

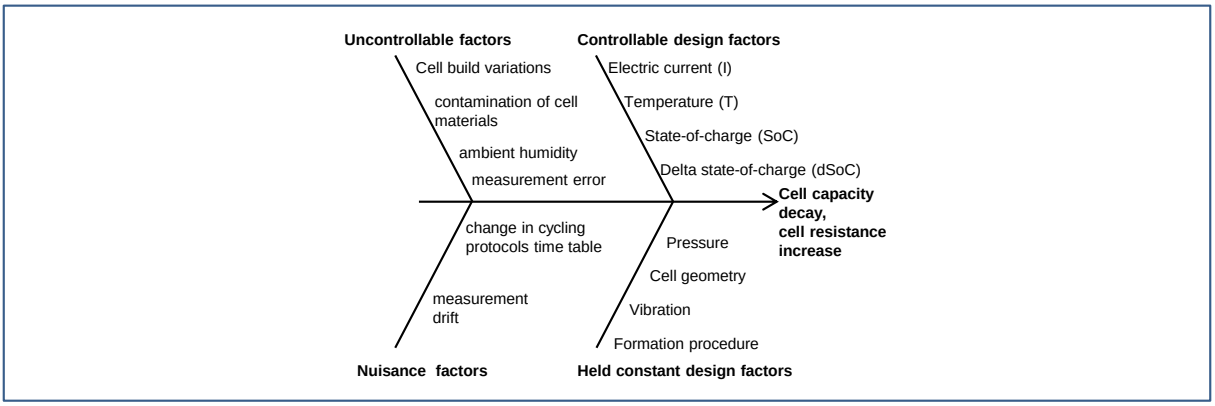

Figure 3.1.1-a – Fishbone diagram showing the majority of possible influence factors on an ageing experiment. Only the controllable design factors are the ones actively varied in DoE.

The four influence factors for this experiment are the temperature, the current (I, always given in c-rate), the average state-of-charge (SoC) and the amplitude or delta state-of-charge (dSoC). The temperature is given in degrees Celsius [°C], the range limits were set to -15°C and 70°C. For the current (expressed as c-rate) the generally accepted definition was applied, that the “c-rate is the current, which corresponds to the cell capacity” [Linden02]. The range of test for the c-rate is 0Cr (pure calendar ageing) to 5Cr for charge as well as discharge. The average SoC is given in a range of [0…1]. The test will not exploit the full SoC range but will stay within 0.1 and 0.9, because it is not expected that a real-life application relies on the outer limits of the cell operation window. The dSoC is the SoC swing which is run through by a single constant-current pulse, which means that the SoC of the cell oscillates around the required average SoC by half of the dSoC value. The range limits of the dSoC will be 0 (calendar ageing) to 0.8.

The full-factorial test plan is constructed out of each combination of the controllable factors in each of its factor levels. Factor levels are the numeric values in which the influence factor range is discretized, meaning for example the current factor range is 0 to 5 C, in which the levels are for example 0, 0.5, 1, 2 or 5 C. When considering the four identified controllable factors with five setting levels each, the full test plan has 45=1024 possible sample points and should be repeated at least 3 times in each point to eliminate the risk of testing an outlier with >90% confidentiality.

If the factor levels are chosen each within a physically possible range, the interaction with other factors’ levels can be limited by the cell physics or the measurement equipment accuracy. The range of each factor, as well as the interaction limits found in literature, are marked as full (LFP) and dotted (NCA) lines in Figure 3.1.1-b.

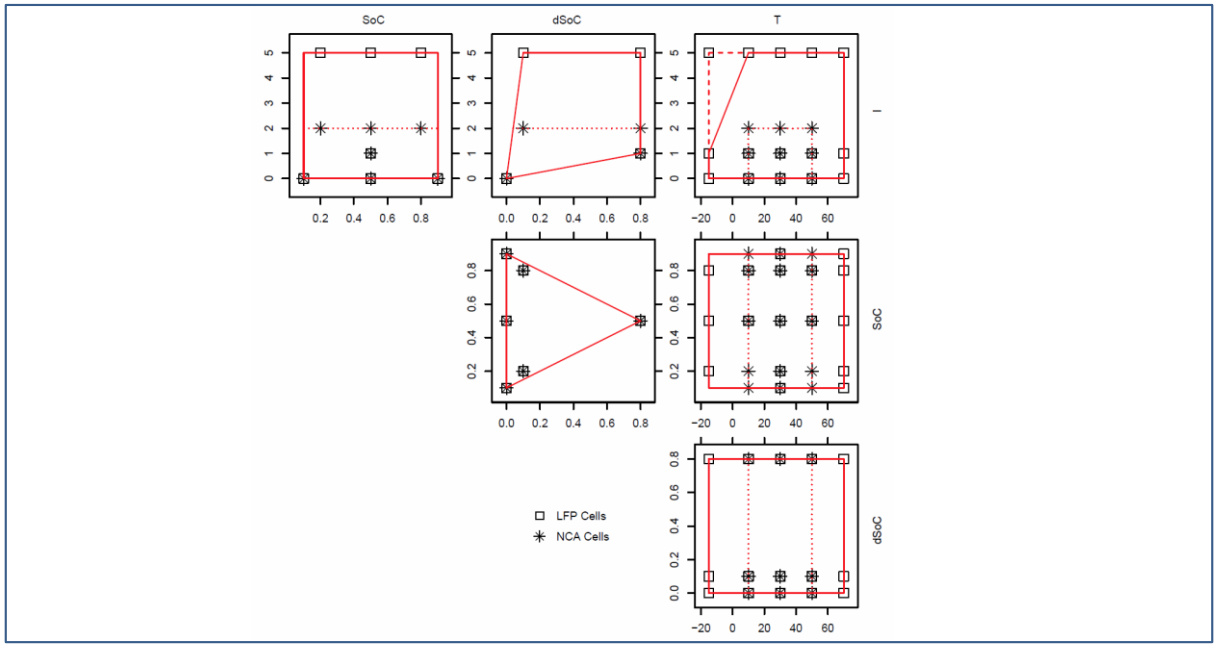

Figure 3.1.1-b – The design space of the experiment displayed in binary combinations of the influence factors, far side labels are valid for the whole column / row. Boundaries are displayed as full (LFP) and dotted (NCA) lines, test load points as squares (LFP) and stars (NCA). T in deg. C, I in h-1 (c-rate), SoC and dSoC in [0..1].

In this figure the influence factors are given in columns and rows, so each plot shows the test space spanned by the two influence factors marked on the outside of the corresponding column and row.

While considering imposable test limits, it is important to keep the test space convex [Haselgruber08], because after cutting away all the restricted spaces from the rectangular test space, a space must remain in which any two points can be connected by a straight line without crossing a limit or range border. Four such physically necessary limits were identified:

The first limit is the combination of dSoC with SoC, giving values larger than the SoC range, when added (3.1.1-1). This limit leads to the triangle shaped test space in the SoC vs. dSoC plot of Figure 3.1.1-b.

$$0.1 \leq SoC \pm \frac{1}{2} dSoC \leq 0.9 \qquad (3.1.1\text{-}1)$$

Second, the interaction of low temperatures and high currents was taken as a limit, since cell cycling in this area could not be maintained within the operating voltage window. The current is empirically limited to 1Cr at -15°C, from 10°C upwards the full 5Cr is available ((3.1.1-2) and Figure 3.1.1-b top right).

$$T \quad \geq \quad -21.25 + 6.25\, I \qquad (3.1.1\text{-}2)$$

In (3.1.1-2) the temperature (T) is given in degrees Celsius [°C] and the current (I) in c-rate [h^{-1}]. These numeric values depend strongly on cell micro and macro geometry as well as cell chemistry. Therefore this limit is not generally applicable with these values, contrary to the first limit.

The third and fourth limits concern the dSoC and current interaction (Figure 3.1.1-b top center plot). Both limits counteract the problem, that at zero current (I=0) the dSoC is also always zero (and vice versa). When approaching this point with very small currents and/or very small dSoCs, the cycling equipment's accuracy will be the limiting factor. The limits were defined as to not restrict the space more than up to the next factor level in current direction (1Cr) and in dSoC direction (0.1).

$$dSoC \leq 0.8I \qquad (3.1.1\text{-}3)$$

$$dSoC \geq 0.02\, I \qquad (3.1.1\text{-}4)$$

Since both limits are dependent of the cell chemistry and cycling equipment accuracy used, they are not applicable with exactly these values to every experiment, but the formulas are generally valid.

For the full-factorial test plan, the limits reduce the 1024 possible sample points by 230 not feasible points. So summing up for the cell count of the full-factorial experiment, a total of 2382 cells in 794 different sample points should be tested.

In the third step of the DoE process, the full factorial test plan is reduced, by using a modular algorithm for the design of large scale D-optimal experiments. The procedure and its implementation is thoroughly explained by Haselgruber in [Haselgruber08] and used unaltered. The reduction is based on a criterion describing the usefulness of a single experimental point for the parameterization of an expected model for the target parameters. The score for the usefulness is called D-optimality of a design plan in statistical terms.

The algorithm selects a set of points in the corners of the test space as well as some points randomly distributed within the space. In each following optimization step it takes another random point out of the full factorial test plan, exchanges it with one point of, or adds it to, the initially selected points and calculates the change in D-optimality [Montgomery05]. If the D-optimality increases, the changes are kept and another point is exchanged. The optimization is finished if no more increase in D-optimality can be found. Such a coded test point matrix is displayed in [Wahdame08, Table2] for a visual reference.

After the screening process, it was assumed that a second-order statistical model would be the best way to express the expectations [Janacek93], without constraining the experiment too much. This means that the target values (capacity decrease and resistance increase) are either linear or quadratic functions of a single factor or linearly dependent of the multiplication of two influence factors. The model was defined such as to incorporate offsetting the centre of a quadratic term into the experimental range, an example of this model for capacity decrease is shown in (3.1.1-5).

$$example: \quad t_{CD} = p_0 + p_1 * I + p_2 * I^2 + p_3 * \left(T^2 - 25\right) + ... \qquad (3.1.1\text{-}5)$$

This model definition accounts for all effects found in literature at the time of setting up the experiment, describing the capacity decrease and impedance increase depending on the chosen ternal influence factors [Vetter05, Kumaresaran06, Jin09]. Table 3.1.1-i gives an overview of influence factor transformations, which can be deduced from literature [Vetter05, Kumaresaran06, Jin09, Harris10, Mehrens04, Smith12] and which were used as a basis for the target parameter model of the DoE.

The exact model formulation, meaning whether every influence factor transformation has enough significance to remain in the resulting model, as well as the values for p_i are not known until the analysis of the experiment.

Using the algorithm of [Haselgruber08] the test plan was successfully reduced to 46 sample points, now fitting to the restrictions of the equipment available (channel number). These points are indicated in Figure 3.1.1-b for LFP cells (boxes) and for NCA cells (stars).

Influence Factor			
Temperature	**Current**	**State-of-Charge**	**Delta State-of-Charge**
T	I	SoC	dSoC
T^2	Sqrt(I)	SoC^2	$dSoC^2$
(T - xx)	I^2	(SoC - x)	
$(T - xx)^2$		$(SoC - x)^2$	

Table 3.1.1-i - Overview of the influence factors and their transformations, deduced from literature, as basis for the target parameter model. The variable x stands for any numeric value within the range of the influence factor and introduces an offset from zero for the change of influencing behaviour. Sqrt(I) … square root of I.

The fourth step of the design-of-experiment procedure is the conduction of the experiment itself, which is explained in the following subchapters. Step 5 is the data analysis, which is presented in the chapters following 3.2.3.

3.1.2 Measurement techniques

3.1.2.1 Experimental time schedule

The experimental planning was conducted under the premise that the measurement data acquisition is intermittent. This was necessary, because the capacity of the cell cannot be measured during 10% dSoC swings. So an experimental time schedule was drawn up, pictured in Figure 3.1.2-a.

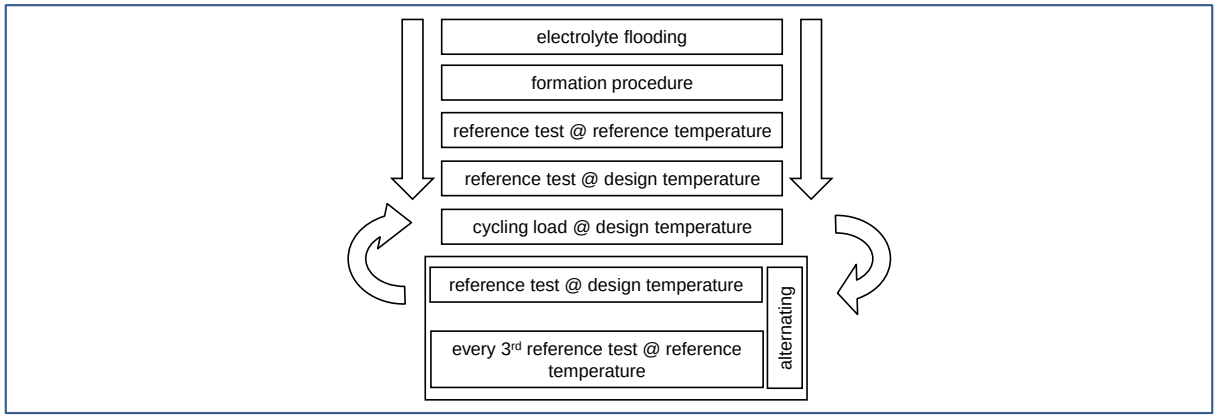

Figure 3.1.2-a – Flow chart showing the time order of the test execution. The first three blocks are performed within one week, the loop continues for the rest of the experimental time. The reference tests deliver the data points for statistical modelling.

The cells were built with the electrolyte in a squashable plastic bag, so they could be activated whenever the cell was required for the experiment. The first step after being

connected to the cycling equipment is the formation procedure. After the initial cycles a reference test follows, which is described in detail in chapter 3.1.2.2, conducted at reference temperature (30°C). Following this initial test in order to make the cells comparable at start, the reference test procedure is applied a second time at the design-point temperature of the cell. The capacity measured in this second test forms the basis for the current rate to obtain the c-rate, at which the load cycling will be conducted. It was decided not to use the nominal c-rate for ageing cycling, because otherwise the current density-dependent ageing effects would be increasingly accentuated.

The cycling load as well as calendar ageing (at a c-rate of 0 and a dSoC of 0), is periodically interrupted by reference tests, conducted at design temperature and at reference temperature. After reaching an end-of-life criterion in a reference test at reference temperature the cell is taken out of the experimental setting.

3.1.2.2 Reference Test Procedure

The reference test procedure (RTP) was designed to be a measurement sequence, which allows for a calculation of capacity decrease, impedance increase and their respective estimation errors as well as additional analysis data sets, such as differential capacity and differential voltage. It consists of an initial segment in which the cell is preconditioned to a full SoC (constant voltage charge at 3.8V (LFP) / 4.2V (NCA) until current < 0.05C). Then, a slow discharge at 0.2Cr is conducted for measuring the actual discharge capacity. This capacity is used as base for the following c-rate scan with 0.5, 1, 2, and 5 Cr (charge and discharge), each including constant voltage full charges in between (same as above). The third section is a galvanostatic intermittent pulse test, which has 5 pulse and rest periods at 0.5Cr in discharge and in charge direction (at SoC = 0.9, 0.7, 0.5, 0.3 and 0.1). This section is the base for calculation of the actual impedance [Bessler07] of the cell. In the last part of the RTP a charge step followed by a controlled 50% discharge step set the cell to be ready to start a new load cycle. The RTP initialization and the load cycling restart are done by hand, because the new capacity has to be manually decreased in the control program of the cycling equipment.

3.1.2.3 Automation of data acquisition

The cycling equipment is an Arbin BT2000 with 96 channels ± 5 A in between 0 and 5 V with a measurement accuracy of ± 0.002 V and ± 40 µA in the used current range of ± 100 mA. Under the assumption that the measurement error follows a Gaussian distribution, the error for the capacity measurement is < 0.25% and the error for the impedance calculation is < 15%, for worst case settings with the given cells.

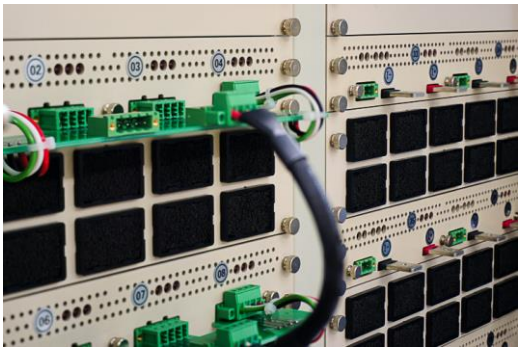

Figure 3.1.2-b – Detail of the 5A / 5V channels of the Arbin cycling equipment. In foreground an auto calibration cabling is visible on the 5A channels.

The status of ageing is always calculated from a single RTP step, including the cell capacity, the cell impedance, the differential voltage and differential capacity:

- The cell capacity is calculated as being the value of the Coulomb counter after the 0.2Cr discharge, which has been reset in end of the preconditioning charge preceding the discharge.

- The cell impedance is calculated from the pulse test of the RTP. For each current pulse of 0.5Cr a pulse impedance is calculated while switching on and switching off [28]. The current rise time of the cycling equipment is <30ms, so a time delta of 500ms was chosen for the highest measurement frequency of voltage and current. Since the pulse test was done in charge and discharge direction, this equals to four calculated values per SoC level. A mean value for the impedance is calculated from all values at the same SoC level, since the expected difference between charge and discharge impedance is smaller than the measurement error. A linear regression is then applied to the mean values for the SoC levels to receive the median impedance for the cell.

- The differential voltage and differential capacity data is calculated from the same 0.2Cr discharge as the capacity. A constant current discharge is not the optimal base for this transformation but is a viable one [Thompson79], where the peaks for the two-phase regions are not in the correct numerical order to calculate kinetic data.

The MITSpro® Software by Arbin stores the measurement data in a database format. One file per cell and per step, according to Figure 3.1.2-a, is generated. Resulting in an amount of data captured during the experiment in excess of 20 GB. These databases are then transferred directly into MATLAB structures per cell using self-written routines. This makes the treatment of data and the calculation of the target values less time consuming.

3.2 Data

3.2.1 Cell data overview

3.2.1.1 Data received from cell measurements

The data received from experiment will be presented in this chapter using an exemplary cell. Namely this cell is an LFP cell with the number 10110314. The cell had its formation runs on the 3rd of November 2010 and was in test a little short of 120 days. This makes the cell a rather short-lived cell, as the longest runs were close to 2 years.

But it also renders it perfect for presentation, since only around 1.72 million data points were recorded and so the graph with its full lifetime voltage response just fits on the following page (Figure 3.2.1-a) on the left. The x-axis is graduated in days since cell activation. The full cycle sequences are RTPs, while the massive blue areas represent the time of cycling at the intended load point for this cell (60°C, 5C, 10% dSoC around 80% SoC). In the right column the topmost graph is a zoom onto the first 3.5 days of test. One can see the cell voltage rise from zero as the anode is being lithiated the first time and the cell capacity stabilizes within the first 5 cycles. Then the initial characterisation is started with the RTP at reference temperature to receive the cell data for SoH = 1. Every further, RTP during the cell life delivers the data used for monitoring the cell degradation and is represented by a dot in the graphs of the chapter on ageing data 3.2.3. The lower two plots compare a detail on the load cycling of day 8 and day 87. The cell shows slightly more overpotential in the aged plot than in the new one. Also it seems the cell has more trouble keeping the load point in the aged cell situation, this is partly due to the fact that the cell has aged since the last capacity adjustment and because the resetting is based on a voltage boundary, which is hit more often due to increased overpotential.

At the RTP around day 100 the cell was marked for removal, having reached SoH = 0. All cycling after that RTP are schedules for the characterization of aged cells needed for the fitting of an aged short-term model.

3.2.1.2 Data for short-term model

The load schedules used to characterize a cell for the purpose of fitting are called “characterisation tests A, B, C, D and Z”. Additionally, a 100h OCV was recorded for every cell type. The data for the new cells was recorded of three cells per cell type and per DoE data point. The tests were repeated at four temperatures (-10°C, 10°C, 30°C, 50°C). The data for the aged cell status was recorded at the end of life of each cell. If the cell had a different load cycling temperature than 30°C, the tests were run at load temperature and at reference temperature. However, the temperature exponents were not fitted for aged points, so this was only additional data.

The characterisation tests for the end of life characterization of the exemplary cell 10110314 are displayed in Figure 3.2.1-b (test A top and B bottom), Figure 3.2.1-c (test C top and D bottom) and Figure 3.2.1-d (test Z top and the final discharge bottom). All tests start with setting the cell to 100% SoC – from there on the voltages are used for fitting.

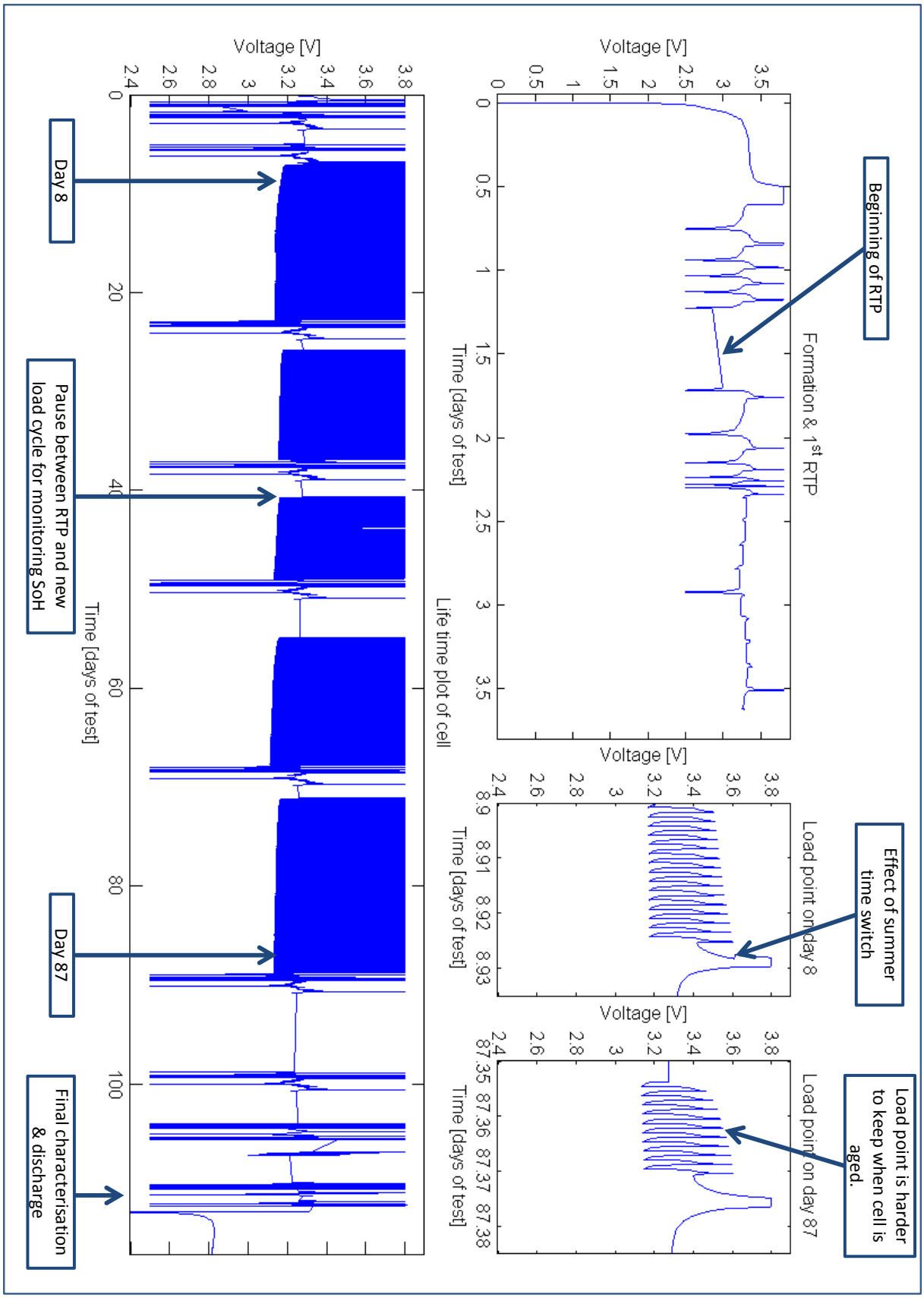

Figure 3.2.1-a – Plot of the complete cell life until SoH=0 of LFP cell 10110314 in the left hand plot. The three right hand plots are top down: the formation and RTP of the cell, load-point cycling on the first day of load and on the bottom load point cycling on day 87 out of 90. The load point is 60°C, 5C, 10% dSoC around 80% SoC. Visible in the load points is also the automated SoC resetting.

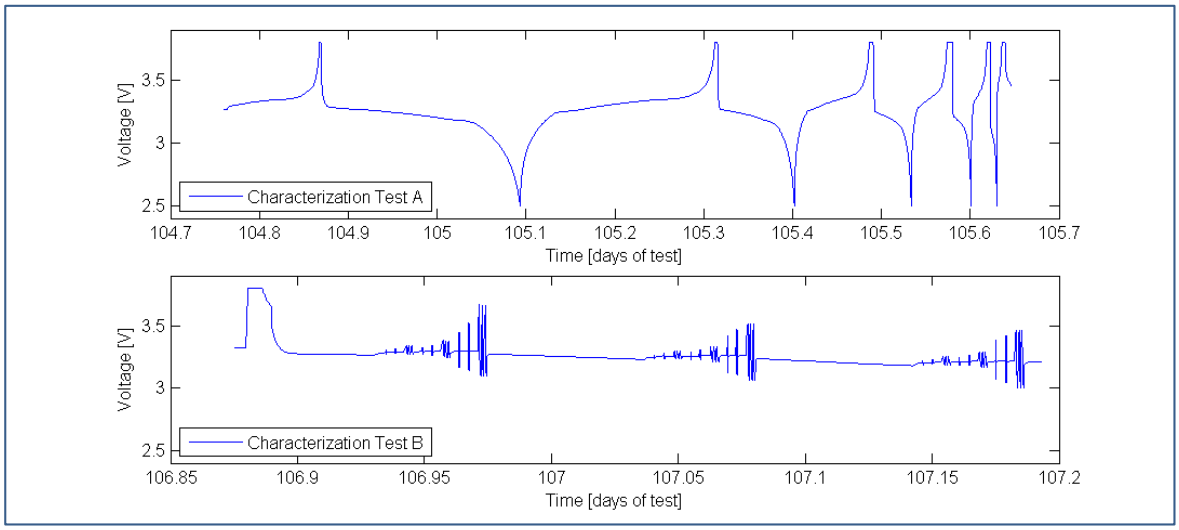

Figure 3.2.1-b – Voltage response plots of the characterization tests A (c-rate scan form 0.2C to 5Cr) and B (alternating pulses @ 80/50/30% SoC from 0.5Cr to 5Cr and from 1sec to 49sec)

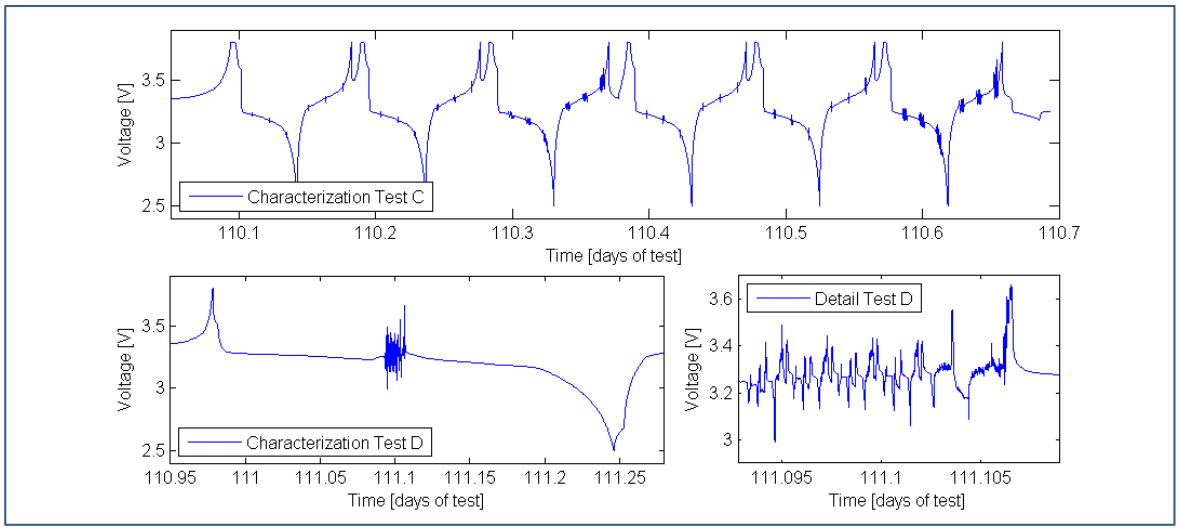

Figure 3.2.1-c – Voltage response plots of the characterization tests C (full cycles 0.5Cr with overlayed pulses as in B) and D (real world hybrid electrical current cycle of NEDC supplied by AVL List GmbH)

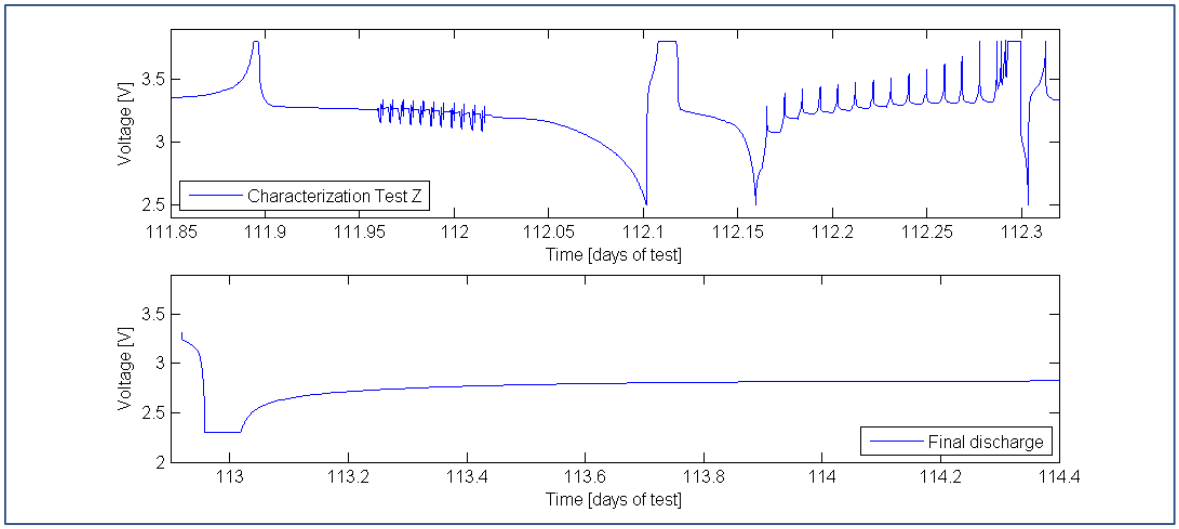

Figure 3.2.1-d – Voltage response plots of the characterization tests Z (cycles at different rates with high dynamics pulse sequences and step pulses) and final discharge

The cells initially placed at 70°C lost capacity too fast to complete the tests. Most of the cells tested at -15 °C were having such strong lithium plating that not all test were successfully finished. Some of the others were lost for various reasons during testing, trying to cope with more than 90 cells concurrently in test. Data sets of cells where all three cells of one data point were available were reduced to a maximum of two. And finally, some cells, which were finished but had anomalies in the tests (measurement disturbances, slight internal short circuit signs,…), were not included for the fitting. For a total of 60 cells in the experiment the full set of characterisation tests was completed and the data was chosen for fitting. Since the computational resources were limited to one workstation, this was a sufficiently large data base, but still reduces the confidentiality of the experimental design significantly.

The characterisation tests cover a very wide field of load excitation. From basic full cycles at different c-rate (A, Z) to highly dynamic sub second pulses (D). The analytical pulse tests (B,C) help the fitting process in the middle of this spectrum.

The lower plot in the last graph (Figure 3.2.1-d) is not part of the fitting data, but rather shows that this cell is still fully functional after the characterisation tests, since its voltage re-stabilizes above 2.5 Volt after a deep discharge. This discharge is made to provide a little measure of safety when taking the cells apart for post-mortem analysis.

3.2.1.3 Data for the ageing model

The ageing model connects the parameter change of the short-term model with the cycling the cell has seen during its life. Therefore the complete dataset is used as basis for the rainflow counting. Contrary to the short-term model, which only uses voltage response for a given current and temperature, the ageing model uses the current, the temperature and the SoC as basis for the calculation.

Not only the testing periods are taken into account, but also the rest periods in between when no measurement equipment was connected to the cell. The MATLAB data acquisition algorithm interpolates between the last point of a run and the first point of the next run to supply average values for temperature and voltage, as well as self discharge rates derived from SoC calculation.

3.2.2 Rainflow data analysis

The rainflow counting algorithm was implemented together with the MALAB data acquisition and delivers the two described (2.1.4.3) matrices for each cell at every run covering formation to that run. The rainflow matrices (RFM) are 2-dimensional histogram matrices. In Figure 3.2.2-a the RFMs for the exemplary LFP cell 10110314 and a NCA cell 10110910, a calendar-aged cell, are shown. The matrices are displayed in a view along the z-axis, giving the amount of cycling / calendar ageing done in one point by colour. Refer to the colourbar on the right of each graph to see how many cycles / hours were spent in a point defined by the x- and y-axis.

Both cells held their load points well, even though a high self discharge rate has to be attributed to the NCA cell. The load point of 10110910 was designed to be 30°C, 0C, 0% dSoC around 50% SoC. In the flow matrix for this cell only the RTPs are inscribed. The 100% cycles are the full cycles and the cycles with close to 0% dSoC are the constant voltage charges within the RTP.

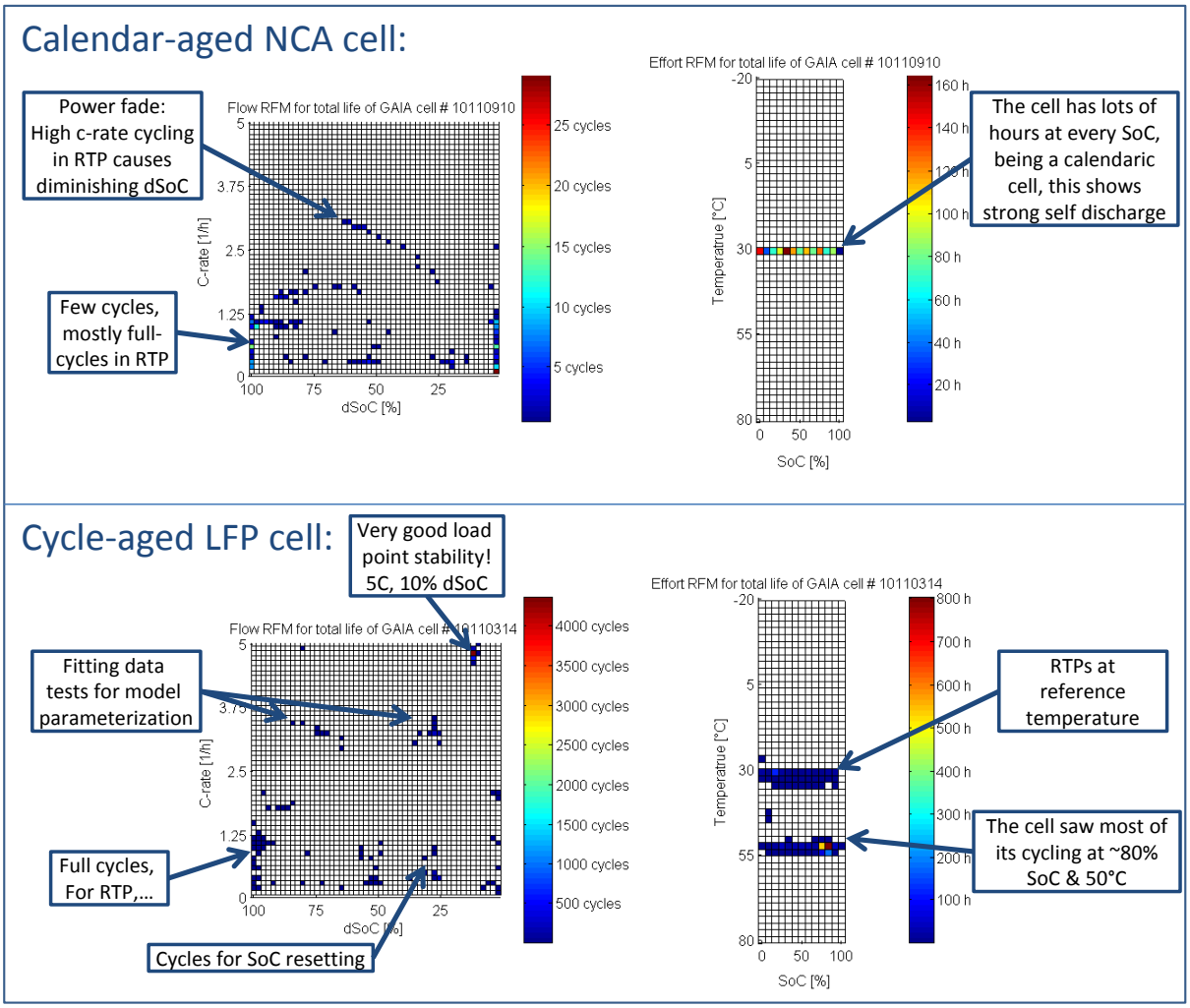

Figure 3.2.2-a – Rainflow load matrices for cells 10110910 & 10110314 covering the whole lifespan. The matrix on the left shows the cycle count over dSoC and c-rate (xCyc), the one on the right shows the hours over temperature and SoC (tCal)

To demonstrate the coverage of the test space achieved by the experiment, the RFMs of all the cells accumulated are displayed in Figure 3.2.2-b. The dark blue space is a little irritating, as this is not the reason for telling this plot shows good results. Rather, one has to compare the coloured points of higher cycle count to the design matrix given in Figure 3.1.1-b to find, that exactly at the locations, where tests should have been conducted, the cycle counts are very high, except for one point the 5 Cr, 80 dSoC. The current load at this point was too strong to actually reach 80% dSoC on most cells, so those cycles create the spread out points along the top edge.

In the effort matrix it is notable, that most cells kept their assigned SoC well, but some showed strong discharge (more NCA cells than LFP). Temperatures were generally within 3°C around their design value. The smearing between 10°C and 30°C comes from tests at “room temperature” being conducted with open door of the thermal chambers.

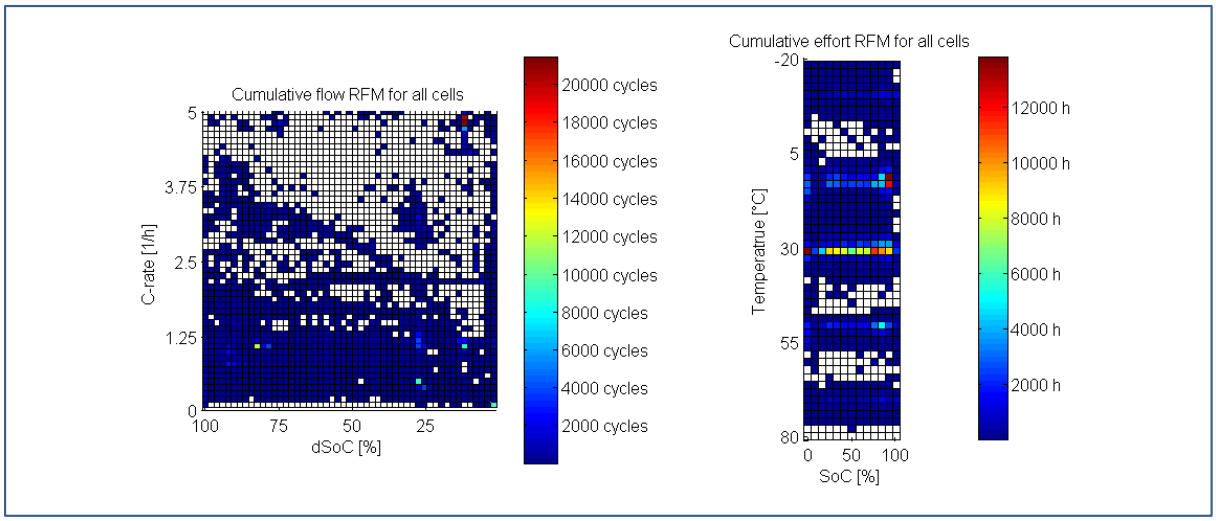

Figure 3.2.2-b – Rainflow load matrix for all cells in the experiment shows the good test space coverage, which was achieved with the experiment. The ageing points can be seen by the brighter colours.

3.2.3 Ageing data [Prochazka13]

This chapter presents the high-level cell-ageing data, capacity and impedance, as measurement results in dependence of averaged influence factors.

In the following figures the experimental results for capacity decrease and resistance increase, the target values of the DoE, are displayed.

The plots are created with the lattice toolbox of R, an open-source statistics program [RHelp]. The lattice-subplots all share their axes with the adjacent plots and throughout one figure. All axes have the same ranges within one figure. The x-axes are assigned the experimental time. The experimental time has been standardized to the longest lasting cell of each chemistry, because of the differences in endurance and the space available for tick marks. For LFP the normalized time range [0...1] is equal to 26 months, for NCA the normalized time range covers 18 months. Each subplot features a head panel showing the code for the displayed sample point. It consists of the four chosen influence values in the order temperature, c-rate, state-of-charge (SoC) and delta SoC (dSoC).

All cells which were run at one sample point are marked by dashed grey lines and the median value per time interval is shown in black. The red line is the cell in this sample point which is closest to the calculated median in most of the time-steps. For further analysis and calculations all measurements of this cell are considered the realizations of the displayed target value per time interval, the other cells are considered repetitions and supply the variance values per time interval. For simplified comparison of the cells all measurements have been standardized to the first measurement after formation.

3.2.3.1 Capacity decrease

The experimental results for the capacity decrease are shown in Figure 3.2.3-a (LFP cells) and in Figure 3.2.3-b (NCA cells). There is a strong dependency of the capacity decrease on the test temperature for both chemistries. Although the test space for the two chemistries was slightly different (range limits for LFP cells: -15°C to 70°C, for NCA: 10°C to 50°C), the tests at 10 °C were the ones resulting in the longest cell life time for both chemistries. For the LFP cells it is remarkable that cells being cycled at 1Cr do not age very much faster than calendar aged cells, whereas cells cycled at 5Cr do age significantly faster. For the NCA cells any cycling load ages the cells faster than calendar ageing samples. For these cells the influence of the dSoC is stronger than the c-rate influence. These effects and additional, not directly visible effects of the other influence factors on the two cell chemistries will be highlighted during model built.

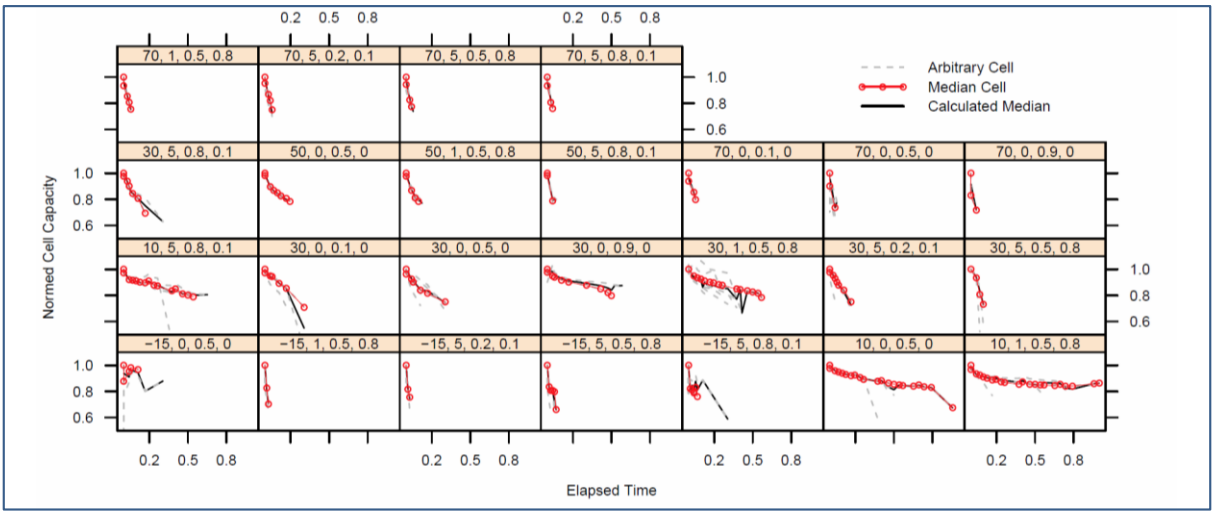

Figure 3.2.3-a – Each lattice box shows the normed cell capacity of all repeats of LFP cells running in a single test point on the y-axis over normalized experimental time on the x-axis. The test point is indicated by the number sequence in the bar above each chart in the following order: temperature, c-rate, SoC, dSoC

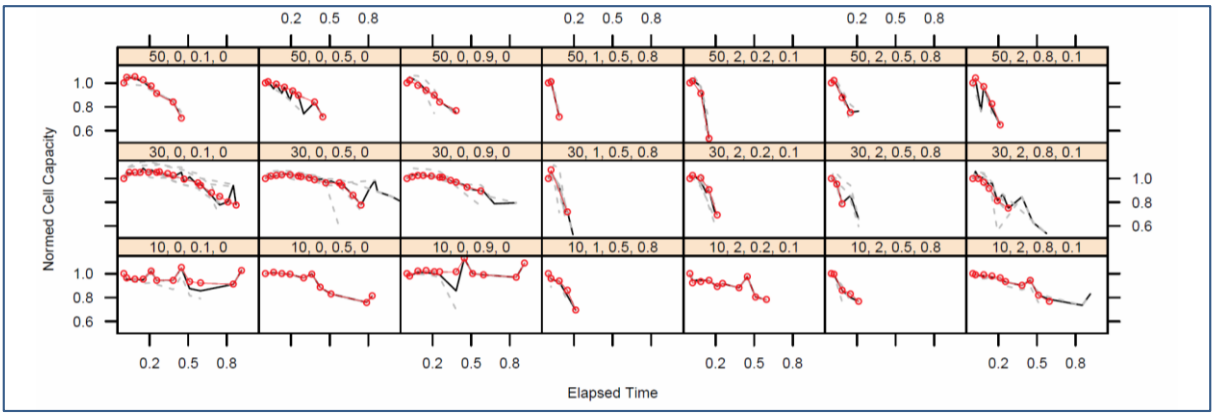

Figure 3.2.3-b – Each lattice box shows the normed cell capacity of all repeats of NCA cells running in a single test point on the y-axis over normalized experimental time on the x-axis. The test point is indicated by the number sequence in the bar above each chart in the following order: temperature, c-rate, SoC, dSoC

3.2.3.2 Impedance increase

The experimental results for the impedance increase are shown in Figure 3.2.3-c (LFP cells) and in Figure 3.2.3-d (NCA cells). The plots are structured the same way and show the data the same way the capacity decay plots do. The impdeance and the time are again standardized to the initial measurement respectively the longest cell endurance.

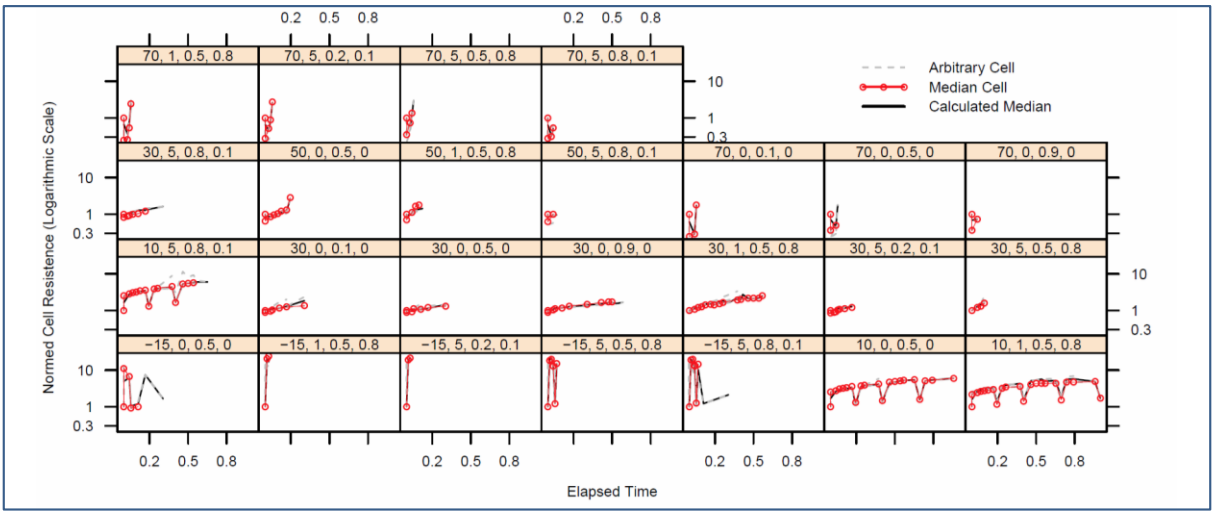

Figure 3.2.3-c – Each lattice box shows the normed cell resistance of all repeats of LFP cells running in a single test point on the y-axis over normalized experimental time on the x-axis. The test point is indicated by the number sequence in the bar above each chart in the following order: temperature, c-rate, SoC, dSoC

The impedance ticks on the y-axes are in logarithmic scales, due to the fact that the impedance is depending rather strongly on temperature. When temperatures below 10°C are applied to new cells, the impedance rises approximately 2.5 times per decade Celsius. Rising temperatures above 30°C do not affect the new cells as strongly, an impedance decrease of a factor of about 1.5 times per decade Celsius is observed. For aged LFP and NCA cells alike, these dependencies become less significant. Influences of factors other than temperature are not directly visible within the impedance data.

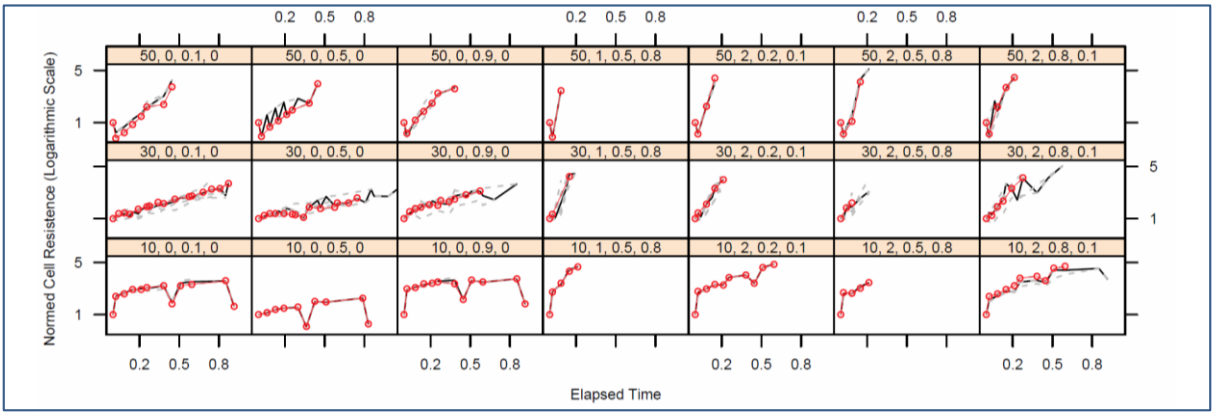

Figure 3.2.3-d – Each lattice box shows the normed cell resistance of all repeats of NCA cells running in a single test point on the y-axis over normalized experimental time on the x-axis. The test point is indicated by the number sequence in the bar above each chart in the following order: temperature, c-rate, SoC, dSoC

3.2.3.3 Differential capacity

Thompson [Thompson79] and more recently Dubarry [Dubarry11] described how to read the changes of differential capacity over ageing. Therefore, differential capacity plots were

generated for the cells, as can be seen in Figure 3.2.3-e for a LFP cell (a and b) and a NCA cell (c and d). However, no other changes than a vanishing peak (upmost plot of b) to the right) for LFP and a shift to lower potentials for NCA could be observed. As both of these features are well visible in the discharge curves already, the peak shift data from differential capacity is not included in statistical analysis.

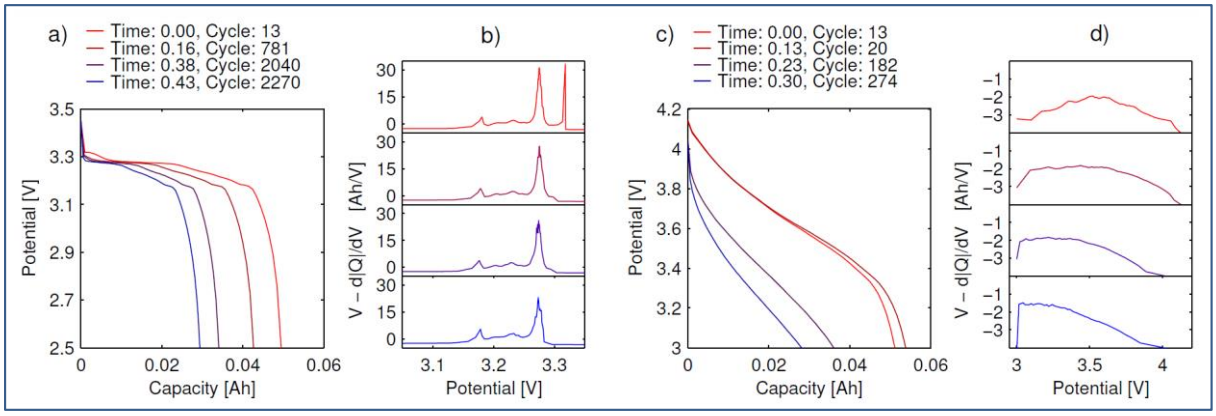

Figure 3.2.3-e – Comparison of the ageing behaviour of slow discharge voltage profiles and their respective differential capacity plots for LFP and NCA cells. a) LFP 0.2Cr discharge voltage versus capacity showing a rather constant behaviour; b) LFP differential capacity, showing no shift of peaks; c) NCA 0.2Cr discharge voltage versus capacity showing a rather strong flattening; d) NCA differential capacity showing a shift of the capacity to lower voltages.

3.2.3.4 Statistical Modelling

The fifth and last step in the DoE process is modelling and analysis. There is a wide selection of statistical model methods available, which can be applied to the generated experimental data. Yet for the analysis of the DoE, the model which has been used for calculating the optimized design plan will be used for modelling. The basic model type is already shown in (3.1.1-5) and is a linear statistical model.

A linear model is not a time-dependent modelling method reproducing the data as seen in Figure 3.2.3-a to Figure 3.2.3-d. The actually modelled data is represented by a single point in time per cell measurement. For the presented models this time is defined as the time needed for the cell to reach the end-of-life criterion for the modelled target value (see also Figure 3.2.3-f).

$$t_{CD}\left(CD = EoLc\left(CD\right)\right) = p_0 + p_1 * I + \ldots \qquad (3.2.3\text{-}1)$$

Each of the two target values, capacity decrease and impedance increase, will be treated in a separate model. Additionally separate models per chemistry were fitted. So a total of four parameter sets are presented in Table 3.2.3-i (capacity decrease) and Table 3.2.3-ii (impedance increase).

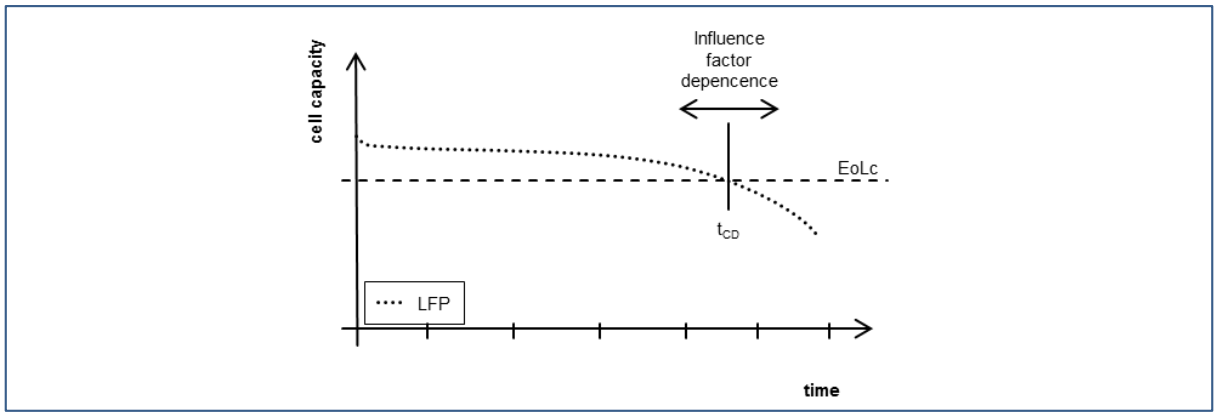

Figure 3.2.3-f – The presented linear statistical models of the cell ageing only model the influence of the factors on the time until the intersection of the ageing curve (ex. capacity decrease) with the end of life criterion and not the exact path behaviour.

The tables show three columns of values for each of the parameter sets. The values in the first columns are the estimates for the parameters of the model, received by least-square fitting. These estimates and the influence factor combinations for each term (found in the leftmost index column) form the model formula. For an increased accordance of the capacity decrease to a linear model (Figure 3.2.3-f), the target variable t_{CD} was transformed to a logarithmic scale. This step was not necessary for the target variable of the impedance increase t_{II}. As examples, the final model formulations of the capacity decrease and impedance increase models for LFP from Table 3.2.3-i & Table 3.2.3-ii are presented in (3.2.3-2) and (3.2.3-3).

	LFP			**NCA**		
Term Name	Parameter Estimate	Standard Deviation	Significance	Parameter Estimate	Standard Deviation	Significance
Intercept	$6.391 \cdot 10^{0}$	$3.350 \cdot 10^{-1}$	***	$8.9 \cdot 10^{0}$	$1.127 \cdot 10^{-1}$	***
T	$4.042 \cdot 10^{-2}$	$4.438 \cdot 10^{-3}$	***	-	-	-
T^2	-	-	-	$-4.488 \cdot 10^{-4}$	$6.854 \cdot 10^{-5}$	***
$(T-15)^2$	$-1.326 \cdot 10^{-3}$	$1.04 \cdot 10^{-4}$	***	-	-	-
T * I	-	-	-	$1.994 \cdot 10^{-2}$	$5.119 \cdot 10^{-3}$	***
I	-	-	-	$-1.29 \cdot 10^{0}$	$1.979 \cdot 10^{-1}$	***
I * SoC	$-7.513 \cdot 10^{-1}$	$2.131 \cdot 10^{-1}$	***	-	-	-
SoC	$1.689 \cdot 10^{0}$	$5.384 \cdot 10^{-1}$	**	-	-	-
$dSoC^2$	$-9.737 \cdot 10^{-2}$	$2.697 \cdot 10^{-1}$		-	-	-
SoC * dSoC	-	-	-	$-2.305 \cdot 10^{0}$	$3.044 \cdot 10^{-1}$	***

Table 3.2.3-i – Model parameters p_i, their standard deviations and the resulting significance of the term for the LFP and NCA capacity decrease model. Empty rows indicate that this factor was insignificant for the respective model. An example for the construction of the model is given in (3.2.3-2).

Term Name	LFP			NCA		
	Parameter Estimate	Standard Deviation	Significance	Parameter Estimate	Standard Deviation	Significance
Intercept	$7.084 \cdot 10^{3}$	$3.295 \cdot 10^{2}$	***	$3.799 \cdot 10^{3}$	$9.812 \cdot 10^{2}$	***
$(T-15)^2$	$-5.193 \cdot 10^{0}$	$5.826 \cdot 10^{-1}$	***	-	-	-
$(T-15)^4$	$1.361 \cdot 10^{-3}$	$2.091 \cdot 10^{-4}$	***	-	-	-
T	-	-	-	$2.076 \cdot 10^{2}$	$6.819 \cdot 10^{1}$	**
T^2	-	-	-	$-3.857 \cdot 10^{0}$	$1.034 \cdot 10^{0}$	***
dSoC	$-4{,}325 \cdot 10^{3}$	$2.556 \cdot 10^{3}$	.	$-1.402 \cdot 10^{3}$	$8.015 \cdot 10^{2}$	.
$dSoC^2$	$5.546 \cdot 10^{3}$	$2.842 \cdot 10^{3}$	.	-	-	-
dSoC * I	$-1.627 \cdot 10^{3}$	$5.701 \cdot 10^{2}$	**	-	-	-
I	-	-	-	$-6.206 \cdot 10^{3}$	$1.273 \cdot 10^{3}$	***
I^2	-	-	-	$2.816 \cdot 10^{3}$	$5.877 \cdot 10^{2}$	***
SoC * I	-	-	-	$-2.184 \cdot 10^{3}$	$7.616 \cdot 10^{2}$	**

Table 3.2.3-ii – Model parameters p_i, their standard deviations and the resulting significance of the term for the LFP and NCA impedance increase model. Empty rows indicate that this factor was insignificant for the respective model. An example for the construction of the model is given in (3.2.3-3).

$$\log(t_{CD}\,(\text{LFP})) = 6.39 + 4.04\text{e-}2 * T - 1.32\text{e-}03 * (T-15)^2 - 7.51\text{e-}01 * I * SoC + 1.68 * SoC - 9.73\text{e-}02 * dSoC^2 \quad (3.2.3\text{-}2)$$

$$t_{II}\,(\text{LFP}) = 7.08\text{e}03 - 5.19 * (T-15)^2 - 1.36\text{e-}03 * (T-15)4 - 4.32\text{e}03 * dSoC + 5.54\text{e}03 * dSoC^2 - 1.62\text{e}03 * dSoC * I \quad (3.2.3\text{-}3)$$

The centre column displays the quadratic standard error for each estimated value coming from the least squares estimation. This value helps in deciding if a model term and the estimate are reliable and useful parameters or not, which is then displayed in the third column. Significance is given by a star rating, as common in many statistics tools such as R, more stars mean better reliability of the estimation (for more information see the R online help manual [RHelp]), the formula for calculating significance is displayed in (3.2.3-4). The hypothesis, which the p-test is testing against, is that the estimate is actually zero. If true, the term is insignificant for the data description model.

$$p - test_{Estimate=0}\left(\frac{\text{Estimate}}{\text{Standard Error}}\right) = 0 \quad (3.2.3\text{-}4)$$

A rating of three stars means that the term is highly significant and should not be left unconsidered. Two and one star are a little less significant. A point means the user should decide based on his knowledge of the subject, if the term should be considered.

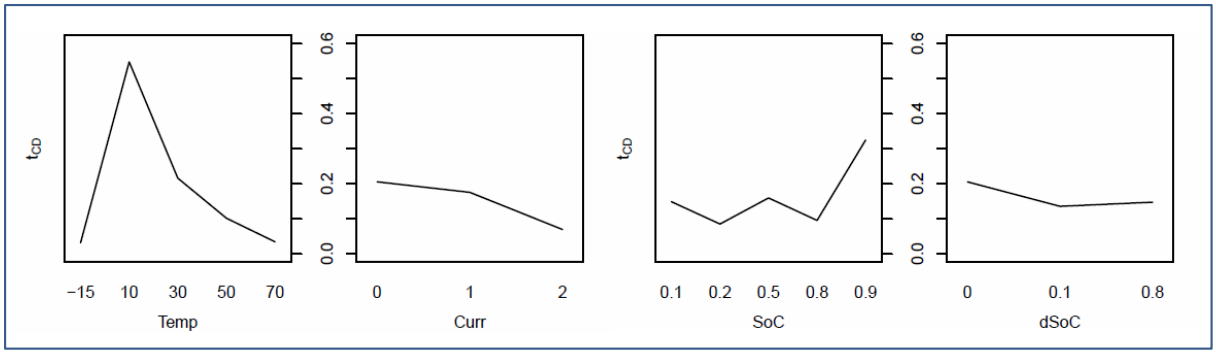

Figure 3.2.3-g – Exemplary influence factor plot for the model deduction (LFP cells). An average of the target variable (y-axis of each plot) over all cell data containing a single setting level of an influence factor (x-axis) is shown per factor. This plot identifies centre offsets, as can be seen in the left most plot for the temperature. The according offset was set to a centre of 15°C. Temperature (Temp) [°C], current (Curr, as c-rate [h-1]), SoC, dSoC (both in [0..1]).

Not all the influence factor combinations mentioned possible in Table 3.1.1-i can actually be found in Table 3.2.3-i and Table 3.2.3-ii, because the models have already been reduced by all insignificant combinations. This process starts with the graphical interpretation of a factor plot as seen in Figure 3.2.3-g. It exemplarily displays one model target parameter (t_{CD}) for the LFP cells in dependence of a single influence factor (x-axis) averaged over all combinations with the remaining three factors. This plot tells which of the influence factor terms will very likely be significant and need to be taken into account for the model. In the upper right hand plot of Figure 3.2.3-g the maximum at 10°C visualizes the need for a centre value different from zero for the quadratic temperature influence term for LFP, since this term would otherwise always be centred at zero. Alike, plots exist for the first order interactions, as shown in Figure 3.2.3-hfor the data of the LFP cells. It tells which interactions are to be retained in the model for t_{CD} of LFP. In the rightmost graph a weak interaction of SoC and dSoC is indicated, which showed to be insignificant during model reduction. It is a repeated process of taking a model, starting out with all possibilities of Table 3.1.1-i, and reducing the insignificant ones, then refitting the model. This process is repeated three times per target value and chemistry, always reducing the model by all parameters which had no or very low significance (< 10% in the p-test). The improvement in model quality during the process is monitored in the four model graphs (Residual vs. Scaled, QQ-Normal, Scale Location and Leverage, see [Montgomery05]) given by the plot model command in R and the decreasing AIC value (Akaike Information Criterion) [Akaike74, Janacek93]. These steps are not explained in detail here, but can be found in the R help files [RHelp]. The models stayed very much the same across the chemistries during the first repetition, but differences arose in the following iterations. All models acquired good model quality during the fitting process.

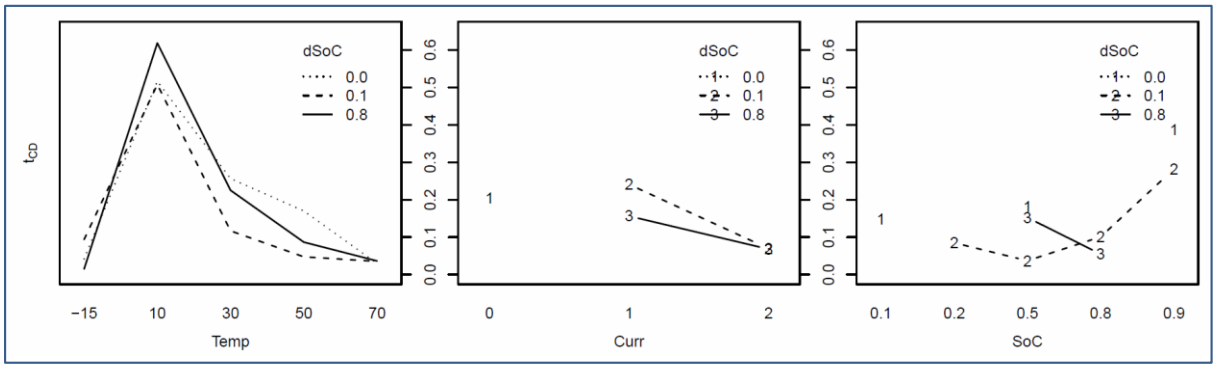

Figure 3.2.3-h – Exemplary factor interaction plot for the model deduction (LFP cells). An average of the target variable (y-axis) is displayed per factor setting, as indicated in the legend, over the factor settings of the y-axis factor. A weak interaction of SoC and dSoC can be seen in the rightmost subplot. Temperature (Temp) [°C], current (Curr, as c-rate [h-1]), SoC, dSoC (both in [0..1]).

3.2.3.5 Measurement results

When reviewing the ageing measurements of the capacity measurements it is notable that the cells do have some variance in their response to the influence factor combinations in a lot of the sample points. Since all cells were hand-made and the cells are only covered by a single layer of pouch bag foil, this was expectable to happen (Figure 3.1.1-a). A countermeasure taken was to steady the active material parts by plastic clamps before the start of the experiment. As a second measure, a larger number of cells than required by the DoE plan was tested in some sample points to characterize the real-cell variance well. These sample points are enlarged in Figure 3.2.3-i for LFP (left) and NCA (right).

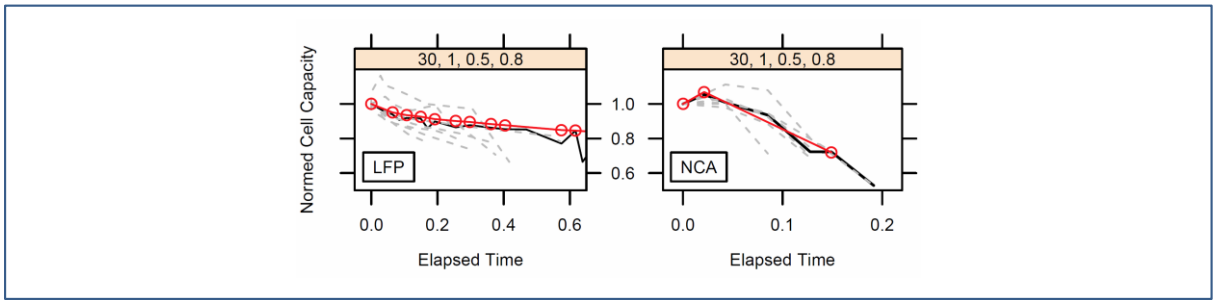

Figure 3.2.3-i – Zoom into two of the plot lattices of Figure 3.2.3-a (left) and Figure 3.2.3-b (right). It shows the normed cell capacity of all repeats (dashed light) of the test point with the most cell repeats per chemistry over the normed testing time. The variance in numeric value is rather large, but the path behaviour is similar per chemistry. The mean value is indicated by a red line with circles, the median cell (the most representative cell) is indicated by a dark line.

The sample point selected was 30°C, 1Cr, 50% SoC and 80% dSoC for reasons of space for additional cells and channels being available in the 30°C test chamber and the electrical load being a medium test point except for dSoC. The resulting variance in this test point is rather large, but it is also visible that most of the cells had the same characteristic path in their capacity decay. Among cells of the same chemistry the path is very common, but not shared by the other chemistry. LFP containing cells seem to age in a double dip behaviour with an elongated plateau in between, while NCA cells experience a capacity rise in the first stage of

their life and decrease their capacity continually down without plateaus later on. For both chemistries the different stages of ageing (Figure 3.2.3-j) are characteristic. Both cell types use the same anode, which indicates that at least the difference in ageing behaviour within LFP stage I & II versus NCA stage I can be attributed to cathode causes. The length in time of single stages is dependent on the influence factors, but the strength of influence factors is different between the stages in each sample point.

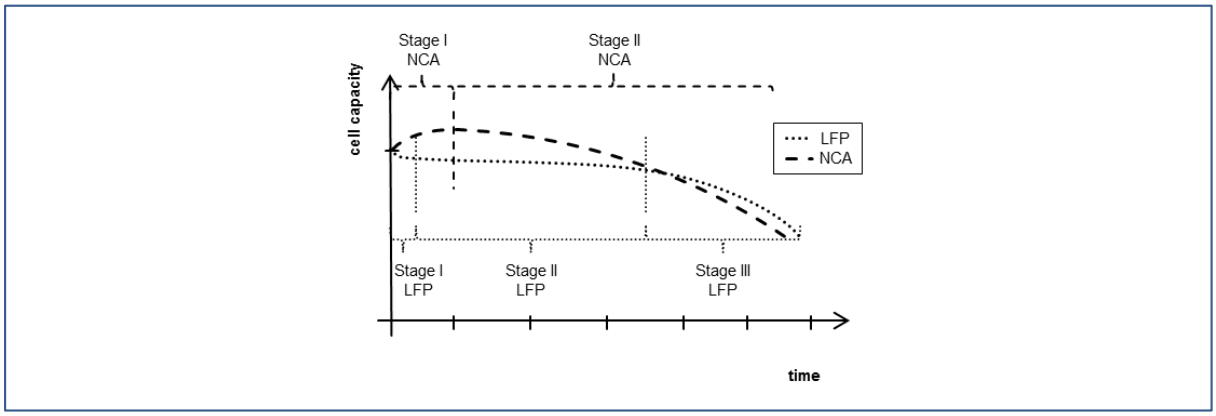

Figure 3.2.3-j – The deduced characteristic ageing paths of the target parameter normed capacity for the two different lithium ion cell chemistries. Indicated are the stages in which the behaviour can be split. For LFP three stages were found: initial losses, stable plateau and fall off. For NCA only two stages were found: run-in and accelerating loss phase.

Additionally having a build variance, some of the cells showed electrolyte leaks at the electrode bushings. This was an effect which was not initially expected and no specific countermeasures were taken. During model fitting it showed that there was no significant alteration of the ageing path for both chemistries due to these leaks presumably due to an electrolyte excess, though it did accelerate the capacity decrease of heavily affected cells. The data of those cells was taken out of the data base before the statistical analysis.

The ageing measurements of the impedance were expected to show visibly more variance than capacity measurements due to the measurement accuracy of just less than 15%. This expectation cannot be directly supported by the data presented in Figure 3.2.3-c and Figure 3.2.3-d, because the measurements show a more articulate dependence on the actual temperature than on the ageing influence factors or the measurement accuracy. The expectation of a characteristic shape of impedance increase has therefore to be reduced to a linear increase, fitting very well to the linear modelling. Still this linear increase has a slope depending significantly on all influence factors, not only temperature. For future experiments all reference tests should be at reference temperature to get less disturbed results. The found impedance increase ranges between factor 2 and 4.5 during the lifetime of the cell. At low temperatures there exist values exceeding the EoLc (factor 3) which was set for the impedance, but only measurements at reference temperature (30°C) were taken for the activation of EoLc.

The results from the impedance increase measurements are especially interesting for the design and sizing of cooling systems and power inverters. It implies that a system able to

cope with all temperature levels of a new cell, can handle an aged cell with very little additional capacities needed.

3.2.3.6 Statistical modelling results

Single factor variation experiments are rather easy to analyse, since one can tell the difference in cell ageing by looking at the graphs of the different sample points. In this study a total of 46 sample points are tested and the factor level combinations are not linearly varied, so one has a hard time to see differences in sample points intuitively. Hence, a discussion of the model parameters of the presented statistical models is needed. In these parameter sets one can see the influence strength, the differences between sample points and chemistries in a more compact way. Figure 3.2.3-k and Figure 3.2.3-l show the capacity decrease model and the impedance increase model respectively in a telling way.

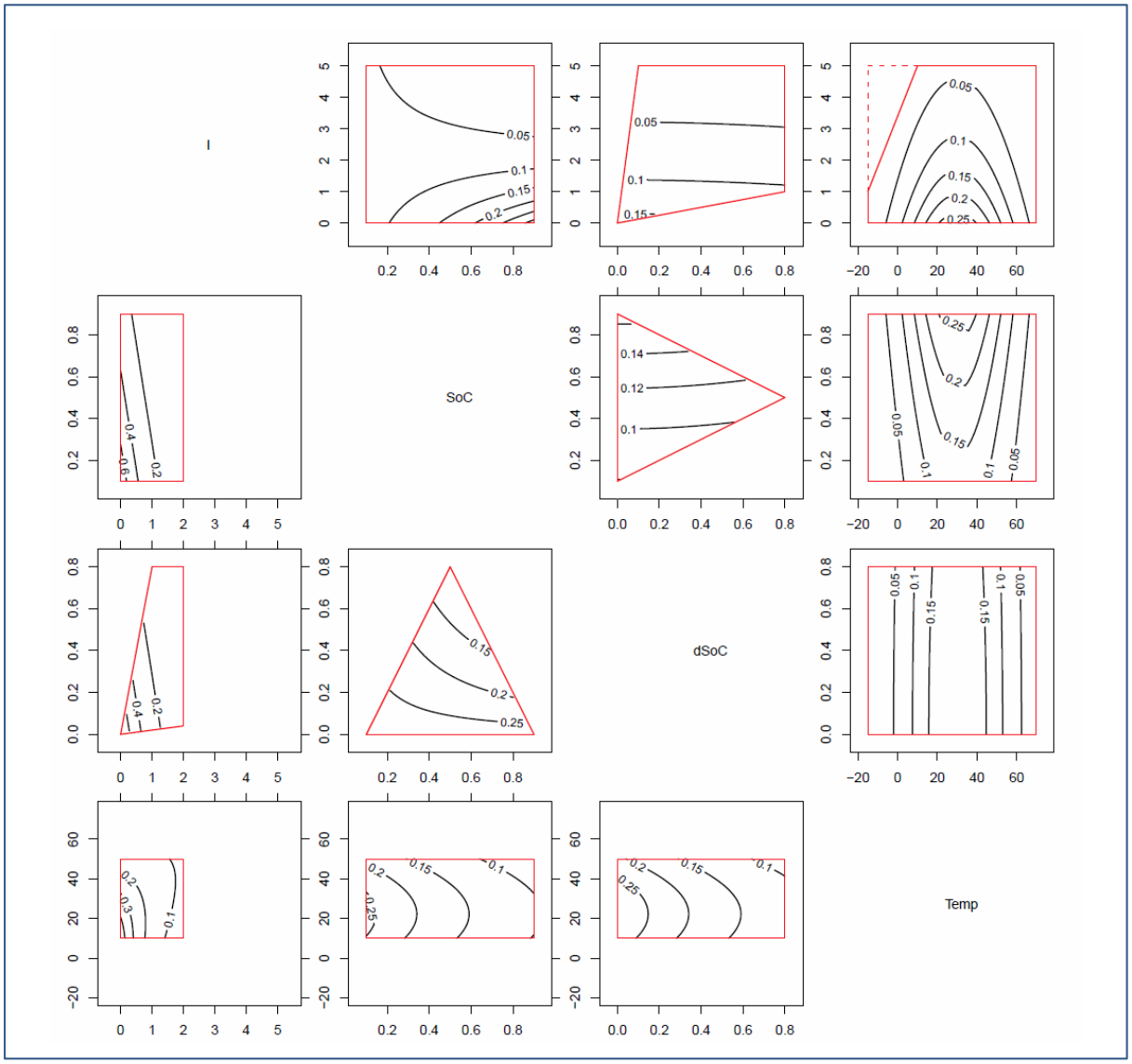

Figure 3.2.3-k – Normalized survival times, as predicted by the capacity decrease model plotted as isocontours within the experimental limits. Above the diagonal is the LFP, below is the NCA data model. Since one plot only shows the variation of two influence factors, the others were fixed to the settings completing the load point of Temp=30°C, I=1 h-1, SoC=0.5, dSoC=0.5.

These plots show within the top right triangle the LFP model and in the lower left part the NCA model. In both halves of the plot are box graphs bounded by the limits of the design space as introduced in Figure 3.1.1-b. The axes of the design spaces are given in the main diagonal, the labelled contour lines within the design space boxes are the model responses (the survival time until EoLc). So a higher contour label encircles an area of an exponentially longer survival area. Each box graph gives the variation in survival deviating from the standard point of 30°C, a current of 1Cr and SoC as well as dSoC equal 0.5. If not varied for the graph, these values rest constant.

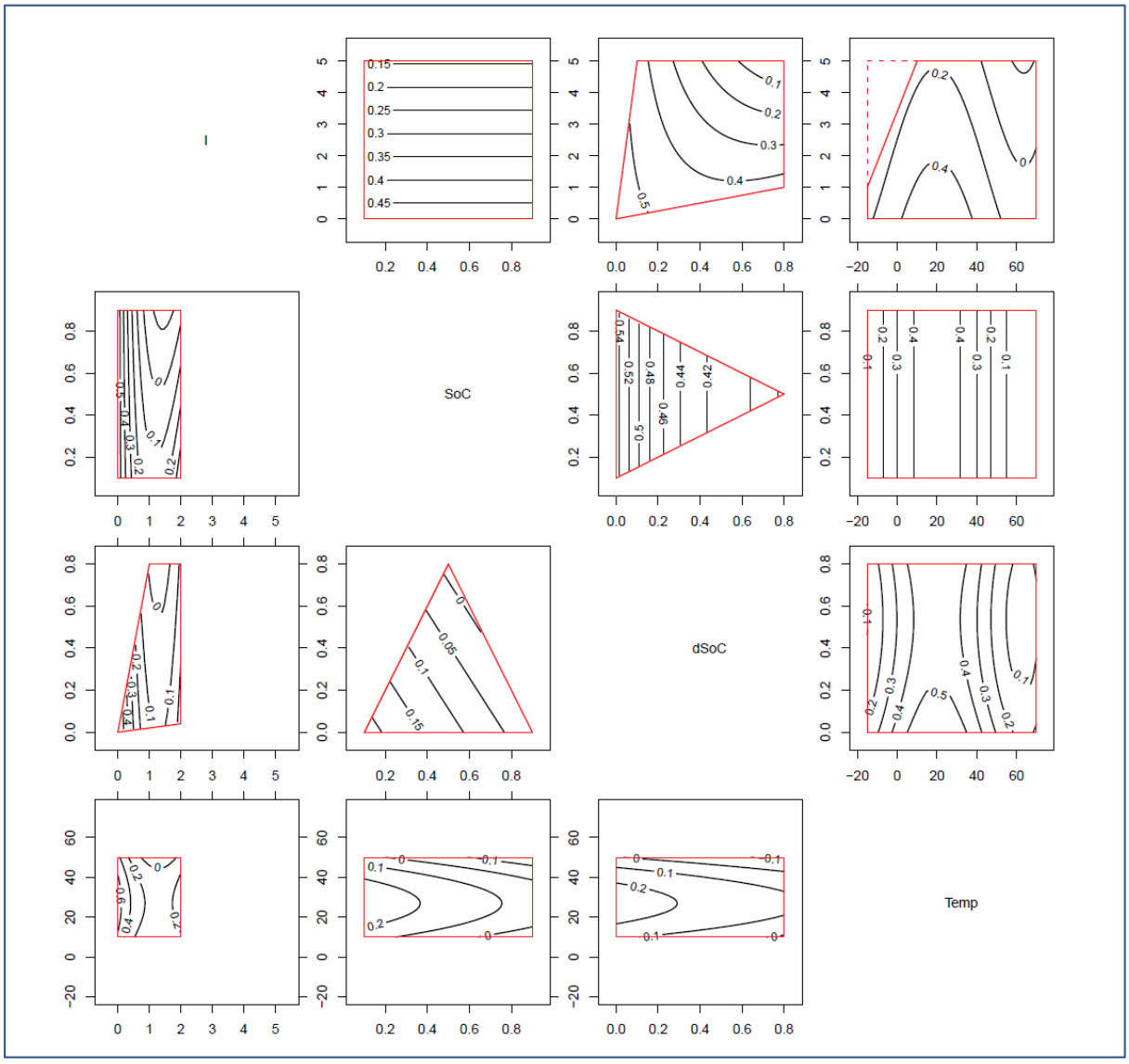

Figure 3.2.3-l – Normalized survival times, as predicted by the impedance increase model plotted as isocontours within the experimental limits. Above the diagonal is the LFP, below is the NCA data model. Since one plot only shows the variation of two influence factors, the others were fixed to the settings completing the load point of Temp=30°C, I=1 h-1, SoC=0.5, dSoC=0.5.

As for the influence parameters in both models it is remarkable – although in different powers and with different centre values – how basic influence factor combinations are reduced per model and chemistry to a maximum of three out of four parameters tested. A stronger

reduction is present in the interactions, which were reduced from 6 possible to about 3 significant interactions per chemistry only.

Temperature

There were five measurement settings in temperature for LFP cells, covering a range of -15°C to 70°C, and only three for NCA cells, ranging from 10°C to 50°C. The measurements suggest a maximum survival time at around 10°C to 15°C (Figure 3.2.3-g), which was modelled by offsetting the temperature influence to +15°C. The effects leading to the maximum in survival time are suggested by literature [Goodenough10, Harris10] also, underlined by the fact that the cells, which operated at low temperatures, showed lithium deposition on the anode upon visual inspection after experiment ending. The strength of the ageing influence due to temperature as postulated from the measurements is schematically depicted in Figure 3.2.3-m. The finding is that a cell operation temperature of around 10°C to 15°C would keep capacity decrease and the impedance increase low, although this temperature shows a higher power derating due to increased impedance compared to standard 30°C operation. So the compromise between life and operation conditions would be an operation in the window of 15°C to 20°C.

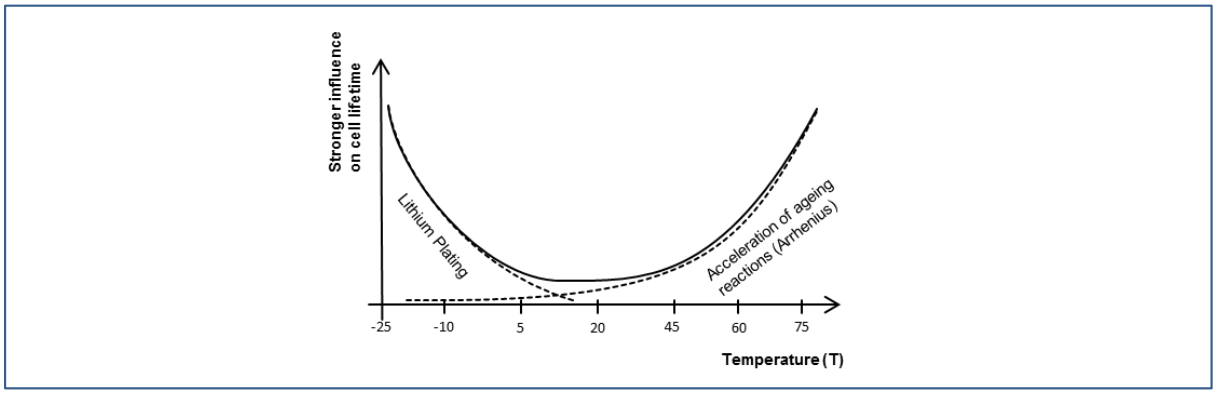

Figure 3.2.3-m – The ageing influence of the temperature is a combination of different ageing effects, producing a centred exponential influence on cell ageing.

Current

All four models favour a smaller current for the reduction of ageing effects. The lowest tested average current over ageing was close to zero, meaning the cell was under calendar ageing only, which also was the most favourable point. However, it is likely that the charging and discharging currents have different influences on the ageing and will therefore be regarded as separate influence factors in future works.

dSoC

All four models favour smaller dSoCs for the reduction of ageing effects. The lowest tested dSoC was equal to zero, meaning the cell was under calendar ageing only, which also was the most favourable point.

The dSoC was found to especially enhance NCA ageing when being high. SEM pictures, taken after disassembling aged cells, point towards a mechanism of particle destruction (Figure 3.2.3-n).

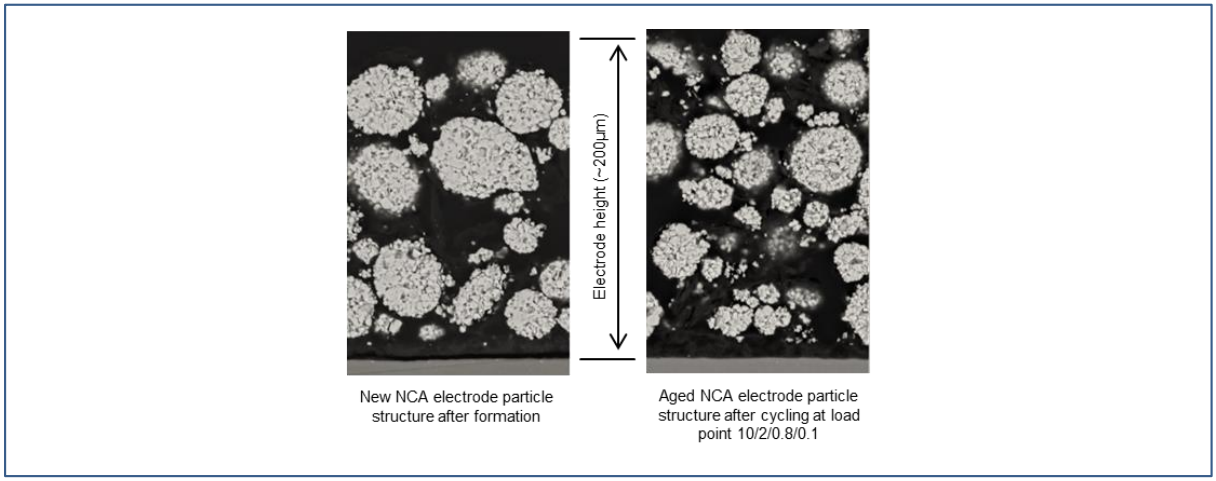

Figure 3.2.3-n – Detail of two REM pictures of a new (left) and an aged (right) NCA cathode. In the right picture the average particle size is smaller and more fragments are visible. The electrodes are shown in their whole thickness, the grey strip on the bottom is the aluminium current collector.

SoC

For the SoC very different results were found for the two chemistries. While for NCA cells low average SoCs were favourable for a low capacity decrease as well as impedance increase, the most favourable SoC for the LFP cells was found to be at higher SoC values for a low capacity decrease, and a non-issue for the impedance increase. A mechanistic explanation for this could be that the issue observed is a matter of mechanical cell balancing. LFP is changing its particle and consequently its electrode volume over SoC. This fact applies for graphite also and, if balancing is right, the ratio is about the same for both electrodes. NCA is changing its volume less [Park11], so the volume expansion of the graphite electrode cannot be counter balanced by the NCA electrode. So a mechanically relaxed electrode stack state in NCA cells is the discharged state. For LFP cells it is the fully charged state, because the graphite has a higher volumetric capacity than LFP but not a comparably larger volume expansion. Other explanations could be electrical contact loss in LFP and inner recrystallization in NCA particles [Srinivasan10].

Interaction of SoC and dSoC

This interaction is strongest for the NCA cell's capacity decrease. In NCA cells a large dSoC causes heavy ageing and if additionally the SoC is high, a high cell pressure (see SoC) could enhance the particle destruction effect (see dSoC). So the interaction accelerates the ageing process when both factors are at high settings.

This interaction is not relevant for LFP cells.

Interaction of current and dSoC

LFP cells exhibited a medium strength interaction of current and dSoC for the impedance increase while having a strong weight on dSoC. This interaction shows that high currents for small dSoCs are not much worse than small currents for large dSoCs, which is an often found result for ageing experiments of lithium ion cells (see various data sheets, e.g. in [Beltran12]), although not often tested for as real interaction.

This interaction is not relevant for NCA cells.

Interaction of current and SoC

For both chemistries alike, this interaction suggests low ageing when large currents are applied to an empty cell and stronger ageing when large currents are applied to a charged cell. Since both cells feature the same graphite anode, the interaction could be an effect coming from anode. In favour of this theory would be the known issue that high charging currents at high SoCs enhance the risk of plating [Vetter05, WohlfahrtMehrens04]. It is likely that the charging and discharging currents have different influences on the ageing.

Looking at the LFP cells separately, this interaction and the single influence of SoC combined give the suggestion that the cell has a window around medium SoC, in which large currents and zero current (storage) are favourable. At high and low SoCs the survival time is decreasing. The current limitation at high SoC exceeds the positive effect of the high SoC at very extreme values only. So a compromise in cell operation is suggested in using only medium to high SoCs as operational range (e.g. 80-35%). Again, it is likely that the charging and discharging currents have different influences on the ageing.

Interaction of temperature and current

This interaction has a positive sign for NCA cells, so it favours larger currents only at higher temperatures for the capacity decrease model. It is a rather strong term in the model. It can be interpreted that local heating due to high currents has less impact when temperatures are already high and the impedance is low. The interaction has no significance for LFP cells.

The remaining, not mentioned interactions of the four influence factors were either not or weakly observed in the results and are therefore not statistically supportable as results. Since this study covered two very different cell chemistries, one could postulate that their influence will be small for other lithium ion cell chemistries as well.

When setting up a new design-of-experiment with the herein discussed influence factors and their ranges, those interactions can likely be neglected. Doing so will distribute the load points during the calculation of the design plan in a different manner. Points, which only add information about one of the neglected interactions, will not be taken into the reduced design plan. Therefore the experiment will be more focused on better description of the model terms identified as important in this study.

3.2.3.7 The model results

The model not only provides a good overview of the experimental results, but also has a real value for someone trying to calculate the survival time a cell under a load profile. Any of the applications mentioned in the introduction demand loads which fit well within the test space and can therefore be safely evaluated with this model. Some current publications [Beltran12, Pourmousavi12] use models which only rely on single data sets of dSoC variation, which could profit very much by applying models like the one presented here.

When an expected profile is at hand, calculation of the average values for the four influence factors is needed. Taking those as input of the model it will return a survival time for the cells used in this experiment. Since the model can very quickly be evaluated for many different load profiles versus battery pack combinations, this can give a very good hint on how to tune the load or size of the pack in order to reach the desired lifetime. The model presented holds true for the cells tested and needs reparameterization every time a new cell is regarded. General trends on cell ageing depending on the cell chemistry can, however, be derived.

3.3 Model & Parameter estimation

3.3.1 MATLAB implementation

The model was implemented in MATLAB for its high calculation speed handling matrices. The code of the function files was written by the author except for OCVppval, wherein only modifications to the original ppval.m of MATLAB were made. A diagram of the call structure is shown in Figure 3.3.1-a.

The model is started using the SimBatt script. There exist two versions of this file, one for standalone simulation of the model and one for the ageing fitting. This function handles the input parameters, the time-stepping (loopback of variables,…) and any plotting of results for the model calculation.

The main function is called U_I_BattSim_stepwise.m. It incorporates the evaluation of the formulas as shown in chapter 2.1.2.5.

The first called support function is filterexp.m, wherein the low-pass filter values are evaluated. The second called is signF.m used for the reaction term. And finally, the OCV is interpolated in OCVeval.m. This function calls onto another two support functions. Linvector.m is very similar to linspace.m in MATLAB, but generates matrices of spaces from vectors, instead of vectors from scalars. Finally, OCVppval.m is a modified ppval.m, in order to make sure, when interpolating different OCVs within the same matrix, no bleeding of one OCV-curve into the neighbouring is happening.

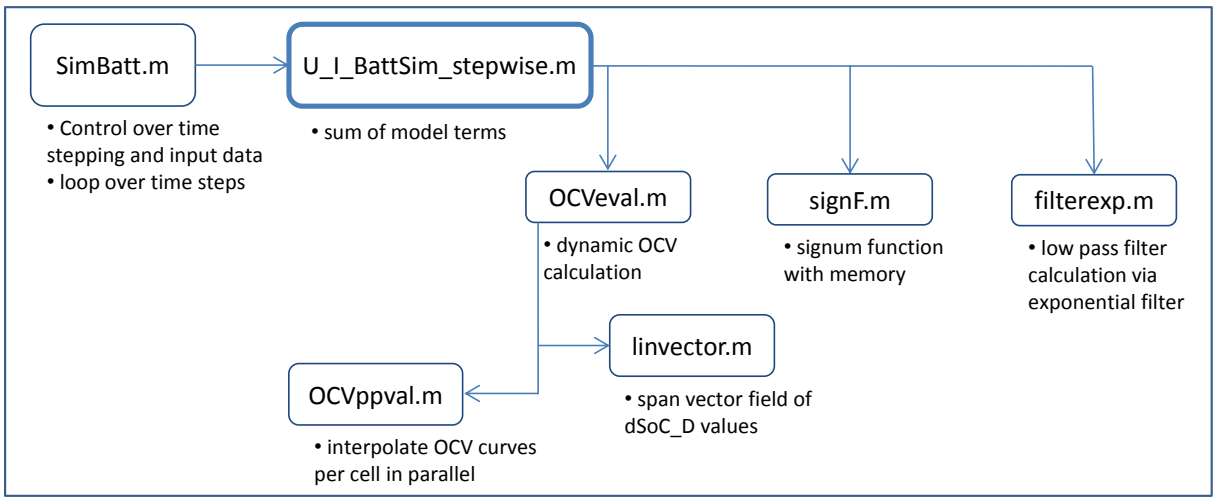

Figure 3.3.1-a – Structure of MATLAB functions and their function descriptions. Main script for simulation is SimBatt, which calls the step-wise calculation of the formulas shown in chapter 2.1.2.5, the other functions are support functions

This implementation is optimized for speed of calculation with many cells in parallel on a single CPU. This feature is important when thinking about coupling the model to a 3D calculation of the cell, where each element of the finite-elements simulation is treated as a micro cell with reduced capacity. Another good application for this feature is the pack simulation, as will be shown in chapter 4.2.1.

The implementation features a free-length second dimension for all model variables and parameters, making calculations of 1000's of cells possible in parallel. The only limitation hereby is the amount of memory installed. The calculation times are very fast and scale nearly ideally up to around 200 cells. However, larger arrays cause the memory organization of MATLAB to rearrange too often and therefore no further gains can be made in run times. In Figure 3.3.1-b the calculation times per cell per time-step are shown over the number of cells evaluated in parallel. Up to about 20 cells, the total runtime does not differ significantly from that of a single cell (green line indicates constant run time). Above 20 cells, each cell will slow down the model calculation a little bit, but doubling cells only means a quarter more runtime. Above 1000 cells the runtime is scaling ideally to the number of cells modelled, which means that 600 cells evaluate in 6/5th of the time of 500. At around 5000 cells, the memory bandwidth is slowing down the calculation to a higher level of calculation time, but still very close to ideal scaling.

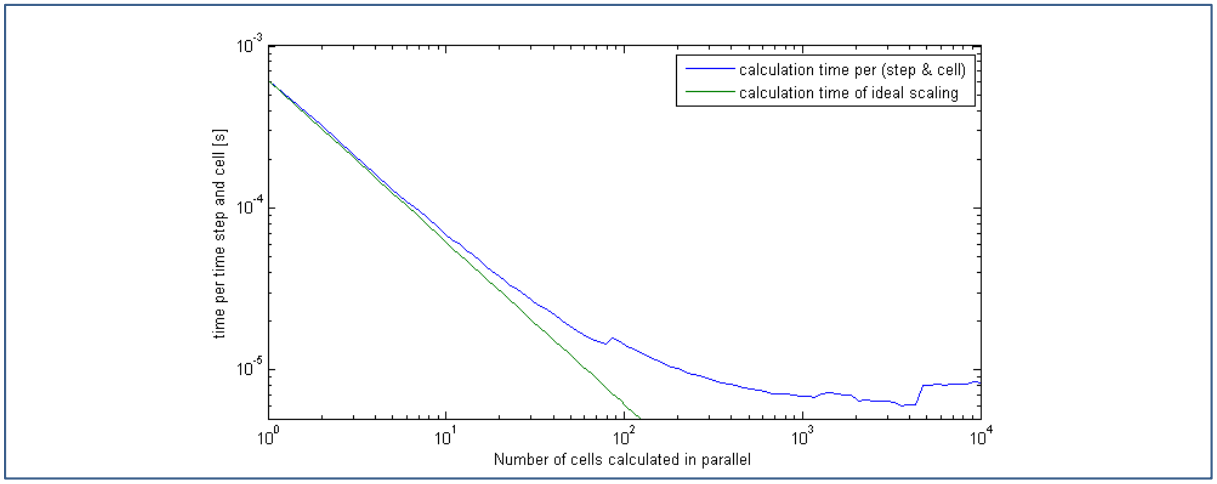

Figure 3.3.1-b – Calculation time given per cell and per time-step in parallel evaluation of the number of cells indicated on the x-axis. The times are mean calculation times of 100 trials per number of cells.

In Figure 3.3.1-c the whole implemented work flow is shown by arrows. Boxes with thick lining indicate parameter data given in the following chapters. Blue is the colour showing the normal work flow for evaluating the model based on given parameters and loads (demonstrated in 4.2.1).

Green lined boxes display all routines implemented for the fitting of parameters only. The numbers close to the arrows in Figure 3.3.1-c show the flow of finding parameters for both, the short-term and the long-term, models, since the flow is not obvious and some boxes are used twice in the process. The content of "fitting of short-term model parameters" has been addressed in chapter 2.2.2.4, while the content of "fitting of SNC curves" has been addressed in chapter 2.2.2.6.

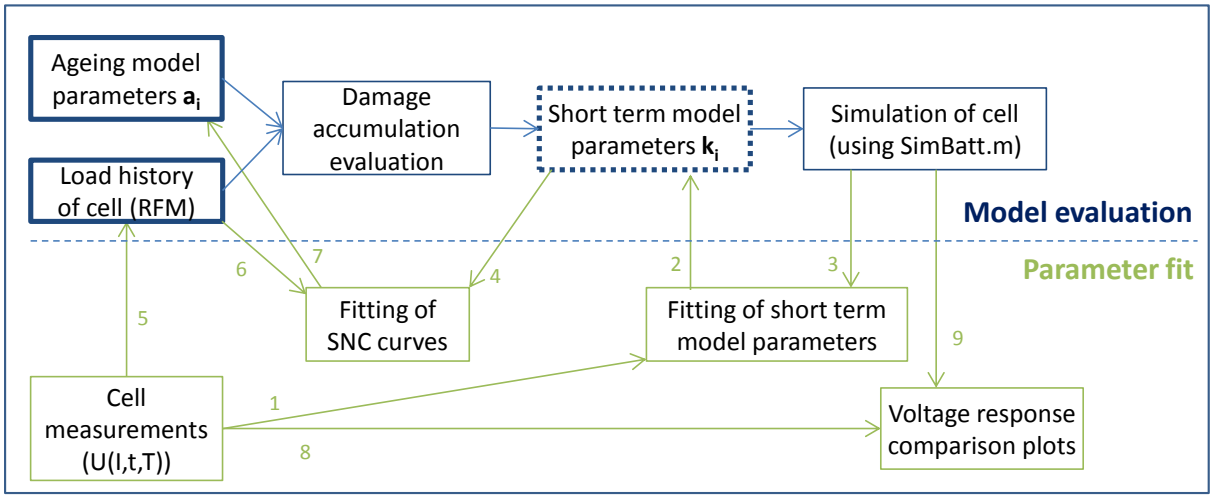

Figure 3.3.1-c – Work flow diagram of a normal model evaluation (top) and the loops taken to find the parameters for the model based on cell measurements at different SoH states of the cell.

3.3.2 Results of parameter estimation for different cells & chemistries compared

The implemented model was used, in conjunction with the implemented Gaussian Bee Colony optimization algorithm, to fit the parameters of the model to measurement data of a total of eight different cells. In this chapter the cells and their different traits are described, then the parameters identified are compared and finally a visualisation of the fitting quality and the parameter induced differences in voltage response is provided. The results guide to the conclusion that the model is indeed applicable for all different lithium-ion chemistry based systems and cell geometries without restriction, as would be awaited when claiming a first principles base.

3.3.2.1 The cells used

Eight different cell types were used to study the model applicability to different lithium-ion cells. Each cell has a special feature even though most of the traits only exist in two or three subtypes. Most cells use either pure iron phosphate or pure nickel-based oxide ceramics as cathodes, except the NN cell with a blend of different cathode materials. The anode is made of various, not closely specified graphites for all cells. The Kokam product uses a polymer solid electrolyte instead of a separator with liquid electrolyte. Another model relevant feature is the form factor, a rolled cell behaves differently than a stacked cell. All these facts, and some more, are put into Table 3.3.2-i for a better overview.

Cell Name	GAIA LFP	GAIA NCA	LiTec	A123	Winston	Lishen	Kokam	NN
Producer	GAIA Akkumula-torenwerke GmbH*	GAIA Akkumula-torenwerke GmbH*	Li-Tec Battery GmbH	A123 Systems, Inc	Winston Battery Ltd	Tianjin Lishen Battery Co., Ltd.	Kokam Co., Ltd.	NN
Chemistry cathode	$LiFePO_4$	$LiNi_xCo_yAl_zO_2$	$LiNi_xMn_yCo_zO_2$	$LiFePO_4$	$LiYFePO_4$	$LiFePO_4$	$LiCoO_2$	blend >4V
Chemistry anode	graphite	graphite	graphite	graphite	graphite	graphite	graphite	graphite
Separator	plastic	plastic	ceramic	plastic	plastic	plastic	polymer solid electrolyte	plastic
Capacity [Ah]	~0.05	~0.06	~40	~1	~39	~16	~4.4	~23
Form factor	rectangular, stacked	rectangular, stacked	rectangular, stacked	cylindrical, rolled	rectangular, rolled	rectangular, rolled	rectangular, stacked	rectangular, rolled
Casing material	pouch	pouch	pouch	Ni-can	plastic	Ni-can	pouch	Ni-can
Connectors	tabs	tabs	tabs	welded tabs	screw	clamped	tabs	screw
Min / max temperature of measurements	-15°C/70°C	-15°C/70°C	0°C/40°C	10°C/50°C	20°C/40°C	10°C/35°C	15°C/40°C	10°C/50°C
dynamics bandwidth of measurements [Hz]	$<10^{-4}$ – 5	$<10^{-4}$ – 5	$<10^{-4}$ – 2	$<10^{-4}$ – 5	$<10^{-4}$ – 5	$<10^{-4}$ – 5	$<10^{-4}$ – 5	$<10^{-4}$ – 5

Table 3.3.2-i – Specification sheet data and boundaries of test space for the cells used for fitting. * non-commercial lab-cells using material from Südchemie AG)

The last two rows of Table 3.3.2-i describe the measurement data taken from the cell, since some cells were more extensively tested than others. The values also indicate the limits of the applicability of the model fitted for the cells.

A feature which is already indicated by the different materials used in the electrodes are the characteristic OCV potentials of the cells. In Figure 3.3.2-a all OCV potentials of the cells are plotted over the respective SoC. It is notable that two groups are formed, the iron phosphate and the oxide ceramics fraction, differing in height and slope of OCV over SoC. The slight differences in the OCVs of LFP mainly arise from different electrode balancing of the cells. Although it is said that the rare earth dopants in the LFP (niobium in A123, yttrium in Winston) do create phase stairs in the LFP OCV, a proof was not spotted so far. Larger differences are seen in the oxide ceramics fraction as materials with differing nickel, aluminium and cobalt content are used, balancing differences cannot be seen as explicitly.

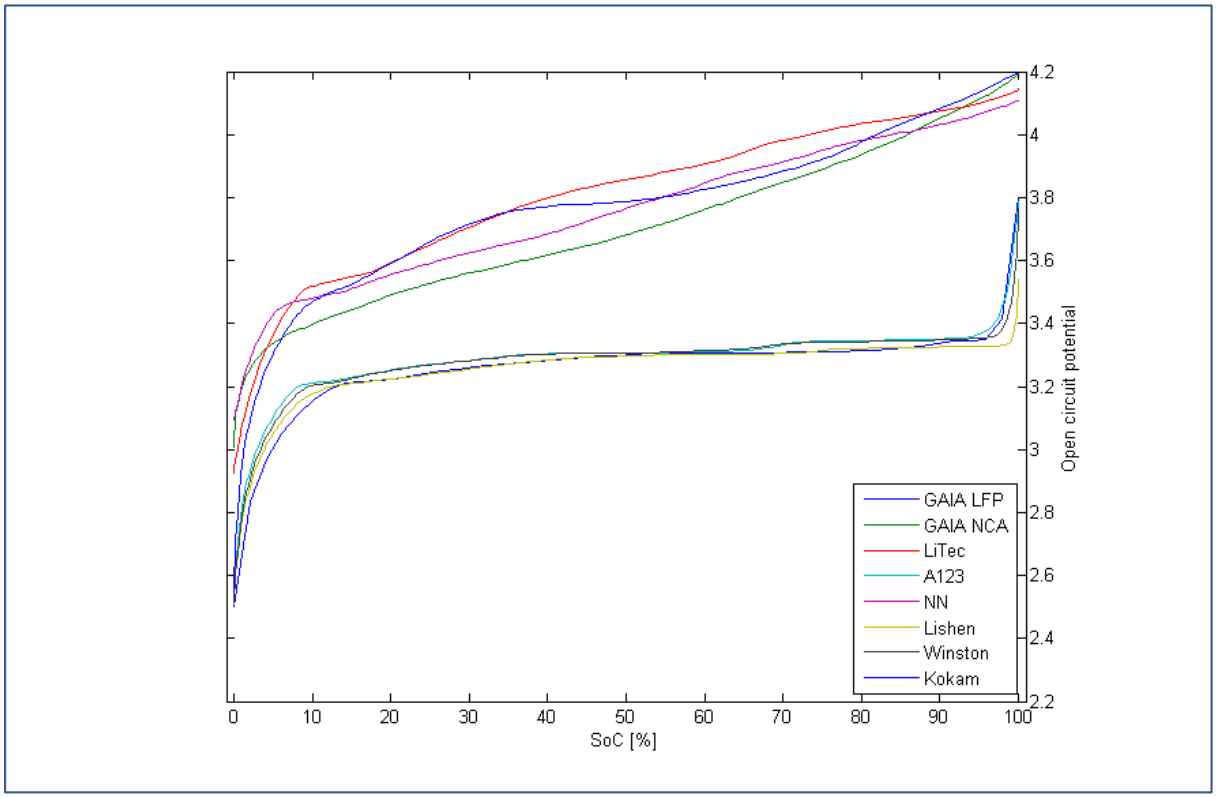

Figure 3.3.2-a – OCV potentials of the cells used for fitting. The lower group are all LFP cells, the upper group are the metal oxide cathode cells.

The cell geometry of the cells is the same only for the cells specifically made for the ageing experiment. All other cells were selected to be differing in size, shape and electrode assembly. Most of the cells can be seen in Figure 3.3.2-b to give an impression.

Figure 3.3.2-b – Picture of cells used for fitting.

3.3.2.2 Fitted parameters

The parameters of the different cell types were fitted to different characterization and load profile tests, since not all cells were measured specifically for the fitting process. The time length, excitation bandwidth and temperature range are different for the cells, as indicated in the last to rows of Table 3.3.2-i. Therefore the error after fitting is, despite its common calculation protocol, not comparable over the cell types when reaching the same quality of fit.

In Figure 3.3.2-c the error of the fitting results are presented as error per time-step of the characterization test. The value given is the average amount a single time-step adds to the fit error of the cell. The errors for the most important cells (GAIA LFP and NCA), because of their usage for the ageing modelling, is the highest, induced by the largest fitting data base. Especially the low temperature (-15°C) characterization tests can be attributed more than 70% of the error. So the fit quality is considered good, in spite of the differences presented.

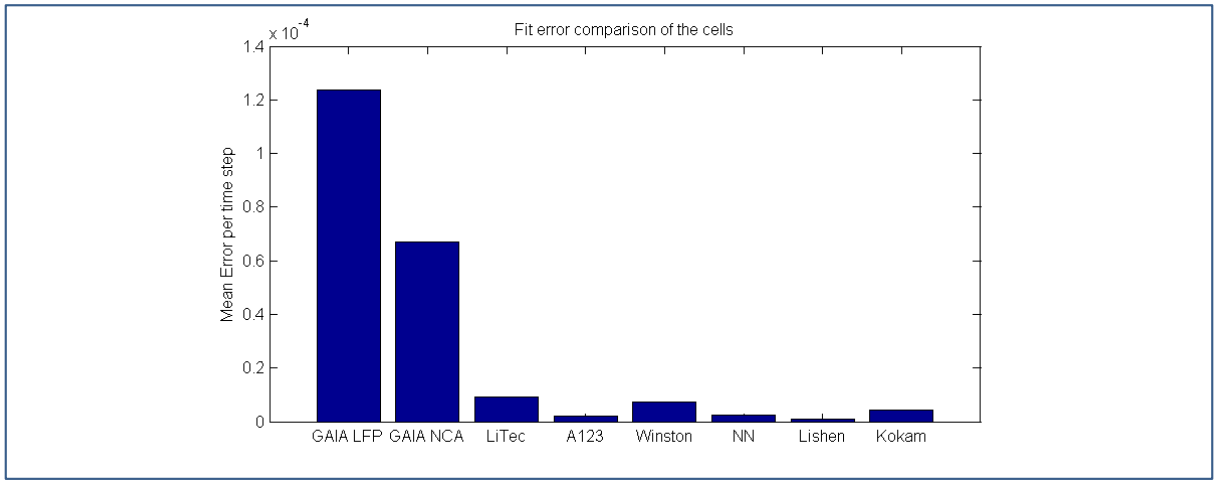

Figure 3.3.2-c – Comparison of fit errors of the different cell types.

As a detail of the fitting parameters the found linear resistances and time constants are compared in Figure 3.3.2-d. In the left graph the resistances for the cell types are plotted. In

the right graph the time constants are given. The lines above the bars on the left indicate the upper parameter boundaries set for the constrained fitting, while the lower was zero. The boxes around the bars in the left graph indicate the upper and lower parameter boundaries.

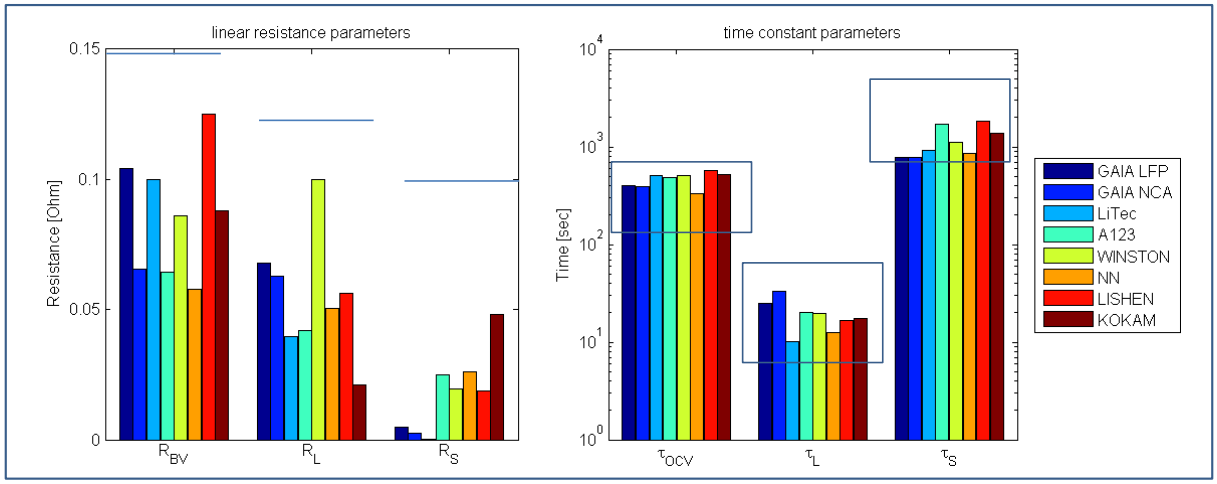

Figure 3.3.2-d – Parameter comparisons. Left the linear resistances, right the time constants, the legend is applicable to both graphs. The parameter boundaries for fitting are indicated by blue lines (only upper boundary) or boxes (both boundaries)

The parameters of the model should be linked to electrochemical features of the cell. In the following some of those links will be suggested, without having had the opportunity to verify those statements by additional testing or building custom cells.

The first two cells plotted are the GAIA pouch cells. Interestingly both of these cells exhibit high R_L and τ_L, while having a very low R_S. Since R_L is actively linked to the separator thickness and the distance of the electrodes (see 2.1.2.5), it could suggest that the pouch cells were not sufficiently pressurized by the plastic clamps around the pouch. On the other hand the low R_S might well be the very simple and square electrode shape with large current tabs. The Lishen cells exhibits the highest reaction term resistance (R_{BV}), which can most likely be attributed to a bad wire contact during the test, since the cells do not offer any screw on or otherwise removable tab design. A larger than average R_L was identified for the Winston cell. An educated guess is that the plastic housing, in analogy to the GAIA cells, does not provide sufficient pressure on the electrode stack. Another interesting feature, concerning all LFP cells in test, is the increased τ_L of those cells. It seems that the small particle size of LFP impedes liquid diffusion. Also liquid diffusion is slowed by the solid polymer electrolyte used in the Kokam cell, explaining the largest τ_L of all the cells marked as power-type cells.

In the following Table 3.3.2-ii all identified parameters per cell are given for readers reference. With these parameter sets, a short-term simulation of the different cells is possible within the boundaries of measurement. Below 0°C the model shows different behaviour than the cells in some working points. This indicates that the electrochemical basis might not be applicable below 0°C.

Cell Name	GAIA LFP	GAIA NCA	LiTec	A123	Winston	Lishen	Kokam	NN
k_1	0.99825	1.00715	1.00000	1.00000	1.00000	1.00147	1.00052	1.00965
k_2	0.09889	0.00155	0.00100	0.00825	0.14992	0.00793	0.15000	0.00158
k_3	405.339	389.279	505.796	488.366	507.173	569.375	525.465	332.102
k_4	12.9140	-17.4703	-27.8691	-13.3683	-47.1016	-19.1513	-0.0057	-23.3703
k_5	-5.36275	-6.51220	52.51879	3.48082	37.43247	9.14491	6.96617	-9.94554
k_6	6718.58	2484.01	3106.90	2972.40	4708.46	2131.74	4465.10	4476.90
k_7	11.76600	2.51318	0.77397	1.89648	0.60157	0.65942	2.33979	1.55324
k_8	1.09687	1.08680	0.70003	1.15693	0.87913	1.00753	1.10748	0.97128
k_9	3522.84	4341.10	4865.13	1847.93	4749.28	2179.32	4999.86	1999.98
k_{10}	25.0761	32.9398	10.0018	19.9957	19.8977	16.4954	17.3668	12.4778
k_{11}	15.15209	16.03810	49.99127	3.73497	29.95562	11.04835	37.55065	9.75495
k_{12}	2306.37	4236.89	3273.20	2514.01	2057.24	2002.72	4998.71	4998.06
k_{13}	1.55778	2.18207	4.69284	7.21616	3.03670	3.31740	3.25985	4.89757
k_{14}	788.060	780.712	928.528	1701.832	1117.954	1819.970	1385.023	850.042
k_{15}	1.82128	4.08027	-4.842964	17.02415	24.99765	-3.00000	-30.32044	12.52157
k_{16}	1.08594	1.00074	1.04190	1.00710	1.05055	1.01803	1.00054	1.01303
R_{BV}	0.10402	0.06541	0.10000	0.06419	0.08621	0.12525	0.08804	0.05767
R_L	0.06774	0.06290	0.03981	0.04185	0.09999	0.05632	0.02099	0.05056
R_S	0.00486	0.00264	0.00010	0.02500	0.01955	0.01869	0.04831	0.02625
C	0.04956	0.06180	40.54670	1.08498	40.11958	16.04589	4.61875	22.36908
η_C	1.00000	0.99900	1.00090	1.00021	1.00091	0.99811	0.99908	0.99929

Table 3.3.2-ii – Complete short-term model parameter table (k_i) as identified for the new cells.

3.3.2.3 Voltage response comparisons

The overall fit quality will be demonstrated by three voltage response examples of different cell types: The commercial Kokam cell and both GAIA lab size cells. The shown test profiles represent a small selection of each cell's fitting data. All presented measurements are in the range of 25-35°C and show a c-rate scanning in the upper graph and a dynamic load profile on the bottom. The c-rate scanning covers a maximum range from <0.2 to 5 Cr (not all for a single cell). The dynamic profiles cover excitation ranges from < 0.2 to 30 seconds per constant current step.

Figure 3.3.2-e shows the Kokam cell's results. The c-rate scanning from ~0.1 to 2Cr is reproduced with errors smaller than 20mV, the dynamic profile with errors lower than 30mV. Even within the constant voltage charge steps the simulation is not too much different from measurement. This cells behaviour can be reproduced very well by the model.

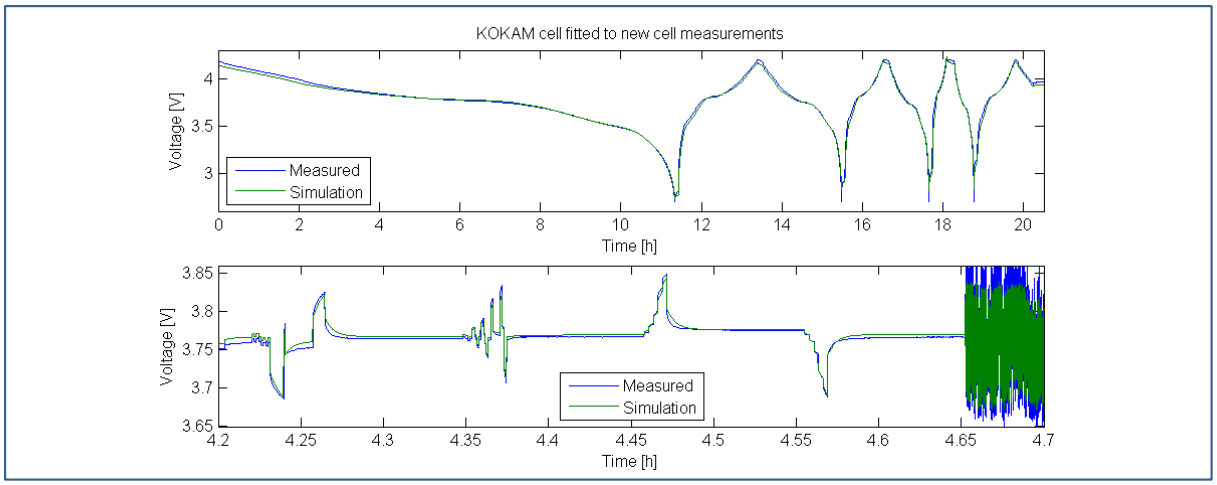

Figure 3.3.2-e – Comparison of fitted versus measured voltage data for the Kokam cell. Top is a c-rate scan, bottom is a dynamic profile with diffusion tests, stair & step pulses and finally a noise simulation.

In Figure 3.3.2-f the simulation versus measured comparison for the GAIA NCA cell is shown. This is one of the two cell types used in the ageing experiment, therefore the reproduction of the new cell's behaviour should be very close, in order to distinguish different ageing mechanisms on parameter level later on. For this cell the c-rate scan is not quite similar to the measurement for the low SoCs at low c-rates. This can be attributed to the quality of the OCV curve in the model. It was recorded at rather high currents for an OCV measurement (~0.05 Cr) and interpolated between charge and discharge. Better OCVs are recorded at ~0.01 Cr and between voltage limits slightly over respectively under the nominal voltage limits, when wanting good correlation in the outer SoC-ranges at 0.2 Cr cycles. The phenomenon appeared in other oxide ceramics based cells as well.

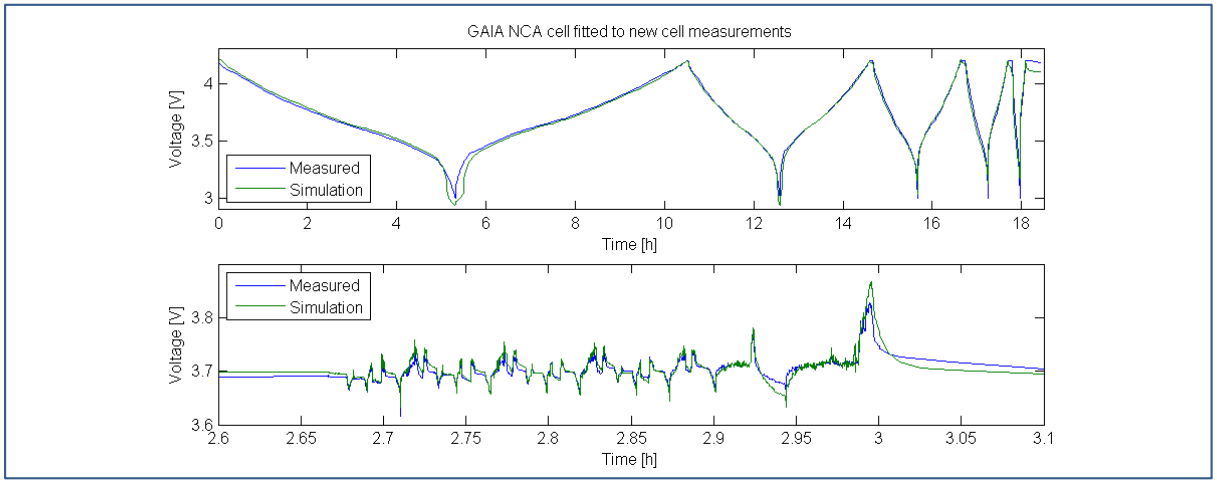

Figure 3.3.2-f – Comparison of fitted versus measured voltage data for the GAIA NCA cell. Top is a c-rate scan, bottom is a dynamic current profile from an NEDC test with a virtual HEV type vehicle.

Figure 3.3.2-g gives the third example, the GAIA LFP cell. LFP cells are very hard to fit, since the OCVs are very flat in the middle part and steep at the outer range. This induces strong dominance of the error values by the OCV term. So the simulated dynamic profile is not quite

as similar to the measurement as in the other two examples. LFP exhibits the OCV interpolation problem of NCA at high SoCs.

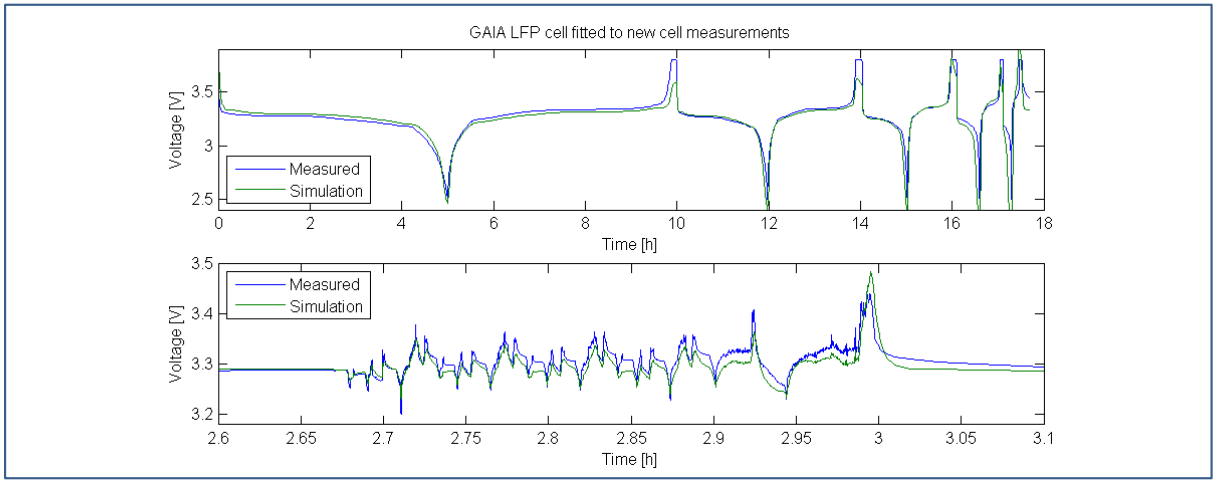

Figure 3.3.2-g – Comparison of fitted versus measured voltage data for the GAIA LFP cell. Top is a c-rate scan, bottom is a dynamic current profile from an NEDC test with a virtual HEV-type vehicle.

The overall reproduction quality of the voltage response of the model is very good considering the extremely large range of excitation and the small number of parameters used. Comparably fast calculating models do either reproduce better using large parameter databases (e.g. Equivalent-circuit models [Vergossen11] 2000+ parameters) or smaller application ranges. Both of these restrictions would not be suitable for an ageing analysis on parameter level of the voltage response behaviour as done in this study. Since, when using large parameter arrays, it is not clear if an effect is shifted to another parameter, but restricting applicability would cause the ageing experiments load-point variation not to be covered with the model.

3.3.3 Aged short-term parameters and ageing parameters

In this chapter the aged short-term model fitting will be shown. Parameters (a_{ij}) will be deduced, which indicate how the identified parameters of the short-term model (k_i) change when the cell ages. For reference of the order in which the parameters are identified and by which models they are linked together, see Figure 3.3.1-c.

3.3.3.1 Comparison of measurement and simulation of aged cells

The identification of parameters for an aged cell works the same way as for a new cell for every aged state in which cell characterization tests were measured, except that not all short-term model parameters are estimated, but only a selection of ageing relevant parameters. All other parameters are held constant at their new cell values. For the selection of ageing-relevant parameters made during model deduction, see 2.1.4.2.

In this study the cells were only characterized in the beginning and the end of life, but for future experiments more intermediate states of cell characterization would be advantageous. The end of life was defined to be a SoH of smaller than zero by definition of SoH given in 2.1.2.3. The cells were characterized for identification as soon as the SoH <= 0 was detected, so some cells do have SoH lower than zero. The cells used for parameter fitting are the GAIA LFP and NCA cells, which were subjected to the ageing experiment described in 3.1 and 3.2.3. So the parameter ageing modelled, depends on to the same four influence factors. The data about the ageing load is input to the model by the form of the two rainflow matrices (3.2.2). The characterization tests for the aged cells were the same as were tested on the new cells. Also, the time scale of the tests is nearly identical, since the characterization test are defined in actual c-rate, rather than nominal c-rate. There will be selected parts of six cells' voltage responses presented, as representative examples for all cells identified. These six cells have been chosen to allow the reader to compare four influences:

1. LFP versus NCA cells
2. Pure calendar versus cycle ageing (per chemistry)
3. Influence of temperature and dSoC (LFP only)
4. Repeatability ageing behaviour in single ageing load points with different cells (NCA only)

In Figure 3.3.3-a one can see three aged GAIA LFP cells perform the same characterization tests as the new cell. The display format has been chosen like the figures from the previous chapter (LFP Figure 3.3.2-g), with the slight difference that cell measurements (dash dotted line) and simulation with the identified parameters (solid line) are in one colour per cell. This format will be kept for all comparison plots in this chapter.

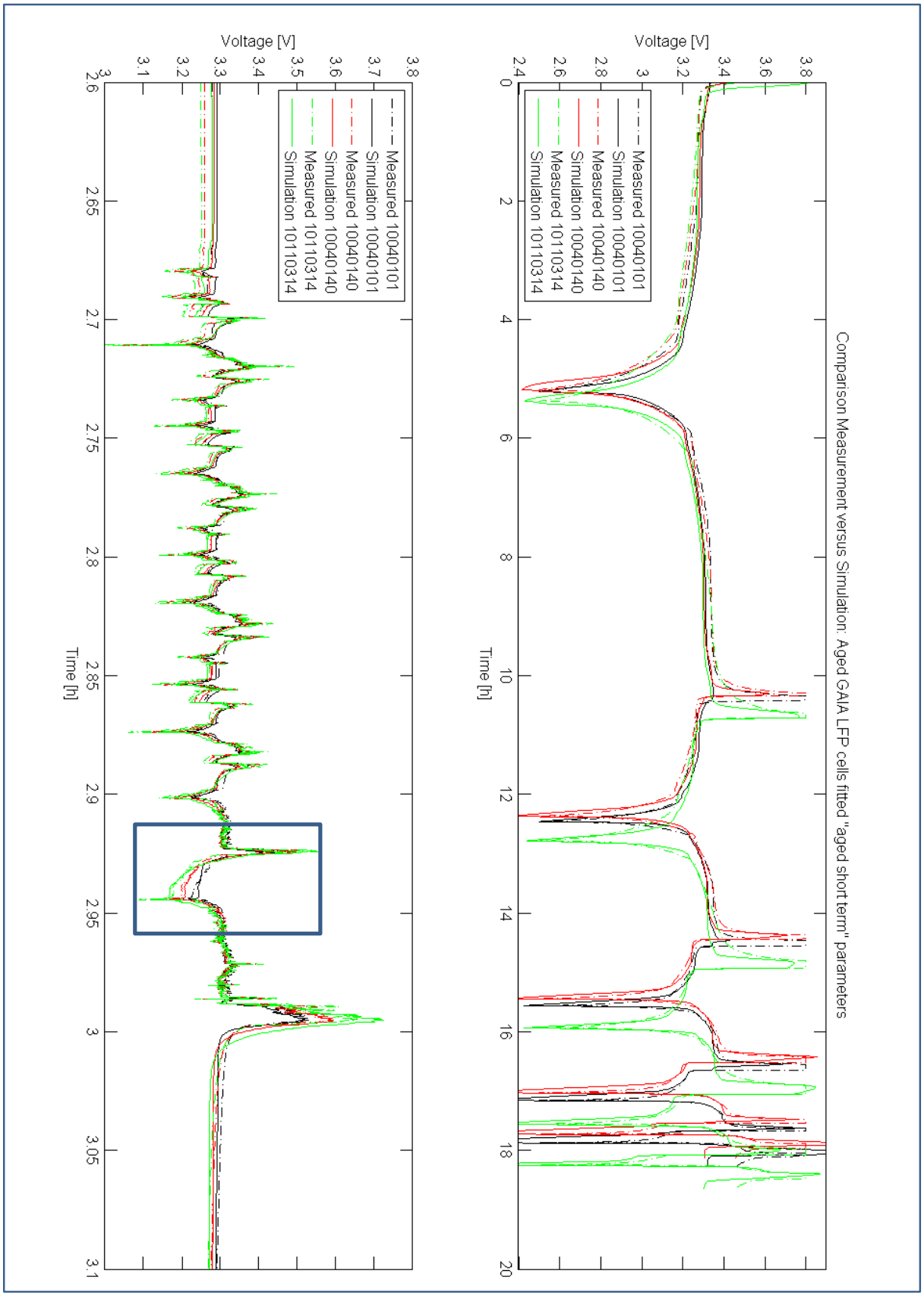

Figure 3.3.3-a – Comparison of fitted versus measured voltage for three GAIA LFP cells. Left for a c-rate scan (0.2, 0.5, 1, 2, 5) and left for the high dynamics part of characterization test D.

As for the identification of parameters for the aged LFP cells, a slight underestimation of resistance for small c-rate is discernible, but the voltage response behaviour to the c-rate cycles of 0.5Cr to 2Cr is reproduced very well. The underestimation is very much alike the one, visible in the new cells' parameters (Figure 3.3.2-g). The dynamic tests are also well reproduced in the large picture. For the detailed view in Figure 3.3.3-b, indicated by the blue box in Figure 3.3.3-a, it has to be stated that the relaxation time constants seem a little bit off, but relaxation ends up at the right voltage level nonetheless. The resistances for small and medium pulses are well identified.

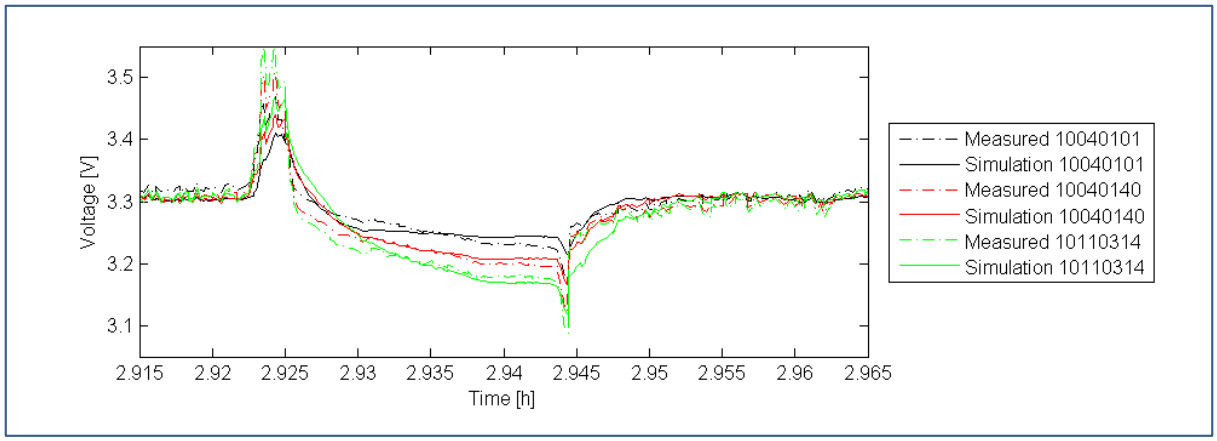

Figure 3.3.3-b – Detail of the comparison of fitted versus measured voltage for three GAIA LFP cells for the high dynamics part of characterization test D.

The three LFP cells have the following ageing load point:

10040101: 30°C / 0 Cr / 0 %dSoC / 90 %SoC / 0 SoH (calendar aged cell)

10040110: 30°C / 1 Cr / 80 %dSoC / 50 %SoC / -0.2 SoH

10110314: 50°C / 5 Cr / 10 %dSoC / 80 %SoC / -0.3 SoH

The lowest pulse overpotential and the fastest relaxation time is displayed by the calendar aged cell. The other cells follow with the cell in the strongest load point being the most damaged in terms of resistance and time constants.

Another detail of the fitting results is plotted in Figure 3.3.1-c. In the upper-left part the dynamic voltage response of cell 10110314 is shown within the discharge to 50% SoC, where the profile from the previous figure is tested. On the bottom-left the values for the three low-pass filters are shown for the whole cycle left, and as detail of the relaxation, on the right. It is easily visible that the liquid diffusion low-pass filter is responsible for the short pulses' overpotential, together with the reaction term (does not include a filter!). The relaxation process and the large overpotentials during the high current charge process in the last steps of the dynamic profile excite the solid filter and the dynamic OCV filter. Whereby the relaxation is mainly covered by the OCV filter, since the solid term drops to small values (the filter value, since the exponential function of 0 is 1) when the current drops to zero. The behaviour of the filters is exactly the same as in the new cell. So it can be stated that the identified aged filter constants do represent the same electrochemical effects in the aged cell as in the new.

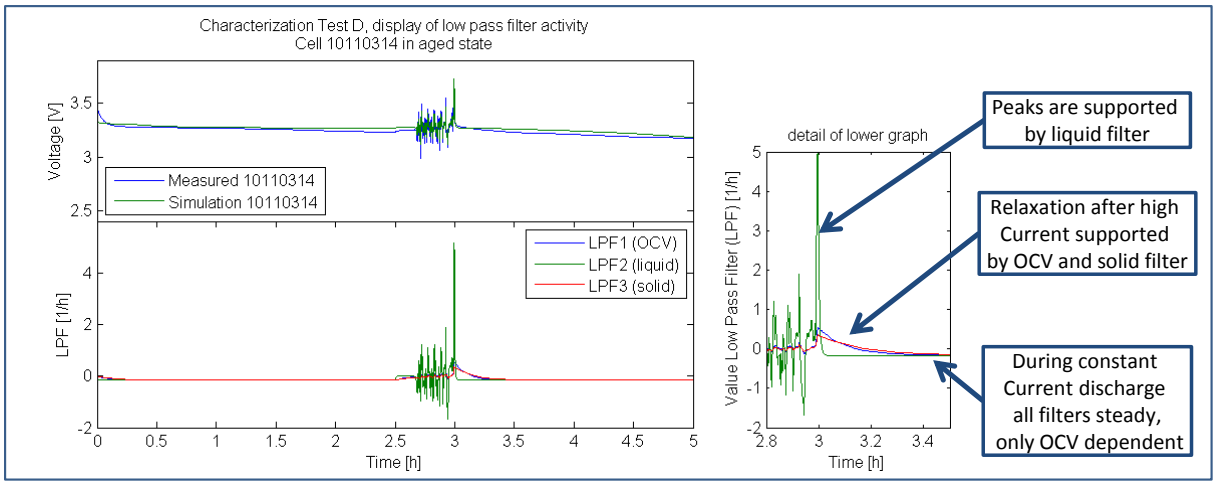

Figure 3.3.3-c – Display of activity of different low-pass filters in certain features of characterization test D. Voltage simulated versus measured voltage data is shown in upper-left graph, in the lower-left graph the output values of the low-pass current filters are shown. To the right a detail is enlarged and explained.

Overall the parameter identification quality can be considered good. The parameters identified for single cells represent the cells' behaviour properly and the parameters stay well within the expected value ranges (Table 2.2.3-i).

The three NCA cells have the following ageing load points:

10110910: 30°C / 0 Cr / 0 %dSoC / 10 %SoC / 0 SoH (calendar aged cell)

10110911: 30°C / 0 Cr / 0 %dSoC / 10 %SoC / 0 SoH (calendar aged cell)

10110916: 30°C / 2 Cr / 80 %dSoC / 50 %SoC / -0.2 SoH

The voltage responses for the characterisation tests of the three NCA cells are presented in Figure 3.3.3-d. For these cells an identification problem can be attested for the c-rate scanning. But the overall as well as the detailed (Figure 3.3.3-e) dynamics are of quite good fit quality, except for an offset due to the above visible problems.

In the detail of the dynamics also the reproducibility of ageing cells in the same load point is shown. The black-lined (10110910) and the red-lined (10110911) cell were subjected to the same ageing conditions. Although the high c-rate (>2C) behaviour differs, the dynamic profile response is very similar. So this part of the cell ageing seems more reproducible than the full cycle behaviour.

For the LFP cells, the cell stored at 90% SoC (and also at other SoCs at the same temperature, see Figure 3.2.3-c) had smaller overpotentials than the cycle-aged cells. For the NCA cells it is different, the calendar aged cells at 10% SoC have larger overpotentials and time-constant increases at SoH = 0 than the cycle-aged cell. Generally, for NCA at low SoCs, a higher increase in resistance was found than for SoCs equal to and above 50% SoC (see Figure 3.2.3-d).

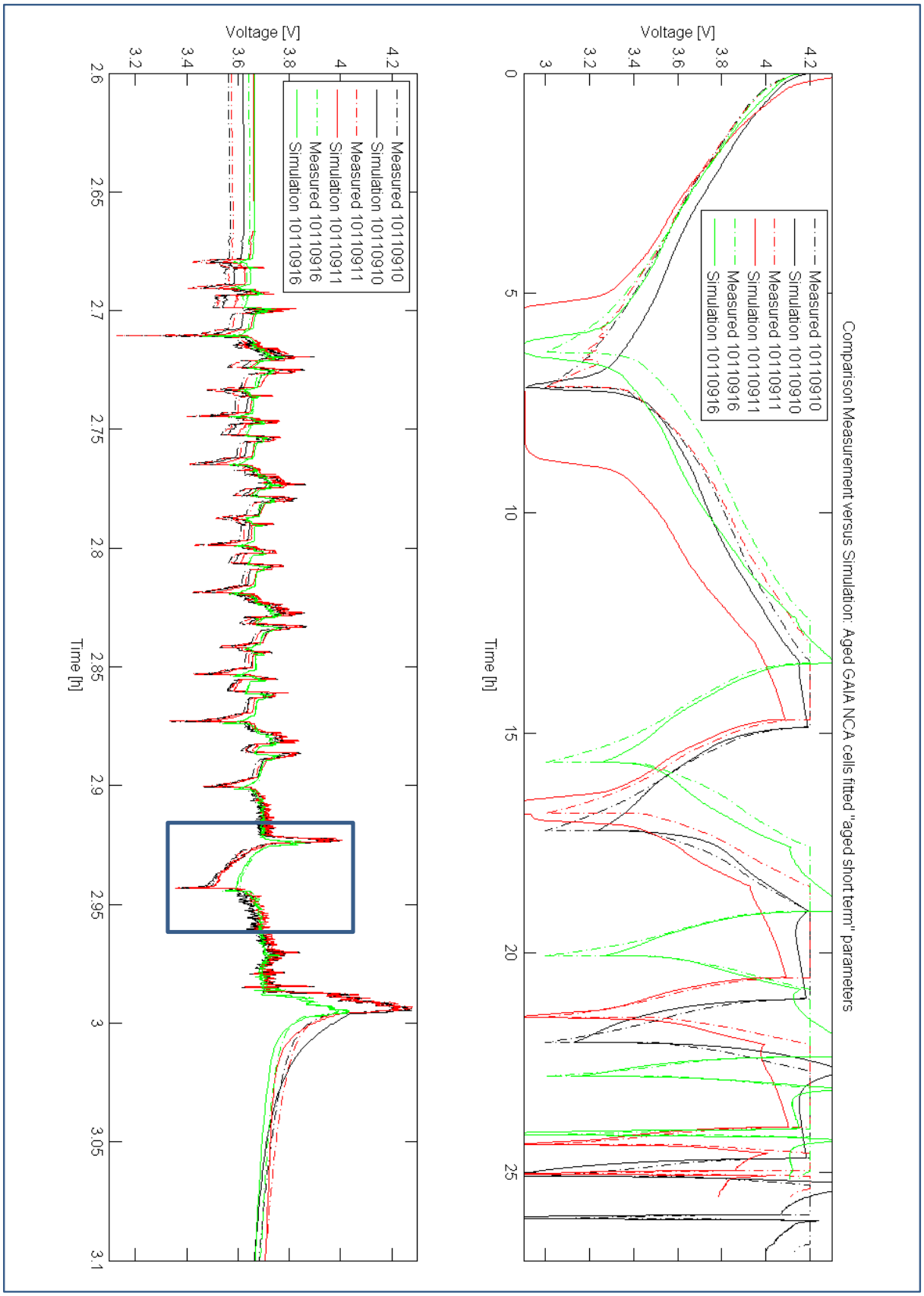

Figure 3.3.3-d – Comparison of fitted versus measured voltage for three GAIA NCA cells. Left for a c-rate scan (0.2, 0.5, 1, 2) and left for the high dynamics part of characterization test D.

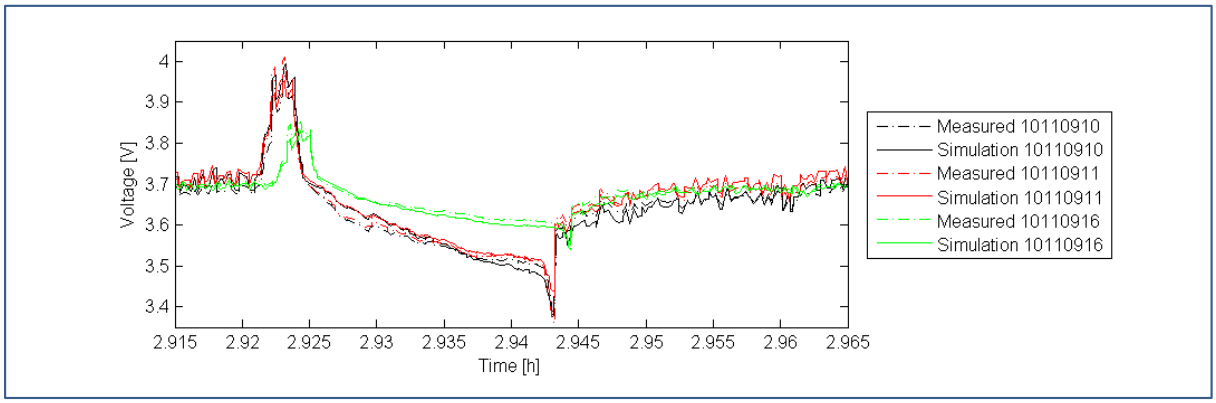

Figure 3.3.3-e – Detail of the comparison of fitted versus measured voltage for three GAIA LFP cells for the high dynamics part of characterization test D.

The reason for the deviations in the c-rate scanning is found in the OCV data of the NCA cells. The model uses the same OCV – SoC relation (plotted in Figure 3.3.2-a) for new and aged cells. The assumption that the basic OCV does not change over ageing is true for LFP cells, but not for NCA cells [Abraham05]. This fact is visualized using the differential capacity technique [Thompson79] in Figure 3.2.3-e. One can see that the differential capacity, giving the intercalation capacity at a certain voltage level, does not change its peaks for LFP (Figure 3.2.3-e b), but it shifts strongly to lower potentials for NCA (Figure 3.2.3-e d). Also one can see that the basic curve form changes for NCA. It seems that the whole operational voltage range is expanded to lower potentials. A definite cause was not yet found in literature and could possibly be given by chemical experiments.

3.3.3.2 Deduction of parameters for the ageing model

Having identified the parameters for the aged cells short-term model and their respective rainflow matrices (RFM) of the cell load available, the next step is to link the changes in short-term model parameters to the values in the RFM. This was done using a damage-accumulation model described in 2.1.4. For each of the ageing relevant parameters (k_i) of the short-term model, the ratio of change from new cell value to aged cell value is estimated by nine parameters (a_{ij}) of the ageing model.

The aged cell's short-term parameter data was fitted per cell chemistry. So two sets of ageing model parameters are available. Each set contains the parameters a_{ij} and an additional parameter value c_i for the form of the damage term chosen by the fitting algorithm. The parameter c_i is either 1, -1 or a value between 0.01 and 0.99. In the first two cases the "normal" ratio term is selected either for a rising or a falling ratio. In the third case the cell capacity value is fitted. The identified parameters are given in Table 3.3.3-i.

Cell type	parameter	a_{i1}	a_{i2}	a_{i3}	a_{i4}	a_{i5}	a_{i6}	a_{i7}	a_{i8}	a_{i9}	c_i
LFP	k_1	2.148E+05	1.155E-12	1.088E+05	1.000E+01	2.675E+03	-2.000E+00	1.392E+01	1.351E+02	5.043E+00	2
	k_2	1.593E+03	2.147E-01	6.236E+02	8.373E+00	5.169E+02	-3.826E-01	4.379E+01	-9.965E+00	3.577E+03	2
	k_3	6.525E+03	8.067E-01	1.679E+03	2.000E+00	5.911E+02	-2.895E-01	4.185E+01	-9.998E+00	1.431E+03	3
	k_{10}	3.572E+02	1.087E-02	2.073E+03	8.126E-01	1.013E+03	-3.779E-01	1.555E+02	-7.768E+00	6.362E+02	2
	k_{14}	1.485E+05	2.220E-14	3.787E+05	1.000E+01	1.204E+04	-1.999E+00	1.275E-01	1.600E+01	8.691E-01	2
	R_{BV}	5.134E+02	1.638E-01	1.016E+03	8.537E+00	3.256E+01	-7.986E-01	8.172E+01	-8.850E+00	5.954E+02	2
	R_L	1.224E+03	2.358E-14	1.141E+03	9.541E-01	1.125E+03	-3.336E-01	1.420E+01	-9.994E+00	9.245E-03	2
	R_S	9.321E+05	2.220E-14	2.261E+06	1.000E+01	2.619E+04	-2.000E+00	2.220E+00	8.784E+00	7.833E-01	2
	C	7.466E+04	8.265E-02	1.154E+01	5.515E+00	1.374E+02	-4.353E-01	4.469E-03	3.271E+00	1.988E+03	0,4
	η_C	2.127E+04	2.310E-14	6.299E+04	1.000E+01	1.100E+03	-1.440E+00	5.206E-01	9.160E+00	9.289E-01	2
NCA	k_1	3.941E+05	2.881E-14	5.786E+05	1.000E+01	1.365E+04	-2.000E+00	8.013E-02	7.185E+00	6.224E-01	2
	k_2	1.287E+03	1.000E+00	5.206E+02	1.122E+00	3.577E+02	3.653E-02	5.849E-01	2.452E+00	1.229E-01	2
	k_3	5.191E+03	9.049E-01	2.296E+05	3.128E+00	4.070E+02	-2.633E-01	2.573E+01	-9.888E+00	1.067E+03	3
	k_{10}	1.246E+03	7.915E+00	9.187E+02	1.504E+00	5.343E+02	-2.844E-01	4.373E+01	-8.876E+00	8.239E-01	2
	k_{14}	8.827E+04	1.000E+01	3.158E+05	1.000E+01	8.229E+03	-2.000E+00	4.587E-01	1.390E+01	8.033E-01	2
	R_{BV}	4.032E+03	1.099E+00	6.029E+02	2.023E+00	6.781E+02	-1.310E-01	1.958E+01	-7.528E+00	6.452E-01	2
	R_L	8.577E+02	2.001E+00	9.464E+02	1.641E+00	4.946E+02	-1.770E-01	1.942E+01	-9.920E+00	1.974E+02	2
	R_S	2.562E+02	2.342E-01	1.020E+03	1.836E+00	3.871E+02	-2.378E-01	2.310E+01	-5.930E+00	3.515E+00	2
	C	7.402E-04	9.613E-01	3.425E+02	1.000E+01	3.666E+03	-3.421E-02	4.141E+00	-1.000E+01	2.981E+03	0,4
	η_C	1.966E+04	2.220E-14	1.105E+04	1.000E+01	7.843E-01	-2.000E+00	4.174E+00	1.874E+01	5.962E-01	2

Table 3.3.3-i – Complete ageing model parameter (a_{ij}) table.

An interesting detail representing the experience made during analysis of the identified parameters is given in form of a plot of the SNC curves for the short-term model parameter capacity (C). In Figure 3.3.3-f and Figure 3.3.3-g the curves for LFP and NCA respectively are plotted. These represent the cycles / hours accumulated until the SoH = 0 is reached.

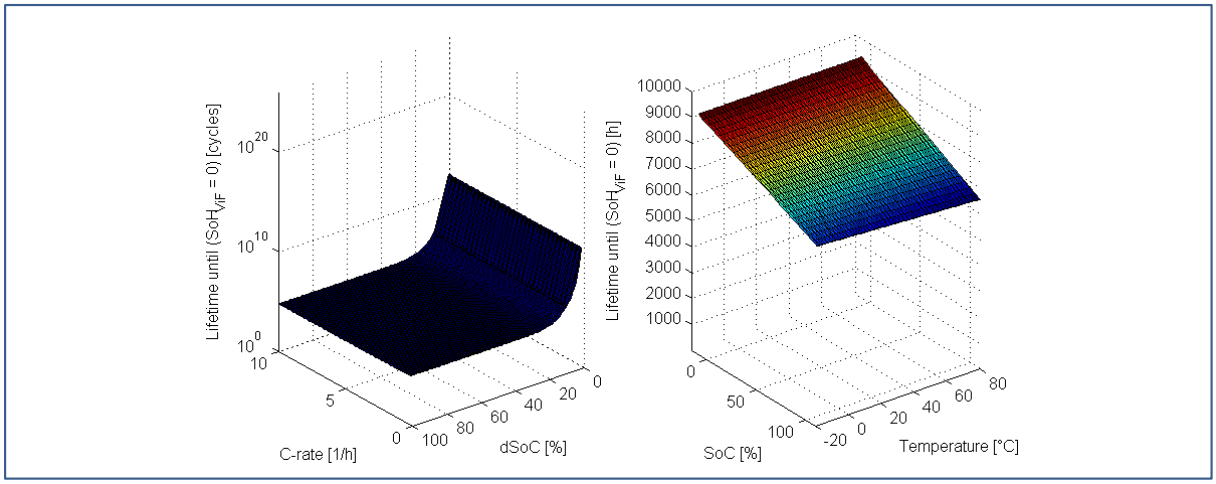

Figure 3.3.3-f – SNC curves identified for the parameter C "cell capacity for c-rate conversion" for GAIA LFP cells

One can see that the influence of the dSoC for both cell types exceeds that of the c-rate by far. This is not quite in line with the findings of the statistical model, where only average values of the influence factors were used instead of the more detailed rainflow matrices.

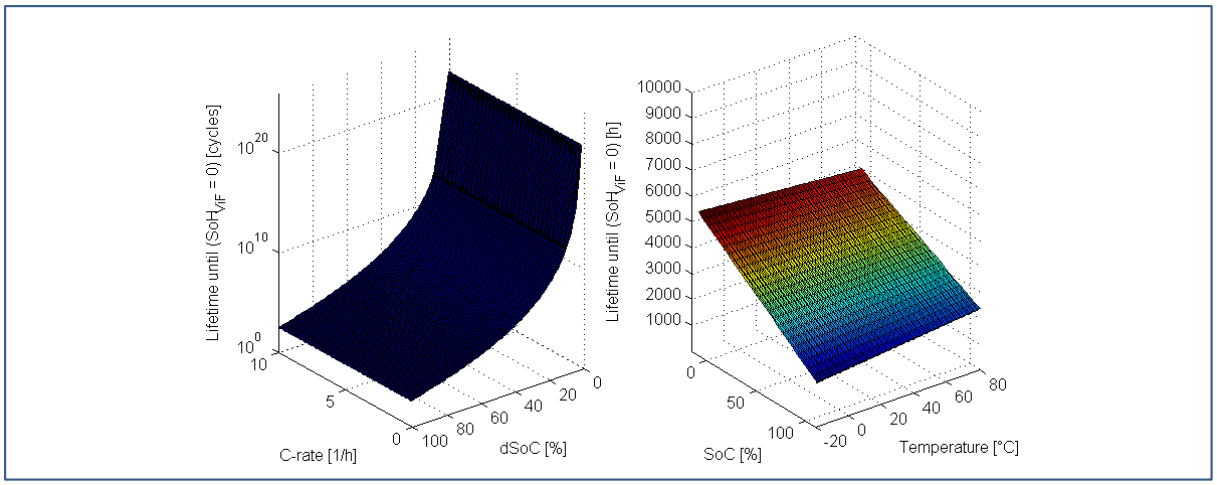

Figure 3.3.3-g – SNC curves identified for the parameter C "cell capacity for c-rate conversion" for GAIA NCA cells

However the LFP cell shows a more resistant plateau against cycling damage, allowing nearly 10000 cycles of any dSoC, while NCA drops down to around 1500 full cycles, which correspondingly was found in statistical analysis (see Figure 3.2.3-k).

In calendar life, displayed in the right plot in Figure 3.3.3-f and Figure 3.3.3-g, LFP cells are slightly superior, although their capacity falls from an initial value to from a plateau and drop later. This behaviour is different for NCA cells, rising first, but then hitting the EoLc-limit of capacity earlier. This staging behaviour is displayed in Figure 3.2.3-j. An average of 9 respectively 10.5 months of calendar life was achieved by the cells. The findings of the calendar life dependence of the capacity parameter are the same, as were found in the statistical analysis of the measured cell capacity.

For the reaction term resistance alone, the results for the resistance in the statistical approach are already rather well replicated: NCA has a SoC and temperature dependence, while LFP is temperature and equally strong dSoC and current dependent. The interaction in the statistical model does not give a relation of the dependencies, just the fact that there is an interaction. This relation can be supplied by the SNC parameters. Another strong interaction of NCA, SoC with current, cannot be modelled by the damage-accumulation approach, since the SNC's are formulated per RFM only. The handling of interaction in this approach would need some further research, since interactions between current and SoC as well as dSoC and SoC were emphasized by the statistical approach.

Another interesting parameter over ageing is k_{10}, the time constant of the liquid diffusion term. It shows a almost singular dependence on temperature for the LFP cells. Whereas for NCA cells it shows high sensitivity to increased temperature, as well as a high exponent in the current SNC. This indicates that the time constant does not increase when the cell is stored, but increases fast if any cycling at all is applied. The behaviour of the time constants was not part of the statistical modelling approach, as in most such models in literature [Duderzert09, Smith09, Safari10].

4 Discussion & Application

In this chapter comments on the achieved results will be made and an example of the targeted application will be given.

4.1 Interpretation of results

Two main aspects of the results are focussed on in the following chapters. First an overview of the model quality and fitness for the targeted application of the model will be given, then some aspects of limitations of the approach will be explored.

4.1.1 Fitness of the model proposed

The model fitness shall be assessed under four criteria: the models accuracy, the completeness of modelled effects found in the real system, the calculation time and the complexity of model handling. These four were chosen for being the first four questions industry representatives were asking when confronted with a new model.

Model accuracy:

The voltage response is at least as accurately reproduced as by an equivalent-circuit model with parameters dependent on all influences (current, SoC, temperature, SoH), if no adaptive SoC estimator is used. [Herb10] If an adaptive SoC estimator (Kalman filter or equivalent) is used, then the RC model is more accurate. [Santhanagopalan06B, Kim11B, Lee12]. The ageing of parameters for both cases does provide equal errors over the whole range of SoH between the RC models and the proposed model. Currently the model with the most extensive range of ageing influences considered is the thesis of F. Herb [Herb10]. Still those are less than are considered in this work, and no effective comparison of differently aged cell simulations has been given by F. Herb.

No electrochemical model has yet been presented in literature with a broad range of excitation. Safari et al. [Safari09] have presented ageing studies on an electrochemical model including surface-layer formation, but no other effects. As far as discharge curves have been presented at various c-rates, the proposed model can match the accuracy [Thomas03, Christensen04, Safari11B, Bernardi11].

Other empiric models, as by Hartmann [Hartmann08] or Shepard [Shepherd65], have good accuracy in smaller ranges of application in the short-term modelling. They can be fitted to either match dynamics or full cycles very well, but not both at the same time as presented here. Hartmann [Hartmann08] presented an ageing approach to his model as well, which had only a single influence on ageing behaviour, the end-of-charge voltage, allowing no comparison.

Completeness of effects:

Since the short-term model is deduced from basic electrochemical equations and cell geometry, this part of the model has got a supporting mechanistic base with one exception: The OCV is not modelled, but given as a measured lookup table. Since the new cell's OCV is mechanistically not the same as for the aged cell, this proofed to increase fitting error for aged NCA cells. A solution to this problem could be an additional model for the OCV potentials, as was recently presented by Dreyer [Dreyer12], though the exact mechanistic causes for the ageing of the OCV potentials are still unexplored. There were estimates of "changing crystal structures" within the FMEA [Cherkashinin12], so further mechanistic research would be a needed step to create a worthwhile model. This does not impede the model from being successfully used for LFP based cells in ageing calculations.

The ageing model itself is entirely empiric, since the causes and interactions disclosed by the FMEA were too many and too complex for mechanistic modelling, they were broken down to four influence factors. The model is limited by the ability of the SNC formulation to consider ageing effects. Different mechanistically deduced SNC's and damage-sum formulations for each parameter, as demonstrated with the capacity, are one of the ways to improvement. Nonlinear damage accumulation and larger parameter counts will very likely be the next step. Also consideration should be given to the low temperature effects (below 0 °C), as those are not yet part of the SNC formulation.

The rainflow-counting matrices are a very complete and easily accessible way of storing the load history of the cells, showing a way to extracting the combined data of the four main influence factors from measurements, which can be considered the most important addition made in ageing modelling during this work, advancing the pioneering work of Dudezert [Dudezert09], which has handled a single factor that way. But the fact that interactions of the influence factors, which were found important during statistical analysis, cannot be modelled sufficiently by the current formulation of the SNC's is a major shortcoming of the presented approach.

Calculation time:

The calculation time of the short-term model is only matched by very well implemented equivalent-circuit models, since look up of all the parameters needed is a time intense operation. The simple empiric models of Hartmann and Shepard [Shepherd65, Hartmann08] match the calculation speed of the short-term model as well.

The ageing model does not consume enough calculation time in any of the compared models to significantly decrease output speed.

Handling complexity:

The proposed model is very simple in handling, since the short-term parameters are calculated by a single script (<100 lines of code) and the model calculation itself is a single loop over time calling a cumulated six scripts (total < 400 lines of code, 250 thereof are for OCV calculation). Handling is also simplified by only relying on current profiles over time as

input. The SoC and temperature are given as start values only, but can be overwritten during the profile calculation.

The parameterization of the model is almost fully automated, so the user can supply any current, temperature and voltage profile over time as input. No special features such as impedance measurements in form of sine-wave excitations are required in the input. The only prerequisite is that the starting SoC of the profile is well estimated, since a wrong initial SoC can slow down or coerce the fitting process to the point of divergence. Also it is of good practice to start with a relaxed cell voltage .

Fitting of new and aged cells is not done in the same optimization run, as the new cells' parameters are the base for the aged fit. So two start scripts are provided for the different fitting runs, wherein the second is to be completed with the new cells parameters upon completion of first fit. The time consumed by the parameter identification depends on calculation power and CPU cores available, but mainly on the time-step count of the characterization tests. It is better to have many short tests, since they can be cheaply parallelized. Few long tests, especially when combined with other shorter tests, do increase the memory usage and time needed by "time-step count * number of tests in parallel". Short tests combined with long ones create a lot of unnecessary computing overhead, since all the OCV interpolations are called for as many time-steps as the longest test has got. This is an inconvenience caused by the fixed data structure of the fastest possible OCV curve interpolation routine, the parallel polynomial evaluation.

Overall handling the model is easy compared to mechanistic models and equal to plain empiric models. Parameterization is easier than for mechanistic models, since the measurements are limited to cycling data, but it is more complex than plain empiric models. Once a better way of handling the limitations in OCV interpolation during fitting is found, handling will be on the same simple level as empiric models.

The ageing model is easy to handle in calculation as it is integrated into the short-term model. Again, parameterization is a little more complex, but can be fully automated to support the inexperienced user.

4.1.2 Applicability of the model proposed

4.1.2.1 Validation

For validation purposes of the short-term model fitting with new cells, a second data set per cell type was measured. These include only two runs per cell type at two different temperatures, although the temperature settings were the same as part of the fitting data sets. These measurements were take from the same cell in all cases, but the GAIA and A123 cell types had an additional set (noted in brackets). Since sufficient supply of cells were available for these types, two other cells were taken for the two additional validation runs. A noticeable cell-to-cell variation explains the high errors in these calculations.

Cell Name	GAIA LFP	GAIA NCA	LiTec	A123	Winston	Lishen	Kokam	NN
Increase in average error per time step for combined profiles	5.4% (17.2%)	3.1% (11.8%)	3.3%	2.9% (10.8%)	12.2%	5.3%	4.1%	5.7%

Table 4.1.2-i – Increase in "per time-step error" when simulating validation data

The rather high error increase in validation of the Winston cell might be explained by slight ageing influence, since the test dates of the initial data and the validation were more than 6 months apart.

Validation for the ageing-experimental results was not possible during the current works, since it would require cells aged at additional load points, which were not available in the current experiment. Also cells which validate the damage-accumulation thesis were not added to the design in the described experiment. Cells running purely on driving cycles would be of great interest, because all of these cells would integrate load accumulation and realistic ageing into the same profile. All of these shortcomings are addressed in the current works of the author.

Cell-to-cell variation proofed to be a critical point during a new cell's validation and it was shown in Figure 3.3.3-d that it is quite pronounced in aged cells as well. So handling of cell to cell variation was added to the model in the applications section, but the values are only rough estimates from the validation-data calculation.

4.1.2.2 Applications

The range of targeted applications for the model comprises those, which require fast calculation of many cells (or elements) in parallel and such were full-fledged testing of cells is not possible but would be required for using a simple empiric model, such as an equivalent circuit model, for aged cells. The presented model is mechanistically deduced, but still with empiric parameters, so it represents a certain level of confidentiality when extrapolating. Still

it is recommended to stay close to the tested ranges. Within the test range, interpolation is supported.

3D-model integration:

The integration of voltage response models into 3D calculation of cells requires fast calculating models, since every element of a 3D mesh is an own elementary cell. These calculations can have many questions as target, like thermal integration of cells into packs, development of procedures for short circuits or thermal runaways or quite simply cell geometry development.

The presented model can be parameterized on very simple cells to act as a model for the 3D calculation. Such basic cells are for example the GAIA pouch-type cells. When trying to use wound cells for parameterization and later simulate on those parameter sets, it is wise only to take parameter sets, which have low R_S, since this parameter is responsible for the distribution of effects in large cells.

Coupled board net simulation:

The integration of the battery model into a vehicle or board-net model is a main target application of the presented model. Board-net simulation requires a rather accurate model to reliably predict driving performance and stability of operation of auxiliaries during hybrid operations. That is why a mechanistically deduced model is preferred over empiric model with limited dynamics.

Coupling the model into a fast vehicle simulation with a parameter database of different cells, or using generic average parameters for the identified cell types, can lead to a vastly improved experience when trying to conceive hybridized or electrical vehicles. The first application of the short-term model was a coupling to AVL Cruise 2010 for the demonstration of the vehicle development of the AVL EVARE range-extended vehicle. [Ellinger11]

Packs of cells are simulated by parallel simulation of the total number of serial cells in the pack. The current is divided by the number of parallel cells in the pack configuration and applied to one cell. The pack voltage is equal to the sum of the cell voltages received from simulation.

Pack simulation for BMS:

During validation of the short-term model the cell-to-cell variation of lithium-ion cells was more closely examined. It was found that a single type of cells can be represented by a single parameter set and a standard deviation for the parameter set. This standard deviation represents the variation of every single parameter for this cell type. This means when simulating a batch of similar cells, one can generate parameter sets by applying a variation to the base parameter set. This enhances the reproduction quality of pack simulations, when only a few cells where measured in advance. This procedure will be shown in 4.2.1. These simulations also provide a very good training base or virtual validation base for a battery management system.

4.2 Model applications to an automotive load profile

In this chapter some applications of the model to the electrical load profile of an electrical car driving the Laßnitzhöhe cycle are presented.

In the first part the driving profile is calculated for a hypothetical pack design using GAIA NCA type cells. The short-term model is used to generate pack voltage responses, then the ageing model is applied to the cycle and some aged pack voltage responses are generated and compared to the new ones.

In the second part, the cell will be simulated in 3D doing the cycle. Only a three electrode stack is simulated and analysed for in-cell gradients of material ageing.

4.2.1 Analysis of ageing distribution for Laßnitzhöhe cycle

The Laßnitzhöhe cycle is a round trip starting out at the AVL main building in Graz, driving through the city and up the Ries, then following the hill stretch called Laßnitzhöhe to Gleisdorf. There, a turn to the south is made entering the highway to return to Graz and the starting point in the city. In Figure 4.2.1-a the aerial view is presented as screenshot from Google maps.

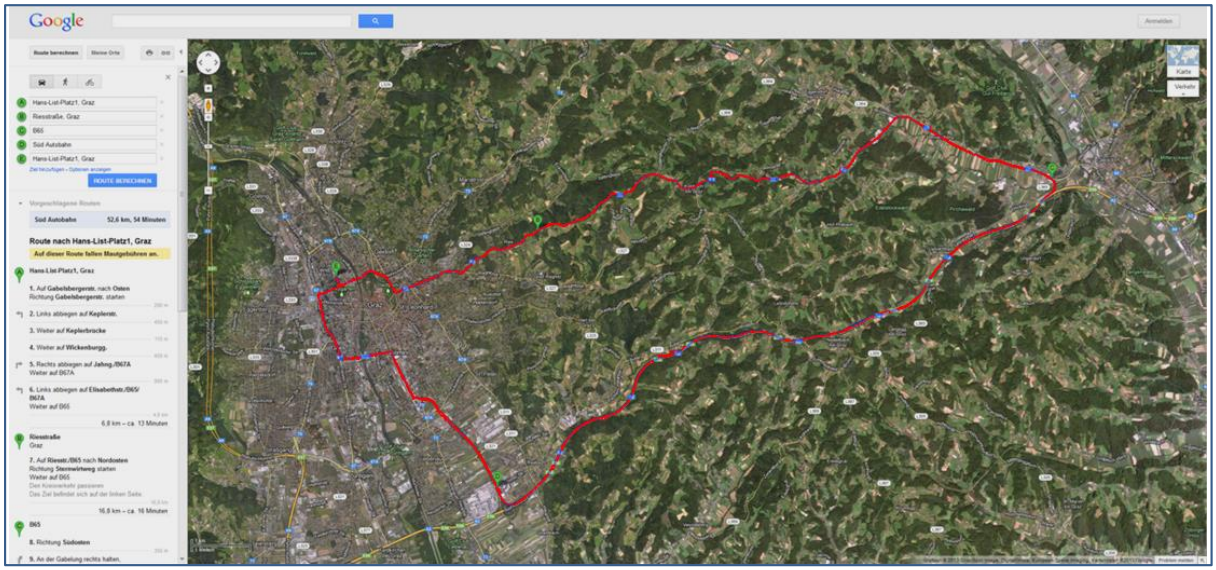

Figure 4.2.1-a – Map of the Laßnitzhöhe cycle. The round trip is done clockwise starting from the green mark in the left upper corner. The northern route part is hill driving on country roads, the southern leg is highway. First and last quarter (time based) are city driving. Picture by google maps [www.maps.google.com].

The battery pack design for this simulation should be a 450 Volt nominal design (so 120 cells in series) and a minimum of 20 kWh. So taking cell sizes of around 25 Ah, 2 cells in parallel will be needed. For this demonstration the cells shall have the same parameters as were

identified for the GAIA NCA pouch cells. One might imagine square pouch cells of 15 cm side length and 50 stacked electrodes.

The presented current profile comes from a simulation with a vehicle model of similar design. The useable SoC range of the cells in the pack shall start at 90% SoC and end at 25% SoC. In Figure 4.2.1-b the current and SoC profile for a single cell is shown. The first section of the profile is the city driving, then mounting the hill requires high discharge currents. Driving along on the sloped down country road the recuperation can help to stay constant in SoC, which drops again as the highway is entered and the vehicle is accelerated. The highway descends to Graz and the vehicle can again recuperate some energy, which it uses to drive in town finally returning. The difference between country road and highway is remarkable in the higher peak currents due to the higher speed driving.

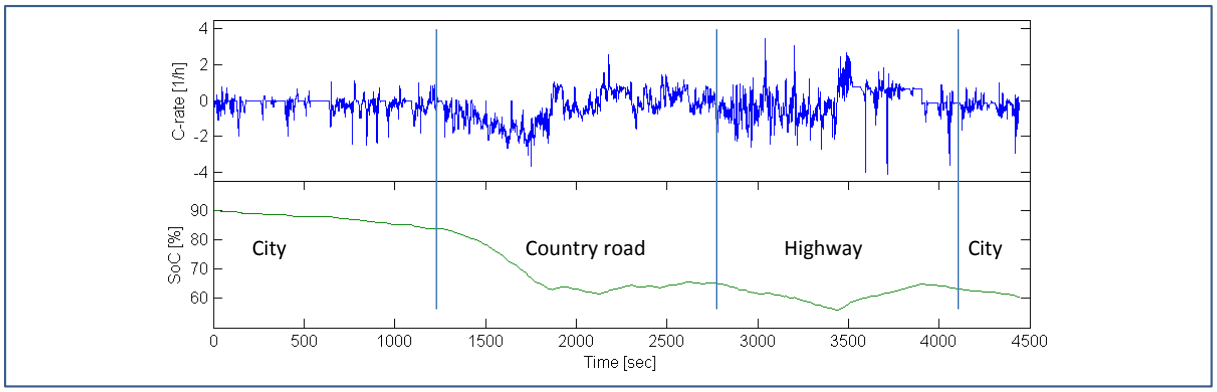

Figure 4.2.1-b – Current (top) and idealized SoC (bottom) profile for the Laßnitzhöhe load profile

For creating the parameter sets for the 240 cells in the battery pack, the parameter set of the GAIA NCA cells is copied 240 times and every parameter is normally distributed, randomly deviated with a standard deviation of 2.5% around its identified value. This random deviation simulates cell-to-cell variations effectively [Dubarry09A].

Figure 4.2.1-c – Total pack voltage (top) and single cell voltage, with maximum and minimum range (bottom), for the Laßnitzhöhe load profile

The total pack voltage response and the average voltage response, with its maximum and minimum variations, are plotted in Figure 4.2.1-c. The distribution of the parameters over the cells, as used for the pack calculation, is shown in Figure 4.2.1-d for the two parameters cell capacity and reaction-term resistance (R_{BV}).

The average cell has 25.5 Ah, the smallest capacity considered for the pack calculation was 24.3 Ah (since nominal capacity was taken to be 25 Ah).

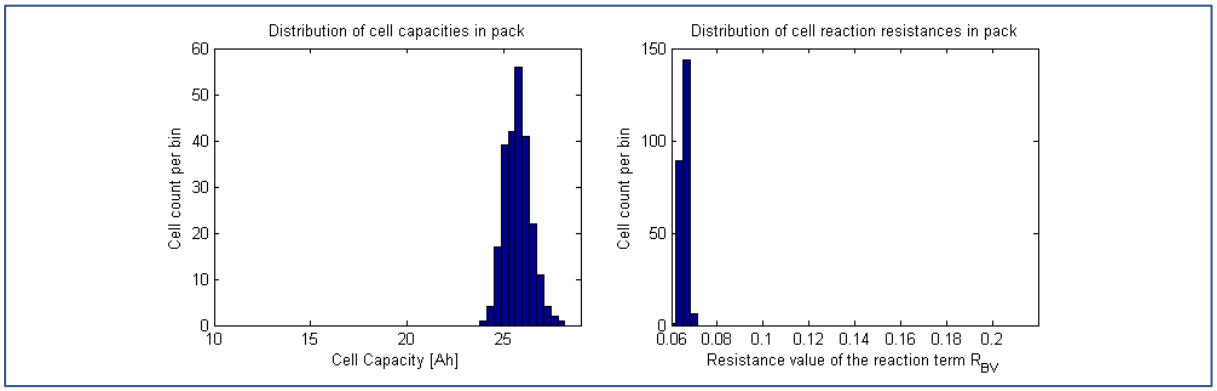

Figure 4.2.1-d – Parameter distributions of new cells after statistical deviation for two exemplary parameters

The calculation time for the voltage response of the 240 cells was 25.7 seconds on a single core 2.4 GHz CPU, so more than 180x faster than real time.

The next step in analysis of the load profile is to derive the rainfow matrices for the cycle and calendar load of the use case. The assumption is one round trip per day with the given load profile. The corresponding cyclic rainflow matrix is shown in Figure 4.2.1-e on the left. For the calendar life assessment, not only the time and SoC times of the profile but also of the storage (parking) time in between is taking into account. The assumption made is that the cell is stored between 80 and 90% SoC and is cooling down to environmental temperature after use. So the climatic temperature profile for Graz for one year is added for the rest times [Muehr07].

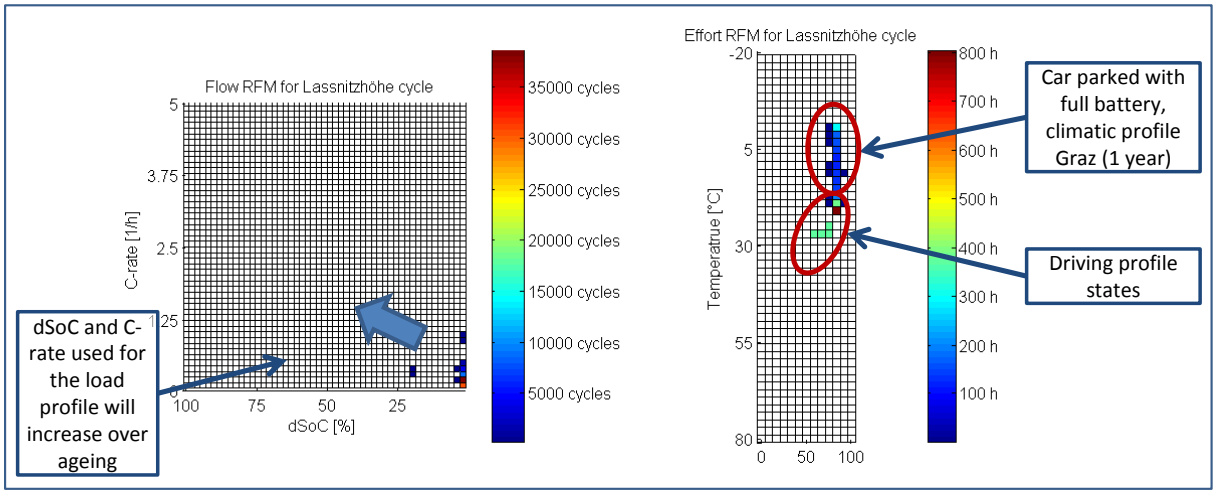

Figure 4.2.1-e – Rainflow matrices for the Laßnitzhöhe cycle once a day for 1 year

Since the NCA cells were in test for about 1 year at the maximum (storage), the ageing model is parameterized for this range. **Cells going into a real vehicle would have much longer (>10x) calendar durability than the experimental cells used for ageing influence testing.** So the simulation in this chapter will only cover one year of ageing, to stay within the model range.

The aged parameter sets for the NCA cells are calculated based on the cell individual loads as displayed in Figure 4.2.1-e. The ageing load is slightly different for the cells, because its initial capacity is different, c-rate and dSoC distributions will be different. Also, if resistance is different, the temperature profile changes. Therefore the aged parameter sets of the 240 cells have a higher deviation than the new cells' parameter sets did. The found aged parameter deviations are in excess of 10%, which is shown in Figure 4.2.1-f. Capacity of cells has dropped to an average of 17 Ah (~70% of initial capacity) and resistance rise for the reaction term is ~2.3x. This is in line with the expectations for the small pouch cells and represents a rather extreme ageing, which would well past the end of life for this pack.

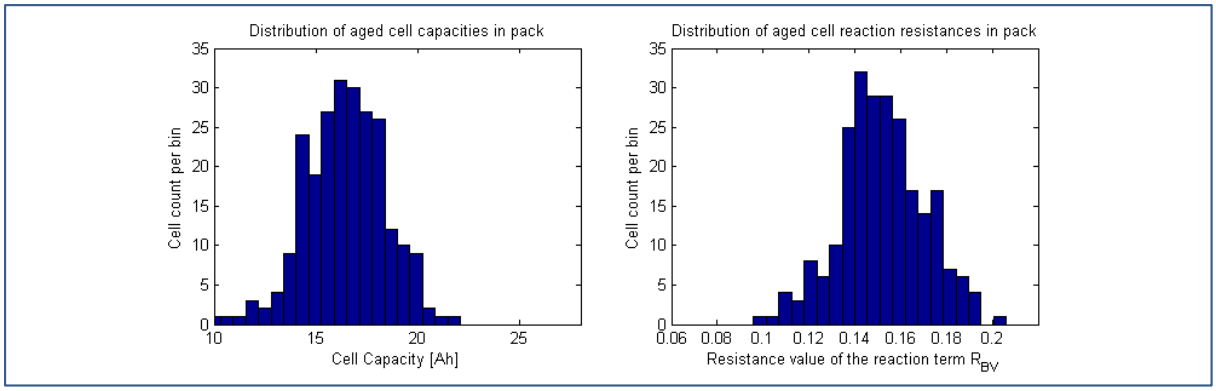

Figure 4.2.1-f – Parameter distributions of cells after the ageing model has been applied. Display for two exemplary parameters.

Due to the ageing, the total pack voltage diminishes, but is still beyond 400 V. Due to the deviation in parameters the total voltage response for the aged battery pack has larger range, as can be seen in Figure 4.2.1-g. The simulation starts with a perfectly balanced pack, so the cell SoC level is at 90% for each cell (having a constant OCV over ageing also all cell voltages are equal). During the driving, some of the cells approach their lower operational voltage limit, due to performance loss. This fact can be handled differently within the BMS, either as dynamic pulse overpotential, which is negligible but requires a model based BMS, or as cell voltage reaching the capacity limit and therefore limiting current and range, as done in simple BMS implementations.

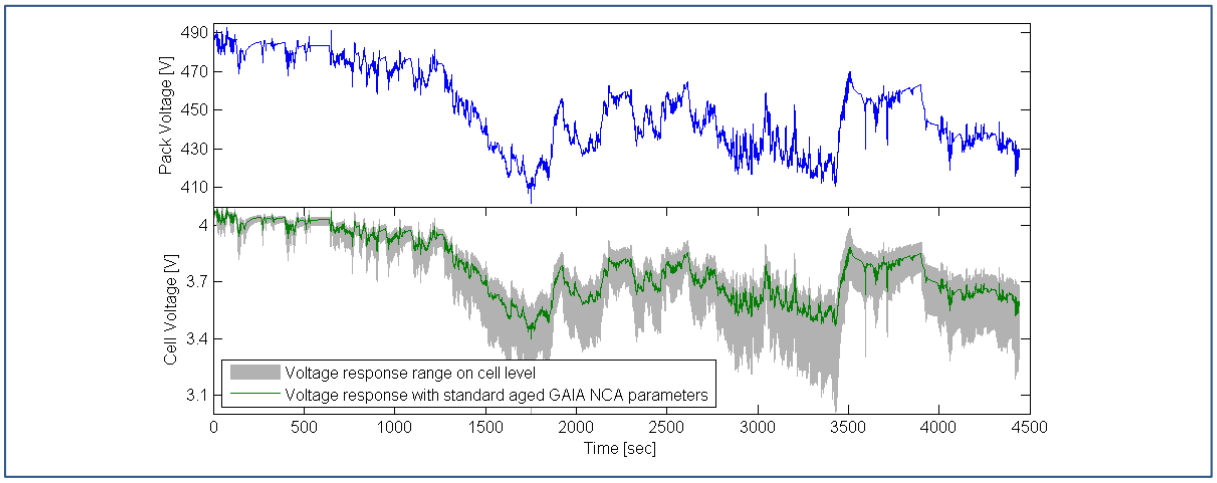

Figure 4.2.1-g – Total pack voltage (top) and single cell voltage of aged cells after one years Laßnitzhöhe load profile once a day.

A detail of the single cells' voltages is displayed in Figure 4.2.1-h. It is interesting to see the differences in the time constants as the relaxation of cell 1 brings the voltage of this cell from being third lowest to top although the cell has a lower SoC in this time window than cell 143 (red). This cell to cell variation is a good training exercise for a battery management system (BMS) trying to calculate a pack SoC from a simple RC model.

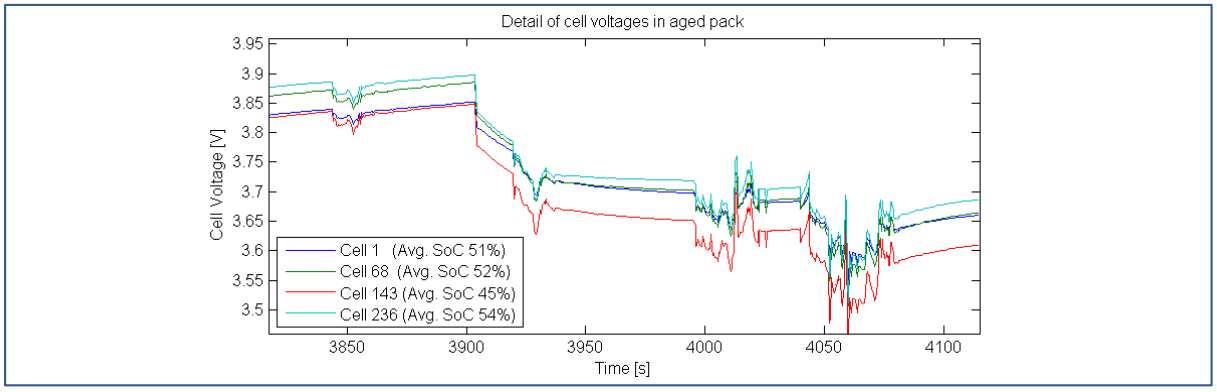

Figure 4.2.1-h – Detail of cell voltages of aged cells after one year Laßnitzhöhe load profile once a day.

In the end of the load profile the cells need charging and balancing, since they do have very different SoC at the end of the profile (see Figure 4.2.1-i left). Also their temperatures are different, but only by a small amount, because it was assumed that sufficient cooling is provided at a constant inlet temperature of 25°C.

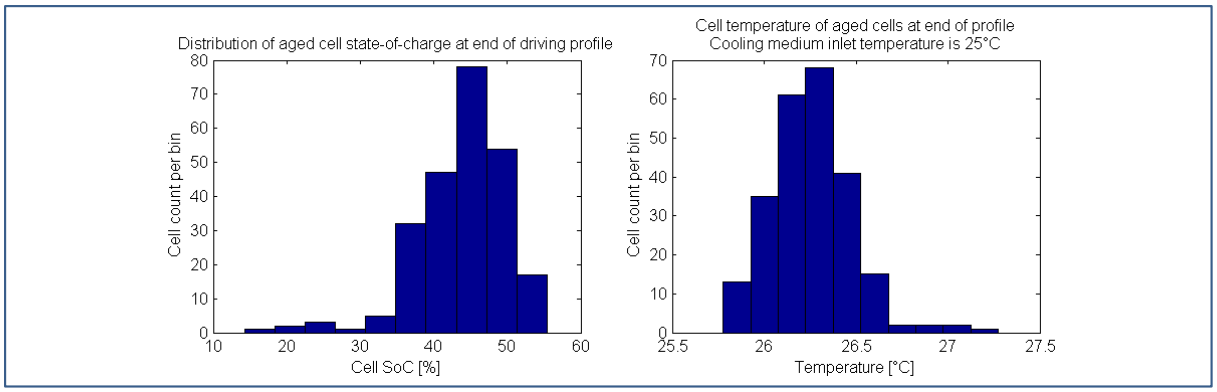

Figure 4.2.1-i – Distribution of SoC and cell temperature at the end of the load profile with aged cells.

The cooling power needed to keep the cells around 25°C is calculated by the short-term model as the overpotential of the reaction, the liquid and the solid term times the current (2.1.2-24). This heat production rate is plotted in the top graph of Figure 4.2.1-j for the new pack (blue) and the aged pack (green). There is approximately a factor of three increase in heat production in the aged pack. So the cooling system in the vehicle has to deliver a three times higher amount of cooling power at the same temperature levels when in aged state. Overall thermal efficiency is about 0.97 for new cells and 0.92 for the aged cells, since the cycle consumes about 6.5 kWh of energy electrically.

In the lower graph the available pack power is plotted. This figure gives the vehicle engine controller the maximum power that is retrievable from the battery pack in the next 5 seconds. The pack is virtually limited to 130 kW, since the maximum component current is limited to 400A. This limit is cost induced, since inverters and current bus bars have the maximum current as main cost driver.

The aged pack is not able to deliver maximum current in every time-step during the driving profile. But even in aged state, the deliverable power is larger than what is in average needed for vehicle operation. So a reduction in maximum available acceleration would be imposed, but the user will in most cases take no notice of it.

This graph is built out of a parallel simulation of each cell in the load point current and 3 higher currents. Then for each time-step, the current at which the lower operational boundary is crossed is calculated and the minimal current of all cell pairs determines the maximum pack current in this time-step. The maximum available output power for this time-step is then calculated a intermediate time-step.

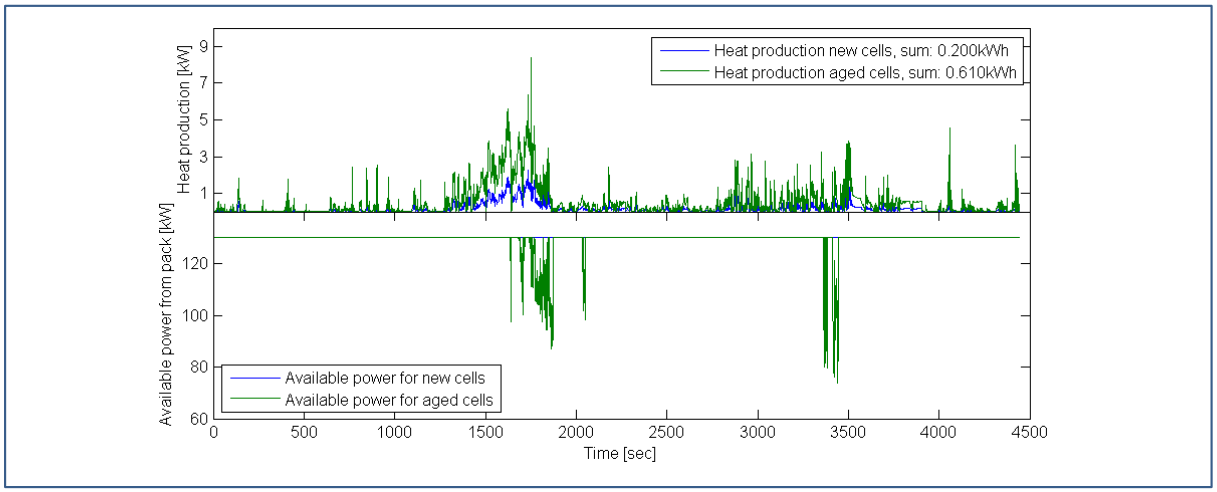

Figure 4.2.1-j – Top: Heat production comparison of new and aged pack. Bottom: Available power from pack, before one cell reaches lower limit of operating range. Upper limit is set to 130kW because of a maximum component current of 400A.

At the end of this year's usage the pack would have slightly less than the often cited 80% of remaining capacity, so it would be considered still functional. But the heat production and the ability to deliver peak power to the vehicle are significantly altered. Driving the vehicle with the initial power profile would therefore result in violations of the operational limits of the cells. Significant power reductions and cooling power increases would have to be dealt with by the vehicle controller and thermal conditioning system. These facts have to be taken care for, while designing the vehicle. With the ability of the presented model to simulate the behaviour of the pack at the aged states, this engineering is facilitated.

4.2.2 Cell ageing computed in 3D

Disclaimer: The 3D model shown in this chapter is based on the presented model but was not implemented by the author himself, but by people in the working group at the Virtual Vehicle [Koplenig11, Koplenig12]. The simulation model and use case was provided by the author for being presented as application example in this work. Another publication of this cooperation was written by Renhart [Renhart11].

The load profile Laßnitzhöhe cycle was applied to the same NCA cell used for the pack analysis in the last chapter. The distribution of variables and states over the electrode area is displayed in a single time step for reasons of brevity and limited 3D or video capability of paper. The displayed time step is following after a section of high-current load, so it exhibits well visible gradients even over the simple and small cell design of the experimental pouch cells [Ghosh09]. In Figure 4.2.2-a the time step, at which the cell's states and variables are displayed, is marked as a red line in the voltage profile known from pack analysis.

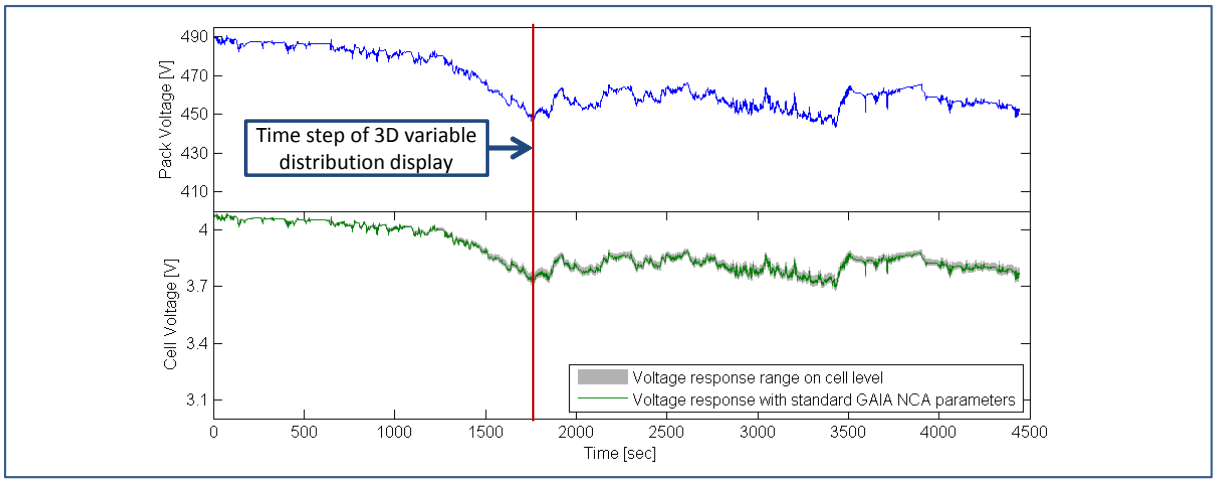

Figure 4.2.2-a – Time step of load profile used for depiction of 3D distributions of variables and states

The coupling of ANSYS for 3D calculation and MATLAB is realized via a text file-based exchange. The solver in ANSYS needs 3-4 iterations of the battery model per time step. In each time step the model value and its derivations are calculated for an inverse relationship, current as function of voltage, additionally. So the total calculation time per step is 20 seconds for 5202 battery elements. A total calculation time of 14 hours on a dual core processor (2.5GHz) system is needed to get to the step in which the following figures are shown.

In Figure 4.2.2-b the potential distribution in the three current collector foils is shown. The cell is stacked cathode – anode – cathode. So the colour legend was split in two parts for the respective electrodes. One can see that the gradient is low in the active material coated areas, whereas in the current-collector tabs, there is a higher gradient (closer sequence of coloured bands).

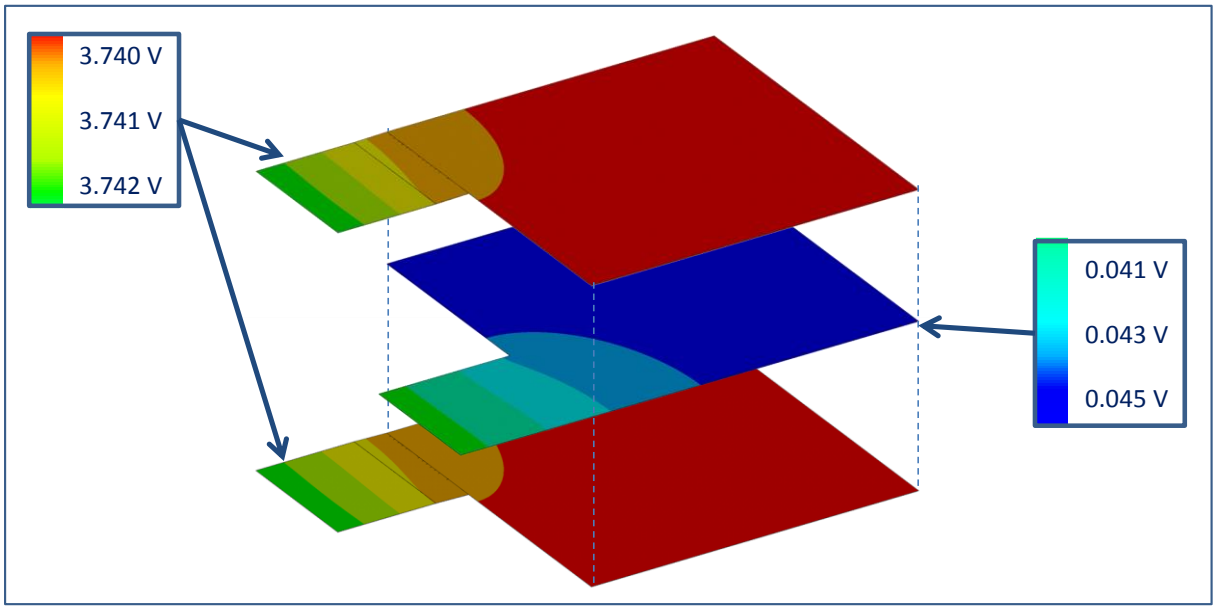

Figure 4.2.2-b –Cell voltage distribution over electrode calculated in ANSYS coupled with the short-term battery model

In the following Figure 4.2.2-c the temperature (left) and the SoC (right) of the cell are shown. In the temperature distribution it is notable that the warmest areas are the lower end of the cell, opposite of the current collectors, because the cell is packaged in pouch foil (low heat conductance) and the current collector tabs stick out of this package and have a very good thermal conductance and act as heat sinks. Overall the temperature increase is rather low, since the cell is small and has a large surface. More interesting is the SoC distribution. Since the cell was discharged heavily in the 500 seconds preceding the time step shown and is back to slight charging regime for the last 20 seconds, the SoC is highest at the border of the cathode current collectors and lowest around the anode current collectors.

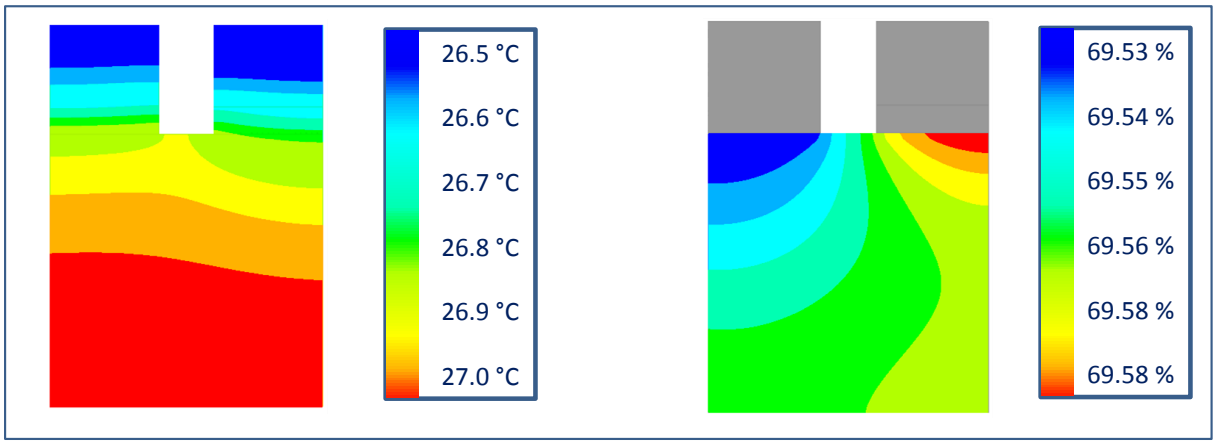

Figure 4.2.2-c –Cell temperature (left) and SoC (right) distribution over electrode calculated in ANSYS coupled with the short-term battery model

The explanation of the overlay of a “historic”, larger cell gradient, due to discharging, with a smaller, newer one, due to charging, is supported by Figure 4.2.2-d too. In this figure the

value for the LPF_2 is shown. This LPF is in the liquid term of the model with a reaction time of about 33 seconds for NCA. It decreases the filter C locally around the cathode current collector only, due to the release of the strong discharging regime. The LPF_2 is the fastest of the low-pass filters.

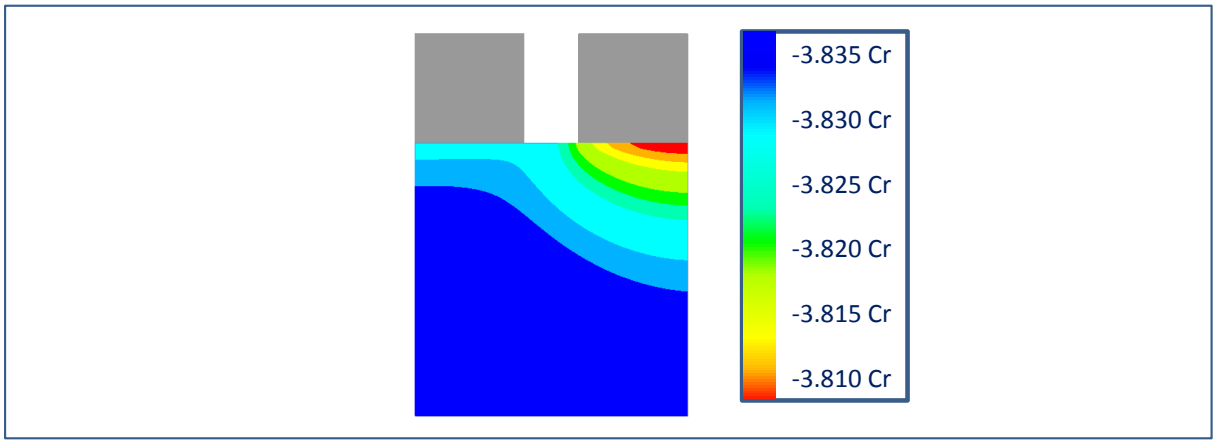

Figure 4.2.2-d – Short-term model liquid low-pass filter value (LPF_2) distribution over electrode calculated in ANSYS coupled with the short-term battery model

In analogy to the pack ageing analysis the single elements' load, instead of the cells in the pack, is put into RFMs for the ageing calculation. All four ageing relevant variables have distributions over the electrode surface, so the cell ages unevenly. Around the current collector tabs, the ageing is much more pronounced than in the lower parts of the cells.

5 Conclusion

An integral short-term and ageing behavioural model for different kinds of intercalation type lithium-ion cells was developed. From the mechanistic deduction of the short-term model and the ageing influences to the integrated and fast implementation the whole process was shown in this work and some application examples were given as proof of concept. The developed model combines know-how from four main areas of expertise needed for the work, chemistry as base for the mechanisms and processes, physics as base for the modelling and derivation methods of first-principles models, mathematics as base for the error calculation and fitting procedures and informatics for the fast implementation and easy handling. It has shown to fulfil the needs of the engineer in charge of designing applications powered by lithium-ion cells, since it can be readily applied to a large number of cells in parallel and the ageing of the cells can be calculated with all data on board of the model. The only downside is the need for extensive parameterization by an experiment, as it has not yet proven that the parameters age in very similar ways for different chemistries.

There are four scientific advances proposed in the work:

1. The mean-value based calculation of an OCV based on the dynamic state of diffusion within the cell. This feature is the key for the model to being able to simulate very different current rates with the same set of parameters, without resorting to the large state variable numbers of the discretization of differential equations in electrochemical models.
2. The error-calculation method incorporating the first and second derivative of the measured and simulated cell voltages as well as a selection of time steps. This error calculation greatly increases the speed and fitting balance between the different parameters.
3. The statistic method of design-of-experiment for large-scale experiments was applied to the question of the ageing-influence dependence of lithium-ion cells. This method allows the test of multiple influence factors with multiple factor settings each in an affordable way, time- and moneywise. The results from this experiments show different dependencies of single factor and of interactions for the two chemistries under test, which are reflected in the differing parameters of the ageing models for the two chemistries.
4. The method of 2-dimensional rainflow analysis in combination with a linear damage accumulation has been used to model the parameter changes of the short-term model over the ageing process.

Some topics, especially on the ageing strength of the cells, are sadly not fully emerged into the light, since the cells used for the experiment were hand made. Such cells always have larger cell-to-cell variances than series-produced cells. Additionally the form factor of a small electrode in a large pouch cell was not helpful in overall lifetime, since mechanic fixation of the components was poor. Also the separation of ageing effects, as identified in the first sections of the work, was not as successful as it was awaited to be due to this blur in ageing

data. Future works of the author will enhance the cell-to-cell variation in the ageing experiment and therefore tighter bounds can be set during ageing modelling.

Another point of future amelioration will be the linear-damage accumulation formula used for all the parameters. In this work it is presented with a variation on the parameter side only, but different accumulation methods, based on mechanistic arguments are awaited to enhance the ageing model greatly.

Finally the author hopes that the model applications shown in the last section of the work are able to demonstrate the help this model brings to designing and engineering vehicles, supporting electrical mobility and enhancing our environment.

6 Abbreviations and Variables

∂B	*change in magnetic flux density*
∂D	*change in electric flux density*
∂N	*change in number of atoms (molecules)*
∂S	*change in entropy*
∂U	*change in inner energy [J/s]*
∂V	*change in Volume*
A	*Ampere*
A	*variable for a chemical species*
AIC	*Akaike information criterion*
a_{xx}	*parameter of ageing model*
B	*variable for a chemical species*
BMS	*battery management system*
BoL	*beginning of cell life*
c	*concentration of a species [mol/L]*
C	*cell capacity*
CD	*capacity decrease*
Cr	*C-rate (see 2.1.2.2)*
CV	*constant voltage*
D	*diffusion constant*
D	*Damage value*
DE	*differential evolution algorithm for optimization*
DEC	*diethyl carbonate*
DMC	*dimethyl carbonate*
DoE	*design-of-experiment*
dSoC	*delta-state-of-charge*
dSoC_D	*dynamic change in SoC for dynamic OCV interpolation*
dt	*time increment*
E	*energetic potential [(V*mol)/L]*
e^-	*electron*
EC	*ethylene carbonate*
ECM	*electrochemical model*

EoL	*end of its life*
EoLc	*end-of-life criterion*
F	*Faraday's constant: F = 9.64853399 x 10^4 [C/mol]*
FMEA	*Failure Mode & Effects Analysis*
G	*Gibbs free energy*
GABC	*Gaussian artificial bee colony algorithm for optimization*
H	*magnetic field strength*
hcOCV	*half-cell open circuit voltage*
i	*surface area specific reaction current [A/m²]*
I	*current rate*
i_0	*assumed equilibrium reaction current [A/m²]*
Index L	*liquid domain*
Index S	*solid domain*
j_{BV}	*Butler-Volmer reaction current [A/m²]*
kW	*kilo-Watt [1000 W]*
k_{xx}	*parameter of empiric model*
LFP	*Lithium-Iron-Phosphate (cathode material)*
LiPF6	*lithium - hexafluorophosphate (lithium salt)*
LPF	*low pass filter*
LTO	*lithium-titanate-oxid*
mA	*milli-Ampere [0.001 A]*
mV	*milli-Volt [0.001 V]*
NCA	*lithium nickel cobalt aluminum oxide (cathode material)*
nom	*nominal value*
n_x	*number of current cycles*
N_x	*number of possible cycles before failure*
OCV	*open circuit voltage [V]*
p	*pressure*
PC	*propylene carbonate*
PDE	*partial differential equation*
P_{heat}	*heat source term [W]*
PP	*polypropylene*
p_x	*parameter of statistical ageing model*

QoB	*quality-of-battery*
R	*gas constant: R = 8.3144621 [J/(K*mol)]*
R	*resistance*
RFM	*rain flow matrix (histogram)*
RI	*resistance increase*
RSS	*residual sum of squares*
RTP	*reference test procedure*
S	*Second*
SEI	*solid electrolyte interphase*
SEM	*Scanning electron microscope*
SNC	*maximum life curves in damage accumulation*
SoC	*state-of-charge*
SoH	*state-of-health*
solv.	*solvent (molecules)*
S_x	*a stress factor (temperature, C-rate,…)*
t	*(at) a point in time*
T	*temperature [°K or °C] degrees Kelvin or Celsius where noted.*
tCal	*hour histogram of average mode counting*
t_{CD}	*time until a certain capacity loss is realized*
t_{II}	*time until a certain impedance increase is realized*
Tref	*reference temperature [K]*
U	*cell voltage [V]*
U_{ocv}	*open circuit voltage [V]*
V	*Volt*
VS	*OCV shift*
W	*Watt*
x	*modelling coordinate*
xCyc	*cycle histogram of rainflow counting*
z	*count of charges of the ion [-]*
Z	*impedance*
ZD	*impedance increase*
γ	*chemical activity of a species*
η_C	*Coulombic efficiency of a cell*

κ	*ionic (electrical) conductivity [S/m]*
τ	*time constant*
φ	*domain polarisation [(V*mol)/L]*
Φ	*potential field strength*

7 References

A

Abraham02 Abraham, D., Twesten, R., Balasubramanian, M., Petrov, I., McBreen, J., & Amine, K. (2002). Surface changes on LiNi0.8Co0.2O2 particles during testing of high-power lithium-ion cells. *Electrochemistry Communications, 4*(8), 620-625.

Abraham05 Abraham, D., Reynolds, E., Sammann, E., Jansen, A., & Dees, D. (2005). Aging characteristics of high-power lithium-ion cells with LiNi0.8Co0.15Al0.05O2 and Li4/3Ti5/3O4 electrodes. *Electrochimica Acta, 51*(3), 502-510.

Abraham08 Abraham, D., Furczon, M., Kang, S.-H., Dees, D., & Jansen, A. (2008). Effect of electrolyte composition on initial cycling and impedance characteristics of lithium-ion cells. *Journal of Power Sources, 180*(1), 612-620.

Abraham08B Abraham, D. P., Heaton, J. R., Kang, S.-H., Dees, D. W., & Jansen, A. N. (2008). Investigating the Low-Temperature Impedance Increase of Lithium-Ion Cells. *Journal of The Electrochemical Society, 155*(1), A41-A47.

Ahn11 Ahn, D., & Xiao, X. (2011). Extended lithium titanate cycling potential window with near zero capacity loss. *Electrochemistry Communications , 13*(8), 796-799.

Akaike74 Akaike, H. (1974). A new look at the statistical model identification. *Automatic Control, IEEE Transactions on, 19*(6), 716-723.

Allen08 Allen, J., Jow, T., & Wolfenstine, J. (2008). Analysis of the FePO4 to LiFePO4 phase transition. *Journal of Solid State Electrochemistry, 12*, 1031-1033.

Andre10 Andre, D., Meiler, M., Steiner, K., Walz, H., Soczka-Guth, T., & Sauer, D. (2010). Characterization of high-power lithium-ion batteries by electrochemical impedance spectroscopy. II: Modelling. *Journal of Power Sources, In Press, Corrected Proof*, - .

Andre11 Andre, D., Meiler, M., Steiner, K., Wimmer, C., Soczka-Guth, T., & Sauer, D. (2011). Characterization of high-power lithium-ion batteries by electrochemical impedance spectroscopy. I. Experimental investigation. *Journal of Power Sources, In Press, Corrected Proof*, - .

Aoshima01 Aoshima, T., Okahara, K., Kiyohara, C., & Shizuka, K. (2001). Mechanisms of manganese spinels dissolution and capacity fade at high temperature. *Journal of Power Sources, 97 (Proceedings of the 10th International Meeting on Lithium Batteries)*, 377-380.

Arora98 Arora, P., White, R. E., & Doyle, M. (1998). Capacity Fade Mechanisms and Side Reactions in Lithium-Ion Batteries. *Journal of The Electrochemical Society, 145*(10), 3647-3667.

Arrebola06 Arrebola, J., Caballero, A., Cruz, M., Hernán, L., Morales, J., & Castellón, E. (2006). Crystallinity Control of a Nanostructured LiNi0.5Mn1.5O4 Spinel via Polymer-Assisted Synthesis: A Method for Improving Its Rate Capability and Performance in 5V Lithium Batteries. *Advanced Functional Materials, 16*(14), 1904-1912.

Aurbach99 Aurbach, D., Weissman, I., Zaban, A., & Dan, P. (1999). On the role of water contamination in rechargeable Li batteries. *Electrochimica Acta, 45*(7), 1135-1140.

B

Bard01 Bard, A. J., & Faulkner, L. R. (2001). *Electrochemical Methods - Fundamentals and Applications* (2nd Ausg.). (D. Harris, Hrsg.) JOHN WILEY \& SONS, INC.

Belt11 Belt, J., Utgikar, V., & Bloom, I. (2011). Calendar and PHEV cycle life aging of high-energy, lithium-ion cells containing blended spinel and layered-oxide cathodes. *Journal of Power Sources, 196*(23), 10213-10221.

Beltran12 Beltran, H., Swierczynski, M., Aparicio, N., Belenguer, E., Teodorescu, R., & Rodriguez, P. (2012). Lithium ion batteries ageing analysis when used in a PV power plant. *2012 IEEE International Symposium on Industrial Electronics (ISIE)*, 1604-1609.

Benasciutti04 Benasciutti, D., & Tovo, R. (2004). *Rainflow Cycle Distribution and Fatigue Damage in Gaussian Random Loadings.* Tech-Report, Dipartimento di Ingegneria dell'Università degli Studi di Ferrara.

Benedek08 Benedek, R., Thackeray, M. M., & van de Walle, A. (2008). Free Energy for Protonation Reaction in Lithium-Ion Battery Cathode Materials. *Chemistry of Materials, 20*(17), 5485-5490.

Bernardi85 Bernardi, D., Pawlikowski, E., & Newman, J. (1985). A General Energy Balance for Battery Systems. *Journal of The Electrochemical Society, 132*(1), 5-12.

Bernardi11 Bernardi, D. M., & Go, J.-Y. (2011). Analysis of pulse and relaxation behavior in lithium-ion batteries. *Journal of Power Sources, 196*(1), 412-427.

Bessler07 Bessler, W. G. (2007). Rapid Impedance Modeling via Potential Step and Current Relaxation Simulations. *Journal of The Electrochemical Society, 154*(11), B1186-B1191.

Bhattacharya12 Bhattacharya, S., & Alpas, A. T. (2012). Micromechanisms of solid electrolyte interphase formation on electrochemically cycled graphite electrodes in lithium-ion cells. *Carbon, 50*(15), 5359-5371.

Bisquert02 Bisquert, J., & Vikhrenko, V. S. (2002). Analysis of the kinetics of ion intercalation. Two state model describing the coupling of solid state ion diffusion and ion binding processes. *Electrochimica Acta, 47*(24), 3977-3988.

Bloom01 Bloom, I., Cole, B. W., Sohn, J. J., Jones, S. A., Polzin, E. G., Battaglia, V. S., et al. (2001). An accelerated calendar and cycle life study of Li-ion cells. *Journal of Power Sources, 101*(2), 238-247.

Boller69 Boller, K. (1969). Fatigue fundamentals for composite materials. *ASTM STP, 460*, 217-235.

Brest06 Brest, J., Greiner, S., Boskovic, B., Mernik, M., & Zumer, V. (2006). Self-Adapting Control Parameters in Differential Evolution: A Comparative Study on

Numerical Benchmark Problems. *IEEE Transactions on Evolutionary Computation, 10*(6), 646-657.

Broussely01 Broussely, M., Herreyre, S., Biensan, P., Kasztejna, P., Nechev, K., & Staniewicz, R. (2001). Aging mechanism in Li ion cells and calendar life predictions. *Journal of Power Sources, 97-98*, 13-21.

Broussely05 Broussely, M., Biensan, P., Bonhomme, F., Blanchard, P., Herreyre, S., Nechev, K., et al. (2005). Main aging mechanisms in Li ion batteries. *Journal of Power Sources, 146*(1-2), 90-96.

Buller03 Buller, S. (2003). *Impedance-Based Simulation Models for Energy Storage Devices in Advanced Automotive Power Systems.* Ph.D. Thesis, RWTH Aachen University.

Buller05 Buller, S., Thele, M., Doncker, R. W., & Karden, E. (2005). Impedance-based simulation models of supercapacitors and Li-ion batteries for power electronic applications. *IEEE Transactions on Industry Applications*, *41*, S. 742-747.

Burch09 Burch, D. (2009). *Intercalation Dynamics in Lithium-Ion Batteries.* PhD Thesis, MIT.

C

Chen11 Chen, D., Indris, S., Schulz, M., Gamer, B., & Mönig, R. (2011). In situ scanning electron microscopy on lithium-ion battery electrodes using an ionic liquid. *Journal of Power Sources, 196*(15), 6382-6387.

Cheng08 Cheng, F., Tao, Z., Liang, J., & Chen, J. (2008). Template-Directed Materials for Rechargeable Lithium-Ion Batteries†. *Chemistry of Materials, 20*(3), 667-681.

Cherkashinin12 Cherkashinin, G., Nikolowski, K., Ehrenberg, H., Jacke, S., Dimesso, L., & Jaegermann, W. (2012). The stability of the SEI layer, surface composition and the oxidation state of transition metals at the electrolyte-cathode interface impacted by the electrochemical cycling: X-ray photoelectron spectroscopy investigation. *Physical Chemistry Chemical Physics, 14*(35), 12321-12331.

Christensen03 Christensen, J., & Newman, J. (2003). Effect of Anode Film Resistance on the Charge/Discharge Capacity of a Lithium-Ion Battery. *Journal of The Electrochemical Society, 150*(11), A1416-A1420.

Christensen04 Christensen, J., & Newman, J. (2004). A Mathematical Model for the Lithium-Ion Negative Electrode Solid Electrolyte Interphase. *Journal of The Electrochemical Society, 151*(11), A1977-A1988.

Christensen05 Christensen, J., & Newman, J. (2005). Cyclable Lithium and Capacity Loss in Li-Ion Cells. *Journal of The Electrochemical Society, 152*(4), A818-A829.

Christensen06 Christensen, J., Srinivasan, V., & Newman, J. (2006). Optimization of Lithium Titanate Electrodes for High-Power Cells. *Journal of The Electrochemical Society, 153*(3), A560-A565.

Colombo05 Colombo, A., & Negro, P. (2005). A damage index of generalised applicability. *Engineering Structures, 27*(8), 1164-1174.

D

Dedryvere08 Dedryvere, R., Maccario, M., Croguennec, L., Le Cras, F., Delmas, C., & Gonbeau, D. (2008). X-Ray Photoelectron Spectroscopy Investigations of Carbon-Coated LixFePO4 Materials. *Chemistry of Materials, 20*(22), 7164-7170.

Dees08 Dees, D., Gunen, E., Abraham, D., Jansen, A., & Prakash, J. (2008). Electrochemical Modeling of Lithium-Ion Positive Electrodes during Hybrid Pulse Power Characterization Tests. *Journal of The Electrochemical Society, 155*(8), A603-A613.

Dodd07 Dodd, J. L. (2007). *Phase composition and dynamical studies of lithium iron phosphate.* Ph.D. Thesis, California Institute of Technology.

DosSantos09 dos Santos Coelho, L., & Alotto, P. (2009). Electromagnetic optimization based on an improved diversity-guided differential evolution approach and adaptive mutation factor. *COMPEL: The International Journal for Computation and Mathematics in Electrical and Electronic Engineering, Vol. 28 Issue 5*, 1112-1120.

DosSantos11 dos Santos Coelho, L., & Alotto, P. (2011). Gaussian Artificial Bee Colony Algorithm Approach Applied to Loney's Solenoid Benchmark Problem. *IEEE Transactions on Magnetics, 47*(5), 1326-1329.

Doyle95 Doyle, C. M. (1995). *Design and simulation of lithium rechargeable batteries.* PhD Thesis, University of California, University of California, Department of Chemical Engineering, Berkeley, California.

Dreyer07 Dreyer, W., Gaberscek, M., & Jamnik, J. (2007). Phase transition and hysteresis in a rechargeable lithium battery. *Preprint of Weierstrass Institute Berlin, -*, 32.

Dreyer11 Dreyer, W., Guhlke, C., & Huth, R. (2011). The behavior of a many-particle electrode in a lithium-ion battery. *Physica D: Nonlinear Phenomena, 240*(12), 1008-1019.

Dreyer12 Dreyer, W., Guhlke, C., & Müller, R. (2012). Overcoming the shortcomings of the Nernst-Planck model. *WIAS Preprint, ISSN 0946 – 8633*.

Drezen07 Drezen, T., Kwon, N.-H., Bowen, P., Teerlinck, I., Isono, M., & Exnar, I. (2007). Effect of particle size on LiMnPO4 cathodes. *Journal of Power Sources, 174*(2), 949-953.

Dubarry09 Dubarry, M., Vuillaume, N., & Liaw, B. Y. (2009). From single cell model to battery pack simulation for Li-ion batteries. *Journal of Power Sources, 186*(2), 500-507.

Dubarry11 Dubarry, M., Liaw, B. Y., Chen, M.-S., Chyan, S.-S., Han, K.-C., Sie, W.-T., et al. (2011). Identifying battery aging mechanisms in large format Li ion cells. *Journal of Power Sources, 196*(7), 3420-3425.

Dubarry11B Dubarry, M., Truchot, C., Liaw, B. Y., Gering, K., Sazhin, S., Jamison, D., et al. (2011). Evaluation of commercial lithium-ion cells based on composite positive electrode for plug-in hybrid electrical vehicle applications. Part II. Degradation mechanism under 2C cycle aging. *Journal of Power Sources, 196*(23), 10336-10343.

Dudézert09 Dudézert, C., Franger, P., Reynier, Y., & Burlet, H. (2009). Application of a mechanical methodology for lithium-ion battery life prediction. Proceedings of *EVS 24, Stavanger, Norway, 1*, 1-11.

E

Dodd07 Ecker, M., Gerschler, J. B., Vogel, J., Käbitz, S., Hust, F., Dechent, P., et al. (2012). Development of a lifetime prediction model for lithium-ion batteries based on extended accelerated aging test data. *Journal of Power Sources, 215*(0), 248-257.

Edström04 Edström, K., Gustafsson, T., & Thomas, J. (2004). The cathode-electrolyte interface in the Li-ion battery. *Electrochimica Acta, 50*(2-3), 397-403.

Ellinger11 Ellinger, R., & Jones, S. (2011). System Simulation Tools for Electrified Vehicles. *Joint EC / EPoSS / ERTRAC Expert Workshop in Berlin.* http://www.green-cars-initiative.eu/workshops/joint-ec-eposs-ertrac-expert-workshop-2011-on-ev-architectures/.

F

Fischnaller11 Fischnaller, M., Lohmann, N., Melbert, J., Lamp, P., & Scharner, S. (2011). Alterungsuntersuchungen und Modellierungen für Li-Ionen Zellen für Hybridfahrzeuge. *VDI-Berichte, 2132*, 103-112.

Fisher08 Fisher, C. A., Hart Prieto, V. M., & Islam, M. S. (2008). Lithium Battery Materials LiMPO4 (M = Mn, Fe, Co, and Ni): Insights into Defect Association, Transport Mechanisms, and Doping Behavior. *Chemistry of Materials, 20*(18), 5907-5915.

Flandrois99 Flandrois, S., & Simon, B. (1999). Carbon materials for lithium-ion rechargeable batteries . *Carbon , 37*(2), 165-180.

G

Gaberscek08 Gaberscek, M., Moskon, J., Erjavec, B., Dominko, R., & Jamnik, J. (2008). The Importance of Interphase Contacts in Li Ion Electrodes: The Meaning of the High-Frequency Impedance Arc. *Electrochemical and Solid-State Letters, 11*(10), A170-A174.

Gardiner10 Gardiner, G. R., & Islam, M. S. (2010). Anti-Site Defects and Ion Migration in the LiFe0.5Mn0.5PO4 Mixed-Metal Cathode Material. *Chemistry of Materials, 22*(3), 1242-1248.

Genet06 Genet, G. (2006). *A statistical approach to multi-input equivalent fatigue loads for the durability of automotive structures.* Ph.D. Thesis, Department of Mathematical Sciences Division of Mathematical Statistics CHALMERS UNIVERSITY OF TECHNOLOGY AND GÖTEBORG UNIVERSITY.

Geoffroy02 Geoffroy, I., Chagnes, A., Carré, B., Lemordant, D., Biensan, P., & Herreyre, S. (2002). Electrolytic characteristics of asymmetric alkyl carbonates solvents for lithium batteries. *Journal of Power Sources, 112*(1), 191-198.

Gering02 Gering, K. L., Sazhin, S. V., Jamison, D. K., Michelbacher, C. J., Liaw, B. Y., Dubarry, M., et al. (2011). Investigation of path dependence in commercial lithium-ion cells chosen for plug-in hybrid vehicle duty cycle protocols. *Journal of Power Sources, 196*(7), 3395-3403.

Ghosh02 Ghosh, D., Maguire, P. D., & Zhu, D. X. (2009). Design and CFD Simulation of a Battery Module for a Hybrid Electric Vehicle Battery Pack. *SAE Technical Paper*(ISSN 0148-7191), 1-1386.

Goodenough10 Goodenough, J. B., & Kim, Y. (2010). Challenges for Rechargeable Li Batteries . *Chemistry of Materials, 22*(3), 587-603.

Gu11 Gu, L., Zhu, C., Li, H., Yu, Y., Li, C., Tsukimoto, S., et al. (2011). Direct Observation of Lithium Staging in Partially Delithiated LiFePO4 at Atomic Resolution. *Journal of the American Chemical Society, 133*(13), 4661-4663.

Guo11 Guo, M., Sikha, G., & White, R. E. (2011). Single-Particle Model for a Lithium-Ion Cell: Thermal Behavior. *Journal of The Electrochemical Society, 158*(2), A122-A132.

H

Hamann98 Hamann, C., & Vielstich, W. (1998). *Elektrochemie.* Wiley-VCH Verlag GmbH.

Harris10 Harris, S. J., Timmons, A., Baker, D. R., & Monroe, C. (2010). Direct in situ measurements of Li transport in Li-ion battery negative electrodes. *Chemical Physics Letters, 485*(4-6), 265-274.

Hartmann08 Hartmann, R. (2008). *An Aging Model for Lithium-Ion Cells.* PhD Thesis, University of Akron.

Haselgruber08 Haselgruber, N. (2008). A Modular Algorithm for Dynamic Design of Large-Scale Experiments. *AUSTRIAN JOURNAL OF STATISTICS, 37*(3), 229-244.

Herb10 Herb, F. (May 2010). *Alterungsmechanismen in Lithium-Ionen-Batterien und PEM-Brennstoffzellen und deren Einfluss auf die Eigenschaften von daraus bestehenden Hybrid-Systemen.* PhD Thesis, Faculty of Natural Sciences of the University of Ulm.

Herstedt04 Herstedt, M., Andersson, A., Rensmo, H., Siegbahn, H., & Edström, K. (2004). Characterisation of the SEI formed on natural graphite in PC-based electrolytes. *Electrochimica Acta, 49*(27), 4939-4947.

Hoang11 Hoang, K., & Johannes, M. (2011). Tailoring Native Defects in LiFePO4: Insights from First-Principles Calculations. *Chemistry of Materials, 11*(23), 3003-3013.

J

Janacek93 Janacek, G., & Swift, L. (1993). *TIME SERIES Forecasting, Simulation, Applications.* (G. Bell, Hrsg.) Ellis Horwood.

Jansen07 Jansen, A. N., Dees, D. W., Abraham, D. P., Amine, K., & Henriksen, G. L. (2007). Low-temperature study of lithium-ion cells using a Li_ySn micro-reference electrode. *Journal of Power Sources, 174*(2), 373-379.

Jin09 Jin, H.-F., Liu, Z., Teng, Y.-M., kui Gao, J., & Zhao, Y. (2009). A comparison study of capacity degradation mechanism of LiFePO4-based lithium ion cells. *Journal of Power Sources, 189*(1), 445-448.

Johannesson99 Johannesson, P. (1999). *Rainflow Analysis of Switching Markov Loads.* Ph.D. Thesis, Lunds Universitet.

Jurczakowski04 Jurczakowski, R., & Lasia, A. (2004). Limitations of the Potential Step Technique to Impedance Measurements Using Discrete Time Fourier Transform. *Analytical Chemistry, 76*(17), 5033-5038.

K

Kang11 Kang, J., Wei, S.-H., Zhu, K., & Kim, Y.-H. (2011). First-Principles Theory of Electrochemical Capacitance of Nanostructured Materials: Dipole-Assisted Subsurface Intercalation of Lithium in Pseudocapacitive TiO2 Anatase Nanosheets. *The Journal of Physical Chemistry C, 115*(11), 4909-4915.

Karaboga07 Karaboga, D., & Basturk, B. (2007). A powerful and efficient algorithm for numerical function optimization: artificial bee colony (ABC) algorithm. *Journal of Global Optimization, 39*(3), 459-471.

Karthikeyan08 Karthikeyan, D. K., Sikha, G., & White, R. E. (2008). Thermodynamic model development for lithium intercalation electrodes. *Journal of Power Sources, 185*(2), 1398-1407.

Kasavajjula08 Kasavajjula, U. S., Wang, C., & Arce, P. E. (2008). Discharge Model for $LiFePO_4$ Accounting for the Solid Solution Range. *Journal of The Electrochemical Society, 155*(11), A866-A874.

Kassem12 Kassem, M., Bernard, J., Revel, R., Pélissier, S., Duclaudd, F., & C., D. (2012). Calendar aging of a graphite/LiFePO4 cell. *Journal of Power Sources, 208*, 296-305.

Kawakami10 Kawakami, N., Iijima, Y., Sakanaka, Y., Fukuhara, M., Ogawa, K., Bando, M., et al. (2010). Development and field experiences of stabilization system using 34MW NAS batteries for a 51MW wind farm. 2371-2376.

Kim07 Kim, G.-H., Pesaran, A., & Spotnitz, R. (2007). A three-dimensional thermal abuse model for lithium-ion cells. *Journal of Power Sources, 170*(2), 476-489.

Kim08 Kim, G.-H., & Smith, K. (2008). Multi-Scale Multi-Dimensional Li-ion Battery Model for Better Design and Management. *PRiME2008, 214th Electrochemical Society Pacific Rim Meeting*, *NREL/PR-540-44350.*

Kim09 Kim, U. S., Shin, C. B., & Kim, C.-S. (2009). Modeling for the scale-up of a lithium-ion polymer battery. *Journal of Power Sources, 189*(1), 841-846.

Kim11 Kim, J., Lee, S., & Cho, B. (2011). Discrimination of Li-ion batteries based on Hamming network using discharging & charging voltage pattern recognition for improved state-of-charge estimation. *Journal of Power Sources, 196*(4), 2227-2240.

Koplenig11 Koplenig, M., & Heubrandtner, T. (Dezember 2011). Integration of an Arbitrary 1D Battery Model into 3D Coupled Electro-Thermal Finite Element Simulations. *Multiphysics, Barcelona.*

Koplenig12 Koplenig, M., Scharrer, M. K., Suhr, B., & Heubrandtner, T. (2012). Optimierung eines 3D elektro-thermischen Batteriemodells. *NAFEMS deutschsprachige Konferenz 2012* (S. 195-198). NAFEMS.

Kramer09 Kramer, D., & Ceder, G. (2009). Tailoring the Morphology of LiCoO2: A First Principles Study. *Chemistry of Materials, 21*(16), 3799-3809.

Kumaresan06 Kumaresan, K., Guo, Q., Ramadass, P., & White, R. E. (2006). Cycle life performance of lithium-ion pouch cells. *Journal of Power Sources, 158*(1), 679-688.

Kurfer12 Kurfer, J., Westermeier, M., Tammer, C., & Reinhart, G. (2012). Production of large-area lithium-ion cells – Preconditioning, cell stacking and quality assurance . *\{CIRP\} Annals - Manufacturing Technology , 61*(1), 1-4.

L

Latz10 Latz, A., & Iliev, J. Z. (2010). *Modeling of species and charge transport in {Li}-Ion Batteries based on nonequilibrium thermodynamics.* Tech.Report., Fraunhofer-Institut für Techno- und Wirtschaftsmathematik ITWM, Kaiserslautern, Germany.

Latz11 Latz, A., & Zausch, J. (2011). Thermodynamic consistent transport theory of Li-ion batteries. *Journal of Power Sources, 196*(6), 3296-3302.

Lee12 Lee, J. L., Chemistruck, A., & Plett, G. L. (2012). Discrete-time realization of transcendental impedance models, with application to modeling spherical solid diffusion. *Journal of Power Sources, 206*(0), 367-377.

Lei05 Lei, J., McLarnon, F., & Kostecki, R. (2005). In situ Raman microscopy of individual $LiNi_{0.8}Co_{0.15}Al_{0.05}O_2$ particles in a Li-ion battery composite cathode. *Journal of Physical Chemistry B, 109*(2), 952-957.

Liaw05 Liaw, B. Y., Jungst, R. G., Nagasubramanian, G., Case, H. L., & Doughty, D. H. (2005). Modeling capacity fade in lithium-ion cells. *Journal of Power Sources, 140*(1), 157-161.

Linden02 Linden, D., & Reddy, T. (2002). *Handbook of batteries* (3rd Ed). McGraw-Hill.

Liu05 Liu, W.-R., Yang, M.-H., Wu, H.-C., Chiao, S. M., & Wu, N.-L. (2005). Enhanced Cycle Life of Si Anode for Li-Ion Batteries by Using Modified Elastomeric Binder. *8*(2), A100-A103.

Liu10 Liu, J., Reeja-Jayan, B., & Manthiram, A. (2010). Conductive Surface Modification with Aluminum of High Capacity Layered $Li[Li_{0.2}Mn_{0.54}Ni_{0.13}Co_{0.13}]O_2$ Cathodes. *The Journal of Physical Chemistry C, 114*(20), 9528-9533.

Liu10B Liu, J., Kunz, M., Chen, K., Tamura, N., & Richardson, T. J. (2010). Visualization of Charge Distribution in a Lithium Battery Electrode. *The Journal of Physical Chemistry Letters, 1*(14), 2120-2123.

M

Markel08 Markel, T., Smith, K., & Pesaran, A. (2008). PHEV Energy Storage Performance/Life/Cost Trade-off Analysis. *8th Advanced Automotive Battery Conference*, *NREL/PR-540-43159.*

Markervich05 Markervich, E., Salitra, G., Levi, M., & Aurbach, D. (2005). Capacity fading of lithiated graphite electrodes studied by a combination of electroanalytical methods, Raman spectroscopy and SEM. *Journal of Power Sources, 146*(1), 146-150.

Marks13 Marks, P. (2013). Not cleared for take-off. *New Scientist , 217*(2901), 22.

Matsuishi68 Matsuishi, M., & Endo, T. (1968). Fatigue of metals subjected to varying stress. *Japan Society of Mechanical Engineers, Fukuoka, Japan*, 37-40.

Miner45 Miner, M., & others. (1945). Cumulative fatigue damage. *J Appl Mech, 67*(12), 159-164.

Montgomery05 Montgomery, D. (2005). *Design and Analysis of Experiments.* John Wiley & Sons.

Moosbauer10 Moosbauer, D. J. (2010). *Elektrochemische Charakterisierung von Elektrolyten und Elektroden für Lithium-Ionen-Batterien.* Ph.D. Thesis, Universität Regensburg.

Mühr07 Mühr, B. (2007). *http://www.klimadiagramme.de/Europa/graz.html.* Tech.Report., http://www.klimadiagramme.de/Europa/graz.html.

Muraliganth10 Muraliganth, T., & Manthiram, A. (2010). Understanding the Shifts in the Redox Potentials of Olivine $LiMyMyPO_4$ (M = Fe, Mn, Co, and Mg) Solid Solution Cathodes. *The Journal of Physical Chemistry C, 114*(36), 15530-15540.

N

Newman93 Newman, J., & Tiedemann, W. (1993). Potential and Current Distribution in Electrochemical Cells. *Journal of The Electrochemical Society, 140*(7), 1961-1968.

Newman03 Newman, J., Thomas, K. E., Hafezi, H., & Wheeler, D. R. (2003). Modeling of lithium-ion batteries. *Journal of Power Sources, 119-121*, 838-843.

Newman04 Newman, J., & Thomas-Alyea, K. E. (2004). *Electrochemical Systems* (3rd Ed.). John Wiley \& Sons, Inc., Hoboken, New Jersey.

Nieslony06 Nieslony, A. (2006). *Rainflow Counting Algorithm.* Tech.Report., Matlab Central.

Nijssen09 Nijssen, R. P. (2006). *Fatigue Life Prediction and Strength Degradation of Wind Turbine Rotor Blade.* Ph.D. Thesis, Delft University of Technology.

Ning04 Ning, G., & Popov, B. N. (2004). Cycle Life Modeling of Lithium-Ion Batteries. *Journal of The Electrochemical Society, 151*(10), A1584-A1591.

Notter10 Notter, D. A., Gauch, M., Widmer, R., Wa¨ger, P., Stamp, A., Zah, R., et al. (2010). Contribution of Li-Ion Batteries to the Environmental Impact of Electric Vehicles. *Environmental Science & Technology, 44*(17), 6550-6556.

Nyman99 Nyman, T. (1999). *Fatigue and Residual Strength of Composite Aircraft Structures.* Ph.D. Thesis, Department of Aeronautics, Kungliga Tekniska Högskolan (Royal Institute of Technology), Stockholm.

Nyman08 Nyman, A., Behm, M., & Lindbergh, G. (2008). Electrochemical characterisation and modelling of the mass transport phenomena in $LiPF_6$-EC-EMC electrolyte. *Electrochimica Acta, 53*(22), 6356-6365.

Nyman10 Nyman, A., Zavalis, T. G., Elger, R., Behm, M., & Lindbergh, G. (2010). Analysis of the Polarization in a Li-Ion Battery Cell by Numerical Simulations. *Journal of The Electrochemical Society, 157*(11), A1236-A1246.

Nyman11 Nyman, A., Behm, M., & Lindbergh, G. (2011). A Theoretical and Experimental Study of the Mass Transport in Gel Electrolytes I. Mathematical Analysis of Characterization Method. *Journal of The Electrochemical Society, 158*(6), A628-A635.

O

Owen72 Owen, M. J., & Howe, R. J. (1972). The accumulation of damage in a glass-reinforced plastic under tensile and fatigue loading. *Journal of Physics D: Applied Physics, 5*(9), 1637.

P

Palmgren24 Palmgren, A. (1924). Die Lebensdauer von Kugellagern. *Zeitschrift des Vereins Deutscher Ingenieure, 68*(14), 339-341.

Park10 Park, M., Zhang, X., Chung, M., Less, G. B., & Sastry, A. M. (2010). A review of conduction phenomena in Li-ion batteries. *Journal of Power Sources, 195*(24), 7904-7929.

Park11 Park, J., Lu, W., & Sastry, A. M. (2011). Numerical Simulation of Stress Evolution in Lithium Manganese Dioxide Particles due to Coupled Phase Transition and Intercalation. *Journal of The Electrochemical Society, 158*(2), A201-A206.

Persson10 Persson, K., Sethuraman, V. A., Hardwick, L. J., Hinuma, Y., Meng, Y. S., van der Ven, A., et al. (2010). Lithium Diffusion in Graphitic Carbon. *The Journal of Physical Chemistry Letters, 1*(8), 1176-1180.

Pesaran09 Pesaran, A. (2009). Thermal Management Studies and Modeling. *U.S. DOE Hydrogen Program and Vehicle Technologies Program Annual Merit Review & Peer Evaluation Meeting*, *NREL/PR-540-45531.*

Peterson10 Peterson, S., Apt, J., & Whitacre, J. (2010). Lithium-ion battery cell degradation resulting from realistic vehicle and vehicle-to-grid utilization. *Journal of Power Sources, 195*(8), 2385-2392.

Pichler11 Pichler, F. (2011). *Anwendung der Finite-Elemente-Methode auf ein Lithium-Ionen-Batterie Modell*. Diploma Thesis, Faculty of Mathematics, University of Graz.

Pourmousavi12 Pourmousavi, S., Sharma, R., & Asghari, B. (2012). A framework for real-time power management of a grid-tied microgrid to extend battery lifetime and reduce cost of energy. 1-8.

Prochazka11 Prochazka, W., & Cifrain, M. (2011). Thermal Losses in Automotive Lithium Ion Cells – A Virtual Localization of Origin. *AABC Europe 2011, Mainz.*

Prochazka12 Prochazka, W., & Cifrain. (2012). An Ageing Experiment for Two Established Lithium Ion Cell Chemistries Using Reference Electrode Equipped Cells. *AABC Europe 2012, Mainz.*

Prochazka13 Prochazka, W., Pregartner, G., & Cifrain, M. (2013). Design-Of-Experiment and Statistical Modeling of a Large Scale Ageing Experiment for Two Popular Lithium Ion Cell Chemistries. *Journal of the Electrochemical Society*.

Prosini05 Prosini, P. P. (2005). Modeling the Voltage Profile for $LiFePO_4$. *Journal of The Electrochemical Society, 152*(10), A1925-A1929.

R

Ramasamy07 Ramasamy, R. P., Lee, J.-W., & Popov, B. N. (2007). Simulation of capacity loss in carbon electrode for lithium-ion cells during storage. *Journal of Power Sources, 166*(1), 266-272.

Reichert13 Reichert, M., Andre, D., Rösmann, A., Janssen, P., Bremes, H.-G., Sauer, D., et al. (2013). Influence of relaxation time on the lifetime of commercial lithium-ion cells . *Journal of Power Sources , 239*(0), 45-53.

Reimers06 Reimers, J. N. (2006). Predicting current flow in spiral wound cell geometries. *Journal of Power Sources, 158*(1), 663-672.

Renhart11 Renhart, W., Magele, C., Brandstätter, H., Koplenig, M., Scharrer, G., Heubrandtner, T., et al. (2011). Combined Electro-Thermal Analysis of Li-Ion Batteries applying the Finite Element Method. *ISEM 2011 Conference Proceedings*.

Rosenbrock60 Rosenbrock, H. H. (1960). An Automatic Method for Finding the Greatest or Least Value of a Function. *The Computer Journal, 3*(3), 175-184.

RHelp R-Project. (2012). Help Manual. *http://www.r-project.org.*

S

Safari09 Safari, M., Morcrette, M., Teyssot, A., & Delacourt, C. (2009). Multimodal Physics-Based Aging Model for Life Prediction of Li-Ion Batteries. *Journal of The Electrochemical Society, 156*(3), A145-A153.

Safari10 Safari, M., Morcrette, M., Teyssot, A., & Delacourt, C. (2010). Life-Prediction Methods for Lithium-Ion Batteries Derived from a Fatigue Approach Part I. *Journal of The Electrochemical Society, 157*(6), A713-A720.

Safari10A Safari, M., Morcrette, M., Teyssot, A., & Delacourt, C. (2010). Life Prediction Methods for Lithium-Ion Batteries Derived from a Fatigue Approach Part II. *Journal of The Electrochemical Society, 157*(7), A892-A898.

Safari11 Safari, M., & Delacourt, C. (2011). Mathematical Modeling of Lithium Iron Phosphate Electrode: Galvanostatic Charge/Discharge and Path Dependence. *Journal of The Electrochemical Society, 158*(2), A63-A73.

Safari11B Safari, M., & Delacourt, C. (2011). Aging of a Commercial Graphite/$LiFePO_4$ Cell. *Journal of The Electrochemical Society, 158*(10), A1123-A1135.

Santhanagopalan06 Santhanagopalan, S., Guo, Q., Ramadass, P., & White, R. E. (2006). Review of models for predicting the cycling performance of lithium ion batteries. *Journal of Power Sources, 156*(2), 620-628.

Santhanagopalan06B Santhanagopalan, S., & White, R. E. (2006). Online estimation of the state of charge of a lithium ion cell. *Journal of Power Sources, 161*(2), 1346-1355.

Sauer08 Sauer, D. U., & Wenzl, H. (2008). Comparison of different approaches for lifetime prediction of electrochemical systems--Using lead-acid batteries as example. *Journal of Power Sources, 176*(2), 534-546.

Sayle09 Sayle, T. X., Ngoepe, P. E., & Sayle, D. C. (2009). Simulating Mechanical Deformation in Nanomaterials with Application for Energy Storage in Nanoporous Architectures. *ACS Nano, 3*(10), 3308-3314.

Scharrer11 Scharrer, M., Cifrain, M., & Prochazka, W. (2011). Mechanistic PDE Model for Impedance Simulation of Lithium-Ion Cells. *Kraftwerk Batterie, Aachen.*

Scharrer12 Scharrer, M. K., Pichler, F., & Suhr, B. (2012). Simulation und Ansätze zur Parameteridentifikation eines 1D elektrochemischen Modells von Lithium-Ionen-Zellen. *NAFEMS deutschsprachige Konferenz 2012* (S. 106-109). NAFEMS.

Scharrer12C Scharrer, M. K., Suhr, B., & Watzenig, D. (2012). Surrogate Parameter Optimization based on Space Mapping for Lithium-Ion Cell Models. *15th International IGTE Symposium on Numerical Field Calculationin Electrical Engineering.* IGTE.

Schmidt10 Schmidt, A. P., Bitzer, M., Imre, Á. W., & Guzzella, L. (2010). Lumped Parameter Modeling Of Electrochemical And Thermal Dynamics In Lithium-Ion Batteries. *IFAC Symposium Advances in Automotive Control, 1*, 1.

Shepherd65 Shepherd, C. M. (1965). Design of Primary and Secondary Cells: II . An Equation Describing Battery Discharge. *Journal of The Electrochemical Society, 112*(7), 657-664.

Sinha10 Sinha, N. N., Shivakumara, C., & Munichandraiah, N. (2010). High Rate Capability of a Dual-Porosity $LiFePO_4$/C Composite. *ACS Applied Materials \& Interfaces, 2*(7), 2031-2038.

Smith12 Smith, A. J., Dahn, H. M., Burns, J. C., & Dahn, J. R. (2012). Long-Term Low-Rate Cycling of $LiCoO_2$/Graphite Li-Ion Cells at 55°C. *Journal of The Electrochemical Society, 159*(6), A705-A710.

Smith09 Smith, K., Kim, G.-H., & Pesaran, A. (2009). Modeling of Nonuniform Degradation in Large-Format Li-ion Batteries. *215th Electrochemical Society Meeting San Francisco, CA*, *NREL/PR-540-46031.*

Sommer12 Sommer, M. (2012). *Implementation of an Electrochemical Model for Lithium-Ion Battery Condition Monitoring.* Ph.D. Thesis, Graz University of Technology, Faculty for Electrical and Information Engineering.

Song10 Song, T., Xia, J., Lee, J.-H., Lee, D. H., Kwon, M.-S., Choi, J.-M., et al. (2010). Arrays of Sealed Silicon Nanotubes As Anodes for Lithium Ion Batteries. *Nano Letters, 10*(5), 1710-1716.

Srinivasan10 Srinivasan, V. (2010). LBNL OVT Merit Review, June 8th 2010. *http://www1.eere.energy.gov/vehiclesandfuels/pdfs/merit_review_2010/electrochemical_storage/es086_srinivasan_2010_p.pdf.*

Stamatis03 Stamatis, D. (2003). *Failure Mode and Effect Analysis: Fmea from Theory to Execution.* American Society for Quality.

Stephan09 Stephan, P., Schaber, K., Stephan, K., & Mayinger, F. (2009). *Thermodynamik Grundlagen und technische Anwendungen; Band 1: Einstoffsysteme Band 2: Mehrstoffsysteme und chemische Reaktionen* (Bd. 1 & 2). (K. S. Peter Stephan, & F. Mayinger, Hrsg.) Springer.

Stewart08 Stewart, S., Albertus, P., Srinivasan, V., Plitz, I., Pereira, N., Amatucci, G., et al. (2008). Optimizing the Performance of Lithium Titanate Spinel Paired with Activated Carbon or Iron Phosphate. *Journal of The Electrochemical Society, 155*(3), A253-A261.

Storn97 Storn, R., & Price, K. (1997). Differential Evolution – A Simple and Efficient Heuristic for global Optimization over Continuous Spaces. *Journal of Global Optimization, 11*(4), 341-359.

Sweitzer05 Sweitzer, K., & Ferguson, N. (11 -14 July, 2005). Mean Stress Effects On Random Fatigue Of Nonlinear Structures. *Proceedings of the 12th International Congress on Sound and Vibration.*

T

Tang09 Tang, M., Albertus, P., & Newman, J. (2009). Two-Dimensional Modeling of Lithium Deposition during Cell Charging. *Journal of The Electrochemical Society, 156*(5), A390-A399.

Täubert10 Täubert, C., Fleischhammer, M., Wohlfahrt-Mehrens, M., Wietelmann, U., & Buhrmester, T. (2010). LiBOB as Electrolyte Salt or Additive for Lithium-Ion Batteries

Based on $LiNi_{0.8}Co_{0.15}Al_{0.05}O_2$/Graphite. *Journal of the Electrochemical Society, 157*, A721 - A728.

Thele08 Thele, M. (2008). *A contribution to the modelling of the charge acceptance of lead-acid batteries – using frequency and time domain based concepts.* Ph.D. Thesis, RWTH Aachen University.

Thomas03 Thomas, K. E., & Newman, J. (2003). Heats of mixing and of entropy in porous insertion electrodes. *Journal of Power Sources, 119-121*, 844-849.

Thomas08 Thomas, E., Bloom, I., Christophersen, J., & Battaglia, V. (2008). Statistical methodology for predicting the life of lithium-ion cells via accelerated degradation testing. *Journal of Power Sources, 184*(1), 312-317.

Thompson79 Thompson, A. H. (1979). Electrochemical Potential Spectroscopy: A New Electrochemical Measurement. *Journal of The Electrochemical Society, 126*(4), 608-616.

Tran11 Tran, H. Y., Täubert, C., Fleischhammer, M., Axmann, P., Küppers, L., & Wohlfahrt-Mehrens, M. (2011). $LiMn_2O_4$ Spinel/$LiNi_{0.8}Co_{0.15}Al_{0.05}O_2$ Blends as Cathode Materials for Lithium-Ion Batteries. *Journal of The Electrochemical Society, 158*(5), A556-A561.

Tröltzsch05 Tröltzsch, U. (2005). *Modellbasierte Zustandsdiagnose von Gerätebatterien.* PhD Thesis, Universität der Bundeswehr München, Fakultät für Elektrotechnik und Informationstechnik, Universität der Bundeswehr München, Fakultät für Elektrotechnik und Informationstechnik, Neubiberg.

V

Valoen05 Valoen, L. O., & Reimers, J. N. (2005). Transport Properties of LiPF[sub 6]-Based Li-Ion Battery Electrolytes. *Journal of The Electrochemical Society, 152*(5), A882-A891.

Vergossen11 Vergossen, D. (2011). Parameterization of a Loithium-Ion Cell Model for Simulation of the Dynamic Baehaviour of a 12 Volt Starter Battery. *Kraftwerk Batterie 2011.*

Vetter05 Vetter, J., Novàk, P., Wagner, M., Veit, C., Möller, K.-C., Besenhard, J., et al. (2005). Ageing mechanisms in lithium-ion batteries. *Journal of Power Sources, 147*(1-2), 269-281.

W

Waag13 Waag, W., Käbitz, S., & Sauer, D. U. (2013). Experimental investigation of the lithium-ion battery impedance characteristic at various conditions and aging states and its influence on the application. *Applied Energy, 102*(0), 885-897.

Wahdame09 Wahdame, B., Candusso, D., François, X., Harel, F., Kauffmann, J.-M., & Coquery, G. (2009). Design of experiment techniques for fuel cell characterisation and development. *International Journal of Hydrogen Energy, 34*(2), 967-980.

Wiedemann07 Wiedemann, U. (2007). *Alterungsuntersuchungen an Nickelmetall-Hydrid-Hochleistungsakkumulatoren für Hybridfahrzeuge.* Ph.D. Thesis, Universität Ulm.

WohlfahrtMehrens04 Wohlfahrt-Mehrens, M., Vogler, C., & Garche, J. (2004). Aging mechanisms of lithium cathode materials. *Journal of Power Sources, 127*(1-2), 58-64.

Y

Yabuuchi03 Yabuuchi, N., & Ohzuku, T. (2003). Novel lithium insertion material of $LiCo_{1/3}Ni_{1/3}Mn_{1/3}O_2$ for advanced lithium-ion batteries. *Journal of Power Sources, 119–121*(0), 171-174.

Z

Zaghib08 Zaghib, K., Mauger, A., Gendron, F., & Julien, C. M. (2008). Surface Effects on the Physical and Electrochemical Properties of Thin LiFePO4 Particles. *Chemistry of Materials, 20*(2), 462-469.

Zhang07 Zhang, Q., & White, R. E. (2007). Calendar life study of Li-ion pouch cells. *Journal of Power Sources, 173*(2), 990-997.

Zhang08 Zhang, X., Sastry, A. M., & Shyy, W. (2008). Intercalation-Induced Stress and Heat Generation within Single Lithium-Ion Battery Cathode Particles. *Journal of The Electrochemical Society, 155*, A542-A552.

Zhang11 Zhang, X., Jiang, W., Zhu, X., Mauger, A., Qilu, & Julien, C. (2011). Aging of $LiNi_{1/3}Mn_{1/3}Co_{1/3}O_2$ cathode material upon exposure to H_2O. *Journal of Power Sources, 196*(11), 5102-5108.

Zhou06 Zhou, J., Danilov, D., & Notten, P. (2006). A Novel Method for the In Situ Determination of Concentration Gradients in the Electrolyte of Li-Ion Batteries. *Chemistry - A European Journal, 12*, 7125-7132.

Zugmann11 Zugmann, S. (2011). *Messung von Lithium-Ionen Überführungszahlen an Elektrolyten für Lithium-Ionen Batterien.* PhD Thesis, Fakultät für Chemie und Pharmazie der Universität Regensburg.

Zugmann11B Zugmann, S., Fleischmann, M., Amereller, M., Gschwind, R., Wiemhöfer, H., & Gores, H. (2011). Measurement of transference numbers for lithium ion electrolytes via four different methods, a comparative study. *Electrochimica Acta, 56*(11), 3926-3933.